UNIVERSITY OF SOUTHAMPTON

Light-Matter Interactions on Nano-Structured Metallic Films

by

Timothy Andrew Kelf

A thesis submitted in partial fulfillment for the
degree of Doctor of Philosophy

in the
Faculty of Engineering, Science and Mathematics
School of Physics and Astronomy

February 2006

UNIVERSITY OF SOUTHAMPTON

ABSTRACT

FACULTY OF ENGINEERING, SCIENCE AND MATHEMATICS
SCHOOL OF PHYSICS AND ASTRONOMY

Doctor of Philosophy

by Timothy Andrew Kelf

This thesis describes a study into the optical properties of nano-structured metallic films. Structures are produced by electrochemically depositing metal through a self-assembled template of polymer micro-spheres. This versatile technique allows nano-structured surface made from almost any metal to be produced quickly and cheaply. Geometries ranging from array of shallow dishes, to sharp metallic spikes and encapsulated spherical cavities can all be produced on the same sample. This thesis presents an in-depth study into the properties delocalised and localised surface plasmon polaritons. These plasmons can be tuned in energy by controlling the sample geometry and angle of the incident light. The coupling between these two types of plasmon is also investigated and theories are put forward to understand the observed results. These findings could prove useful in the design of plasmon guiding and computing devices. With an understanding into the plasmonic properties of the metallic nanostructures, research is undertaken to explore how the associate local electric field couples to molecules adsorbed onto a samples surface. A strong correlation between surface plasmons and enhanced Raman scattering is found, leading the observation of the beaming of the Raman scattered light. The nano-structured substrates are also shown to have excellent reproducibility as well as enhancement of the Raman signals, leading to applications such as high sensitivity molecular sensors. Finally, the interaction between organic semiconductor molecules and surface plasmons is explored. A strong interaction between the different states is found and plasmon enhanced fluorescence is also observed. These studies open the way for greater control over the exciton states, which have potential for the use in novel laser systems.

Contents

List of Figures

Declaration of Authorship

I, Timothy Andrew Kelf, declare that the thesis entitled 'Light-Matter Interactions on Nano-Structured Metallic Films' and the work presented in it are my own. I confirm that:

- this work was done wholly or mainly while in candidature for a research degree at this University;

- where any part of this thesis has previously been submitted for a degree or any other qualification at this University or any other institution, this has been clearly stated;

- where I have consulted the published work of others, this is always clearly attributed;

- where I have quoted from the work of others, the source is always given. With the exception of such quotations, this thesis is entirely my own work;

- I have acknowledged all main sources of help;

- where the thesis is based on work done by myself jointly with others, I have made clear exactly what was done by others and what I have contributed myself;

- parts of this work have been published as listed on the following page.

Signed:

Timothy A Kelf

February 2006

Publications

Plasmonic bandgaps and Trapped Photons on Nanostructured Metal Surfaces
T.A. Kelf, Y. Sugawara, J.J. Baumberg, M.E. Abdelsalam, P.N. Bartlett.
Phys. Rev. Lett. **95**, 116802 (2005)

Angle-Resolved Surface-Enhanced Raman Scattering on Metallic Nanostructured Plasmonic Crystals
J.J. Baumberg, T.A. Kelf, Y. Sugawara, S. Cintra, M.E. Abdelsalam, P.N. Bartlett, A.E. Russell.
Nano. Lett. **5**, 2262 (2005)

Sculpted substrates for SERS
S. Cintra, M.E. Abdelsalam, P.N. Bartlett, J.J. Baumberg, T.A. Kelf, Y. Sugawara, and A.E. Russell.
Faraday. Discuss. **136**, 16 (2005)

Electrochemical SERS at a structured gold surface
M.E. Abdelsalam, P.N. Bartlett, J.J. Baumberg, T.A. Kelf, S. Pelfrey, and A.E. Russell.
Electrochem. Commun **7**, 740 (2005).

Interaction between localized and free plasmons on a nanoporous metal surface
T.V. Teperik, V.V. Popov, J.F. Garcìa de Abajo, T.A Kelf, Y. Sugawara, J.J. Baumberg.
Submitted *Opt. Express.* (2005)

Whispering Gallery Mode Emission at Telecommunications-Window Wavelengths Using PbSe Nanocrystals Attached to Photonic Beads
C.E. Finlayson, P.J.A. Sazio, R. Sanchez-Martin, M. Bradley, T.A. Kelf, J.J. Baumberg.
Senicond. Sci. Tech. **21**, L21 (2006)

Wetting of Regularly Structured Gold Surfaces
M.E. Abdelsalam, P.N. Bartlett, T.A. Kelf, and J.J. Baumberg.
Langmuir. **21**, 1753 (2005)

Tuneable Resonant Optical Microcavities by Self-Assembled Templating
G.V. Prakash, L. Besombes, T.A. Kelf, and J.J. Baumberg.
Opt. Lett. **29**, 1500 (2004)

Acknowledgements

I would like to thank my supervisor, Professor Jeremy Baumberg, for giving me the opportunity to undertake the research outlined in this thesis. Along with his help and support, as well as his hard work on the project, his enthusiasm has maintained my growing interests in the various field of research that the projects have touch over the years. I would also like to thank Dr. Yoshihiro Sugawara for his hard work. This has helped advance this research project enormously over the past two years, as well as help me understand many of aspects of the project. A big thank you must also be extended to the members of the chemistry department, Dr. Mamdouh Abdelsalam and Suzanne Cintra for producing the samples that allowed all my research to become possible, as well as all the other work they have done on other aspects of the chemistry side of this project. I would also like to thank Professor Phil Bartlett and Dr. Andrea Russell for their input and discussions, which have helped shape the direction my research has taken. I also would like to thank Dr. Steve Coyle who started this project, and has provided me with invaluable help and continued support through my research. Further thanks are given to Dr. David Smith, Matthew Markham and Nic Perney for all their help on various aspects of the projects I have worked on. I would also like to thank everyone in nano-photonics group for all their support, discussions and mainly providing sufficient distractions to maintain a healthy level of sanity. I would finally like to thank my family for their encouragement over the years, along with everyone else who has helped me to fulfil this goal.

Nomenclature

i	Imaginary number $= \sqrt{-1}$
h	Planck's constant $= 6.626\text{x}10^{-34} Js$
e	Electron charge $= 1.602\text{x}10^{-19} C$
c	Speed of light $= 2.998\text{x}10^{8} ms^{-1}$
N_A	Avogadro's number $= 6.022\text{x}10^{23} mol^{-1}$
μ	Free space magnetic permeability $= 4\text{x}10^{-7} Hm^{-1}$
$\mathbf{E}$	Electric field vector
$\mathbf{B}$	Magnetic induction vector
$\mathbf{H}$	Magnetic vector
$\mathbf{D}$	Electric displacement vector
$\mathbf{J}$	Current density
$\mathbf{r}$	Spatial vector
ρ	Charge density
σ	Conductivity
τ	Relaxation time
δ	skin depth
t	Time
x	Displacement
m	Mass
ν	Frequency
ω	Angular frequency $= 2\pi\nu$
λ	Wavelength
ϵ	Dielectric constant
$\hat{\epsilon}$	Complex dielectric constant $= \epsilon_1 + \epsilon_2$
a	Period of a structure
G	Reciprocal lattice vector
k	Wave vector
$\hat{k}$	Complex wave vector $= k_1 + k_2$
n	Refractive index
κ	Extinction coefficient
$\hat{n}$	Complex refractive index $= n + \kappa$
b	Damping coefficient

K	Spring constant
ω_p	Plasma frequency
ω_0	Resonant frequency
γ	Damping coefficient
N	Number of molecules
M	Transition moment
P	Dipole moment
I	Intensity
θ	Incident angle
ϕ	Sample orientation
$\bar{t}$	Normalised sample thickness
TE	Transverse Electric
TM	Transverse Magnetic
SPP	Surface plasmon polariton
$SERS$	Surface enhanced Raman scattering

The most beautiful thing we can experience is the mysterious. It is the source of all true art and science.

Albert Einstein

Chapter 1

Introduction

Within a few short decades the field of nanotechnology has risen from fiction into pure science. Whilst still in its infancy, nanotechnology brings together physics, chemistry and biology as well as mathematics, engineering and computer science. This provides rich grounds for new research, and the growing potential to fulfil one of science's greatest quests: to understand and mimic biological systems. Over the past 1.5 billion years nature has optimised structures and systems of such breath-taking complexity that modern research is only now starting to unlock their secrets. Nature's success comes from the nano-scale molecules that all life forms are made from. Individually, these molecules can perform simple tasks, but do not represent a living entity. However, when combined, the feedback between molecules allows the system to respond to stimuli, and ultimately reproduce - the essence of life.

Richard Feynman was one of the first to appreciate the capabilities opened up if one is able to control nano-scale systems[13], and since then solid state physics has made great progress. It is now possible of accurately fabricate devices on the hundreds of nanometres scale; however, the main limitation of such devices is their planer structuring. This creates ever-growing difficulties to ensure that every individual component is linked to the whole system. The harnessing of self-assembled biological systems could provide means to build three-dimensional devices, and so allow, among other things, smaller and faster computers. Currently this is still in the realm of science fiction as there are many challenges still facing this goal.

Today, science is capable of controlling and understanding the behaviour of atomic systems as well as objects with dimensions greater than about a micron. The region between these two length scales is more difficult to study. A major reason for these difficulties is that much of science relies on optically detecting the objects under study. Unfortunately, light can only provide information on structures larger than its wavelength. Visible light has wavelengths between 400nm and 900nm and so objects smaller than this cannot be directly studied. A further problem is that the coupling of light to nanometre structures is poor. This provides yet more challenges in the understanding of nano-scale objects.

This thesis concentrates on an entity known as a surface plasmon polariton (SPP), a quantised charge fluctuation pinned to a metal's surface. Whilst at first appearing to have no obvious link to the above discussion, it will be shown that these SPPs can effectively bridge the gap between optical and molecular systems. In so doing, SPPs hold great potential for understanding nano-scale physical systems, along with providing a means to study molecules in greater detail.

To produce SPPs a regular structured metal surface can be used, such as a diffraction grating. For this thesis, two-dimensionally periodic metal nano-structures are produced using a self-assembly and electrochemical deposition process. A scanning electron microscope image of one such sample is shown in figure 1.2a. The surfaces produced through this 'natural lithography' are of excellent quality in terms of both smoothness and regularity. This allows many interesting and varied experiments to be performed. All sample production, characterisation and experimentation is performed within the photonic metals group at the University of Southampton, a group which spans the departments of chemistry and physics.

Surface plasmons were discovered almost 50 years ago[14], however, it has been the last decade that has seen a rapid growth of research in this field. Early work on SPPs employed a coupling mechanism through a prism; whist this produced many interesting results, the recent progress has been obtained through the ability to produce and characterise grating structures on the 100's of nanometre length scales. Such structures are highly diffractive and allow light to couple to SPPs through scattering processes. Figure 1.1 outlines three important pieces of research of recent years.

Figure 1.1a demonstrates the direct imaging on SPP mode, performed by W. L. Barnes *et al.*[2]. This work records the spectra of white light total internally reflected off the base of a prism of different angles. The top image shows the result when a smooth silver film is brought within 100nm of the base of the prism. The image shows inverse wavelength plotted against angle of the incident light. The colours are representative of wavelength and black corresponds to a reduction in the intensity of the reflected light relative to that when no metal film is present. As can be seen, there is a well defined region of the image where light is coupled onto the surface of the metal (hence a reduction in the observed intensity). This occurs evanescently and corresponds to the excitation of a SPP wave. The second image in figure 1.1a shows a scanning electron microscope (SEM) image of a silver surface pattered with a triangular array of dots. The dots are separated by 300nm and are have radii of 100nm. The bottom image shows the optical coupling to this modified silver surface. Clearly this is quite different from the top image and what can be seen is a region of frequency where there exists no SPP mode - a plasmonic band gap. This result is important as it shows that the propagation of SPPs can be controlled

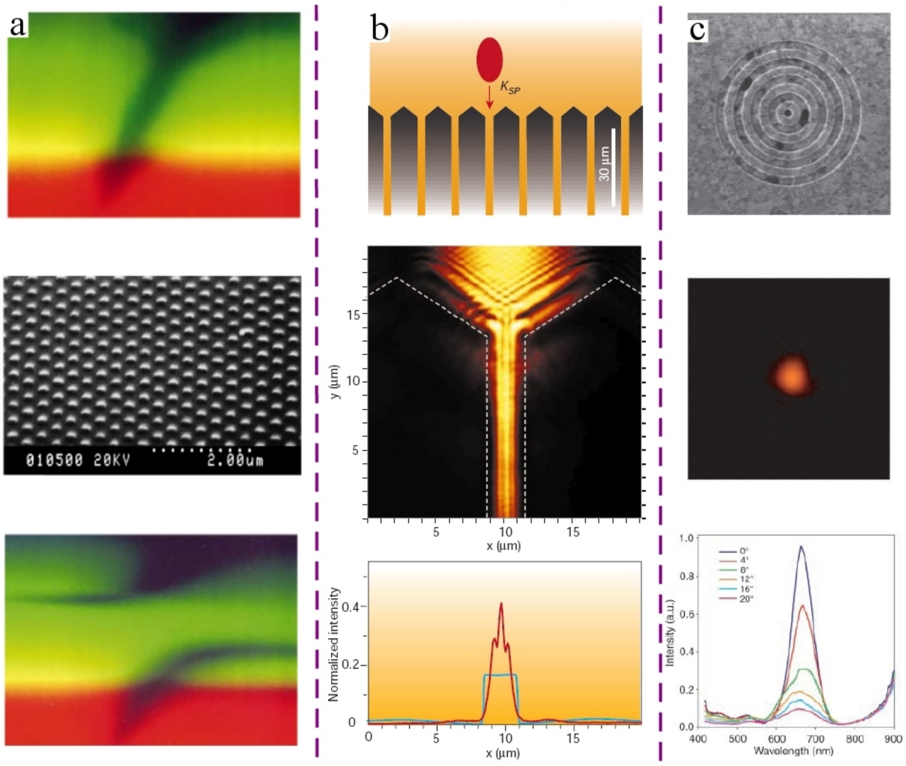

FIGURE 1.1: (a) Top: Direct imaging of a SPP on smooth silver. Middle: SEM image of a nano-structured silver sample, this structuring radically alters the SPP dispersion as shown in the bottom image. Taken from [1], original work from [2]. (b) Top: Schematic of a SPP waveguide. Middle: Near-field imaging of a SPP wave travelling along the guiding region, cross-section of this shown in the bottom image. Taken from [1], original work from [3]. (c) Top: SEM image of structure used for the enhanced transmission experiments. Middle: Image of transmitted light, cross-sections of this shown in the bottom image. Taken from [4].

through modifying the surface structure. This is reminiscent of photonic crystals and the photonic band gaps which have received a huge amount of interest over the last decade for routing and controlling the flow of light. Plasmonic crystals, however, have a number of advantages over their photonic counterparts. Firstly, plasmons are completely confined to the metal/dielectric interface so pattering in a third dimension is not required (as will be shown later in this thesis this is quite tricky). Secondly, there is a significant difference in size scales involved between plasmonic and photonic devices. Photonic crystals are limited in size to structuring on the wavelength scale. As shown in the figure, plasmonic crystals can be made significantly smaller than this value, and so one day could be useful in computing of networking applications.

The first steps towards this goal are shown in figure 1.1b, showing work done by J. -C. Weeber *et al.*[3]. Here a gold strip 2.5μm wide is used to form a SPP waveguide. The SPP is launched viva a grating situated off the top of the image and is channelled into the waveguide using the funnelling structure. The SPP is imaged using a near-field scanning microscopy and can be seen to be well pinned to the wave-guiding structure. Again, the structure is of sub-wavelength width and it can also be seen the losses incurred through absorption within the metal are small over the distance observed.

Figure 1.1c shows an interesting, if slightly controversial, result that brought the field of plasmonics to into the public eye. This work was carried out by T. W. Ebbesen *et al.*[15, 4] and is concerned with the transmission of light through pattered metal surfaces. The top image shows an SEM image of a structure milled into a silver surface; the central hole is 300nm in diameter and is drilled right through the silver layer to the glass surface beneath. The structure forms a grating, and hence excites SPP modes. What were interesting about this research is the transmission properties of the structure. The hole is significantly smaller than the wavelength of light and so no transmission would immediately be expected. The middle image shows the resulting transmitted light, and the bottom image graphs the transmission spectra for different incident angles. What can be seen is that light of wavelength twice the size of the hole is effectively coupled through the silver surface. While the absolute transmitted intensity is small, relative to the size of the hole the transmission is found to exceed 100%! This is an intriguing result and understood through the incident light exciting a SPP mode which can travel through the central hole. On the other side the SPP can couple back to optical field, and hence induce a transmission of light. Since the light is coupling to the SPP mode over the whole area of the pattered structure, this is the effective amount of light possible to be transmitted - hence the above unity value. Recently this effect has been used to perform nano-lithography in the sub-wavelength regime[16]. This allows the production of smaller feature sizes without having to develop UV-laser sources, thus greatly reducing the cost of processing.

While the work outlined so far has concentrated on SPP waves travelling at close to the speed of light over metal surfaces, other research has been performed on SPP modes localised through restrictive geometries. These localised SPPs are standing waves, and most work has concentrated on spherical geometries usually with diameters of order 100nm. The electromagnetic interactions on these structures can be described in terms of Mie scattering, and it is this which allows the coupling of the localised SPP to the incident light. Much of this work has been carried out by the group of N. J. Halas *et al.*[17] and has shown that small changes is the diameter of a silver particle can significantly alter the resonance energy of a SPP mode.

Both localised and delocalised plasmons - SPP modes and standing wave SPP modes - physically correspond to surface charge oscillations with an associated electric field. Over the years a great deal of work has been done on modelling SPP in nano-systems, most notably the work by M. I. Stockman and D. J. Bergman[18]. These theoretical models have primarily been involved with understand how, when tightly confined, SPPs can produce electric field strengths many orders of magnitude above that of the incident light. This enhanced electric field aids an effect which has now become deeply connected with the field of plasmonics, that of surface enhanced Raman scattering (SERS). This effect enhances Raman transitions within molecules on a metallic surface by seven or more orders of magnitude! While still not fully understood, this effect is known to mainly come from the plasmonic behaviour of the metals used (metals that show no plasmonic behaviour produce no enhanced Raman signals). Using SERS, single molecule spectroscopy has been achieved[19, 20], providing proof of concept of extremely high sensitivity devices. 'SERS active substrates' as they are often referred, are most often made from silver colloids. It is believed that the electric fields where the colloids touch provide much, if not all, of the observed Raman signal. With high sensitivity and the advantage of easy molecular analysis from the observed Raman transitions SERS is currently a field beginning to be commercialised[21] for bio-medical applications[22] as well as homeland security. Indeed, as will be shown later in this thesis the plasmonic surfaces studied are in many ways ideal to studying and applying the SERS process to real world applications.

This thesis is a collection of related experiments performed by the author over the past three years. The topics span from the fundamental characterisation of the surfaces, through the analysis of the plasmonic properties, to the interaction of these surfaces with molecules adsorbed on their surface. This requires the partitioning of this thesis into a number of chapters as outlined below.

Rather than jumping straight into the field of plasmonics, it is useful to understand the fundamental optical properties of nano-structures. This is outlined in chapter 2, which also provides a background into the field of self-assembly.

Chapter 3 then details the fundamental properties of metals, before looking at the formation of SPPs from a theoretical viewpoint. SPPs are shown to exist as both localised and delocalised states, which exhibit very different characteristics, shown schematically in figure 1.2c.

Chapter 4 subsequently concentrates on the characterisation and physical properties of the nano-metallic structures. Not only are these nano-structures highly opalescent and support a variety of plasmon modes, they also possess interesting physical properties. Figure 1.2b shows a droplet of water sitting on one such surface. Detailed experiments have shown that by adjusting the surface geometry, the contact angle of the droplet can be varied. This is interesting from a fundamental viewpoint but could also have potential uses in, for example, self-cleaning structures.

Chapter 5 then outlines the setup of the experiments performed using a computer controlled goniometer, shown in figure 1.2d. This setup produces large volumes of data and so an explanation into the different graphical representation techniques is also presented.

After this thorough background, chapter 6 outlines the experiments performed to characterise the different types of SPP found on the nano-structures surfaces. These fall

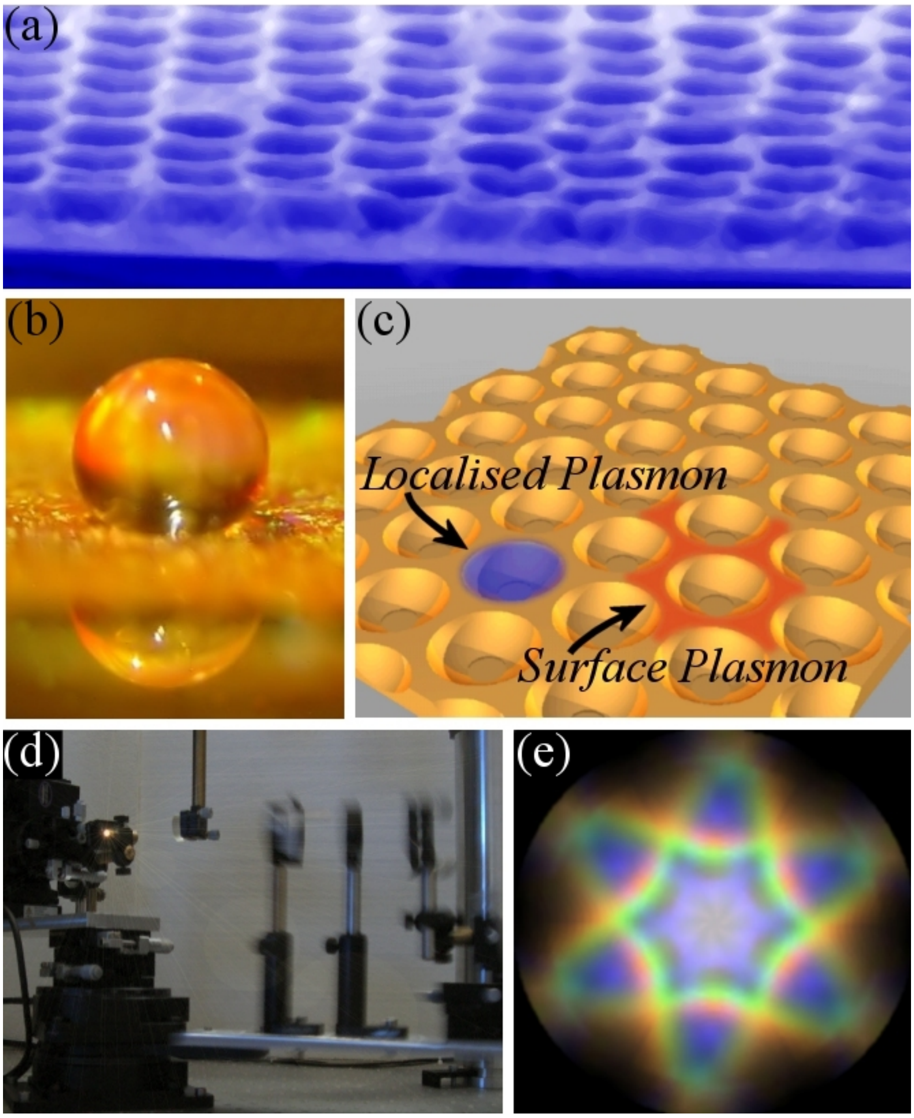

Figure 1.2: (a) Scanning electron image of a typical nano-structured sample. (b) Photograph of a water droplet sitting on a sample, by varying the geometry of the surface the contact angle of the drop can be altered. (c) Cartoon showing schematically the different types of plasmons found on the surfaces. (d) Photograph of the automated goniometer used to acquire reflectivity data. (e) Simulated distribution of Raman scattered light leaving a sample. This image corresponds to the expected Raman image collected in the back focal plane of a microscope objective.

into two categories, shown in figure 1.2c, those of localised and delocalised modes. Delocalised plasmons are highly dependent on the sample orientation as well as the incident angle of the light source, and have sharp absorption resonances. Localised plasmons, on the other hand, have broader resonances and an isotropic dispersion. These plasmons are studied in detail and an understanding of their properties is presented.

With the fundamental properties of the plasmons acquired, chapter 7 then discusses the interactions between the localised and delocalised plasmon modes. It is shown that the two types of plasmon can be brought into resonance, where they strongly couple together. This creates a mixing into new plasmonic modes, which are studied in detail.

Further research is then outlined on the control of the plasmonic properties by varying the dielectric and metallic media.

These chapters provide a detailed understanding into the plasmonic surfaces, allowing a study into other topics of current interest throughout the fields of plasmonics and nano-technology. Chapter 8 explains the current theoretical knowledge of surface enhanced Raman scattering (SERS). Chapter 9 the outlines the experimental SERS results obtained. Notable, these show the beaming of the Raman scattered light from plamsonic modes on the nano-structured surfaces. This is important for understanding the SERS process because it shows that the molecules scatter into plasmonic modes, not photonic ones. These finding are useful in the optimisation of potential sensor devices. For example, figure 1.2e shows the simulated output Raman scattered light that would be observed from three vibrational bands of the molecule benzene thiol when it is absorbed onto a particular nano-structured substrate. This clearly shows the beaming and splitting of the vibrational modes, and could be directly linked to a CCD camera for detection and analysis.

Chapter 10 then discusses some more recent work, looking at the interactions between delocalised plasmons and the excitonic states of organic dye molecules. These experiments show strong coupling between plasmon and excitons, and paves the way for further interesting research. The plasmon modes are also shown to enhance the fluorescence from the exciton states, which could be of potential use for greater efficiency light emitter.

Finally, chapter 11 summarises the finding of the previous chapters and speculates on the many future directions that may be of interest to understand the processes at work behind the many phenomena presented.

Chapter 2

Introduction to Nano-Structuring

The periodic structure of atoms within a conducting medium gives rise to different electronic bands, allowing the control of electrons through a material[23]; mastering the use of these bands has lead to the semiconductor revolution and ultimately the personal computer. This has been understood for many years, however, it was not until 1987 that an analogous system was proposed to control the properties of photons[24, 25]. These photonic crystals are made from dielectric materials patterned on the sub-micron scale. Light in such materials is scattered into photonic crystal modes and can give rise to photonic bandgaps where the propagation of light of certain frequencies is forbidden. This work allows a fine degree of control over the optical field within a material, a feat mastered by nature many millions of years ago (fig 2.1). Here the structure of the butterfly's wing forbids the transmission of blue light, giving the wing a bright opalescent blue colouration[5]. The production of photonic crystals allows fantastic control over light, and can be used to produce micron-scale optical circuits, though which the light is squeezed and manipulated. This technology could one day be used to produce all-optical computing devices, capable of faster processing speeds than current electron-based systems.

Whilst not directly related to plasmonics, knowledge of pure photonic systems is essential in understanding the properties of the more complex photonic metal systems presented in this thesis. It is also of historical interest to trace the interwoven paths of the different areas of research discussed in this thesis. This section will start from the very beginning - Maxwell's equations - and from here build up an understanding of the properties of materials patterned on the wavelength scale. With this understanding, a discussion into more complex photonic structures will be presented.

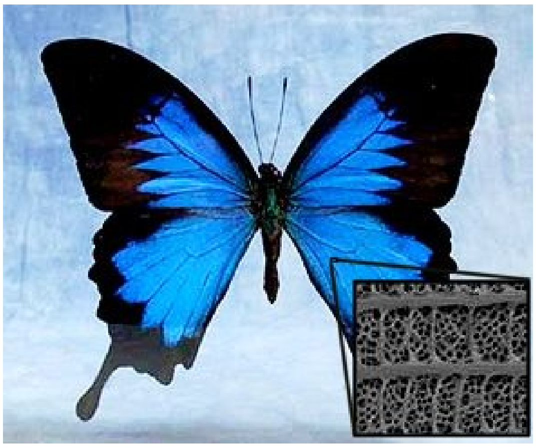

Figure 2.1: This Papilio Ulysses butterfly, indigenous to rainforests of Oceania, is highly iridescent due to nano-structuring of its wings (inset), from [5].

2.1 Photonic Structures

The structuring of a dielectric medium gives rise to a change in its optical response. If the material structuring is much smaller than the wavelength of light, the optical properties of the medium can be accounted for using an effective refractive index. This is calculated using a weighted average of the refractive indices of the different dielectrics and the whole structure act as a single material. If the structuring is very large compared to the wavelength of light, then a ray optics approach can be employed to easily calculate the behaviour of the light. However, when the structuring becomes comparable to optical wavelengths many interesting properties emerge. Thus, a good starting point in understanding these structures is that of Maxwell's equations describing the properties of light within a constant dielectric medium.

An electromagnetic wave can be expressed in terms of an electric field vector, **E** and a magnetic induction vector **B**. When incident on a material the terms **H**, the magnetic vector, **D**, the electric displacement, **J**, the current density and ρ, the charge density are also defined. Maxwell's equations, in S.I. units, take the following form.

$$\nabla \cdot \mathbf{B} = 0 \tag{2.1}$$

$$\nabla \cdot \mathbf{D} = \rho \tag{2.2}$$

$$\nabla \times \mathbf{E} + \frac{\delta \mathbf{B}}{\delta t} = 0 \tag{2.3}$$

$$\nabla \times \mathbf{H} - \frac{\delta \mathbf{D}}{\delta t} = \mathbf{J} \tag{2.4}$$

To simplify these equations, a number of assumptions can be applied. First, it is assumed that the medium contains no free charges, currents or sources of light; this means that both **J** and ρ can be set to zero. Next, the considered field strengths are assumed to be small enough to consider the relationships **D** to **E** and **B** to **H** as linear. Thirdly the material is set to be macroscopic and isotropic, enforcing a scalar dielectric constant, $\epsilon\left(\mathbf{r},\omega\right)$, where $\mathbf{r}$ is a spatial vector and ω is the angular frequency of the light. Finally, it is assumed that ϵ is constant with frequency and real, corresponding to a loss-less material in a sensible frequency range[26]. These assumptions give rise to the following relationships between the electric field and material quantities.

$$\mathbf{D}\left(\mathbf{r}\right)=\epsilon\left(\mathbf{r}\right)\mathbf{E}\left(\mathbf{r}\right)\quad\text{and}\quad\mathbf{B}=\mu\mathbf{H}\quad\text{and}\quad\mathbf{J}=\sigma\mathbf{E}=0 \tag{2.5}$$

Where μ is the magnetic permeability and σ is the conductivity of the medium. These assumptions also allow the time dependence of the field to be written simply as:

$$\mathbf{H}\left(\mathbf{r},t\right)=\mathbf{H}\left(\mathbf{r}\right)e^{i\omega t}\quad\text{and}\quad\mathbf{E}\left(\mathbf{r},t\right)=\mathbf{E}\left(\mathbf{r}\right)e^{i\omega t} \tag{2.6}$$

for a mixed dielectric medium and using of the previous assumptions, Maxwell's equations can be rearranged into an expression purely in terms of the magnetic vector $\mathbf{H}(\mathbf{r})$ [6].

$$\nabla\times\left[\frac{1}{\epsilon(\mathbf{r})}\nabla\times\mathbf{H}(\mathbf{r})\right]=\mu_0\omega^2\mathbf{H}(\mathbf{r}) \tag{2.7}$$

This general expression governs the response of an optical field in a mixed dielectric medium, where the dependence on position arises through the dielectric constant. Therefore, if the positional dependence of the dielectric constant of any medium is know, the solutions to equation 2.7 will provide the solutions to the optical modes. Unfortunately, this is non-trivial and, outside of the simplest cases, requires a fair amount of computational power to provide answers. This is beyond the scope of this thesis so, instead, a more intuitive approach will be discussed.

2.2 One Dimensional Photonic Crystals

A one-dimensional photonic crystal is made of layers with alternating of dielectric constant, as shown in figure 2.2a. This system repeats in the z-direction with period a, which will be of order the wavelength of the light. If the system is viewed in 'k-space', where $k=2\pi/\lambda$, this can be represented as a one-dimensional line of scattering points with separation equal to the reciprocal lattice vector, $G=2\pi/a$, (fig 2.2b and c). From this representation, since every point looks identical, it is possible to write $k = k_0 \pm nG$, or more specifically a mode with wave vector k_0 and a mode with wave vector k_0 ± nG have the same dispersion and couple together, forming a new set of modes. A plane wave travelling in the z-direction, along the line of periodicity, will be scattered every distance a. This gives rise to forward and backward propagating waves within the structures. These waves will interfere to form standing waves. Now, the light can no longer be described as a pure optical field as it has become intimately linked with the structure. The optical field is now mixed state known as a polariton.

The dispersion for light in an isotropic dielectric material is given by the equation:

$$\omega(k) = \frac{c\,|k|}{\sqrt{\epsilon_d}} \tag{2.8}$$

where c is the speed of light and ϵ_d is a constant, given by the properties of the dielectric medium. This equation shows that the energy of light varies linearly with momentum, with zero momentum corresponding to zero energy. This dispersion is plotted in figure 2.2c, and corresponds to the x and y directions along a given line of the photonic crystal. The gradient of the dispersion will be different depending on the medium considered due to the different dielectric constants. In the z-direction, along the line of the periodicity, the point $k = 0$ can be defined at any of the scattering sites. This translational symmetry allows $k = 0$ to be defined at *every* scattering site, and so the vacuum dispersion relation is repeated, as shown in figure 2.2b. Due to the repetition of the structure, there is a lot of degeneracy throughout k-space. Attention can, therefore, be restricted to the small, non-degenerate, region inside what is known as the Brillouin zone. The dispersion of this structure is drawn in red on figure 2.2b and shows that the optical modes fold back on themselves when they reach the Brillouin zone. This folding arises from the scattering of neighbouring sites and leads to a quite different dispersion for a periodically structure surface over that of an isotropic material.

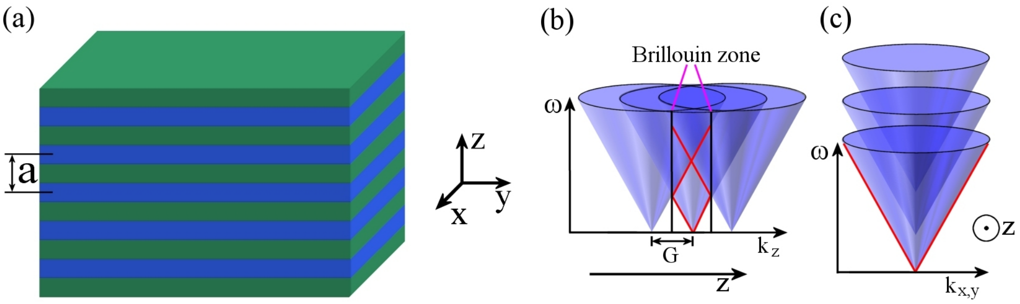

FIGURE 2.2: (a) Periodically structured dielectric stack with periodicity a, (b, c) k-space representation of dielectric stack showing schematic of the dispersion relation. Lattice vector, G, incident light wave-vector, k and Brillouin zone also defined

The schematic drawn in figure 2.2 assumes that there is no interaction between the dispersion bands from the different lattice sites, a condition known as the weak scattering approximation. This allows complicated dielectric structures to be modelled with relative ease, but is limited to situations where the contrast between the different dielectric constants is small. To emphasise this, figure 2.3 plots the dispersion relation of the previous structure under two conditions using the full mathematical calculations.

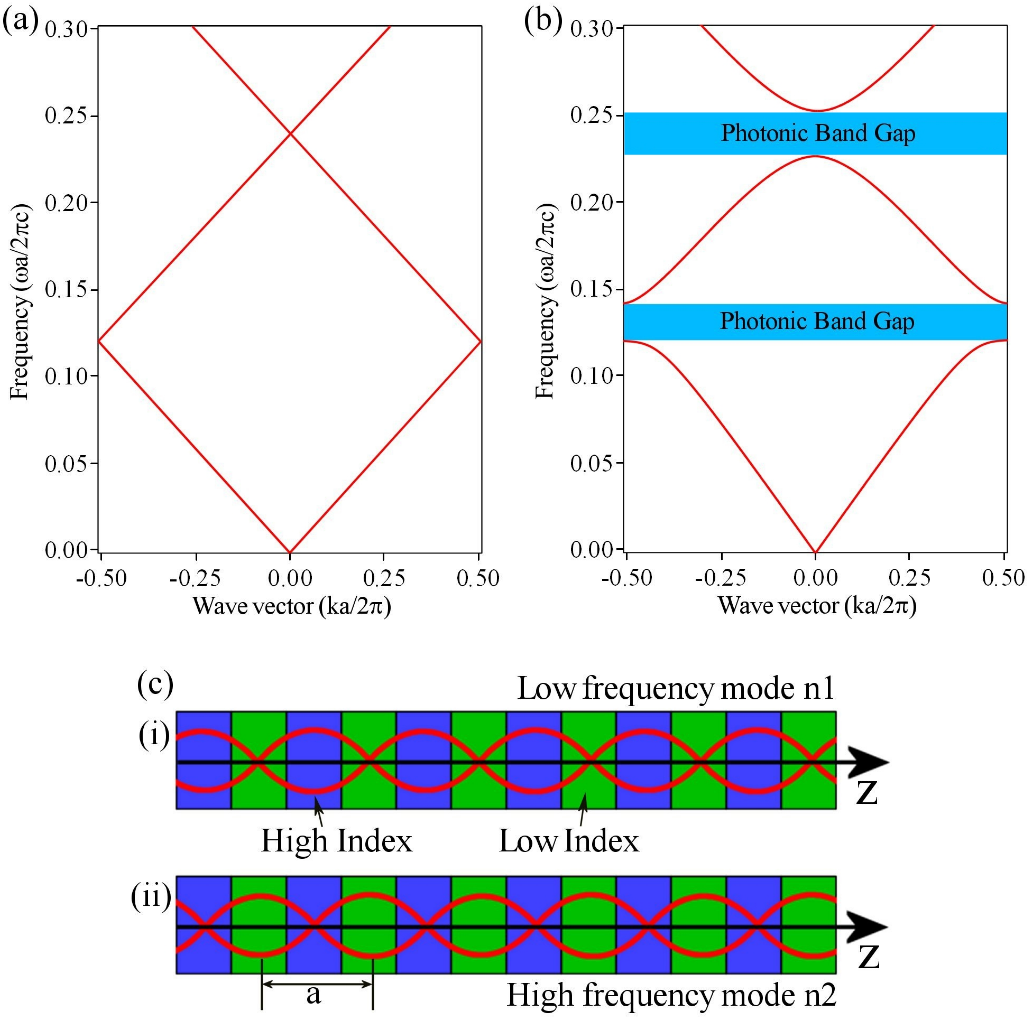

FIGURE 2.3: Dispersion relation for light traversing a periodic dielectric structure with, (a) zero dielectric contrast and (b) dielectric contrast of three. (c) Schematic of modes in periodic slab at the bandgap wavelength. From [6]

In figure 2.3a, both dielectric regions have the same dielectric constant, forming a single slab of material assigned an artificial periodicity. The frequency spectrum follows that shown in the previous figure. Figure 2.3b plots the dispersion of light propagating through a dielectric stack where the different layers have a difference in dielectric constant of three. Many aspects of this graph are similar to that of the first image, except now there is a region of frequency space where no photonic mode exists; this is known as a photonic bandgap. This bandgap arises from the interaction between the different photonic bands. For a physical insight into this bandgap formation it is useful to return to real space and consider the electric field directly above and below the gap, where $k = \pi/a$. Here, the modes are standing waves with wavelengths equal to

$2a$. These modes have only two possible configurations within the structure (fig 2.3c.), their nodes positioned within either the high or low dielectric constant layers. Any other configuration violates the symmetry of the system, and hence is forbidden.

It now becomes clear that while both modes have the same wavelength, the mode concentrated in the high index material will experience a shorter effective distance, and hence a lower frequency, than the mode concentrated in the low index material. This difference in frequency provides the energy gap in the photonic dispersion relation analogous to the energy gap between the valence and conduction bands in a semiconductor material. Indeed, the two systems are almost completely analogous, allowing the photonic system to be written in 'Bloch form', consisting of a plane wave modulated by a function arising from the periodicity of the lattice. This approach becomes particularly useful when considering the coupling of light into two and three dimensional photonic crystals. One-dimensional photonic crystals are commonly used as optical filters in both reflection and transmission. If a dielectric stack is designed to completely exclude a certain range of frequencies, this light will be reflected very efficiently, leading to an excellent quality mirror over the bandgap frequency region. Alternatively, the transmission properties of the stack can be utilised to efficiently remove undesirable frequencies, such as the laser line from low level signals. These two applications have become commonplace over the last 30 years with the creation of fabrication techniques capable of accurately depositing complex multi-layer structures. With this wealth of uses from just one-dimensional structuring, the use of a second dimension was seen as the next logical step towards total photon control.

2.3 Two Dimensional Photonic Crystals

A two dimensional photonic crystal, as the name suggests, is a dielectric slab patterned in the xy-plane but homogeneous in the z-direction (fig 2.4a). These structures can be designed to restrict the passage of light in the plane, and hence form wave guiding devices[27]. In a similar way to the one-dimensional case, by knowing that light has no restriction in the z-direction, and that its propagation will be modified by a two-dimensional Bloch mode in the xy-plane, the solutions of the standing waves in the system can be calculated. It is now important to note that the dispersion will change with crystal orientations.

Again, to understand the fundamental dispersion relation of these structures it is useful to invoke the weak-scattering approximation. For the surface of interest in this thesis the structures can be represented as a close packed array of scattering sites; the primary lattice vectors of these systems are of equal length, and at a 60^o angle to one another (fig 2.4a). The first set of scattered modes corresponds to those of one lattice vector, of which there are six solutions. If a Fourier transform of the surface is taken, equivalent to scattering light off it, the first set of scattering planes are found to be in the direction shown in fig 2.4b, with a 30^o rotation between the lattice vectors of real- and k-space. In this direction the periodicity is $\sqrt{3}.a$, however, the planes repeat every $\frac{\sqrt{3}}{2}a$, and it is this distance that is used as the length of the primary lattice vector, G. It is also important to remember the directions as well as magnitudes of the initial k-vector and the lattice vector. This is shown in figure 2.4b for the $(1, -1)$ direction. Whilst the incident light is scattered in the six lattice directions, the propagation of the polariton modes will be in the direction $\boldsymbol{k} = \boldsymbol{k}_0 + \boldsymbol{G}$.

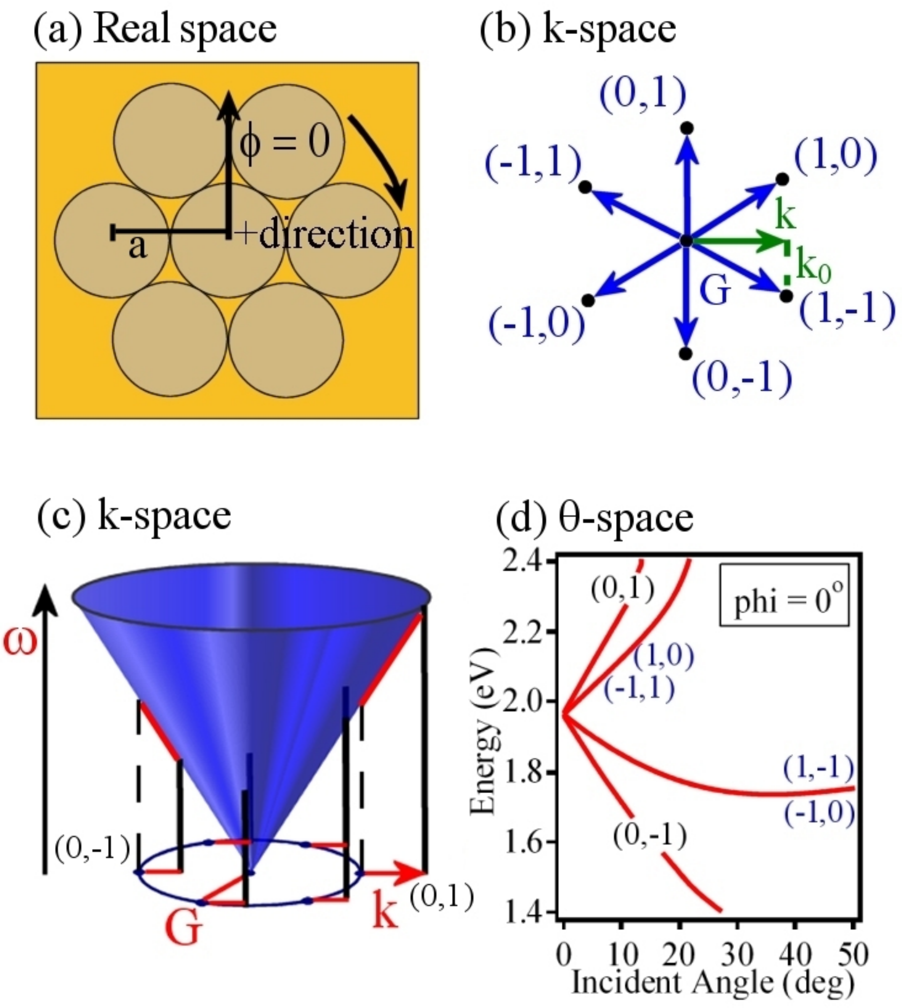

FIGURE 2.4: (a) A close packed array of circular structures, these can be represented in (b) k-space as a triangular lattice of scattering points. (c) Representation of the dispersion relation of this surface (d) solutions for $\phi = 0$ in terms of energy and incident angle.

By drawing the dispersion of light from each scattering site the dispersion relation of the two-dimension photonic crystal can be created (again neglecting interactions between the bands). However, this starts to become difficult to visualise, and so again it is useful to remember the equivalence of all scattering sites. Instead of plotting the dispersion cones from all scattering sites and looking along one k-vector, figure 2.4c shows one light cone and takes lines in k-space from each of the adjacent scattering sites. This will map out the dispersion from this first set of scattering sites, which corresponds to the second and third bands in the dispersion relation. This shows that when $k = 0$, only one energy is observed. However, away from $k = 0$ light scattered in different directions will have different angular frequencies, shown as the red lines for the $(0, -1)$ and $(0, 1)$ bands only. This shows that the dispersion relation for these six-fold symmetric photonic crystals will have a maximum of six bands, and all of which will depend strongly on the propagation direction.

All the previous discussion has assumed that the light is travelling in the plane of the periodicity, however, for the experiments in this thesis coupling is done at an angle θ to the plane. To take this into account the vacuum dispersion relation formula is modified slightly:

$$E(\mathbf{k}) = \frac{\hbar}{e} c\sqrt{\epsilon}\left(\mathbf{k}_0 sin\left(\theta\right) \pm n\mathbf{G}\right) \tag{2.9}$$

this resolves the momentum of the incident light on the structure and uses the in-plane component. This equation has also now been converted from angular frequency to energy through the factor $\frac{\hbar}{e}$. Putting this together with the model shown in figure 2.4c, gives rise to the set of modes shown in figure 2.4d, for a sample orientation, $\phi = 0^o$.

When the full numerical calculations are performed to find the band structure of a two-dimensional photonic crystal, similar results are obtained. However, the formation of a bandgap shifts and splits different modes. Again, borrowed from solid state physics, it is customary to show this by plotting along the edge of the irreducible Brillouin zone (fig 2.5b). The different bands again represent optical modes confined mainly within either the high or low refractive index regions; however, the modes are now two-dimensional and thus more complicated, two of these modes are shown in figure 2.4c.

By introducing carefully controlled defects into a photonic crystal array, it is possible to create localised optical modes within the bandgap. This technique can be used to bring function to these crystals[21]. For example, a line of defects creates a waveguide that can force light through tight junctions not possible with ordinary waveguides or fibres[27]. Using defect engineering, photonic crystals have been used to make micro-beam splitters[28] and micro-interferometers[29], which in turn can be used for sensor applications[30]. Other applications of photonic crystals range from the suppression of spontaneous emission[31] to the formation of high Q-factor cavities for the study of cavity quantum electrodynamics[32].

All these techniques, however, use two-dimensional photonic crystals fabricated within a waveguide to achieve lateral confinement. A natural continuation, therefore, would be to build three-dimensional photonic crystals with all-axis confinement.

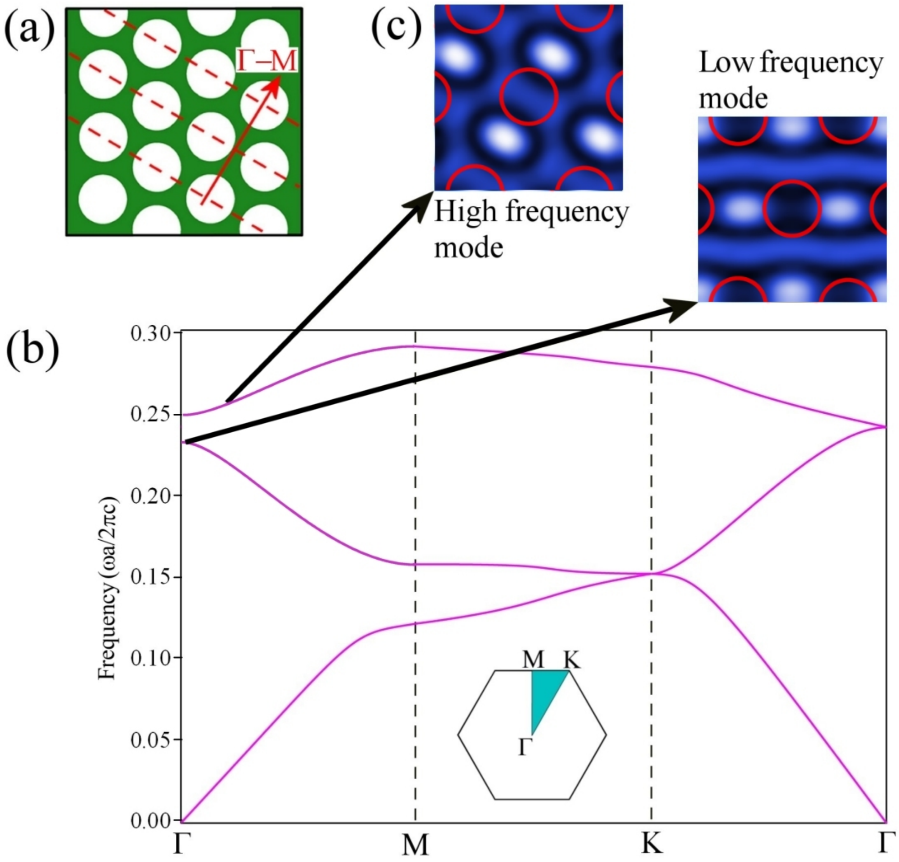

Figure 2.5: Two dimensional triangular lattice of air holes in silicon forming a photonic crystal. (a) real space view showing scattering direction (b) k-space dispersion relation for photonic modes. (c) intensity distributions for different modes near the Γ point.

2.4 Three Dimensional Photonic Crystals

Whilst time consuming, modern lithography techniques have little trouble creating 200nm holes in the top surface of silicon slabs to form two-dimensional photonic crystals. However, a major technological challenge is how to produce three-dimensional structures, where no direct access is possible to any of the dimensions. The first solutions to this problem required painstakingly stacking dielectric micro-rods into a woodpile type structure[33], or milling holes at different angles to build up a three-dimensional lattice[34]. These techniques, along with many others[35, 36] produced results, but were time consuming and difficult to manufacture; the final crystals were also often extremely fragile and only supported a narrow bandgap in all three dimensions. An alternative to using these expensive 'top down' processing techniques was to change tack and let nature perform the structuring through self-assembly.

2.4.1 Self Assembled Three Dimensional Structures

When a solution of micro-spheres is confined and the solvent is allowed to evaporate, the spheres will naturally sediment into a close packed three-dimensional structure. With careful control, well-ordered crystals can be produced[37]. Due to this structuring, these samples are highly iridescent, sharing many similarities with natural opal (fig 2.6).

Figure 2.6: Natural opal is iridescent and colourful due to its structure (inset), ideal for jewellery. Picture taken from [7]

Calculations have shown that while these artificial opals do not possess a full photonic bandgap, the inverse structures, high index material interwoven with a close packed array of air holes, do[38]. These structures are difficult to manufacture because they require filling the narrow channels between the spheres with material without blocking the channels themselves. A number of techniques have been utilised to perform this task[39], including chemical vapour deposition, oxide reduction, nano-crystal sintering and electro-deposition. Of these techniques, only the one we have adopted, electro-deposition, fills the structure from the bottom, eliminating the problem of blockages and allowing exact casts of the initial template. Furthermore, after the spheres have been removed, the electrodeposited structures are robust, durable and do not suffer from shrinkage. Using this technique it is possible to produce structures made from polymers[40], semiconductors[39], or metals[41].

Unfortunately, whilst self-assembly techniques have succeeded in producing three-dimensional photonic bandgap structures[42], the control of defects makes the structures somewhat unreliable at the present time and, as yet, there are no means to engineer defect sites such as waveguides. With the improvements in holographic lithography it has now become possible to build perfectly controllable, large, three-dimensional photonic crystals[43]. In these structures, it is still hard to create the necessary refractive index contrast to form a full photonic bandgap. However, the absolute control achieved using this technique, whilst time consuming, makes it a more attractive fabrication route than self assembly.

In the pursuit of perfect quality photonic crystals the field of self-assembly is perhaps not ideal. However, many applications do not require stringent levels of quality, and can flourish on the quick and cheap techniques mastered over the past decade. The topic of this thesis is just such an example; not only do the nanostructure metal films produced using a self assembly and electro-deposition route provide excellent ground for studying the fundamental properties of surface plasmons[44], they can also be used for ultra-high sensitivity molecular sensors[45].

Chapter 3

Optical Properties of Metals

Metals make up a significant fraction of the periodic table. It is not surprising, therefore, that much of human advancement has relied on understanding and utilising the properties of at least the most common of these elements. The earliest use of metals dates back to around 9000 B.C. when copper was used to create decorative jewellery; this began a long relationship between humans and metals, which is still strong today.

The first known examples of using metal nano-particles date back to Roman times where exquisite colourations were achieved in stained glasses (fig 3.1), however, it was not until the end of the 19th century that an interest in understanding the optical properties of metals truly began[46]. This work was performed by Michael Faraday and concentrated on exploring the properties that give the Lycurgus cup shown in figure 3.1 its beautiful colours. Here, the surface plasmon resonances of the metal particles efficiently scatter the green light, giving the cup its usual colour. This allows only red light to be transmitted, providing the strong contrast in colours that must have amazed the people of Roman times. It is these types of interactions, along with many others, which has produced the continued interest in the interactions between light and metals - the topic of this thesis.

This chapter will first examine the fundamental properties of metals by, again, analysing Maxwell's equations. An exploration into light-metal interactions will then be presented, building up to studying the properties of surface plasmons in varying guises.

3.1 Fundamental Optical Properties

As a first approximation a metal can be considered to be an isotropic medium of dielectric constant, ϵ, permeability, μ and conductivity, σ. Using the material equations stated in chapter 2 (equation 2.5), Maxwell's equations take the form:

Figure 3.1: The Lycurgus Cup, made in the 4^{th} century AD. The glass contains 70nm particles of silver and gold with a ratio of about 7:3, this make the cup appear green in reflection but red in transmission.

$$\nabla \cdot \mathbf{H} = 0 \tag{3.1}$$

$$\nabla \cdot \mathbf{E} = \frac{\rho}{\epsilon} \tag{3.2}$$

$$\nabla \times \mathbf{E} + \mu \frac{\delta \mathbf{H}}{\delta t} = 0 \tag{3.3}$$

$$\nabla \times \mathbf{H} - \epsilon \frac{\delta \mathbf{E}}{\delta t} = \sigma \mathbf{E} \tag{3.4}$$

these equations can now be manipulated to provide information on the optical properties of this general material. Using equations 3.4 and 3.3 as expression for the time variation of the electric charge density, ρ, can be obtained[26], see appendix A for the full derivation. On integration, the solution to this equation can be found to take the form:

$$\rho = \rho_0 e^{-t/\tau} \quad \text{where} \quad \tau = \frac{\epsilon}{\sigma} \tag{3.5}$$

the metals considered in this thesis all have large conductivities so the electrons have exceedingly short relaxation times, τ; for gold this value is of order 10^{-14}s. As the variations in an optical field happen on much longer time scales we can realistically set ρ to zero. Now equations 3.4 and 3.3 can be rearranged to eliminate **H**. By considering monochromatic light and assuming the plane wave solution to Maxwell's equations,

$$\mathbf{E} = \mathbf{E}_0 \exp\left(i\mathbf{k}\cdot\mathbf{x} - i\omega t\right) \tag{3.6}$$

The wave equations for a metal can be written:

$$\nabla^2\mathbf{E} + \hat{k}^2\mathbf{E} = 0 \quad \text{where} \quad \hat{k}^2 = \omega^2\mu\left(\epsilon + i\frac{\sigma}{\omega}\right) \tag{3.7}$$

these equations are identical to those of a non-conducting medium if a complex dielectric constant, $\hat{\epsilon} = \epsilon + i\frac{\sigma}{\omega} = \epsilon_1 + \epsilon_2$ is defined. Now it is possible to also define a complex refractive index, $\hat{n} = n + i\kappa = \sqrt{\hat{\epsilon}\mu}$, where κ is known as the extinction coefficient. Refractive index and dielectric constant are linked through the following equations:

$$n = \sqrt{\frac{\sqrt{\epsilon_1^2 + \epsilon_2^2} + \epsilon_1}{2}} \quad \text{and} \quad \kappa = \sqrt{\frac{\sqrt{\epsilon_1^2 + \epsilon_2^2} - \epsilon_1}{2}} \tag{3.8}$$

now the plane wave equation can be rewritten, taking into account the complex wave vector:

$$\mathbf{E} = \mathbf{E}_0 \exp\left(\frac{-2\pi\kappa x}{\lambda}\right) \exp\left[i\left(\frac{2\pi n x}{\lambda} - i\omega t\right)\right] \tag{3.9}$$

here, the first exponential is real and so quantifies the absorption of the wave, the second part is imaginary, corresponding to the oscillatory part of the wave. A value for the penetration depth, δ, can now be defined as the distance into a material the light has travelled when it reaches a field strength $1/e$ of its initial strength, this is known as the skin depth.

$$\delta\left(\lambda\right) = \frac{\lambda}{2\pi\kappa\left(\lambda\right)} \tag{3.10}$$

For near infrared frequencies the skin depth of gold is of the order of 20nm. This distance is small compared to the wavelength of the light, so there is little interaction between the metal and the optical field, in this regime the gold can be considered a perfect reflector. This situation changes as the frequency is increased to the blue region of the spectrum; to understand why, a closer look at the optical response of metals is required.

3.2 Optical Response

In the previous section it was assumed that a metal's conductivity, dielectric constant and magnetic permeability were all constants; in reality these properties are dependent on the frequency of the incident light. This can be accounted for by calculating the frequency response of the dielectric constant, while the other properties can be considered constant over the spectral region of interest.

The dielectric constant of a medium is purely dependent on how the electrons within the material respond to an optical field. Electrons can either be bound to the host atoms, as in a dielectric material, or be free to move through the material, as in the case of a metal. Since an applied optical field is oscillatory, both cases can be described in terms of simple harmonic motion and are known as the Lorentz and Drude models for dielectrics and metals respectively. The equation for simple harmonic motion of an electron in a material can be written as:

$$m\ddot{x} + b\dot{x} + Kx = e\mathbf{E} \tag{3.11}$$

where m and e are the electron mass and charge, b is the damping coefficient describing the energy loss due to scattering, K is the spring constant describing the restoring force due to electrostatic attraction of the binding atom and $\mathbf{E}$ is the electric field. In a dielectric, electrons fill the valence band so only interband transitions with large energies are allowed. If it is assumed that the incident field is less than that required to induce an electronic transition the material is described directly by equation 3.11. For a perfect metal, free electrons occupy a partially filled conduction band, allowing intraband transitions of very low energies; this can be described by setting the spring constant to zero. For the metals described in this thesis, as well as the free electrons in the conduction band, electrons loosely bound to the atoms contribute to the optical properties; hence a combination of both descriptions will be required.

To find the dielectric constant, equation 3.11 can be solved in terms of the amplitude and phase of the oscillations. By considering the polarisation of the medium and performing some lengthy mathematics[26], solutions for the real and imaginary parts of the dielectric constant can be found for both the dielectric and metal cases.

Metal, Drude solution:

$$\epsilon_1 = 1 - \frac{\omega_p^2}{\omega^2 + \gamma^2} \quad \text{and} \quad \epsilon_2 = \frac{\omega_p^2 \gamma}{\omega\left(\omega^2 + \gamma^2\right)} \tag{3.12}$$

Dielectric, Lorentz solution:

$$\epsilon_1 = 1 + \frac{\omega_p^2\left(\omega_0^2 - \omega^2\right)}{\left(\omega_0^2 - \omega^2\right)^2 + \gamma^2\omega^2} \quad \text{and} \quad \epsilon_1 = \frac{\omega_p^2 \gamma\omega}{\left(\omega_0^2 - \omega^2\right)^2 + \gamma^2\omega^2} \tag{3.13}$$

Here the plasma frequency is defined by $\omega_p = ne^2/m\epsilon_0$, the relationship $\gamma = b/m$ quantifies the damping in the system and $\omega_0 = \sqrt{K/m}$ corresponds to the resonant frequency of the bound electrons in a dielectric medium. These values are plotted in figure 3.2 along with the corresponding complex refractive indices, found using equation 3.8.

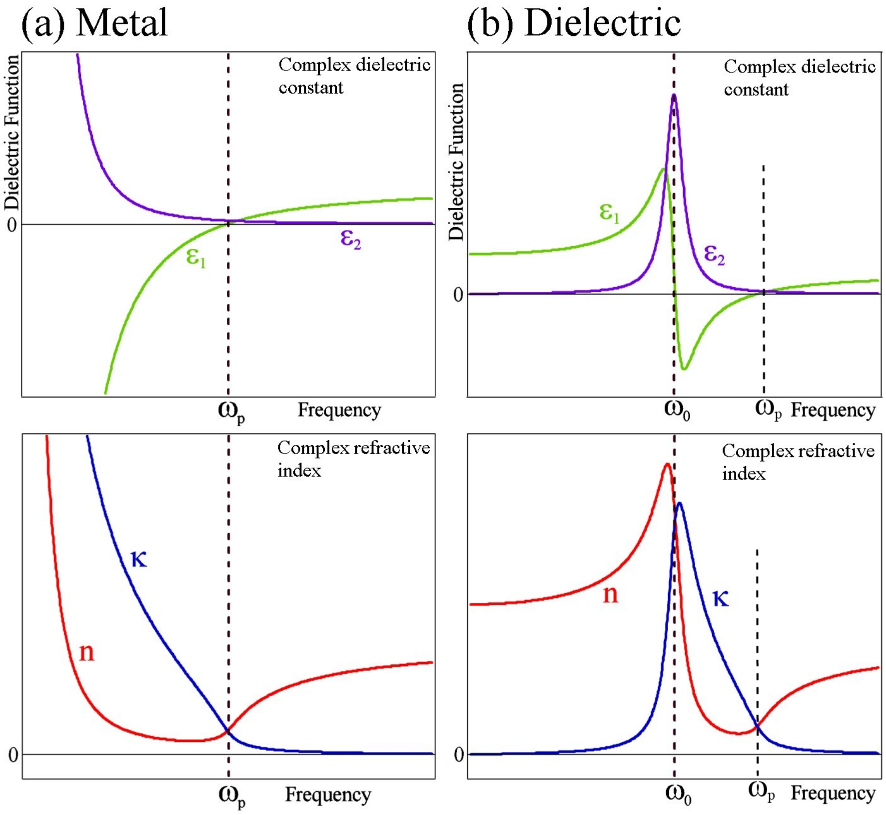

FIGURE 3.2: Graphs showing the components of the complex dielectric function (top) and the complex refractive index (bottom) for (a) metals, modelled using the Drude equations and (b) dielectrics, modelled using the Lorentz equations.

In the case of a perfect metal, the electrons are free ($\omega_0 = 0$) and embedded within a matrix of positive ions, giving the system zero net charge. Under illumination these free electrons will oscillate and form a charge distribution within the metal, this in turn will create an electric field that will try to restore charge neutrality. At a certain frequency, neglecting damping, the dielectric constant passes through zero (fig 3.2a). At this point, there can be no transverse electromagnetic modes in the material - the wave is purely longitudinal - corresponding to a collective oscillation of the electrons in the direction of the wave propagation. This is known as a plasma oscillation with corresponding plasma frequency, ω_p. In a quantum mechanical treatment of this problem the collective plasma oscillation is known as a plasmon, a single entity made up of the combined effect of many particles. This notion of a complex effect being redefined as a single entity is a powerful concept, and will subsequently be used throughout much of this thesis.

Figure 3.2b shows the frequency response of a dielectric material. In this case the binding of electrons to atoms gives rise to a natural frequency of oscillation, ω_0; which, in turn, leads to a peak in absorption as energy is efficiently directed into the crystal lattice.

Above ω_0 the electrons can oscillate strongly and the real and imaginary parts of the dielectric constant acquire the same form observed for metals, with ϵ_1 going negative. The dielectric is, therefore, highly reflective in this frequency region, although absorption significantly reduces the effect. Using the Lorentz and Drude expressions, it is possible to calculate the optical properties of many materials; however, for many metals, such as silver and gold, interband transitions makes life a little more complicated.

3.3 Real Metals

As previously mentioned, the Drude model does not accurately compute the properties of a number of metals, including those used in this thesis. To understand this breakdown one must consider the electron shell configuration of these elements, figure 3.3 shows this for gold.

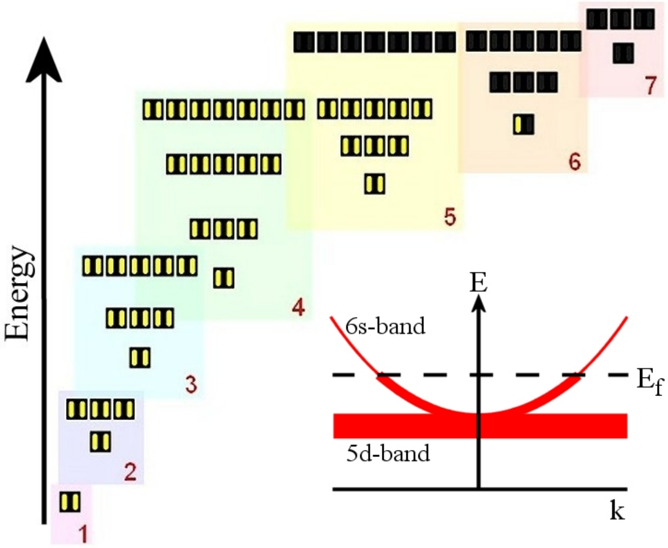

Figure 3.3: Plot depicting the electron shells and energies for a gold atom, filled boxes represent electrons, from [8]. Inset sketches electron dispersion for gold, the outer 6s electron delocalises, leading to the conduction band.

The outermost, 6s, electron is responsible for the delocalised electron sea that gives gold it metallic properties, however, it is clear that the closed 5d shell has a very similar energy. Figure 3.3 also sketches the electron dispersion near the Fermi energy. This clearly shows the delocalised s-band crossing the Fermi energy, thus allowing intra-band transitions. Also shown is the localised 5d-band, which consists of a number of modes (not shown, see [47] for more details) and represents a large number of electron states just below the Fermi energy. It is this that adds complexity to the optical properties of gold and is why modelling requires a mixture of Lorentz and Drude methods[48]. Rather than attempting such a calculation it is perhaps better to turn to experiment to find the precise refractive indices of these metals[49, 50, 51], shown in figure 3.4.

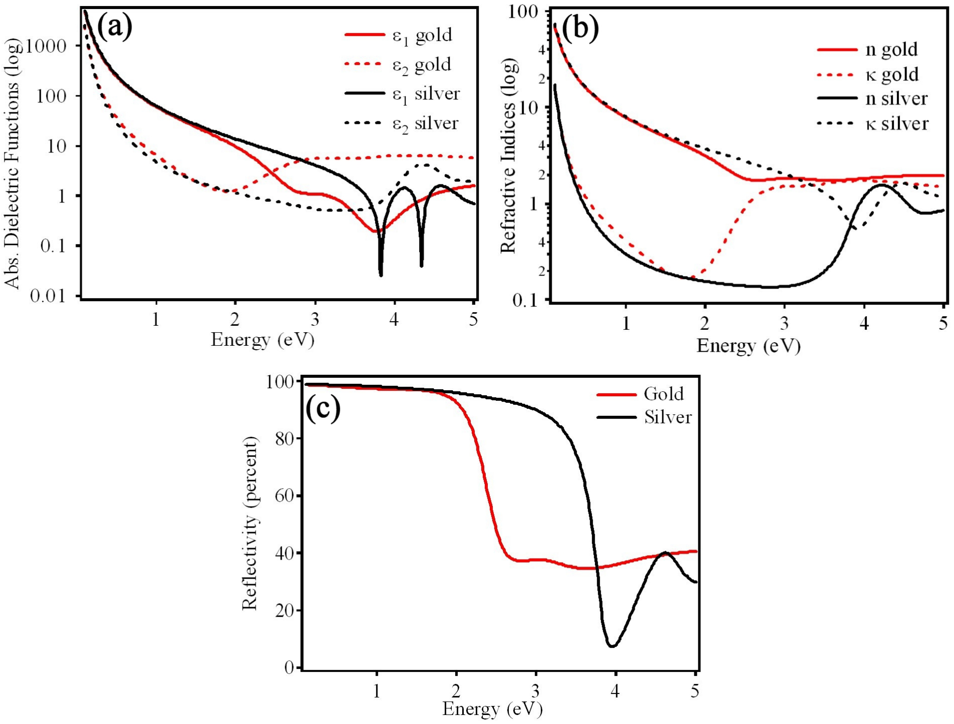

Figure 3.4: Experimentally deduced values for silver and gold of (a) complex dielectric function, (b) complex refractive index and (c) reflectivity.

If these plots are compared to those of the precise models in figure 3.2, it can be seen that the dielectric constants and refractive indices follow the trends of a pure metal, decreasing with increasing frequency (the absolute value of the real dielectric constant is shown, hence the positive value). However, around 2.5eV and 3.5eV for gold and silver respectively, some rapid variations in the values occur. These correspond to the interactions with bound electrons in the outer shells; this is most notable for silver, where the graphs closely follow the dielectric model in this regime. Also plotted is the reflectivity of these metals. As expected at low frequencies in the 'pure metal' region of the spectrum 100% reflection is observed. However, as the interactions with the bound electrons become stronger, energy is more efficiently coupled to these oscillating modes, and so the reflectivity drops substantially. For the experiments performed in this thesis the energy of the incident light never exceeds 3eV, allowing silver to be considered a perfect metal and gold suffering absorption towards the higher frequency end of the spectrum. For all metals considered in this thesis the experimental values of the real and imaginary dielectric constants are taken from the classic paper published by P. Johnson and R. Christy[50]. With this knowledge, the absorption of light from a metal can be fully understood. However, experiments which observed the absorption of electrons fired through thin metal films found other sources of absorption not observed optically[14]. This marked the discovery of the surface plasmon and the birth of the field of plasmonics.

3.4 Surface Plasmon Polaritons

In the previous section a plasmon was introduced as a quantised charge density fluctuation within an isotropic infinite conductor. At a metal interface, however, this picture must break down with the loss of one of the dimensions. Electrons will still oscillate along the interface creating a variation in charge density (fig 3.5a). By analysing Maxwell's equations it can be found that the possible range of oscillation frequencies range from $\omega = 0$ to $\omega_p/\sqrt{2}$, hence, surface plasmons will be excited at energies below that of the bulk plasmon.

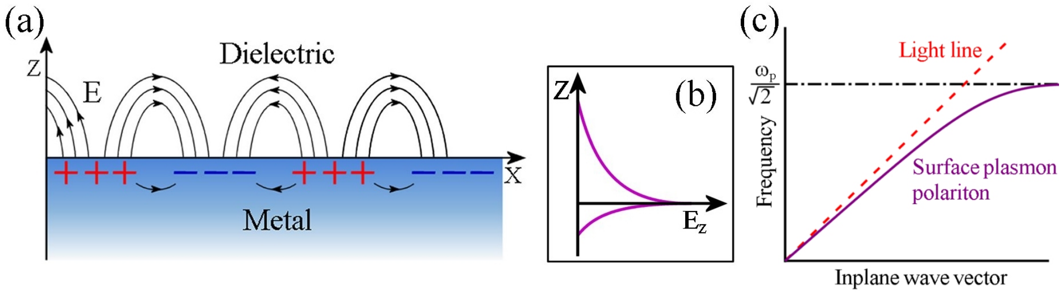

FIGURE 3.5: The surface plasmon. (a) Schematic of the surface charge and electric field, from [1]. (b) Electric field distribution perpendicular to the surface. (c) Dispersion relation for a surface plasmon, light line represents dispersion for light in a vacuum.

The longitudinal surface charge oscillations give rise to an electric field perpendicular to the interface which decays exponentially with distance (fig 3.5b). This corresponds to an evanescent field above the surface with a decay length similar to that of the wavelength of light. On the metals, the surface plasmon exists as a charge fluctuations which penetrating a distance equal to the skin depth. If the dielectric constants of the metal and dielectric are taken to be ϵ_m and ϵ_d respectively, then by solving Maxwell's equations for an optical mode at the interface, the momentum of the surface plasmon is found to be[52]:

$$\hat{k} = \frac{\omega}{c}\left(\frac{\hat{\epsilon_m}\epsilon_d}{\hat{\epsilon_m} + \epsilon_d}\right)^{1/2} \tag{3.14}$$

for completeness, this equation can be split into real and imaginary components:

$$k_1 = \frac{\omega}{c}\left(\frac{\epsilon_{m1}\epsilon_d}{\epsilon_{m1} + \epsilon_d}\right)^{1/2} \quad \text{and} \quad k_2 = \frac{\omega}{c}\left(\frac{\epsilon_{m1}\epsilon_d}{\epsilon_{m1} + \epsilon_d}\right)^{3/2} \frac{\epsilon_{m2}}{2\epsilon_{m1}^2} \tag{3.15}$$

since these equations have assumed an input electromagnetic wave, the solutions are for an optical field interacting with the metals surface, not just a charge fluctuation. This is known as a surface plasmon polariton (SPP). The SPP dispersion relation, $\omega(k)$ plotted in figure 3.5c, shows that for small wave vectors the plasmon is close to that of the light line, but always to the right hand side. Therefore, the plasmon has similar properties to the optical field but always has a greater momentum and is, as already discussed, non-radiative. This increased momentum is associated with the binding of the mode to the surface. For larger wave vectors the surface plasmon dispersion tends towards a maximum value of $\omega_p/\sqrt{2}$, and resembles that of the bulk plasmon, the energy becoming independent of wave vector.

Since SPPs do not directly couple to an optical field they must be created via some intermediate step[1, 53]. This requires either converting the incident light into an evanescent mode by means of total internal reflection, or by scattering the light to higher momentum via a grating or scattering site. The prism coupling method has been used extensively when studying the properties of SPPs[53]. In this technique light is total internally reflected off the base of a glass prism, which is then brought within several hundred nanometres of a thin metal film. The spatial extent of the SPP at the metal-air interface is very small, so has the same dispersion as discussed previously. The light is within the glass and so, due to the higher refractive index, has an increased momentum. The evanescent mode of the light can carry this increased momentum through the air gap and, if tuned to the appropriate angle (or in-plane momentum), excite a SPP mode[54]. Using this technique, many of the properties of SPPs have been characterised, such as decay length and the interaction between plasmon modes on either side of the metal film[55, 56]. This technique, however, is limited to a very precise geometry and does not produce some of the interesting features found when a grating is used as the coupling mechanism.

In chapter two, it was shown that when the wavelength of light is twice that of the periodicity of a dielectric structure, forward and back-scattered waves give rise to a polariton wave. This polariton was shown to have markedly different properties from a pure optical wave, and produced effects such as photonic bandgaps. If a slightly corrugated metal sheet is considered (fig 3.6a), there will be an effective variation in the refractive index at the surface. This will cause the optical field to scatter into different photonic modes in the plane of the surface, very similar to that of a photonic crystal. The SPP mode will also encounter the surface perturbation and scattered in a similar way, (fig 3.6b). Because of the similarities between the optical and plasmonic descriptions the SPP mode will also be referred to as ‘Bragg’ mode in later chapters, to distinguish it from other plasmon modes.

Now the surface plasmon mode also exists to the left of the light-line on the dispersion relation. This is now in the radiative regime, allowing directly coupling to the optical field[57]. This corresponds to photons scattering off the grating to a higher momentum states of the plasmon mode. Since the surface plasmon is bound to the surface, it will be attenuated due to absorption within the metal. At visible frequencies, the typical propagation distance for a surface plasmon on silver is 20μm, increasing to a millimetre in the infrared. This distance is sufficient for the mode to be multiply scattered, allowing the formation of a standing SPP wave[58, 59]. This standing SPP wave has many

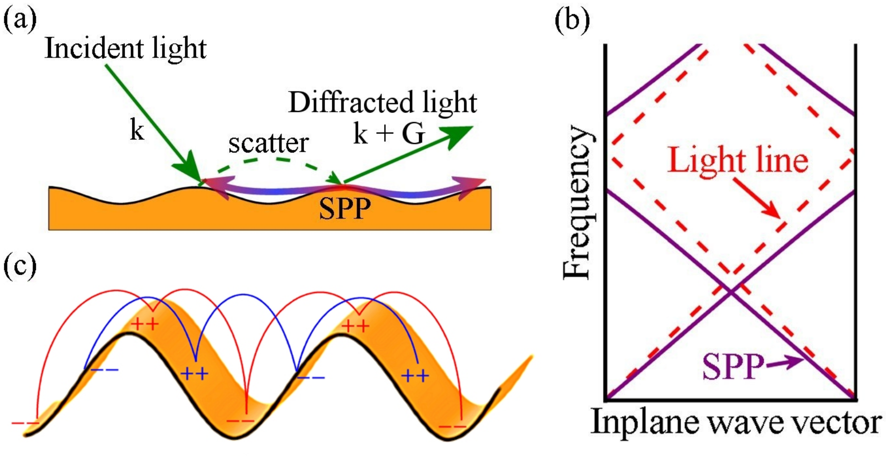

FIGURE 3.6: (a) Incident light is scattered and diffracted by a metal grating, the scattered light has sufficient momentum to excite a surface plasmon that will couple to the optical field and form a surface plasmon polariton. (b) Dispersion relation of a SPP. (c) Schematic of the SPP waves at the plasmonic bandgap.

parallels to the photonic crystal modes and can have nodes at the turning points of the grating (peaks and troughs) or on the side walls (fig 3.6c). As can be seen, whilst both SPP modes have the same wavelength the 'red mode' has to travel a greater distance than the 'blue mode'. This increased distance between surface charges causes a greater distortion to the electric field, increasing the energy of the mode. This, of course, means that for a single wave vector, two modes of different energy exist and hence a SPP bandgap[2, 60]. In two dimensions, the SPP can be considered as a Bloch mode that light can couple into and out of. Besides the consideration of symmetry, this is precisely the same as the one-dimensional case, for example on a triangular lattice there will be six SPP modes corresponding to the different scattering directions. This neat picture begins to break down as the aspect ratio of the grating is increased beyond the point where it can be considered as a perturbation of a flat surface.

3.5 High Aspect Ratio Structures

For shallow gratings, SPP modes can be considered to scatter off the periodicity of the structure, propagating simply in the plane. However, as the depth of the grooves increases localisation effects start to become important[61, 62], this is shown schematically in figure 3.7. The electric field of the SPP extends above the surface of the metal by a distance similar to that of the wavelength of light. In the first instance, for a low aspect ratio structure, the SPP will traverse the surface as if it were flat. As the grating aspect ratio increases, the electric field of the SPP on either side of the groove will start to interfere (fig 3.7b). If the groove depth is equal to a whole number of plasmon oscillations then a SPP standing wave will be set up within the groove[61, 63]. The localisation of the SPP causes the field strength at the surface to be concentrated into the groove, further localising the mode from adjacent cavities. The cavity mode exhibits a flat dispersion due to its localised nature except near the light-line, where anticrossing is observed[64] due to the strong coupling between optical and SPP waves.

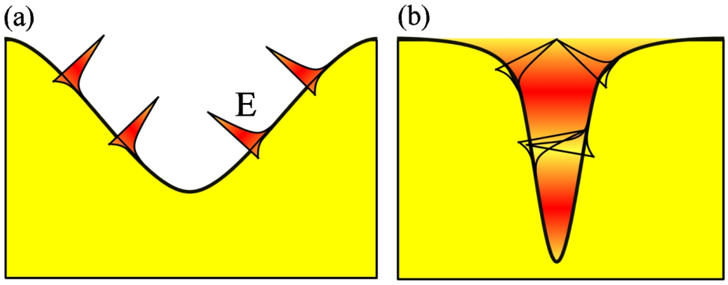

Figure 3.7: (a) On a normal grating the SPP will traverse the surface unperturbed by the structuring. (b) As the aspect ratio of the structure is increased the evanescent modes of the SPPs propagating on either wall will interfere. This leads to a confined standing mode within the grooves.

The nano-void samples considered in this thesis are similar to the high aspect ratio grating, especially near thicknesses approaching the void diameter. However due to the spherical shape of the cavity the localised modes take a different form, more closely represented by a Mie scattering field solution.

3.6 Mie Scattering and Plasmons

The field of plasmonics can be traced back to the first studies of the optical properties of metals when Michael Faraday observed changing colourations of solutions of gold colloids. Since then a great deal of progress has been made in this field, but metallic colloids are still used in forefront research; none more strongly than in the field of surface enhanced Raman scattering. Whilst the work presented in this thesis does not use metal particles, many of the results require an understanding of the tools developed from colloidal theory[65].

It has been shown that in two-dimensions the optical properties of metals can be significantly modified by surface plasmon resonances; it will, therefore, not be surprising that such surface effects dominate the optical properties of small metal particles. It has also been noted that a SPP can travel up about a 10μm over a silver film at visible frequencies. If a metal particle with a diameter of several nanometres is considered, a SPP will traverse the particle many times before decaying. In reality, a SPP mode will interfere with itself as it travels around the particle, leading to an electro-magnetic standing wave. This standing wave will follow the field of the incident light, taking a dipole form for particles much smaller than the wavelength of light (fig 3.8a). Higher order multipolar resonances will become excited as the particle size reaches that of the wavelength scale due to spatial variations of the electromagnetic field across the breadth of the particle[66]. It is also interesting to note that an electromagnetic wave probes structures many times smaller than its wavelength; this is shown beautifully in figure 3.8b where gold coatings have been applied to sub-micron sized dielectric particles in solution. By varying the thickness of the gold layer by tens of nanometres the SPP is tuned, in turn tuning the maximum scattering frequency, altering the colour of the light transmitted through the solution[17].

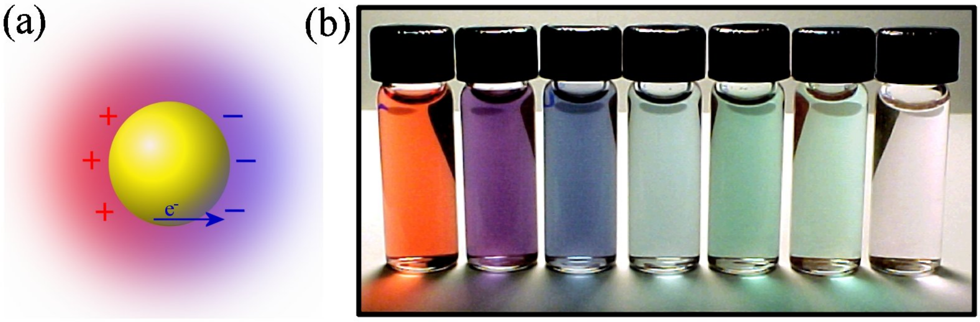

Figure 3.8: (a) Pictorial representation of the electric field around a colloidal particle when illuminated. (b) Solution of nano-shell particles from [9], increasing the shell thickness (left to right) alters the surface plasmon energy to longer wavelengths and changes the scattering efficiency.

To obtain the solutions for the electromagnetic modes of a sphere of arbitrary size, Maxwell's equations must again be solved. By enforcing the boundary conditions that the tangential components of both **E** and **H** are continuous at the interface between the sphere and the surroundings a set of solutions can be obtained[67]. These solutions take the form of a set of spherical Bessel, j_l, and Hankel, h_l, functions, and for transverse magnetic waves the solutions can be written as:

$$\epsilon_d h_l(k_0R)[k_iRj_l(k_iR)]' - \epsilon(\omega)j_l(k_iR)[k_0Rh_l(k_0R)]' = 0 \tag{3.16}$$

where $\epsilon(\omega)$ and ϵ_d are the dielectric functions of the sphere and the dielectric medium respectively, R is the radius of the sphere and k_i and k_0 are the wave vectors inside and outside the sphere. The solutions, and hence modes, of this equation take the form of complex numbers. This reflects the fact that the modes have finite life times due to radiative decay, and hence all solutions can couple to electromagnetic waves in the surrounding medium[67]. The scattering of a plane wave by a sphere is given by Mie theory, and the solutions are found to be the same as that shown in equation 3.16. The full calculation for electromagnetic field within the sphere and medium can also be calculated, of which the lowest two orders are shown in figure 3.9. For small particles these are the only modes which need to be considered[66].

The calculated scattered modes correspond to an electric field distribution surrounding the particle and are already somewhat similar to the expected standing wave results of

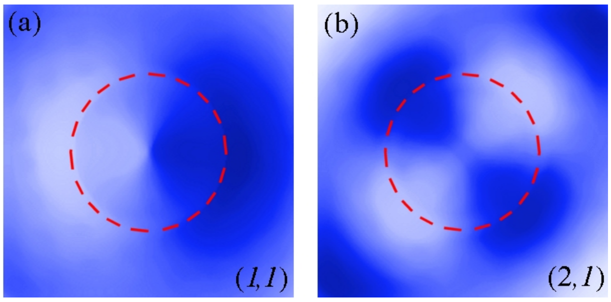

FIGURE 3.9: Calculated Mie scattered electric field distributions of a metal sphere in a vacuum for (a) (l,m) = (1,1) and (b) (l,m) = (2,1). Red dotted line indicates boundary between the metal and the vacuum. From [10]

surface plasmons on small metal particles, discussed previously. If now the dielectric constant of the sphere is modified to express it as a metal, a resonance condition is found where $\epsilon_1 = -2\epsilon_d$ and $\epsilon_2 = 0$. This is often referred to as the Fröhlich frequency and describes SPP resonances for a spherical metal particle. When these equations are substituted into equations 3.14, the resonances are found to occur when:

$$\omega_F = \frac{\omega_p}{\sqrt{1-2\epsilon_d}} = \frac{\omega_p}{\sqrt{3}} \quad \text{when} \quad \epsilon_d = -1 \tag{3.17}$$

where ω_F is the Fröhlich frequency. This is not too much of a surprise as equation 3.17 showed that for two dimensional confinement the resonance occurred at $\omega_p/\sqrt{2}$. From this understanding, it is possible to use Mie scattering results to calculate plasmon resonances on colloidal metal particles with remarkable success[66], bringing about the substantial amount of work performed in this area. This shows qualitatively the field profile in the dielectric medium to be the same as shown in figure 3.9.

The Mie scattering equations for spheres are quite general so, by swapping the dielectric constant of the sphere and surrounding medium, the modes of a dielectric bubble within an infinite expanse of metal can be calculated. The solutions, of which the lowest two modes are shown in figure 3.10, are very similar to those of the particles.

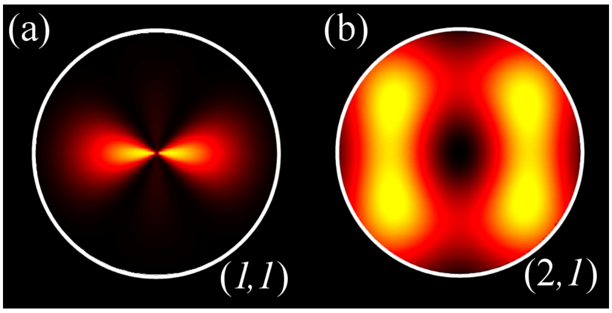

FIGURE 3.10: Calculation showing the Mie scattered magnitude of electric field distributions of a dielectric sphere in a metallic continuum for (a) (l,m) = (1,1) and (b) (l,m) = (2,1).

Since the equations for calculating the field distributions of both spheres and voids are very similar, the resulting plasmon modes are also closely related. However, there are some very important and interesting differences between the two situations.

If first a perfect metal is considered, the energies of plasmon modes of different angular momentum can be found for both spheres and voids of varying sizes; the angular momentum corresponds to the number of electric field nodes in the system, and can be written as:

$$|\mathbf{L}| = \hbar l = \mathbf{rp} = \hbar \mathbf{rk} \tag{3.18}$$

leading to the relationship between angular momentum, l, and wave vector:

$$k = \frac{l}{r} \tag{3.19}$$

where r is the radius of the sphere (dielectric voids or metallic spheres). Figure 3.11 uses this relationship to construct a dispersion relation for spheres and voids of different sizes using the energies calculated using equation 3.16. As would be expected, if the sphere (or void) radius is made sufficiently large, the shape of the SPP dispersion relation is recovered.

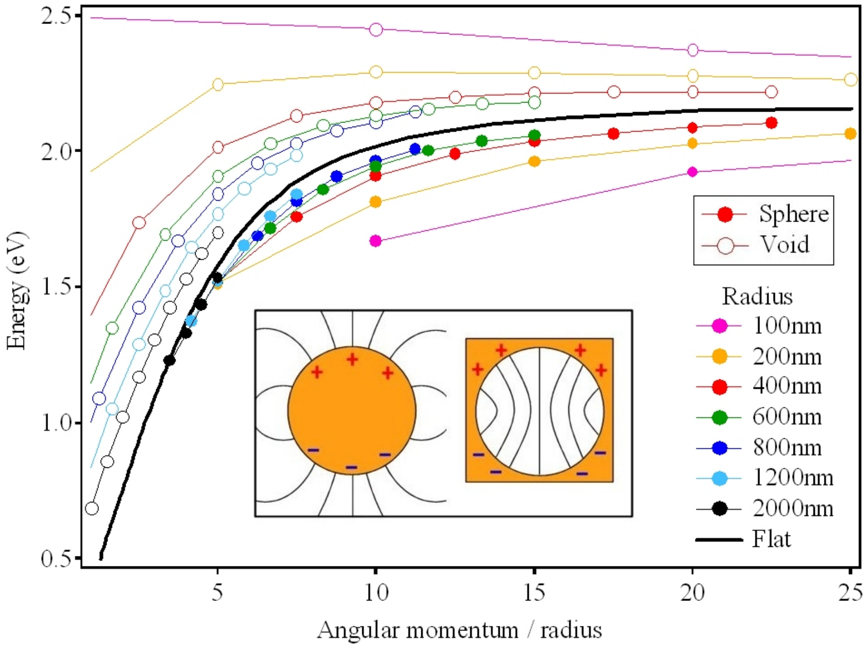

FIGURE 3.11: Energy of Mie scattered solutions for both spheres and voids plotted against angular momentum divided by radius of structure. Inset: cartoon showing field lines in each case.

The first point to note in figure 3.11 is the symmetry between the voids, spheres and the flat surface; for some understanding into this it is useful to consider the case when both spheres and voids are much smaller than the wavelength of light[68]. In this limit the electric field can be considered electrostatic and the mode of a sphere follows the equation[67]:

$$\begin{gathered} \omega = \omega_p \left(\frac{l}{2l+1}\right)^{1/2} l = 1, 2, 3... \\ l = 0,\ \omega = \frac{\omega_p}{\sqrt{3}},\ l = \infty,\ \omega = \frac{\omega_p}{\sqrt{2}} \end{gathered} \tag{3.20}$$

and similarly the equations for voids can be written:

$$\begin{gathered} \omega = \omega_p \left(\frac{l+1}{2l+1}\right)^{1/2} l = 0, 1, 2... \\ l = 1,\ \omega = \omega_p,\ l = \infty\ \omega = \frac{\omega_p}{\sqrt{2}} \end{gathered} \tag{3.21}$$

in this limit, with changing angular momentum, it can be seen that the modes within the voids will start at ω_p and *decrease* to $\omega_p/\sqrt{2}$, while the modes for spheres will start at $\omega_p/\sqrt{3}$ and *increase* to $\omega_p/\sqrt{2}$ (it should be noted that the $l = 0$ modes for spherical particles are not allowed). This trend can indeed be seen by following pairs of lines of the same colour, most easily observed when the radius is 100nm (purple), although neither limit is observed due to the limited momentum range considered here. A similar trend can be seen when, for a single angular momentum state, the radius of the sphere or void is changed. As the radius increases, the surfaces flatten and the mode energies tend to that of the surface plasmon. However, spheres again start at low energies and increase to this value while voids start at a higher energy and decrease. These features can be understood by considering the electric field for voids and spheres. The field lines must be perpendicular to a metal surface and, therefore, for spheres disperse into free-space. For voids the field lines are concentrated together, and can only travel a limited distance given by the diameter of the void, figure 3.11 inset. This confinement of the electric field leads to an increase in the energy of the associated mode relative to that of the sphere. The difference in curvature also leads to around an order of magnitude concentration of the electric field lines between spheres and voids, producing larger field strengths. Furthermore, much of the void dispersion lies in the radiative part of the dispersion relation, allowing direct coupling to an optical field[69, 70]. This all indicates that voids provide greater enhancement of the local electric field over spheres, and this is one of the primary reasons the nano-void sample considered in this thesis produces such outstanding Raman spectra, as will be seen later.

Whilst figure 3.11 shows that at large angular momenta, both void and sphere plasmon modes tend to that of the surface plasmon energy, the behaviour in the two cases is very different as l tends to zero. For spheres, the dispersion grows ever closer to the light-line, corresponding to a reduced pinning of the mode to the surface. At $l = 0$ the field is no longer influenced by the particle, becoming purely optical in character, and, therefore, has no solution. For voids the energy of the $l = 0$ mode occurs at different, well defined, energies depending on the radius of the cavity. These solutions correspond to circular symmetric cavity modes, similar to those found within an optical resonator.

Further modelling of the void geometry has been performed by collaborators on the project[71]. This work considers a layer of spherical voids embedded within a metals surface. The impedance, Z_{eff}, of the structure is found by converting the nano-void structure into an equivalent electric circuit, as shown in figure 3.12.

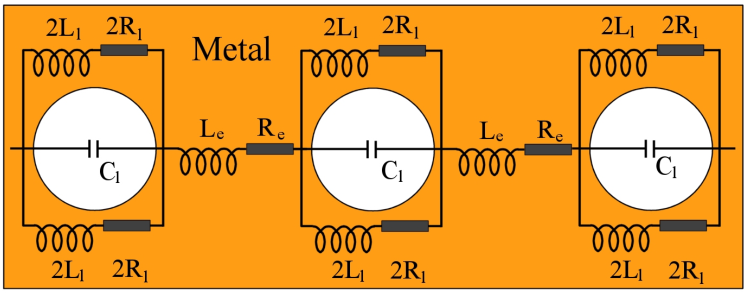

Figure 3.12: Lattice of voids and its equivalent electric circuit, taken from [11]

The Mie plasmons are modelled as charge accumulations across the void. For the l^{th} plasmon resonant mode, this is equal to a capacitance C_l connected in series with an inductor and a resistor, $L_l R_l$. This allows the impedance of the surface to be written as:

$$Z_l = \frac{R_l - i\omega L_l}{1 - \omega^2 L_l C_l - i\omega R_l C_l} \tag{3.22}$$

by finding L_l, R_l and C_l in terms of the fundamental properties of the metal, the frequency dependent solution to the impedance of the structure is found[11]. Maxwell's equations can subsequently be solved for light incident on a thin metal film of impedance Z_{eff}. This leads to exact solutions for the transmission, reflection and absorption from an array of nano-voids just below the surface of a metal. The final solutions take the form of a spherical harmonic expansion of a scattered plane-wave into an isolated cavity[71]. Coupling to the cavity mode is performed by making the top surface thinner than the skin depth of the metal. This, therefore, allows evanescent coupling between the cavity and the top surface. This approach has been used to calculate the interaction of the optical field between separated voids, as well as the interaction between a localised plasmon mode and a surface plasmon[71, 72]. The localised plasmons will often be termed 'Mie plasmons' due to their origins.

Unfortunately, at present there are no known analytical solutions to the modes of a truncated void. This is because all current solutions to the problem require the spherical symmetry of the cavities. Without spherical symmetry, no precise solutions to Maxwell's equations can be found and so no modes can be computed. A discussion into possible theories for such structures will be considered in the light of the experimental finding in chapter 6.

3.7 Plasmonic Applications

This chapter has so far introduced the existence, and explained the form of surface plasmon polaritons. However, as yet no real concept of their use has been put forward. Largely this is because, to date, there are few commercial applications of SPPs and much of the work is for academic curiosity. This said, plasmonics holds great potential for coupling together the worlds based on light and on matter, and hence are not just of scientific interest[73, 74]. Whilst very much in its infancy, the field of plasmonics has a number of conceptual uses along with some very practical ones. This section will briefly explore the work of current interest across the globe, with the aim to realise practical plasmonic devices.

3.7.1 Extraordinary Transmission

This highly controversial area of research was discovered back in 1998 by T. W. Ebbesen *et al.*[15]. It was found that by milling a periodic array of sub-micron holes through a thin silver film the transmission of light was increased above the expected level. It is believed that the structuring excites SPP modes on the top surface, which can partially travel through the sub-wavelength size holes and excite a SPP on the underside of the film. If the two SPPs are in resonance, energy can be efficiently passed through the holes and converted back to light on the underside. Refinements in analysis also found that the light was collimated as it was beamed out of the sub-wavelength apertures[4]. Since the original article, many lively discussions have entered the literature arguing whether or not SPPs are responsible for the enhanced transmission or whether it is a near field optical effect only[75, 76]. This aside, the effect of extraordinary transmission could potentially be useful for sub-wavelength imaging as well as nano-lithographic techniques[16].

3.7.2 Integrated Plasmonic Circuits

Plasmons link the worlds of the photon and the electron; as shown in the previous example this can allow light to move through structures that are smaller than the diffraction limit. This work has been extended to the concept of SPP waveguiding to produce small-scale optical components suitable to integrate into standard microchips. It has been shown that a grating can be used to couple light into and out of a SPP mode, and recent advances have started to place components between these two steps. To date SPP waveguides, reflectors and interferometers[77, 78] have all been demonstrated experimentally as well as discussed theoretically[79]. One of the current problems facing this work is the controlled conversion of SPPs back to optical radiation. Current work observes the SPP mode in the near field, detects fluorescence from dye excited by the

SPP or records random scatter from a SPP mode from defect sites. These techniques are used because SPPs are easily scattered by defects and decay over relatively short length scale. This makes any re-radiated signal too weak to be detected. With the continued advancements in nano-lithography and thin film production, SPP waveguiding and processing does hold some potential for the future.

3.7.3 Sensors

Sensor based applications is the field where SPPs currently find most use. Since the 1980's there has been interest in using surface plasmons to characterise thin metallic films, as well as in the detection of gas and biomolecules[73]. Many of these sensor applications have utilised the sensitivity of the surface plasmon to changes in refractive index of the dielectric medium, equation 3.14, and a number of companies produce products to this effect[21, 80].

Another means of utilising SPPs in sensors is through the enhanced electric field produced at the metals surface. Interest has been shown in plasmon enhanced fluorescence[81, 82], but of greatest current interest in this field is surface enhanced Raman spectroscopy (SERS). This uses the enhanced electric field of the SPP to induce Raman scattering in molecules adsorbed on the metals surface, a process with allows detailed ‘fingerprinting’ of many molecules. This will be discussed in detail in chapters 8 and 9, and has been commercialised by the company Mesophotonics[21], a spin-out company linked to the work presented in this thesis.

Chapter 4

Sample Production and Analysis

All the samples studied in this thesis are produced using a two-step process: first, latex spheres are allowed to self-assemble into a close packed array on a conducting substrate. Metal is then electroplated through the template to form a nano-structured surface. Using this technique, samples of almost any metal and cavity diameter can be produced. Most of the samples used in this thesis were fabricated by M.E. Abdelsalam, part of the photonic-metals collaborative group. This simple approach elegantly produces complex nanostructures that support a wealth of optical properties, which this thesis can only start to understand. What is more the technique is quick, cheap and lends itself to possible mass production applications.

This chapter will give a brief insight into sample preparation, then outline the analysis techniques used to characterise the physical properties of the samples.

4.1 Sample Preparation

This section describes the techniques used to produces templates of self-assembled microspheres. The electrochemical deposition procedure used to invert the template into a structured metal surface is then discussed. There will then be a brief summary into some of the more complex sample architectures also possible using multiple templates or materials.

4.1.1 Template Deposition

From previous work on this project, it has been found that one of the most important aspects is to control the morphology of the surfaces as well as the regularity of the surface features. This is done by controlling the formation of a self-assembled template, which has now been optimised to allow large monolayer domains of close packed spheres[83].

This feat can only be achieved by understanding how forces work at the micro- and nano-scale.

Mono-dispersed polystyrene latex spheres (Duke Scientific Corporation) are purchased at a 1 wt.% solution in water. Sphere sizes between 350nm and 1μm have been used with a typical variation in diameter of 1%. Initial work in this field used a technique of sedimentation to deposit the spheres onto a substrate[41]. Whilst this approach produced results[70, 69], the templates were comprised of varying layers of spheres and large numbers of defect sites, making the optical features complex and quantitative analysis difficult. An alternative method using capillary forces was subsequently developed, allowing far greater control over template formation[83]. This allowed the formation of monolayers of well ordered spheres, greatly simplifying the surface geometries and allowing easier analysis of data.

Typical templates are produced using the method depicted in figure 4.1. Substrates are made of 250nm of gold evaporated on a glass side coated with 25nm of chromium. These substrates are extensively cleaned by sonication in isopropanol, followed by a deionised water rinse and dried using argon. All solvents used were of reagent grade quality and obtained from Aldrich. Substrates are subsequently immersed in an ethanolic solution of cysteamine for three days; this allows a monolayer of cysteamine to assemble onto the surface. This cysteamine layer is more hydrophilic than gold and so reduces the contact angle of liquids on the substrate, aiding the final template production.

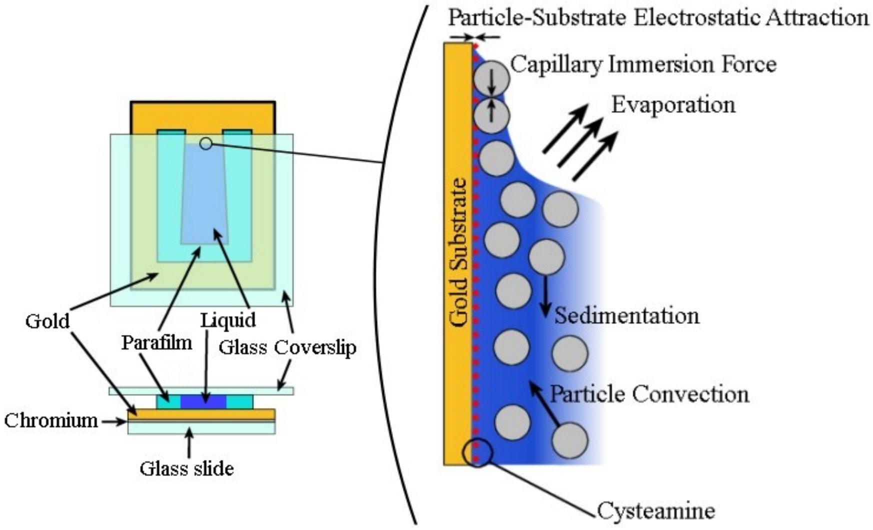

Figure 4.1: Left: cell used for template deposition. Right: Schematic of the meniscus edge at the top of the cell. Spheres are drawn out of solution by the meniscus tail and forced into a close packed domain by the surface tension between spheres.

The substrate, along with a clean cover slip, is then made to form a small fluid cell by means of a thin layer of Parafilm (Pechiney Plastic Packaging, Inc). This cell has a thickness of around 100μm and an area of 1cm^2. Held vertically, the aqueous sphere solution is added, and the cell is placed in an incubator at 25^{o}C.

The latex spheres are slightly negatively charged and so, when in solution, do not aggregate. Evaporation of the solution can only occur at the top edge of the cell, and here the cysteamine forces the water into a thin layer of approximately the diameter of the spheres. As the solution evaporates, the sweeping meniscus tail draws spheres out of solution and deposits then on the gold surface. Since deposition only occurs at the meniscus edge and the rate of deposition can be controlled by the evaporation rate, the seeding of a single domain becomes highly probable. Subsequent spheres will add to the initial domain and, if the sphere concentration is carefully controlled, the entire surface will form a single ordered close packed structure. The meniscus tail also prohibits the formation of a second layer of spheres, keeping the geometry of the system to the simplest case: that of a monolayer. This allows the optical properties of nano-voids to be understood, before the more complex structures using multiple layer templates are analysed (a topic for a future project). The capillary force is greater than that of the electrostatic forces between the spheres as well as that of gravity; hence, deposited spheres will be drawn together as the template edge dries, ensuring the spheres are touching and helping the final domain orientation to be well defined.

Figure 4.2 shows a scanning electron microscope (SEM) image of a typical region of a template. The template appears to be a single, monolayer domain of close-packed, touching spheres. The spheres are resistant to re-suspension when, in the next production step, the sample is lowered into an electrochemical plating solution.

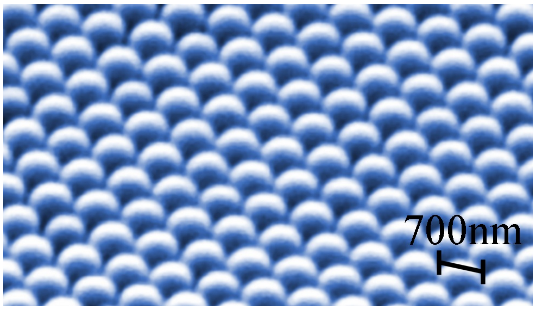

FIGURE 4.2: SEM image of a template made from 700nm spheres.

4.1.2 Electrochemical Deposition

Electrochemical deposition is performed using a three-electrode arrangement, depicted in figure 4.3a. The sample on which the metal is to be grown forms what is known as the working electrode. The counter electrode supplies the charge to complete the circuit while the reference electrode is used to monitor the total charge passed through the cell. A commercial plating solution (Technic Inc), containing gold ions, forms the connection between the electrodes. For the sake of simplicity, the plating of gold will be specifically reported here, other metals follow very similar lines, using different solutions and voltages. Figure 4.3b shows the time dependence of the charge when plating through a micro-sphere template, where throughout plating the voltage is kept constant.

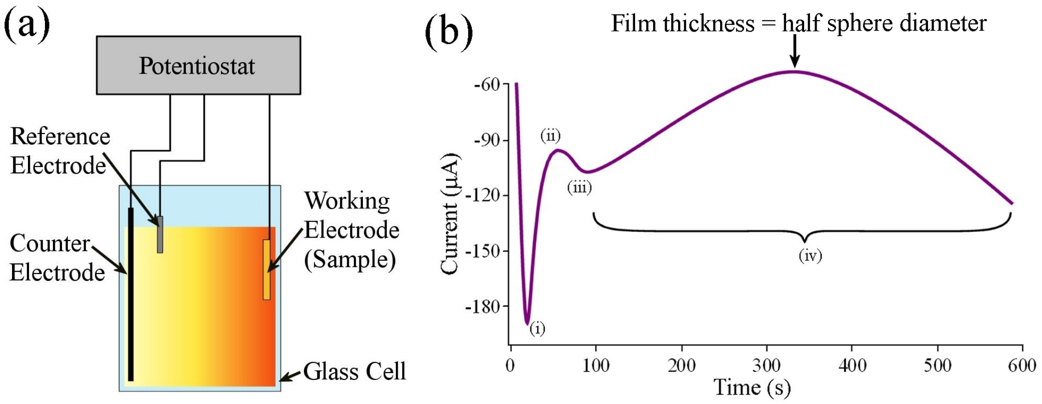

FIGURE 4.3: (a) Electrochemical deposition setup (b) Current vs. time for the deposition of gold through a close packed sphere template, initially a voltage is applied that causes a capacitive effect in the cell (i), then gold will begin to deposit (ii) until a steady deposition rate is reached (iii). The changing area of deposition through the template causes a change in current (iv).

At time t = 0 a voltage is applied through the cell and the working electrode becomes negatively charged. Positive ions in the solution are drawn towards the negative electrode, while negative ions accumulate near the positive one; this effect gives rise to a current (point i), which quickly returns to zero. The voltage in the cell is sufficient for gold ions to overcome the coulomb potential and undergo the reaction: $Au^{+} + e^{-} \rightarrow Au$. First, the nucleation of single gold atoms occurs, then the formation of islands as more gold is deposited (point ii) and, finally, the formation of a gold film. The speed of growth is now limited by the rate at which gold atoms can diffuse out of solution and into the plating region; this steady state is determined by the diffusion-limited current (reached at point iii). By monitoring the charge passed in region (iv) the thickness of the deposited film can be calculated. When producing a nano-structured film the growth occurs through the sphere template, causing a modulation in the growth area and a corresponding variation in charge. The peak, corresponding to a charge minimum, in region (iv) corresponds to a thickness equal to the radius of the spheres, where the deposition area is a minimum.

To grade the thickness of a deposited layer the sample is mounted on a micrometer stage, allowing the systematic retraction of the surface out of the plating bath. At every step the new plating area is measured, allowing the absolute thickness of each deposited step to be calculated. After deposition the samples are washed in tetrahydrofuran for two hours to completely remove the latex spheres, leaving a free-standing array of nano-voids, (fig 4.4).

Using this technique samples graded from zero to one ball height can be reliably produced. To date, samples made from gold, silver, nickel, platinum, palladium, copper

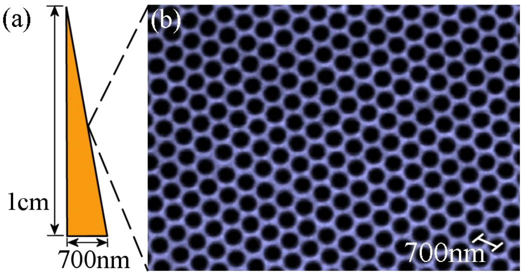

FIGURE 4.4: (a) Schematic of a graded thickness sample (b) SEM image of a nanostructured gold film with a void size of 700nm.

and poly-pyrolle have been produced. The versatility of this technique also allows the production of more complex structures.

4.1.3 More Complex Structures

Using the techniques described above a variety of more complex structures can be produced. These fall into three categories: multilayer structures, double-deposition sample and nano-dots. These structures provide excellent control over the optical properties of the surfaces. However, due to the time constraints associated with this PhD, these projects have only just been started and so will not feature heavily in this thesis.

4.1.3.1 Multilayer Structures

This technique is performed by depositing a metal film of thickness less than one ball height through a template. The sample is then placed in a plating bath of a different metal to complete the growth. This is a very flexible technique and can be repeated many times to form a multi-layer structure. Of interest to the current work is when a combination of plasmon active and inactive metals is used. The first metal is graded in the usual way, then the second metal makes up the top 100nm of the whole structure (fig 4.5). This architecture allows separate control over surface and localised plasmons, and hence control over SERS active regions on samples. The disabling of surface plasmons also helps to distinguish them from diffraction effects.

4.1.3.2 Double Templating

In this technique, a thin layer of metal, typically 100nm, is deposited through a template. After the template is dissolved, this pre-pattered substrate is coated in cysteamine and again forms the substrate on which spheres will be deposited. Spheres will preferentially deposit in the dishes on the substrate so, by varying the relative diameters of the spheres in the first and second template, a variety of geometries can be achieved. Two examples

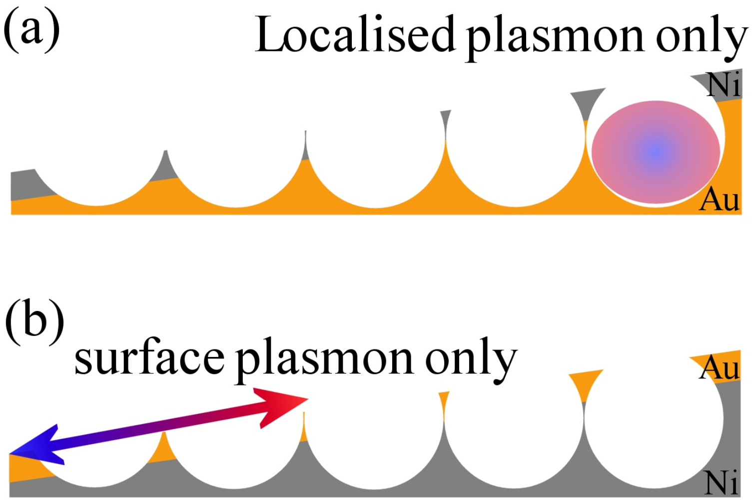

FIGURE 4.5: Double deposition samples. (a) 100nm of nickel topping a graded gold sample, this should only support localised plasmons. (b) 100nm of gold topping a graded nickel sample, allowing only the existence of surface plasmons.

of this technique are shown in Figure 4.6, where the second template consists of spheres with smaller and larger diameters compared to those in the initial template respectively.

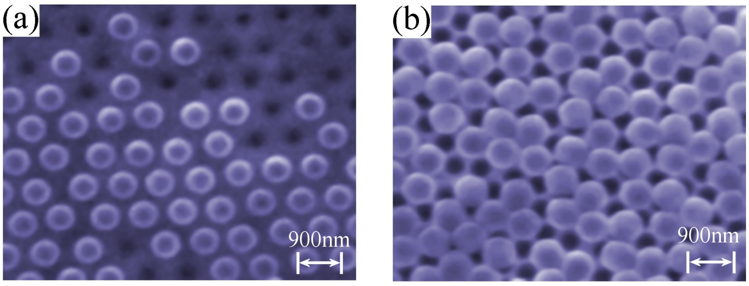

FIGURE 4.6: SEM images of spheres deposited on top of a pre-structured substrate, (a) 700nm spheres on a surface structured with 900nm dishes. (b) 900nm spheres on 700nm dishes.

For smaller spheres, this process creates samples where the cavity diameter is different from that of the cavity spacing. This decoupling of sphere diameter and spacing give much greater control of localised and delocalised plasmon energies. When spheres of a larger diameter than those of the initial template are deposited the mismatch in size leads to a more complex ordering, reminiscent of the quasi-crystal structures of current interest in photonic crystal research[84].

4.1.3.3 Nano Dots

Much of the current research into SERS concentrates on colloidal particles deposited onto a substrate. This technique provides very little control over the separation of the particles and thus results prove hard to quantify. In the production of nano dots discussed here, whilst the scale of the particles is larger than those used in colloidal experiments, absolute control is gained over the dot sizes, separations and arrangement. To achieve this, the properties of the polymer poly-pyrolle are exploited; this is a conducting polymer that can be deposited in the usual manner but when exposed to UV light becomes an insulator. If now a second electro-deposition step is performed, metal can only seed in the small region at the bottom of the dishes where no polymer could be deposited (the region where the base of the spheres touched the gold substrate). Subsequent deposition will, in effect, invert the template, creating metallic nano-spheres. Figure 4.7 shows an SEM image where the dots were only grown to half height, forming an array of gold hemispheres.

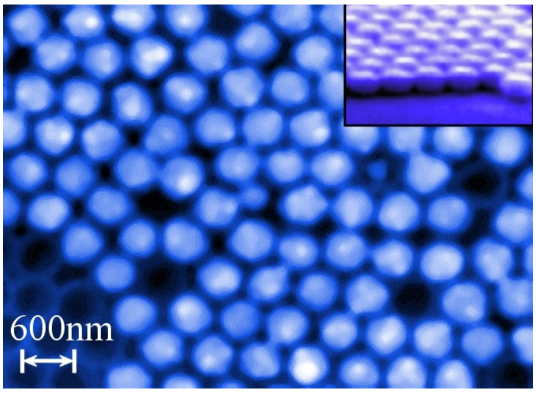

FIGURE 4.7: SEM images of gold nano-dots with diameters of 600nm, inset shows side view.

4.2 Sample Characterisation

After production, samples undergo a rigorous set of analysis experiments. Some of these characterisation methods are applied to all samples to understand the morphology over the film. Other tests are conducted to understand specific sample properties, the results of which can be used to understand other experimental details. The biggest challenge facing this project is finding the precise structural geometry at the different thicknesses across different samples. This information is crucial to accurately compare and correlate the complex optical spectra outlined in the coming chapters; hence, each characterisation method has been used to try to gain more information to fulfil this goal.

4.2.1 SEM Characterisation

Directly after growth all samples are viewed using a Philips XL30 ESEM. This provides information about the short-range order and crystalline structure of the films along with some information about the thickness. Figure 4.8a shows a typical SEM image, viewing about fifty voids. Clearly, the voids have formed an almost perfect close packed crystal structure, although variations and small discrepancies are present; by analysing the image further statistics can be built up. Figure 4.8b shows the angle between voids varies only fractionally from the expected 60^o, but the void separation has a larger spread of values. On closer inspection of the SEM image it can be seen that this spread of void separations is due to stacking faults which, whilst maintaining the same domain orientation, have distanced adjacent voids by varying amounts. This is probably due to small variations in the drying rate of the templating solution. When larger fields of view are observed it is often possible to find larger faults and occasional sub-domains. At the largest scale the primary sample domain is observed to wander in orientation over the length of the sample. It is worth noting that whilst the imperfections of the sample growth technique have been outlined, these samples are very well ordered for samples formed via a self-assembly route and compare very favourable to others shown in the literature[85, 86]. Whilst not of the same standard as structures produced using an electron-beam system, the self-assembly route is much quicker and cheaper and is more than capable of producing sufficient quality to observe strong preferential diffraction from the hexagonal array (fig4.8c).

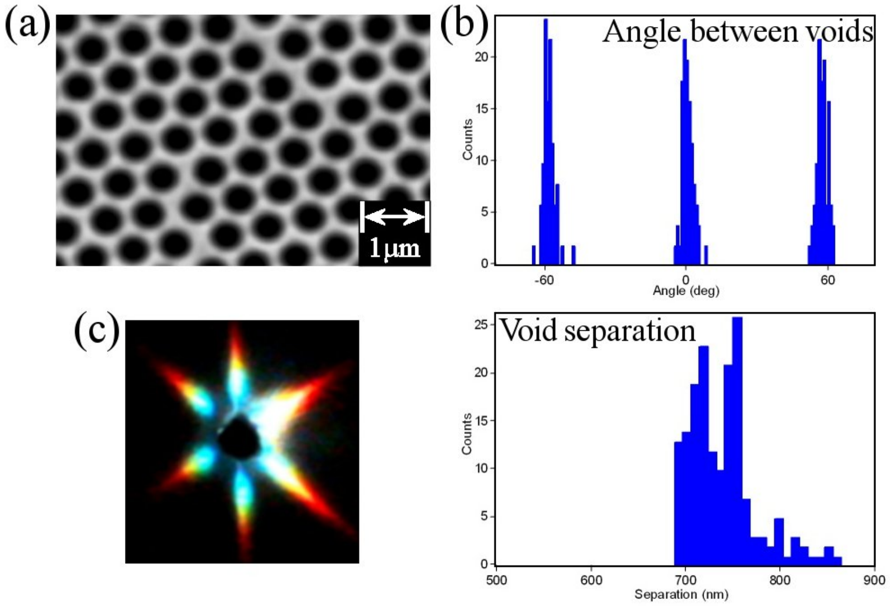

FIGURE 4.8: (a) SEM image of a 700nm structured film from which (b) statistics of angle between voids and void spacings can be calculated. (c) Diffraction pattern of a white light laser beam off a nanostructured sample, 6-fold symmetry is clearly evident.

Since the voids are spherical, further analysis of SEM images can be performed to find an approximate film thickness by measuring pore mouth diameter as defined in figure 4.9 and using the equation.

$$\bar{t} = \frac{r_{void} \pm \sqrt{\left(r_{void}^2 - r_{pore}^2\right)}}{2r_{void}} \tag{4.1}$$

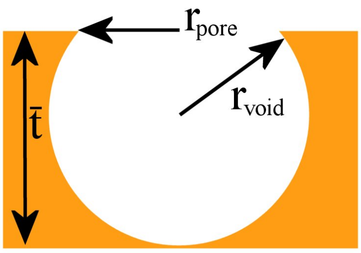

FIGURE 4.9: Definition of normalised thickness $\bar{t}$ = $thickness/diameter$ along with other parameters required to calculate the film thickness from SEM images.

Here, the normalised thickness, $\bar{t} = sample\,thickness/diameter$, is defined, and will be consistently used throughout the rest of thesis to define sample thickness.

SEM images of three different thicknesses are shown in figure 4.10. Using equation 4.1 it is possible to calculate approximate thicknesses for each of these positions. This image highlights the variation in surface geometry with changing thickness. When thin, the sample consists of an array of well-spaced shallow dishes, with a smooth interstitial top surface. Near half void height, $\bar{t} = 0.5$, the cavities are separated by triangular pillars and touch the neighbouring six dishes in between these spikes. Above $\bar{t} = 0.5$, the metal is forced to grow out from these islands over the non-conducting spheres, leading to increased roughness and less efficient growth. In this thick regime the cavities start to resemble spherical cavities, and at $\bar{t} = 1$ become almost completely encapsulated.

The work done in this thesis focuses on samples made from a template of only one sphere thickness, keeping the geometry described above at its simplest. If multiple layers of spheres are used then above $\bar{t} = 0.5$ the structure starts to take a different appearance, forming a honeycomb structure.

At first sight it appears that the SEM images can provide sufficient information about the film thickness. However, the error in knowing the exact position of the void rim gives rise to large errors in the calculated thickness, for this reason atomic force microscopy (AFM) has also been performed on many samples.

4.2.2 Atomic Force Microscopy Characterisation

Using a TopoMetrix Explorer atomic force microscope the fine details of a number of samples were characterised. To minimise tip damage when traversing the high aspect ratios surfaces the AFM was used in non-contact mode. For consistency AFM scans were performed at the same positions that the SEM images were taken. Figure 4.11 shows a typical image and associated profile from a sample made of 700nm voids.

The AFM images show the plated metal to be smooth down to around the 50nm length scale and follow the spherical geometry well. From this data, an accurate film thickness

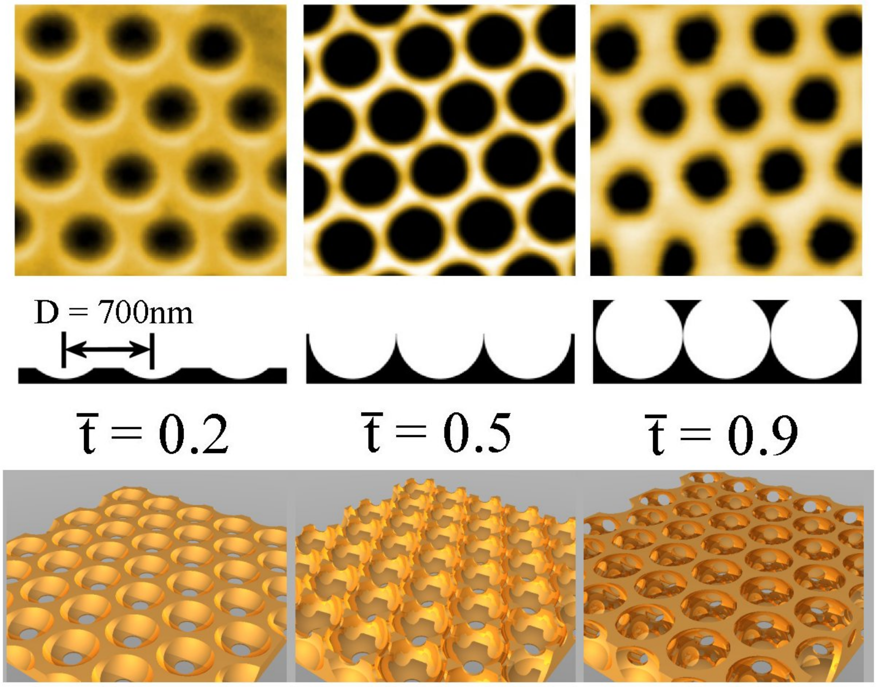

FIGURE 4.10: Top: SEM images of a 700nm nanostructured surface at normalised thicknesses of $\bar{t}$ = 0.2, 0.5 and 0.9. Middle: Schematic cross-section showing geometry. Bottom: Three-dimensional reconstruction of surface structure.

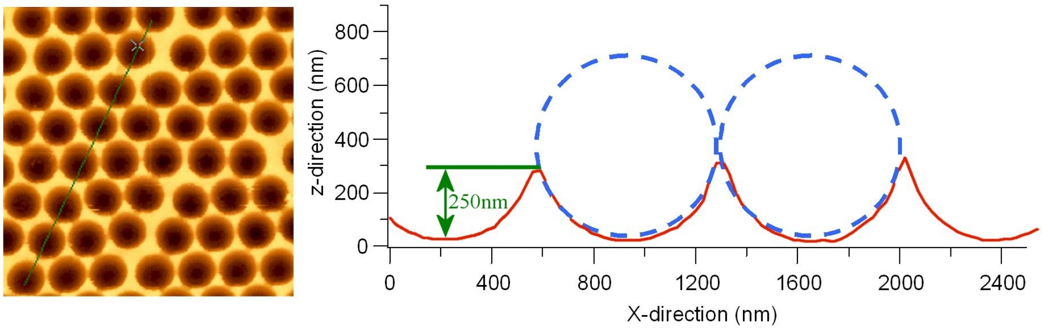

FIGURE 4.11: AFM data from a 700nm sample at a thickness of 250nm. Voids appear smooth, spherical and close packed.

can be calculated. It is also possible to confirm that the voids do not suffer any shrinkage from the size of the template, thus the observed disconnected voids are caused during template formation. Taking the average thickness of twenty voids for each measured position on the sample, a map of sample thickness can be constructed (fig 4.12).

Below $\bar{t} = 0.5$ the AFM can accurately map the surface. However, for greater thicknesses the geometry prohibits accurate reconstruction and the thickness has to be inferred from the measured pore mouth diameter. This again leads to inaccuracy and uncertainly but much can be learned from the data below half-void height. This shows the thickness to be linear with position and so gives a reasonable guess for the true thicknesses above $\bar{t} = 0.5$. This information is useful to calibrate other techniques and has proven to

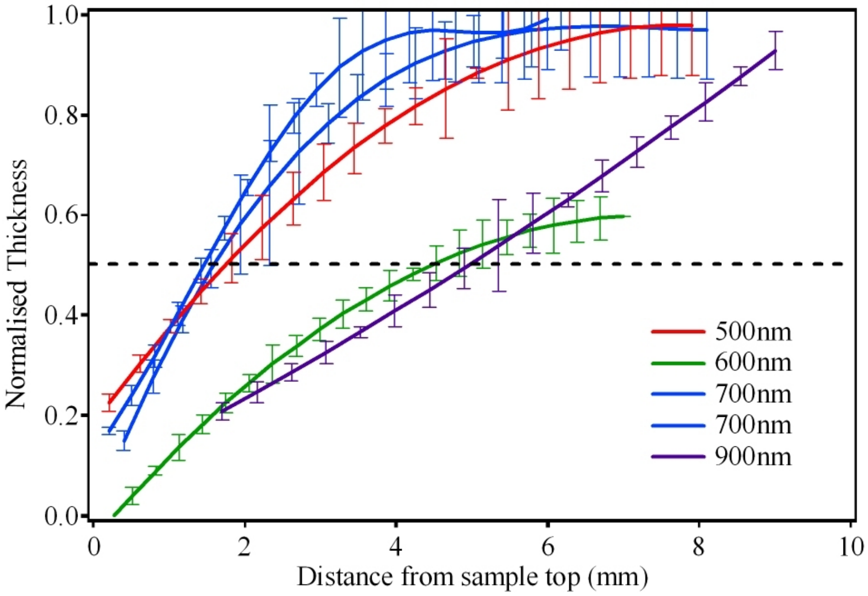

Figure 4.12: Graph showing normalised thickness as measured by AFM as a function of position for five samples of various void sizes, as shown.

be accurate for samples down to void diameters of 500nm. When initially performed, the observed asymptotic behaviour towards $\bar{t} = 1$ was of some confusion, however, the reason for this will be found in following experiments.

4.2.3 Voltage - Current Analysis

In the section on sample production it was stated that the template geometry enforced the shape of the current-time diagrams. Therefore, it might be considered that working back from the current time graph the precise sample geometry could be found. This indeed should be true; however, when grading the thickness of the sample the templating is performed out of equilibrium. This makes it more difficult to know precisely what current corresponds to what geometry, if this could be found with absolute accuracy, the problems of subsequent analysis would no longer exist. To try to solve this problem the AFM data for the 600nm sample was correlated with the corresponding current time curve, shown in figure 4.13. This sample was used as the thickness is mainly below $\bar{t} = 0.5$ and so the data is more trustworthy.

This figure shows the current characteristics of the deposition of different layers (plotted in colours) against the theory for plating through a perfect template (plotted in black). Due to the non-equilibrium nature of the plating a varying level of offset has been applied to the different current curves, shown in the inset. This offset has been done with the aim of aligning each curve with the previous one and corresponds to the accuracy of the guess to the 'correct' equilibrium current used for each plating step. Each curve starts with a sharp spike, corresponding to the re-charging of the capacitive layer between the

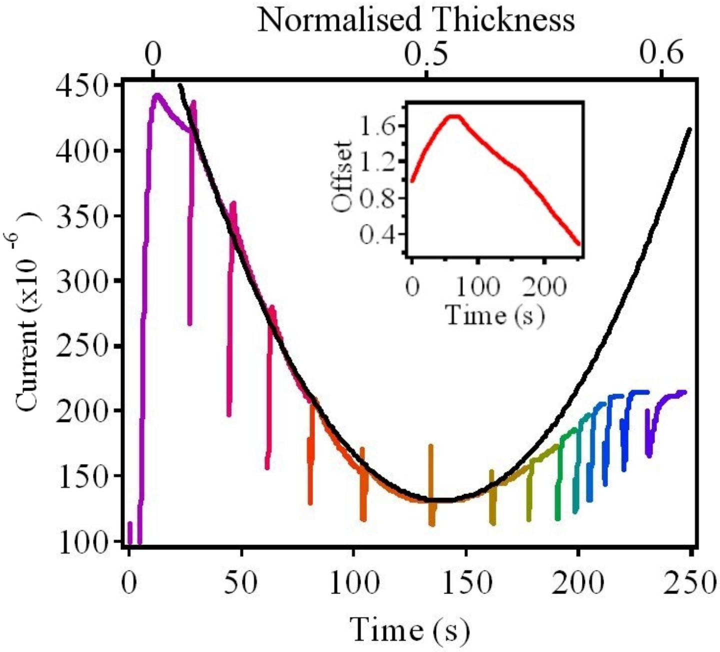

Figure 4.13: Graph showing current passed vs. plating duration through a template of 600nm spheres. Different colours represent different steps as the sample is retracted from the solution. Inset shows offset of each step required to align the different plated regions.

electrodes, the size of which is related to the required offset. After this data fix has been performed, a comparison can be made between the current and the observed thickness of each plated step, shown on the top axis. It can be seen that the tuning point in the current plot closely relates to $\bar{t} = 0.5$. If the current-time plot is used to estimate the total film thickness it can also be related to the AFM data, both giving a final thickness of $\bar{t} = 0.6$. These connections make this characterisation technique promising, however, above $\bar{t} = 0.5$ the plating becomes less controlled and the current seems to fit the theory less well. Coupled with this problem is the uncertainty in the AFM data above $\bar{t} = 0.5$ also limiting further conclusions. It is hope that soon direct knowledge of the film thickness will be ascertained from the current-time plots, however, before this can become reality further characterisation must be done, the likes of which are outlined in the following section.

4.2.4 Further SEM Analysis

Whilst a huge amount of information on a number of samples has been gathered, one problem is outstanding, the exact geometry and thickness of the films. Below $\bar{t} = 0.5$ the AFM analysis appears accurate, but for the extreme geometries and overhangs above this only educated guesses can be made. To answer this problem, samples are viewed at 45^o using a LEO 1455VP SEM. For thicknesses approaching $\bar{t} = 1$ it was found to be helpful to cleave the samples to expose the cavity geometry. Figure 4.14 shows several images of a 700nm sample at different thicknesses.

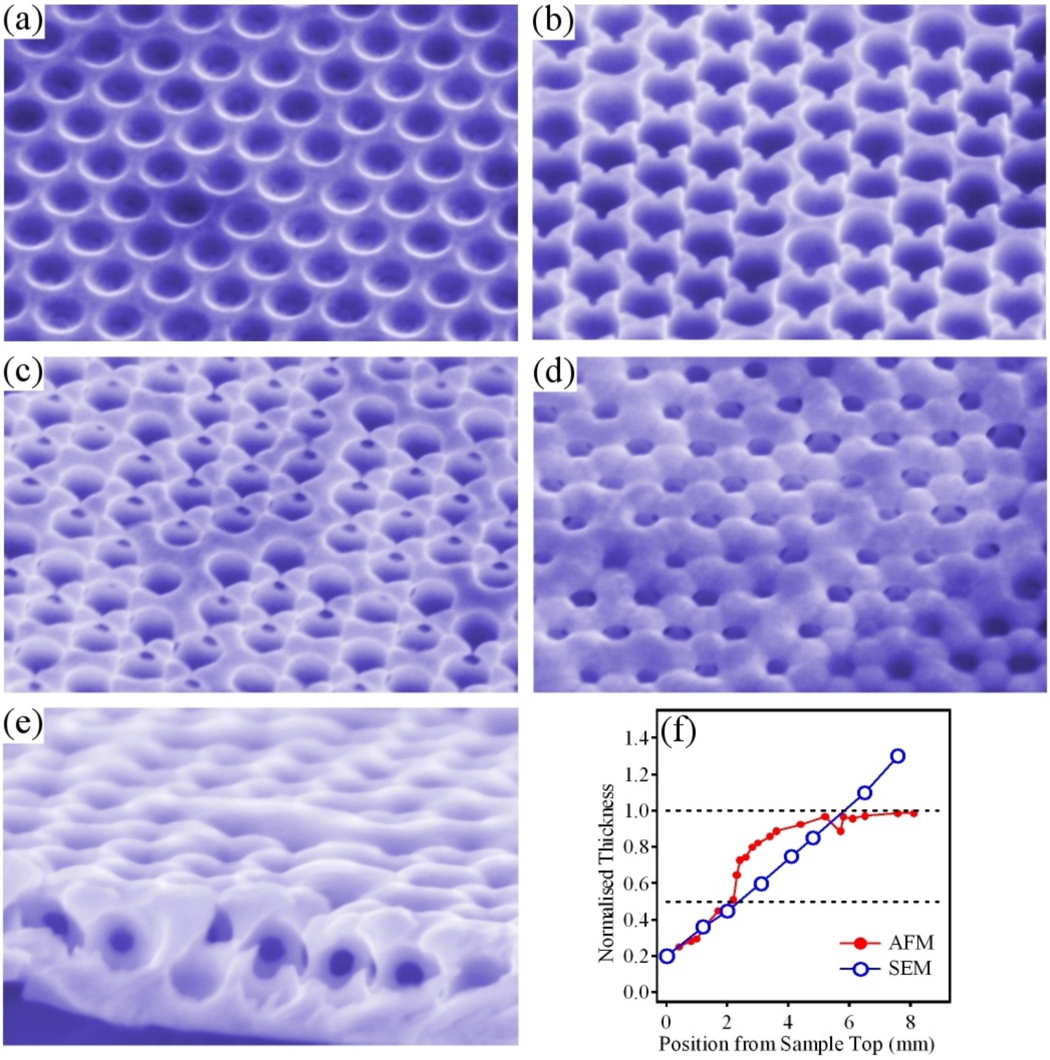

FIGURE 4.14: SEM images of a 700nm void size sample at (a) $\bar{t} = 0.1$, (b) $\bar{t} = 0.5$, (c) $\bar{t} = 0.65$, (d) $\bar{t} = 1$ and (e) $\bar{t} = 1.3$ after cleaving to observed precise void geometry. (f) AFM and new SEM extracted thicknesses as a function of sample position.

Below $\bar{t} = 0.5$ the sample appears exactly like the AFM images. Good uniformity in height is observed and the cavities precisely taking the form of well spaced nano-cups, figure 4.14a. At $\bar{t} = 0.5$ the metal grows between the spheres and forms an array of tetrahedral islands, figure 4.14b. These are spaced by about 100nm tip to tip with the separation arising from the windows connecting the voids. As the thickness increases further, the growth from these islands is easier upwards than outwards due to the insulating nature of the spheres. This causes the islands to form domes and leads to the apparent rapid increase in thickness observed by AFM. The islands connect around $\bar{t} = 0.6$ leading to bowtie-shaped structures surrounding each void figure 4.14c. The plating technique struggles to encapsulate the spheres and the final geometry is that of a spherical cavity connected to the surface via a funnel type structure, shown in figure

4.14d and e. The faster interstitial growth forms lumps on the top surface, running down to the pore mouth. These are precisely what is observed using AFM analysis, although the holes were assumed to lead directly into the cavity. This effect leads to the apparent asymptotic behaviour re-plotted in figure 4.14f. By carefully calculating the void depth over the sample it is possible to confirm that the growth rate is linear and leads to thicknesses well above one-void-height. This data also correlates well with the optical data presented in later chapters, where it was found a linear gradation of thickness increasing to above $\bar{t} = 1$ gave the most sensible results. The presence of almost perfectly spherical voids also makes the modelling of the structures easier than attempting to understand electric fields in non-symmetric structures.

Sample were also viewed using a Hitachi FEGSEM, one such image is presented in figure 4.15. The higher resolution of the FEG-SEM makes it possible to resolve the fine details of the voids.

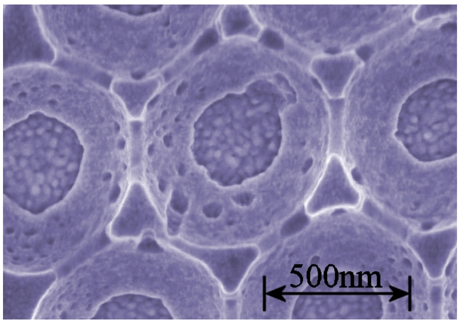

FIGURE 4.15: High resolution FEGSEM image of 700nm diameter gold dishes.

This image confirms the results from larger structures and other inferred measurements. The voids have a hole at their base corresponding to a region where the sphere was touching the substrate. This 'window' has already been utilised in the formation of nano-dots, discussed previously. The holes at the base are quite large and allow a good view of the evaporated gold substrate on which the films have been grown. Strikingly the electrochemically grown surfaces are significantly smoother than the evaporated substrate, with both possessing a roughness on the scale of 50nm and below (out of the range of previous imaging techniques).

These final two characterisation techniques nicely confirm the cavities are smooth and spherical, with a linear thickness gradient with sample position. Importantly, this allows all samples to be calibrated, allowing direct comparisons between the different optical phenomena observed on samples of different pitches.

4.2.5 Silver Samples

Whilst the gold samples have been shown to be smooth and well structured, SEM images of silver samples show a different story, shown in figure 4.16.

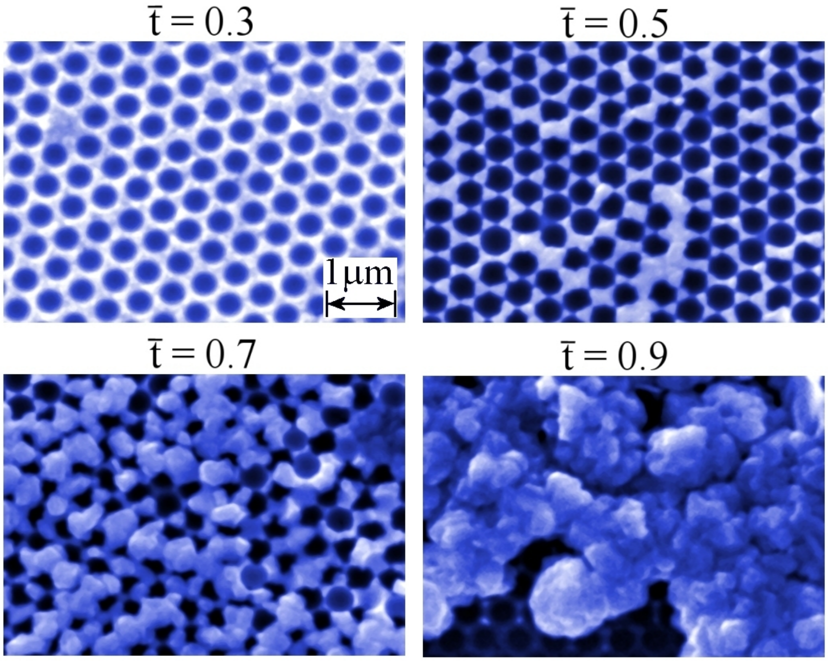

FIGURE 4.16: SEM images of a silver sample, void diameter 500nm, thicknesses as shown.

These images show that the silver plates well up to $\bar{t} = 0.5$, however, above this thickness the growth becomes somewhat erratic. This is probably because above $\bar{t} = 0.5$ the silver surface comes into direct contact with the plating solution. At this point more rapid growth becomes possible and the slight difference in growth between spheres will now lead to large difference in thickness at different positions. When the metal grown from the different interstitial sphere sites meets, the effect of multiple electrodes makes the deposition process more difficult to control. This effect leads to the observed irregular surface. These effects are not observed on the samples made from other metals due to more controllable growth. Another feature of the silver samples is an increased roughness of the surface, again due to the less controllable plating conditions. Work is ongoing to solve this problem, but it is sufficient for now to limit analysis of silver films to below $\bar{t}$ = 0.5.

4.2.6 (Quick) Optical Analysis

With a full understanding of the structural properties of a sample, it is useful to perform a quick optical experiment to find the fundamental absorption features present. This optical characterisation gives direct information about the thickness and ordering of a sample, as well as an indication of the overall appearance. Samples are viewed using an Olympus BX51 optical microscope. The first step is to find the best horizontal sample position to perform reflectivity experiments down the thickness gradation, figure 4.17a. This is required to avoiding intrinsic scratches and blemishes found on some samples.

Images and spectra are then taken along this line to form a data set such as the one shown in figure 4.17 b and c.

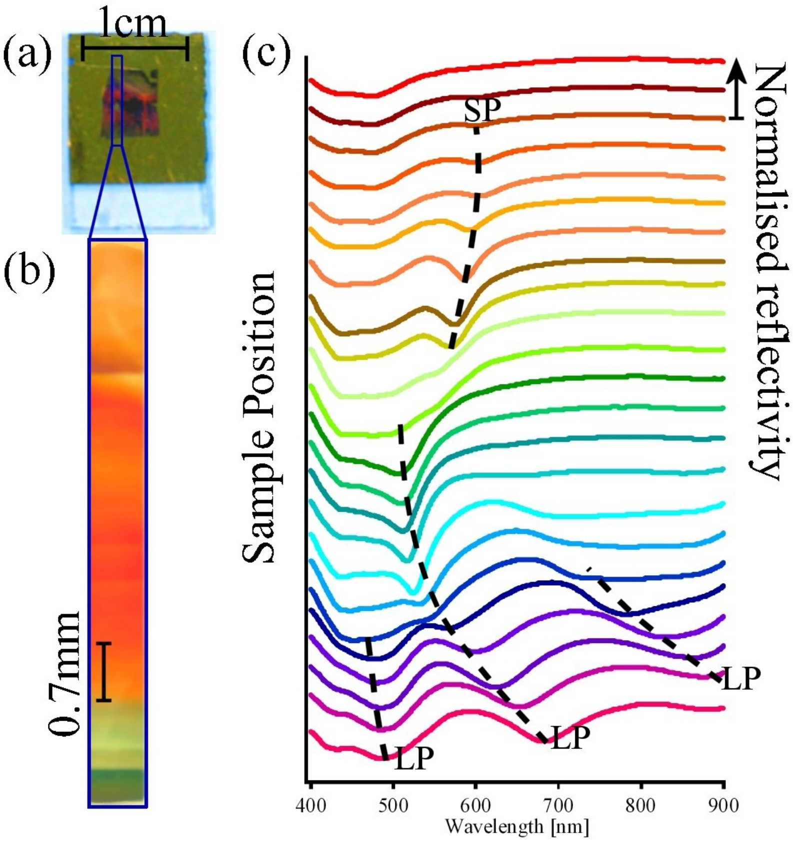

FIGURE 4.17: (a) photograph of a sample made from 600nm voids, graded from $\bar{t} = 0$ to 0.8. (b) 10 times optical image of the surface from top to bottom. (c) Normalised spectra taken at regular intervals down the same line of the sample, surface plasmon (SP)and localised plasmon (LP) features are indicated.

The clear variation in colour of the optical image shows the varying absorption of the sample at different thicknesses, the purity of the colour also indicates that the sample is well ordered and smoothly templated. This image is also useful in showing the top and bottom points of the line over which all subsequent data will be taken; this allows well-correlated data on samples where variations are inherent. The set of normal incident, unpolarised reflection spectra are normalised to the reflection off a silver mirror and show the fundamental features of the sample: at the top, sharp surface plasmon absorptions are visible, while the broader sweeping localised absorptions over the bottom half of the sample are also clear. Using this data, it is easy to select samples that absorb well at different wavelengths for experiments where these resonances play a fundamental role. The microscope can also be used at 200 times magnification to observe an extended region of the surface domain; this information is useful when relating orientation dependent features at different positions.

4.2.7 Contact Angle

The wetting of a solid surface is characterised by the contact angle, this is the angle between the water/air and water/solid interface and is controlled both by the surface energy and the geometric micro-structuring of the substrate. Manipulation of the contact angle is commonplace in chemistry and has already been mentioned in the previous section on template formation. Here, cysteamine was used to alter the surface energy and reduce the contact angle of the gold, forming a long meniscus tail in the solution of micro-spheres. While the effect of surface energy on the contact angle is well understood, the effect of altering the surface geometry on the micro- and nano-scales has been less thoroughly explored. Again nature has been utilising this effect for many millions of years, the butterfly *Papilio Ulysses*, shown at the beginning of chapter 2 (figure 2.1), uses the nano-structuring of its wings not only to produce the vibrant blue colour but also to help water droplets slip off with ease. The droplets carry with them dust and so the structuring provides a mechanism for self-cleaning as well as protection against becoming waterlogged. With a similar structure to the butterfly wings, the samples detailed here are ideal for testing the effect of changing contact angle with structural geometry. In these experiments 5μl droplets of water are placed on a sample at different thicknesses, photographs were then taken and analysed to find the contact angles of the droplets for the different geometries, figure 4.18a, b.

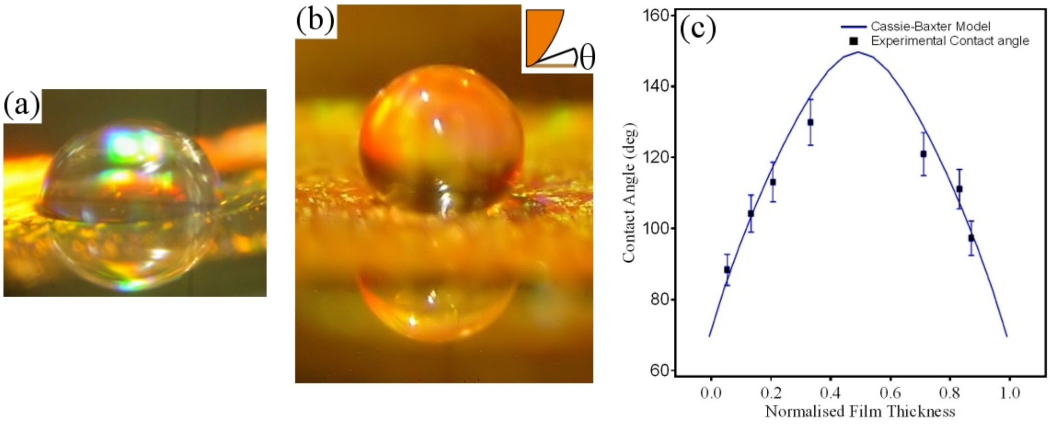

FIGURE 4.18: Images of 5μl droplets of water on samples of thickness (a) $\bar{t} = 0.1$, and (b) $\bar{t} = 0.6$. (c) Graph showing contact angle vs. normalised sample thickness, solid line shows theory predicted by the Cassie-Baxter model.

On smooth gold the contact angle is measured to be 70^o as expected, while on the structured surfaces contact angles up to 130^o are recorded, showing the surfaces have become significantly more hydrophobic. There are also clear variations in how proud of the surface each droplet stands between the images. Since the material and pitch of the structures are constant this effect comes purely from surface geometry[87]. A plot of contact angle vs. thicknesses is presented in figure 4.18c. This shows that the maximum contact angle occurs when $\bar{t} = 0.5$, corresponding to sharp features separated by large air spacings.

There are two well-established contact angle modelling techniques, these are based on different assumptions, as shown schematically in figure 4.19.

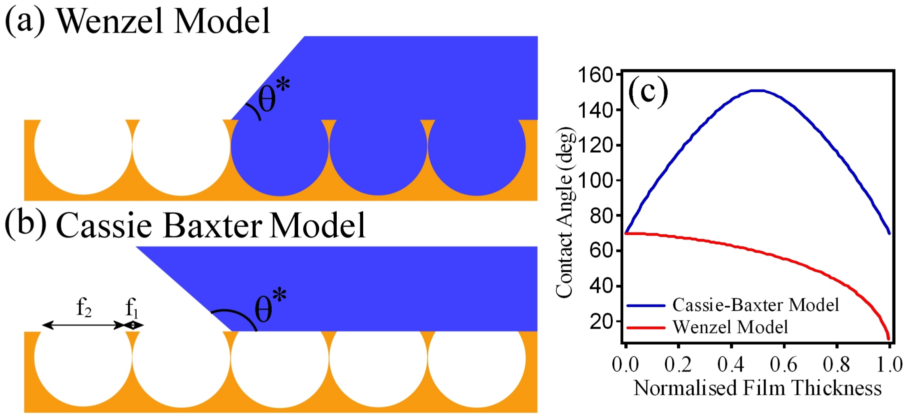

FIGURE 4.19: (a) Schematic of Wenzel model. (b) Schematic of Cassie-Baxter model. (c) Plot of contact angle against normalised sample thickness using both models.

The first model, attributed to Wenzel[88], assumes that liquid fills a nano-structured surface completely, fig 4.19a. The apparent contact angle, θ^*, of the liquid is given by:

$$cos\theta^* = r.cos\theta \tag{4.2}$$

where r is the roughness factor of the surface, equal to the ratio of the total surface area to the area projected in the horizontal plane. This model effectively considers the ratio of the surface tensions between the solid/liquid interface and the solid/air interface. An increase in surface area gives rise to an increased importance of the solid/liquid surface tension. Since the smooth gold surface wets, the increased surface area thus leads to a further increase in wetability, and a reduction in the contact angle.

The second model, attributed to Cassie and Baxter[89], assumes that air is trapped below the contact line within the structures, fig 4.19b. The apparent contact angle in this case is given by:

$$cos\theta^* = f_1 cos\theta - f_2 \tag{4.3}$$

where f_1 and f_2 are the fractions of surface made up of solid material and air filled voids respectively. This model is solely dependent on the topology of the top surface and so follows a parabolic relationship with film thickness due to spherical nature of the voids. Figure 4.19c plots the apparent contact angle according to both models between $\bar{t} = 0$ to 1. The Cassie-Baxter model predicts a maximum contact angle at $\bar{t} = 0.5$ due to the minimisation of the solid surface. The Wenzel model on the other hand predicts a continuous reduction in contact angle due to the continuous increase in surface area.

Figure 4.18c shows the experimentally recorded contact angle over a fully graded sample. Also presented on the image is the theory given by the Cassie-Baxter approach. A clear correlation between the Cassie-Baxter model and the experimental data strongly indicate that water does not enter the cavities for the majority of the surface geometries, instead sitting on a cushion of air trapped within the voids.

A further interesting feature of the data is that at $\bar{t} < 0.1$ where the contact angle drops below 90^o; this means the surface turns from hydrophobic to hydrophilic. This change from wetting to non-wetting implies that the dishes should become filled with liquid for these geometries and change to the Wenzel modelled scenario. Unfortunately, the possible step in contact angle is close to the experimental errors so may be hard to observe and so this conclusion currently remains unresolved. A similar change from hydrophobic to hydrophilic is also observed above $\bar{t} = 0.9$. In this case the change corresponds to water wetting the top metal surface, not penetrating the almost encapsulated voids. Understanding the wettability of these nano-structured surfaces is important to understand how liquids act on the nano-scale, a topic of particular importance if the surfaces are to be used in sensor applications.

4.3 Conclusions

The process of self-assembly and electroplating has been shown to be a powerful means of producing nano structured surfaces both quickly and incredibly cheaply. The analysis of the samples has shown that the samples are well ordered and that excellent control and understanding of the surface geometry has now been achieved. Samples can be made from a wide variety of materials along with combination of them, providing the means to produce an almost limitless variety of structures. Work using these techniques, combined with that of photolithography, to produce square array of holes along with wires and other structures, is also currently being considered although too preliminary to feature in this thesis. With a solid understanding of the sample properties, the way is paved to begin to understand the complex and varied optical response of nano-structured metals. However, first, a discussion into the experimental setup will be presented.

Chapter 5

Experimental Setup

The detailed optical experiments performed in this thesis use a computer controlled goniometer along with a number of different lasers. The data produced is quite substantial, so this chapter will provide an explanation into the different imaging techniques applied to the data in the forthcoming chapters, as well as a discussion into the experimental setup.

5.1 Experimental Setup

Much of the work undertaken to date has been performed using a computer-controlled goniometer. For the experiments exploring surfaces plasmons on the nano-metal surfaces, a super-continuum white-light laser performs the job of illumination. The full setup is shown in figure 5.1.

A passively mode locked, 1064nm, 1ns, microchip laser (JDS Uniphase) is focused into a holey fibre (Blaze Photonics). The fibre has a very small core and is designed to have zero dispersion at the pump wavelength as well as being single mode for all guided frequencies. The high confinement in the fibre core leads to strong non-linear effect, for this particular fibre the most important of these is four-wave mixing[90]. As the light travels through the fibre this mixing process efficiently broadens the spectra of the pump laser; after 20 meters the emerging light is well collimated and has an optical spectrum from 480nm up to at least 2μm. The spectral characteristics are stable over time scales of months for both intensity and shape.

The polarisation of the white-light laser beam is selected before the beam is guided onto a sample. The sample can be moved in both in-plane directions (x and y) as well as rotated in the θ/ϕ directions, as defined in figure 5.1. This requires the laser beam to be incident on the sample at the centre of both planes of rotation as well as the sample being precisely aligned in the same planes; this requires a high degree of precision to

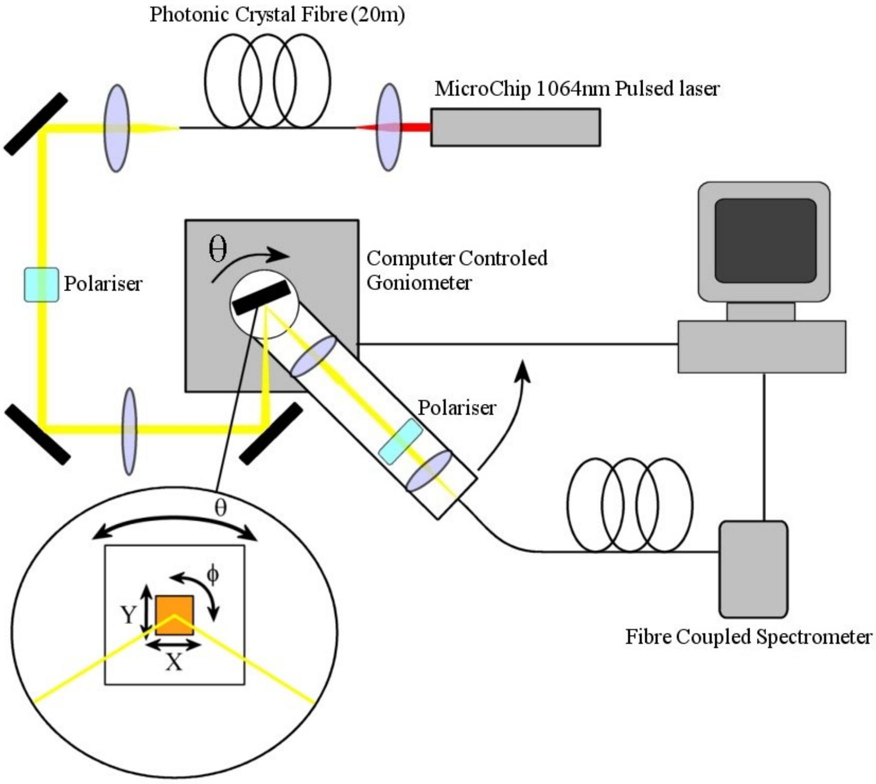

Figure 5.1: Experimental setup for measuring the angle resolved reflectivity of nanostructured samples. Inset shows definitions for θ - incident angle ,ϕ - sample orientation, and x/y movement directions.

ensure the reflected laser beam will always precisely land on the opening of an optical fibre attached to the collection arm. The goniometer has no limit to the positive angles it can record, however, this enforces a limit on the negative angles possible. When the arm reaches $(-)60^o$, a reflection direction of $(-)30^o$, it reaches the beam focusing optics, stopping its motion (the last mirror in the beam line is suspended from above to allow the arm to pass under it). All sample movements, as well as the arm, are computer controlled. The collection fibre feeds into an Ocean Optics 2000 optical spectrometer, with a range from 340nm-1000nm, resolution 0.3nm. The spectrometer is also directly connected into the software written to control the goniometer. The whole system can therefore be programmed to record the reflectivity of the sample at different positions and for both rotations of θ and ϕ, over the complete visible spectrum. This data is subsequently normalised to the reflectivity of smooth gold and compiled into a four dimensional matrix, $R(pos, \theta, \phi, \lambda)$. The setup takes a spectrum of smooth gold for each different recorded angle to remove any reflectivity effects associated with angle and polarisation. Finally, cuts are taken to present various aspects of the data.

5.2 Data Presentation

To gain a clear understanding into the optical activity on the nano-metallic samples, three different types of data plot are utilised. These show different aspects of the whole data set and are shown in figure 5.2 together with the aspect of the data set they represent.

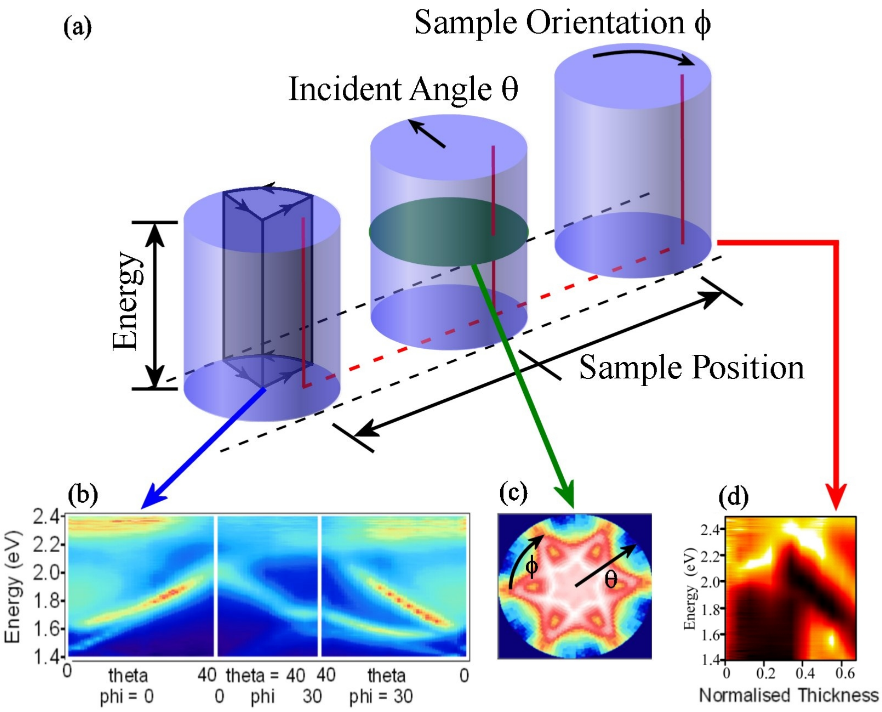

FIGURE 5.2: (a) Schematic representation of the four-dimensional data set produced by the reflectivity setup. (b) Dispersion plot, energy of reflected light vs. incident angle around the Brillouin zone. (c) Angle plot, incident angle plotted radially, sample orientation plotted in the polar direction. (d) Position map, plotting energy of reflected light vs. sample position, and hence geometry.

Dispersion plots (fig 5.2b) display the energy of the reflected light vs. the angle of the incident light. These images form a figure analogous to the zone schemes used for photonic crystals. The only difference being that here the bottom axis is the angle of the input light, not the k-vector of the dispersion bands, although these are related by $k_{//} = \frac{2\pi}{\lambda} sin\theta$. Dispersion plots start at normal incidence, then scan out along $\phi = 0^o$ to a certain incident angle, ideally the Brillouin zone, then pan around the sample orientation ($\phi = 0^o \rightarrow 30^o$) before scanning back to normal incidence along the $\phi = 30^o$ direction. These plots are extremely useful as they provide information about the dispersion of different features, for this reason they are the most widely used in this thesis and will often appear with only the first section, scanning incident angle at one phi orientation. Dispersion plots are at a single position and are presented in a colour scheme where dark blue represents negligible absorption, going through green to red, with white representing maximum absorption.

Dispersion plots mainly map out energy vs. incident angle, however, it is also interesting to observe the full angular dependence of the data, which requires what is termed as an 'angle plot' (fig 5.2c). Angle plots show how, at a single sample position and energy, the intensity of the reflected light varies with respect to incident angle (plotted radially) and sample orientation (plotted in the polar direction). Angle plots cut the dispersion plot at a single energy but show the full orientational spectrum; this provides a valuable way of distinguishing features that are localised, which appear circular, and delocalised, which possess a six-fold symmetry stemming from the close packed nature of the surface. By overlaying the theoretical dispersion of the delocalised features, the exact sample orientation can be calculated or verified for every sample position, allowing accurate comparisons between different positions on a sample. The colour scale used for angle plots is identical to that of the dispersion plots.

The final graph type is the 'position map'(fig 5.2d). As the name suggests, this shows how, for a single sample orientation and incident angle, the position of the sample - and hence the sample geometry - effects the energy of different modes. The position map is much like the spectra taken from the microscope reported in chapter 4, but can be viewed at different θ and ϕ. The most practical use of the position map is when comparing different samples, but it is also good for providing intuitive information on the two plasmon types. The information provided by the position map is unlike that of the previous two plots and so is coloured from black (negligible absorption) to yellow (maximum absorption).

Between the three image types, all required information about the samples can be obtained; however, each individual plot requires that two parameters be fixed. For this reason, the data will often be presented in the form of filmstrips, on the electronic version of this thesis many images will link to a video of the data with one of the variable altered in the temporal dimension. These videos are available on the accompanying CD in the front sleeve of the paper version, labelled correspondingly to the figure numbers. This significantly aids in the visualisation of the data and hence the understanding.

5.3 Raman and Fluorescence Setup

For both the Raman and fluorescence experiments the computer-controlled goniometer, used to measure reflectivity, is again utilised. There are, however, a few important changes which are detailed in figure 5.3.

A diode-pumped, frequency-doubled Nd:YVO_4 laser operating at 532nm can be used either to directly excite the sample or to pump a continuous titanium sapphire laser,

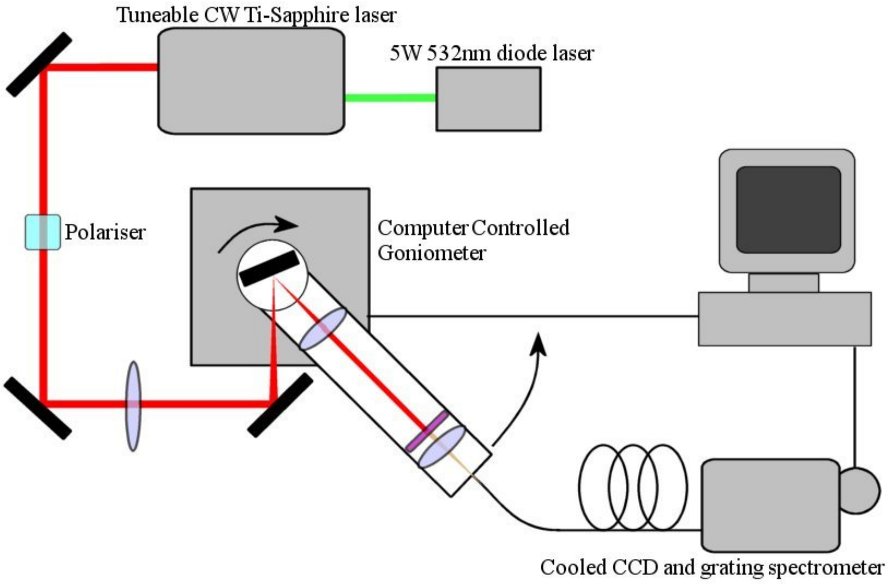

Figure 5.3: Experimental setup for angle resolved Raman and fluorescence experiments.

tuneable from around 720nm to 850nm. Either beam can be easily positioned onto the sample at the same point that the super-continuum laser was focused, allowing accurate correlation between reflectivity and other measurements. A filter is positioned before the sample to allow only the precise laser frequency into the experiment. A filter is then also positioned after the sample to remove the laser line from the emitted light. Spectra are recorded using a liquid nitrogen cooled Jobin Yvon Spectrum One CCD camera, attached to a Triax 320 spectrometer. This provides spectra with a resolution of 0.2nm. Again, the spectrometer is fibre coupled and connected to a computer to allow full automation of these experiments.

5.4 Raman and Fluorescence Graphics

While in no way producing the volumes of data generated in the reflectivity experiments, Raman and fluorescence measurements have an extra degree of freedom, because now the pump and detection angle need no longer be correlated. It has been found that the best method to present this data is in two different types of dispersion plot, known simply as pump-scan and detector-scan plots, shown schematically in figure 5.4.

Both plots are for a single sample position and orientation and have the energy of the emitted light as the y-axis. In a detector scan the sample is held at one angle - and hence a single pump angle - and the detection arm is scanned through a range of angles, plotted on the x-axis of the corresponding image. This type of graph detects changes in the output coupling of different processes. A pump scan maintains a constant angle between the sample and the detector arm, while scanning the pump angle, now plotted

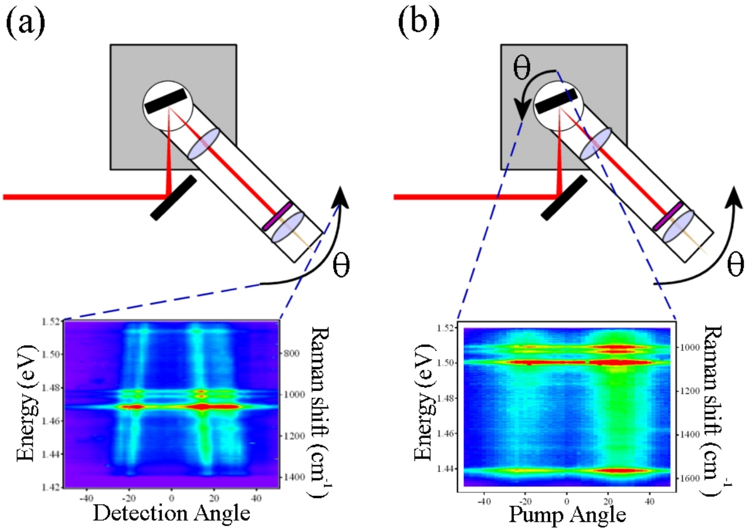

FIGURE 5.4: (a) Detector scan, sample does not move giving constant pump angle, detector is scanned through fifty degrees either side of sample normal incidence. (b) Pump scan, both sample and arm are scanned by the same angle so a constant detection angle is maintained, pump angle is scanned fifty degrees either side of normal incidence.

on the x-axis of the associated image. These plots map out changes in the input coupling efficiency of a given process. To maximise intensity while one angle is scanned the other is kept on resonance, estimated from the maximum absorptions of the reflectivity. The colour scale of these images is that of a rainbow, violet representing zero intensity up to red for maximum intensity.

Chapter 6

Types of Plasmons

6.1 Introduction

Using the experimental setup shown in the previous chapter, the reflectivity of many different nano-structured substrates has been recorded. Throughout these experiments two types of feature are observed. These correspond to delocalised Bragg plasmons and localised Mie plasmons, shown pictorially in figure 6.1a. Bragg plasmons are surface plasmon polaritons that are excited through Bragg scattering off the periodicity of the surface. Mie plasmons are also surface plasmon polaritons, however, are localised within the truncated spherical geometry and have electric field distributions closely related to those of Mie scattering.

As the incident angle of the laser beam, the sample orientation and the sample thickness are varied strong variations in the observed reflectivity are recorded. Figure 6.1b shows a set of reflection spectra taken from a gold sample with a void size of 900nm. The sample thickness was set to $\bar{t} = 0.2$ and the incident angle was 20^o, the sample orientation was then rotated through 60^o, one symmetry rotation for a close packed array, with spectra taken every 10^o. The spectra are normalised to the reflection off smooth gold to remove effects due the spectral shape of the laser light, along with the absorption of the gold. Two types of features are clearly present in the data. The first, centred around 1.7eV, is a sharp absorption mode that changes energy and splits with sample orientation. This is a delocalised Bragg plasmon. The second absorption feature is positioned at 2.3eV; this is broader than the Bragg plasmon and has no dependence on sample orientation. This feature is a localised Mie mode.

Bragg plasmons are delocalised SPP modes that freely propagate over the top surface of the samples. Excited through scattering off the periodicity of the surface, the energy of the observed Bragg plasmons is highly dependent on incident angle as well as the sample orientation. The first section of this chapter will explore this relationship and

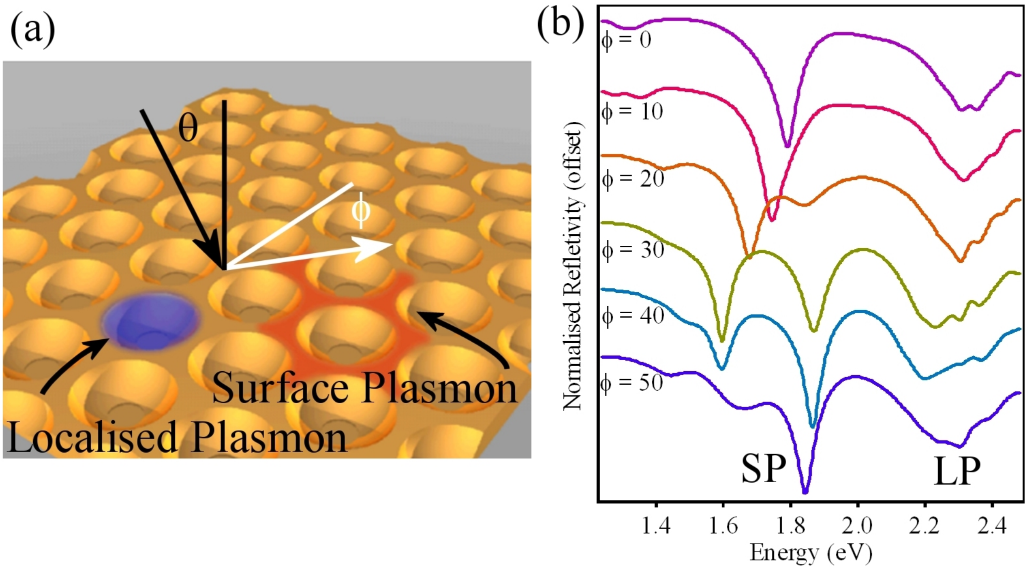

Figure 6.1: (a) Pictorial representation of Bragg and Mie plasmons on the nano-structured surfaces. Definition of incident angle, θ, and sample orientation, ϕ, also shown. (b) Set of reflection spectra taken at $\bar{t} = 0.2$ on a gold sample with void size 900nm. Incident angle is set to 20^o and sample orientation is varied as shown, spectra offset for clarity.

find that, when the samples are very thin, it is sufficient to model these energetics using a weak scattering approximation. This means no knowledge of the actual surface structure is required, only the periodicity. As the film thickness increases this model begins to break down and an extension to the weak scattering model is provided to account for an observed reduction in mode energies. Bragg plasmons are also found to scale universally with sample pitch, in agreement with predictions. The polarisation dependence is measured and found to be quite complex. A model is presented based on polarisation rotation and re-absorption to account for many of the observed features.

Mie plasmons are localised electric field distributions pinned inside the voids on the surface. Experimentally, these modes are found to be independent of incident angle and sample orientation, as expected for a localised mode. The energy of the Mie plasmons is, however, found to be highly dependent on the sample thickness. Further experiments have found that the Mie plasmon modes scale with void diameter and, again, exhibit an interesting polarisation dependence. Whilst it is possible to calculate the energy of a Mie plasmon in an enclosed spherical cavity, currently it is not possible to do the same in the truncated spherical geometries used experimentally. For this reason two intuitive models are put forward to quantitatively explain the observed behaviour. The first is based on a ray optics approach. This calculates the interference between the different ray paths through a truncated spherical cavity. This provides a set of reflectivity minima which agree, to some extent, with experimental findings. The second model assumes a plasmon standing wave exists within the void. This standing wave is pinned at the void rim, and so is dependent on thickness. Again, this model shows a good qualitative agreement with the data and is extended using the modified dispersion relation for a gold cavity calculated in chapter 3. Finally finite difference time domain modelling is employed to help visualise the electric field distributions present within the void geometries.

6.2 Bragg Plasmons

At thin regions of the samples the shallow, well spaced, dishes form a two-dimensional grating. These structures are highly diffractive (fig 4.8) since the ordering of the surface structure is good. Since diffraction and Bragg modes are both delocalised, studying the diffractive nature of the substrates will provide some insight into the plasmonic dispersion. To do this, a sample is set to a particular incident angle and a detector scan is performed to collect the light exiting the sample away from the reflection direction, an example of this data is shown in figure 6.2.

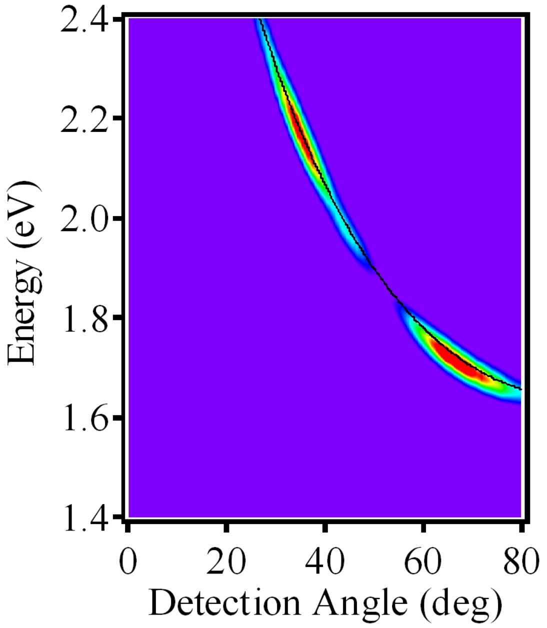

FIGURE 6.2: Detector scan of the diffracted light from a gold sample, void size = 500nm, incident angle = 45^o. Colour scale from purple (zero intensity) to red (maximum intensity). Black line shows theoretical diffraction behaviour.

Here, the sample is illuminated at 45^o and orientated to collect the first order diffracted light ($\phi = 0^o$). The black line, overlaid, shows the expected trend assuming the sample diffracts according to the weak scattering approximation. This means that the depth of the structures is much less than the wavelength of light, and so the surface can be considered to be flat with some scattering centres of zero size separated by the void diameter. The k-vector, $k(E)$, of the scattered light can then be calculated for different energies, E, using equation 6.1.

$$k = \frac{eE}{\hbar c}\sqrt{\epsilon_d}\,(sin\theta \pm n\Gamma) \tag{6.1}$$

where $\epsilon_d = 1$ as the sample is analysed in air, n is an integer expressing the diffracted order (n = -1 in the case of figure 6.2) and Γ is the grating vector, taken to be $\sqrt{\frac{3}{4}}D$ as discussed in chapter 2. The high degree of correlation between the data and the theory suggest adequate modelling using the assumptions of point scattering and a plane spacing of $\sqrt{\frac{3}{4}}D$. The intensity of the diffracted light is about two orders of magnitude less than the incident light intensity. This is because the thickness of the diffraction grating is much smaller than the wavelength of light, and so the diffraction efficiency is low[91]. The variations in diffracted intensity are something of a complexity in the data and will be discussed in more detail later in this chapter.

If now the reflectivity of a 600nm pitch sample is recorded for all sample orientations, as well as incident angles from 0^o to 50^o, Bragg plasmon modes and diffraction effects will appear as reductions in the reflected intensity. In the case of diffraction, this reduction is purely due to the light being redistributed into different, un-detected, directions as shown above. This will be true for the Bragg plasmon modes as well, however, absorption will be a much stronger effect. Figure 6.3 shows how the intensity of the reflected light at different energies depends on the angle of the incident light for three different sample orientations. It should be noted the figures only shows Bragg modes that couple to the optical field, so does not image the full dispersion of the Bragg plasmon modes, purely the radiative part. However, the data presented can be considered to map much of the Bragg plasmon dispersion.

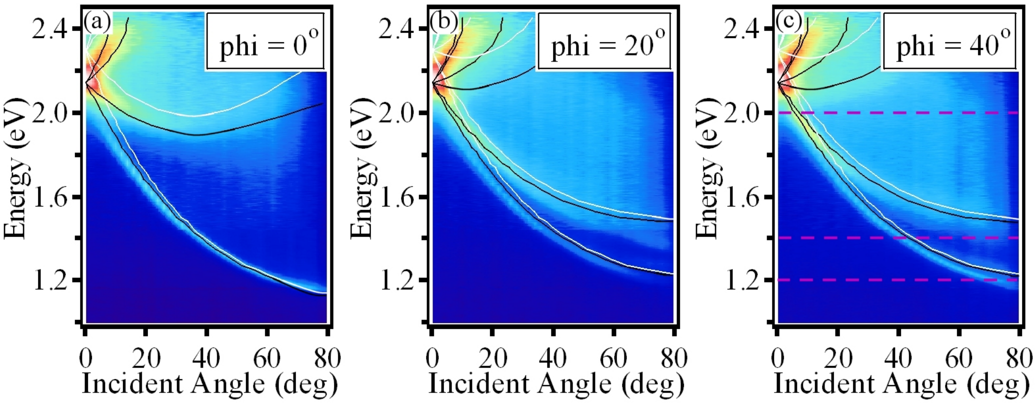

FIGURE 6.3: Dispersion map for a gold sample with void size 600nm, $\bar{t}$ = 0.1, at several sample orientation, as shown, light is transverse magnetic polarised. Black and white lines show theoretical positions of SPP modes and diffractive features respectively. Purple dashed lines in (c) show energies where data from figure 6.5 is taken. [hotlink to video by clicking on image in electronic version]

Also included in figure 6.3 are the theoretical curves showing the behaviour of diffraction effects and Bragg plasmon modes. The diffraction theory has already been discussed and shown to be accurate in the previous experiment. The Bragg plasmon modes are modelled using the same weak-scattering approximation. This approach allow the SPP to be modelled using the same equations used for diffraction, but applying the effective refractive index, ϵ_{SPP}, given by the surface plasmon dispersion, equation 6.2, in place of the constant ϵ_d.

$$\hat{\epsilon}_{SPP} = \sqrt{\frac{\epsilon_d \hat{\epsilon}_m}{\epsilon_d + \hat{\epsilon}_m}} \tag{6.2}$$

Where ϵ_d and $\hat{\epsilon}_m$ are the dielectric constants of the dielectric medium and the metal respectively. At very small values of $\bar{t}$, this approximation is reasonable, however, revisions will have to be made as the surface becomes more structured.

A further experimental complexity is the requirement for the reflected light to pass under the mirror responsible for directing the incident light onto the sample, as shown in figure 6.4.

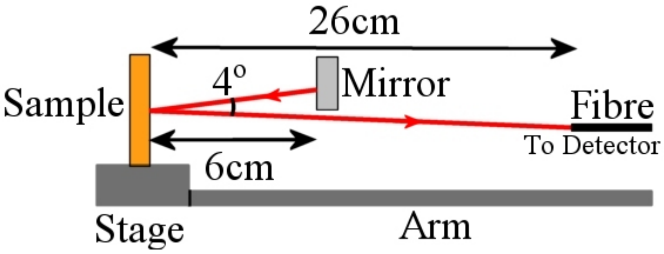

Figure 6.4: Schematic of light path from the last mirror in the beam path to the fibre. This setup require an incident angle of about 2^o in the plane perpendicular to that of collection.

This forces the use of an angle of incidence $\theta_y = 2^o$ perpendicular to the detection plane. This means that the data is only recorded down to $\theta = 2^o$. Both data and theory are corrected for this slight angle, causing the sharp band through the data at $\theta = 0^o$ and the splitting in energy of the theoretical (and experimental) modes around the normal. In the case of figure 6.3 the incident light and detection optics are transverse magnetically (TM) polarised. In this thesis TM polarisation is defined as the electric field vector of the light being orientated perpendicular to the metals surface. Finally, it should be noted that there is a weak localised plasmon mode around 2eV, causing extra absorption and slight shifts in the pure Bragg plasmon mode. These features will be discussed in detail in the next chapter.

Since both Bragg plasmon modes and diffraction are delocalised, these features are expected to vary with sample orientation, following the six-fold symmetry. This is shown clearly in figure 6.5, plotting sample orientation against incident angle for three different energies as indicated in figure 6.3c.

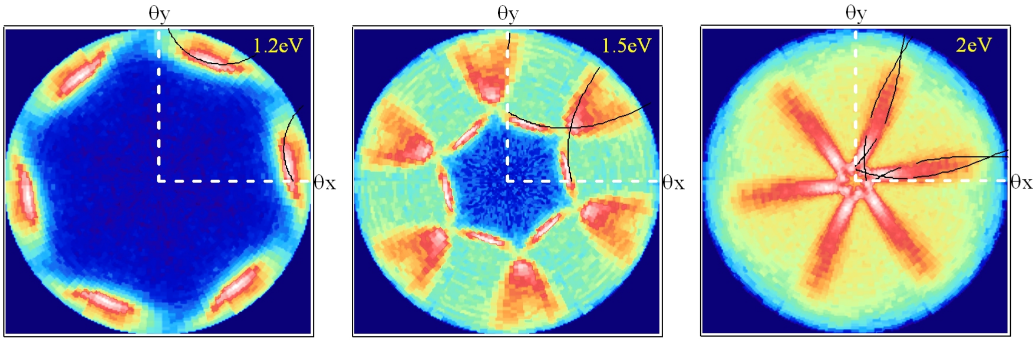

Figure 6.5: Angle plots for a gold sample with void size 600nm, $\bar{t} = 0.1$, taken at energies of (a) 1.2eV, (b) 1.5eV and (c) 2eV. Light is transverse magnetic polarised. Black lines show theoretical positions of SPP modes. [hotlink to video by clicking on image in electronic version]

A good fitting between the Bragg mode theory and experiment is observed throughout incident angle, sample orientation and energy, although the presence of the localised mode near 2eV causes some small discrepancies. It is interesting to note that there is not such a strong correlation between the data and the predicted diffracted modes. Whilst the samples are clearly diffractive, the measured intensity of the diffracted light is much smaller than that of the incident laser. This means the reduction in reflected intensity will be small. Further to this, the Bragg plasmon modes are highly absorptive and so swamp any diffractive features present. In fact, for most experiments very little diffraction is clear in the data; so, while its presence is acknowledged, only the plasmon theory will be considered for much of the rest of this thesis.

Excellent correlation between experiment and theory is observed in the angle maps (fig 6.5), with features strengthened when different modes cross. These figures show that the weak scattering approximation does indeed hold true for these samples and can be used with confidence to model the delocalised modes present on thin samples. A further test is presented in figure 6.6, where the k-vectors of the Bragg plasmon modes are calculated from the sample pitch and the angle of the incident light. This is plotted against the observed energy of the Bragg mode, and the dispersion compared to that of the theoretical plasmon dispersion. Again, a good correlation is observed between the data and the theory until near the surface plasmon energy. Theoretically, the dispersion passes through this energy, however, experimentally an asymptotic behaviour is observed toward the surface plasmon energy. This is due to increasing attenuation near resonance greatly decreasing the observed Bragg mode to below detectable levels.

6.2.1 Pitch Dependence

The model for the Bragg modes so far proposed is quite general and should work for a range of sample pitches. This is verified by repeating the above experiment on a range of samples made from different void sizes, and hence pitches. Pitches between 500nm

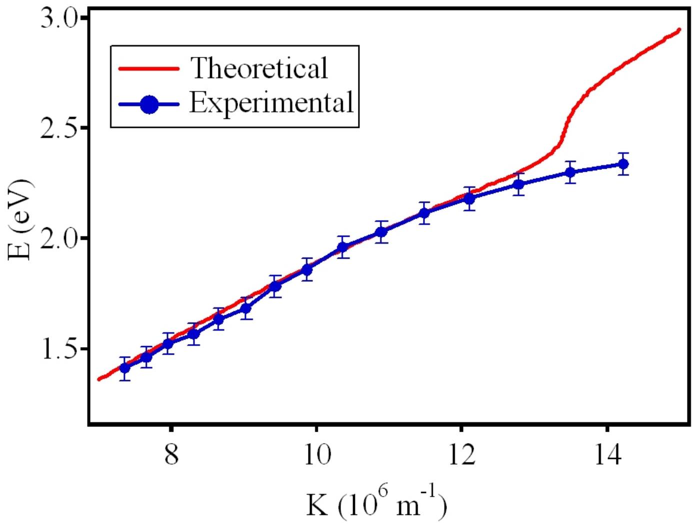

Figure 6.6: Graph showing theoretical and experimental energies of the Bragg modes vs. k-vector. Sample has a pitch of 700nm

and 900nm are presented in figure 6.7a. Since pitch is related to the mode energy, this covers much of the range easily accessible with the spectrometer although pitches up to 20μm have been recorded by observing higher order modes[64].

As can be seen, the expected correlation between theory and experiment is again observed, although to get this fit a slight adjustment to the theoretical pitch is required. Figure 6.7b shows the energy of the Bragg modes at $\theta = 0^o$ plotted again their effective k-vector ($k = \frac{2\pi}{pitch}$), which illustrates this shift in energy below the expected plasmon dispersion. For low k-vectors (large pitches) the observed energy is very similar to that predicted from the Drude oscillator model as well as the experimental dispersion of gold. However, above 2eV, increasing k-vector leads consistently to lower energies than would be expected from the observed plasmon dispersion. It should be noted that the final point of the graph is inferred by fitting the theoretical model to the data and reading off the normal incident energy. This has to be done because the normal incidence Bragg mode energy is inside the plasmon absorption band and so is not detectable.

Analysis of the SEM images shows that the template packing is not perfect. This leads to an average void spacing of about 30nm greater than that of the sphere diameter. This, in turn, leads to an increase in effective pitch as the void size decreases, and so an increase in the effective k-vector. The points on graph 6.7b are for extracted experimental energies but assumed sample pitch. This means the k-vectors have been over estimated, and this accounts for the observed discrepancy. For all subsequent data in this thesis the true void spacing is used when showing the theoretical dispersion.

The equivalence of the Bragg modes on different samples is neatly demonstrated in figure 6.7c, where the ratio of observed wavelength to sample pitch is plotted against incident angle. In this graphic, the different colours (red, green and blue) correspond to the

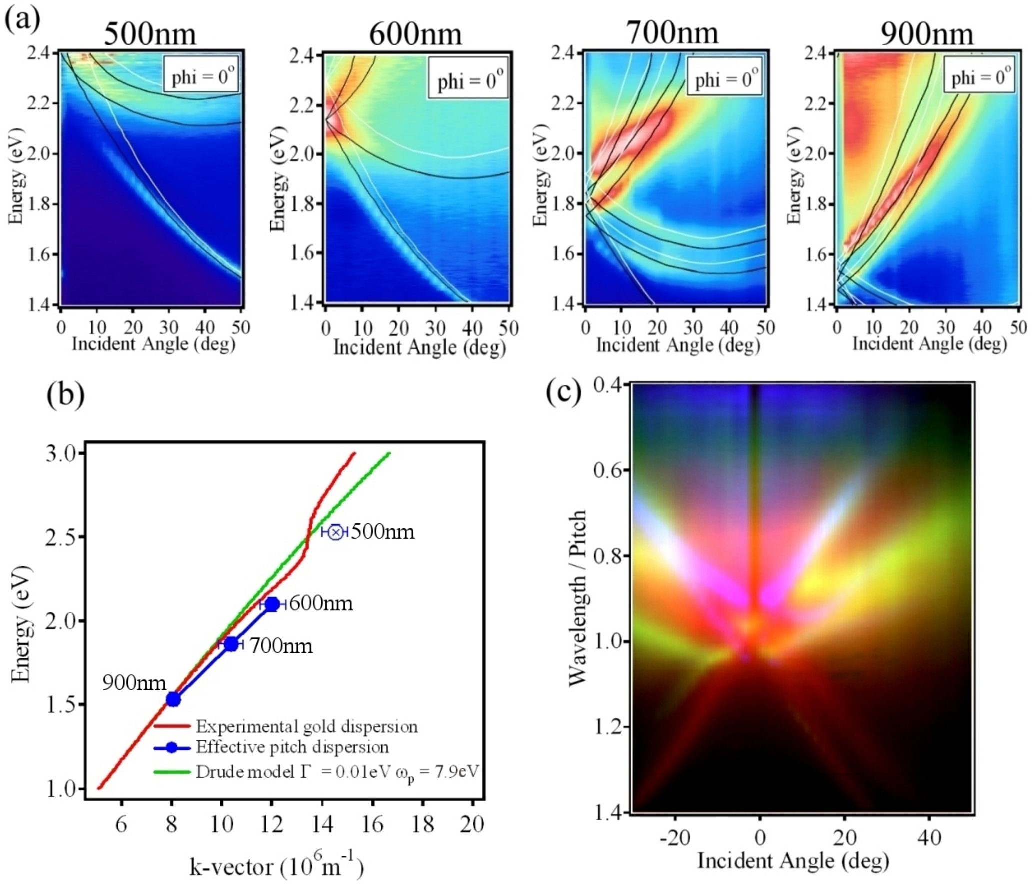

Figure 6.7: (a) Dispersion plots for samples at $\bar{t} \approx 0.1$, of different pitches as shown. (b) Extracted energy of normal incidence SPP modes as a function k-vector calculated using sample pitch. (c) Combined image showing the 600nm (red), 700nm (green), and the 900nm (blue) dispersions, normalised by effective sample pitch.

dispersion from samples of pitches 600nm, 700nm and 900nm respectively. The different dispersions neatly match up producing the expected shape for any given Bragg mode for this generalised case.

6.2.2 Thickness Dependence

As the thickness of the samples increases the weak scattering approximation becomes less valid. However, since this model has worked so well up to this point, and the data below $\bar{t} = 0.3$ follows a similar trend, only a slight modification to incorporate film thickness will be considered. This modification assumes the Bragg modes are strongly pinned to the surface, and so the increasing thickness will lead purely to an effective increase in the sample pitch. This assumption is valid since the decay length of the SPP into free-space is of order 5 to 10 times smaller than the void diameter. Figure 6.8 shows schematically the distances used and allows a simple mathematical model for the pitch as a function of thickness:

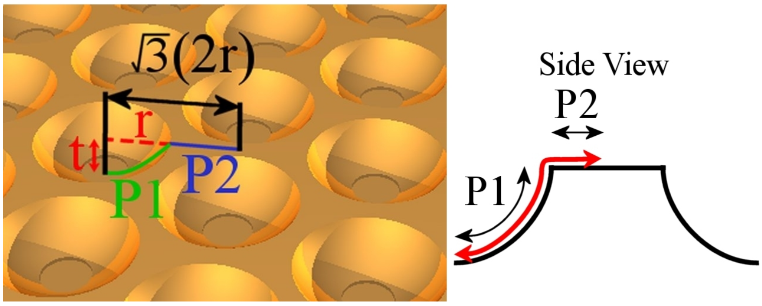

FIGURE 6.8: Definition of parameters used in the thickness dependency Bragg plasmon dispersion

$$P_{tot} = P_1 + P_2 = r\left[cos^{-1}\left(1 - \frac{t}{r}\right)\right] + r\left[\sqrt{3} - \sqrt{1 - (1 - t/r)^2}\right] \tag{6.3}$$

this expression comprises two terms, the first calculates the distance from the bottom to the top of a dish of thickness t, where the cosine term is in radians. The second term calculates the distance from the rim of the dish to a point midway between the two dish centres - there are two scattering planes for every complete symmetry translation. When this expression is used in place of the sample pitch in the scattering model, a new function in terms of sample thickness is produced. Figure 6.9 shows a position map of the 600nm sample for various incident angles. For every position the same domain orientation is used ($\phi = 0^o$ in this case). This is estimated from the data set to remove the effect of variations in the domain orientation at different sample positions (this is done for all position maps presented in this thesis).

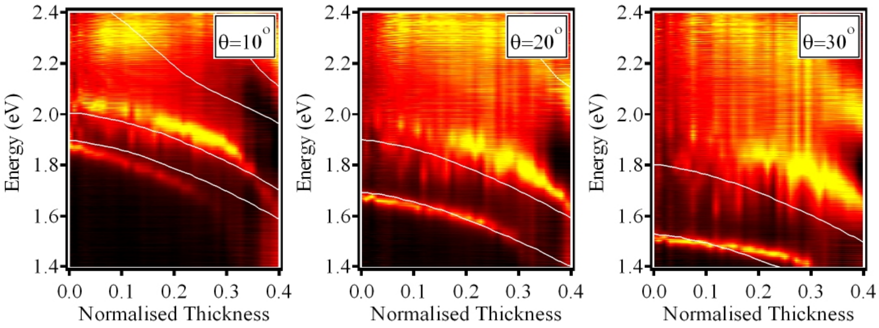

FIGURE 6.9: Position maps of a gold sample at $\phi = 0^o$, void diameter = 600nm. White lines show theoretical behaviour of Bragg modes as a function of thickness. [hotlink to video by clicking on image in electronic version]

Although quite simplistic this modified model again fits well with the observed data for all thicknesses below $\bar{t} = 0.4$. Above this thickness, the Bragg modes disappear as the geometry of the surface becomes too structured to allow propagation. Similar behaviour is observed for all samples indicating that the initial assumption that the Bragg plasmons are tightly pinned to the surface can be viewed as accurate. Of the two observed Bragg plasmons in figure 6.9 the higher energy mode deviates from the predicted values as the incident angle is increased. This is due to the presence of a Mie plasmon situated around 2eV. Interaction between the Bragg and Mie plasmons lead to the observed disagreement in energy between theory and experiment. As already mentioned a more thorough analysis of these interactions will be presented in the following chapter.

As the depth of the surface structuring increases, the SPP modes should experience a change in the effective dielectric constant. This is due an increased level of electric field distortion, and is analogous to an increase in refractive index contrast in a photonic crystal. It was shown in chapter 2 that for a photonic crystal with a dielectric contrast of zero, the structure could be exactly modelled using the weak scattering approximation. However, when a refractive index contrast was included the actual solutions required the solving of Maxwell's equations and lead to the formation of a photonic band. Figure 6.10 sketches the normal incident energy of a photonic crystal as the refractive index contrast in increased, for this figure the average refractive index is kept constant.

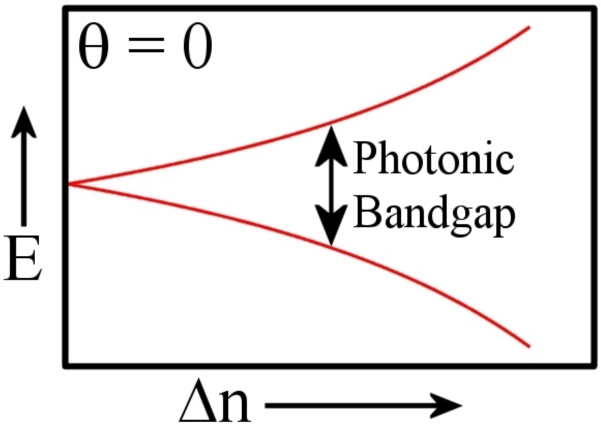

Figure 6.10: Schematic of photonic bandgap formation with increasing refractive index contrast, average refractive index is kept constant.

This shows that, for a refractive index contrast of zero, there is a single energy at normal incidence, as predicted by a weak scattering solution. As the contrast increases, two energy levels open up, with no states within the band gap inbetween. As the contrast is increased further the bandgap widens. This result is much like that shown in the data (where increasing thickness is equivalent to increasing refractive index contrast), and provides a different explanation for the observed trend. To precisely model the experimental data, this means a full solution to Maxwell's equations on the various geometries would be required, which is currently not possible. However, it is interesting to note that this approach predicts the data shows the possible formation of a plasmonic bandgap. Unfortunately the mixing of Mie plasmons at this thickness makes analysis difficult, and no band increasing in energy with thickness has been observed to date. This implies that either no bandgap has formed, the effective refractive index causes both bands drops in energy, or the upper mode is not optically allowed.

6.2.3 Polarisation Dependence

The final tests to be performed on the Bragg modes are those of polarisation dependence for both incoming and reflected beams. While surface plasmons are purely transverse magnetic (TM), the strong structuring of the surfaces allows the possibilities of the excitation of surface plasmons from transverse electric (TE) polarisations[92]. Figure 6.11 shows the dispersion maps from a point, $\bar{t} = 0.2$, on a 600nm void diameter sample for both possible co-polarisations.

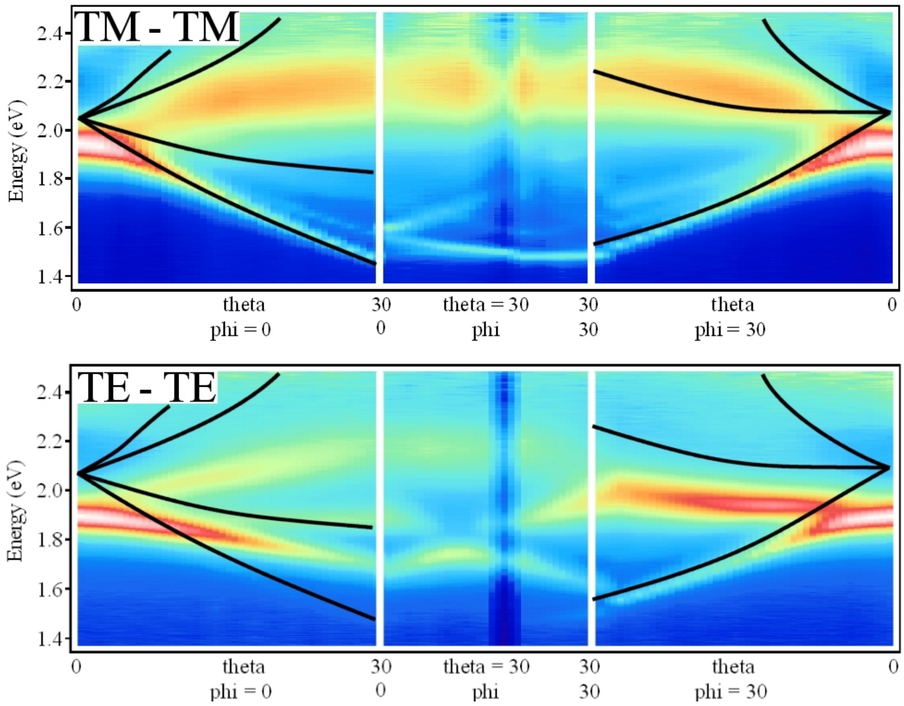

FIGURE 6.11: Dispersion maps for a 600nm sample at $\bar{t} = 0.1$. Laser light and detection polarisation are co-polarised, TM - TM and TE - TE, as shown.

The TM - TM (input light transverse magnetic polarised, output detection transverse magnetic polarised) is similar to data shown previously. This shows the direct coupling of the incident light into a surface plasmon mode. There is good correlation between experiment and theory for the lower plasmon bands and the appearance of a localised mode near 2.1eV leads to some complications to higher energies. The anomalous vertical band near the centre of the image is due to a slight imperfection in the system alignment. This leads to a reduced collection efficiency for some phi orientations, and so an effective reduction in absorption. This anomaly underlines the difficulties associated with perfectly aligning the goniometer in all directions and should be ignored. The TE - TE data also shows the coupling of incident light into plasmon modes. To convert an incoming TE photon into a TM plasmon the light must scatter at some azimuthal angle to the incident beam. This principle is shown in figure 6.12a.

If a TE polarised beam of light is incident on a smooth metal surface (red line) the surface charge will be polarised purely in the plane, and reflect a TE polarised beam of

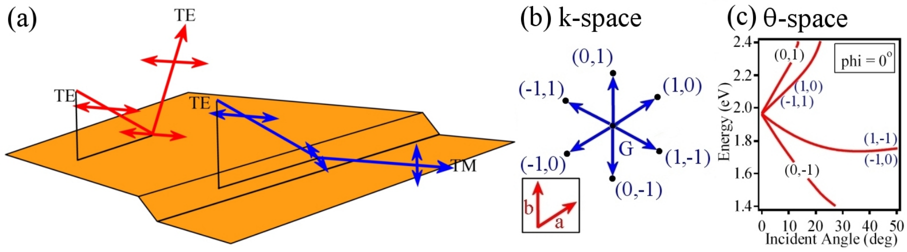

FIGURE 6.12: (a) Schematic of polarisation rotation from a step in the surface profile. (b) k-space representation of nano-structured surface (c) Dispersion relation showing scattering direction of different bands at $\phi = 0^o$

light. Therefore, TE polarised light cannot couple to surface plasmons as there is no out of plane component of electric field. If, however, the surface is structured, the electrons on the surface will no longer oscillate in the plane of the incident polarisation (blue line). This now allows the excitation of an electric field perpendicular to the surface, and so the excitation of a surface plasmon. For a scattering angle of $\phi = 90^o$ the resolved component of the out of plane electric field will be maximised. For the six fold symmetry of the surfaces studied here, at $\phi = 0^o$ no polarisation rotation is possible in the (0,1) or (0,-1) directions as these are in the plane of the incident light, figure 6.12b, c. The other directions will allow polarisation rotation so TE polarised light will be able to excite Bragg plasmons in this direction. This means that the TE polarised light cannot couple to the highest and lowest energy Bragg modes at $\phi = 0^o$ and should only weakly couple to these modes at $\phi = 30^o$. This is, indeed, what is observed in the data, with the TE polarised light coupling only very weakly to the modes the TM polarised light couples to most strongly. The TE - TE data does not fit the theoretical dispersion as well as the TM - TM data. The reason for this is unclear, and appears to be due to a drop in energy of some of the plasmon modes. This could be related to the presence of the localised plasmon at 2.1eV - the modes that fit the theory are all situated at lower energies. Again full justification of this will be given in the following chapter.

Figure 6.13 show the light collected in a cross polarised configuration. For a flat surface no polarisation rotation is observed, as discussed previously. The data, therefore, shows the amount of light collected, rather than the amount absorbed (as is the case for the co-polarised data). For easier comparison with the co-polarised data the colour scales of these images have been reversed. It should also be noted that the intensity of the polarisation rotated signal is 100 times weaker than that of the incident light. For a simple one-dimensional diffraction grating, TM polarised light couples to the plasmon mode most efficiently at $\phi = 0^o$, and TE light at $\phi = 90^o$. Therefore, since input and output resonances need be considered, the greatest polarisation conversion occurs at $\phi = 45^o$[93]. Due to the six fold symmetry of the samples presented here, again the situation is a little more complicated.

The experimental data clearly shows delocalised features; however, they do not directly correlate with the co-polarised data. Work on diffraction gratings has shown that the

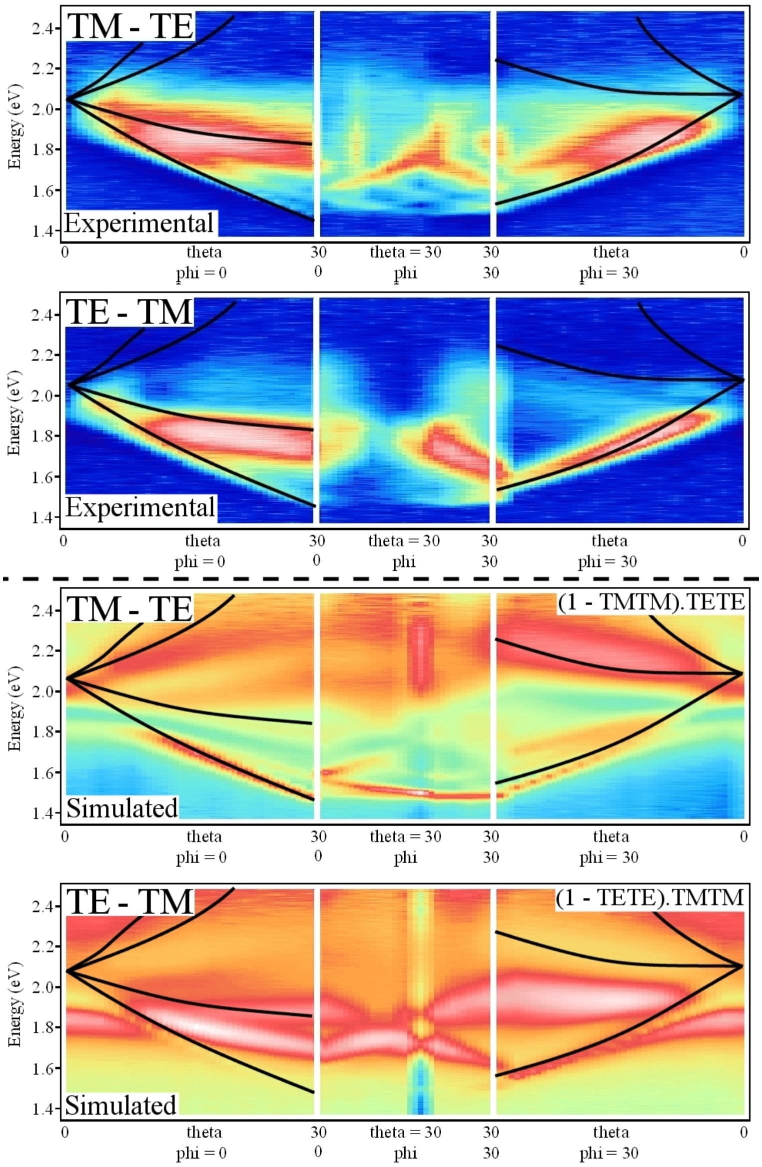

FIGURE 6.13: Experimental and simulated cross polarisation data. (TM - TE and TE - TM). Colour scale of experimental data is reversed to allow direct comparison with the co-polarised data. Simulated distributions use co-polarised data, as shown.

shape of the polarisation rotated signal is equal to one minus the normalised absorption of the incident light[92]. Due to the reversal of the colour scales between co- and cross-polarised data, this would lead to identical looking data sets, which is unfortunately not true. The co-polarised data represents a coupling into the different Bragg plasmon modes. As a next approximation the input and output coupling strengths could be multiplied to find the amount of coupling between the two polarisation states. This, however, leads to the same intensity distributions for both types of polarisation rotation (TE to TM and TM to TE). Since this is clearly not the case, further ideas must be considered.

Figure 6.13 also shows two simulated intensity distributions, using the co-polarised data.

In these data sets the light is first considered to be converted into a Bragg plasmon (using (1 - co-polarised absorption data)). These plasmon modes are then considered to be re-emitted into the optical field, as in the case of the grating. However, it is also assumed that the output light suffers absorption from the output plasmon state (by multiplying by the output polarisation absorption data). This leads to the simple mathematical treatment of the co-polarised data for each cross-polarised simulation, as shown in figure 6.13. These simulated data sets show some nice correlations with the experimental data. This is especially true for the middle segment at $\theta = 30^o$, where the TM - TE data shows much sharper features than in TE - TM. In fact, using this technique the TE - TM data is quite well simulated for all angles, although the intensities of the different modes are not always accurate. The TM - TE data appears to be less well simulated, mainly due to the expected mode around 2.1eV. It has already been mentioned that there is a Mie plasmon resonance at this energy. Mie plasmons modes are independent of polarisation and so will not conform to the same theory being used to simulate the effect of the Brag modes. With this consideration the shape of the simulated TM - TE data is also quite close to that observed, although again the absolute intensities of the modes are sometimes different from those observed.

Therefore, this model can be seen as a first approximation to the complex behaviour observed in the polarisation data. Further complexities will be found in the following section, when the polarisation dependence of Mie plasmon is examined.

6.3 Mie Plasmons

At the thicker end of the samples the cavities form almost encapsulated spherical voids. A discussion into the theory behind the expected modes present within a spherical void was presented in chapter 3, and now it is possible to combine theory with experiment. It will be shown that at $\bar{t} = 1$ good agreement between experiment and the Mie mode calculations is observed. However, the Mie plasmon calculations are limited to the symmetry of a sphere, and do not directly provide any information on the mode profiles from within truncated voids. For this reason a number of intuitive, less mathematically rigorous, models have been developed and will be presented in this section, aiming to bringing some light to these interesting electromagnetic phenomena.

6.3.1 Isolated Voids

To remove the effects of Bragg plasmons a sample of isolated, randomly positioned, voids was grown. The void diameter of this sample was 600nm and the graded thickness was confirmed through SEM images taken along the edge of a cleaved sample. Other SEM images confirmed that most of the voids were in fact isolated, although some grouping was observed, presumable due to capillary action between spheres during templating, figure 6.14a. Figure 6.14b shows a dispersion map for this sample.

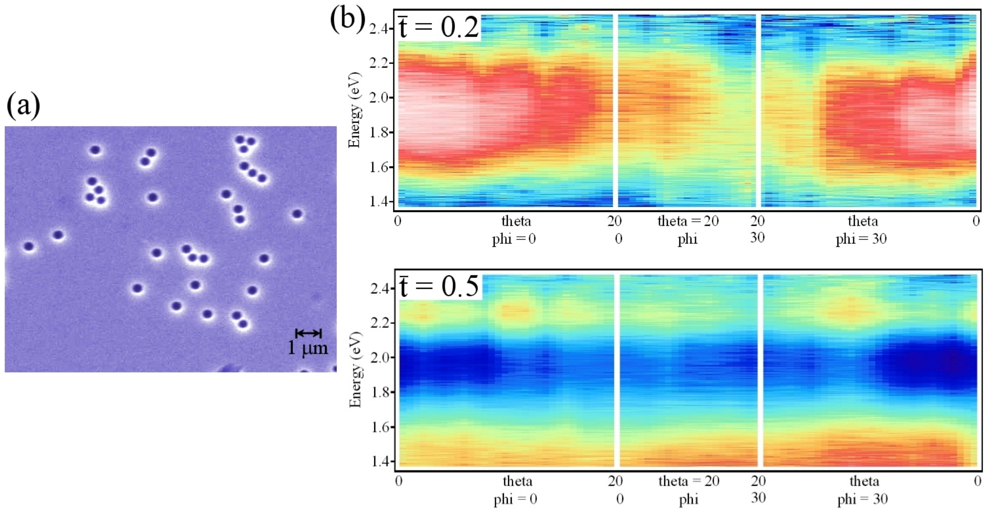

Figure 6.14: (a) SEM image of a gold, isolated, 600nm void sample at $\bar{t} = 0.5$. Dispersion maps of the sample shown in (a) at thicknesses of $\bar{t} = 0.2$ and 0.5. [hotlink to video by clicking on image in electronic version]

The dispersion map clearly shows that the observed modes are independent of incident angle and sample orientation; this is true for all positions across the sample, of which two are shown. This proves that the observed modes are indeed localised, and not affected by the surface structure. The quality of the data is less than that shown previously due to the low absorption cross section of the small number of voids under illumination. The only possible localisation of the electric field is within the dishes, and so by varying the sample thickness the effect of varying levels of void truncation can be observed. Figure 6.15 shows two position maps of the sample at different incident angles; the independence of the modes to angles is again shown. Using the solutions to Maxwell's equations of a spherical void in an infinite expense of gold (outlined in chapter 3), the energies of the expected Mie plasmon modes at $\bar{t} = 1$ can be calculated, these are also shown on figure 6.15.

Two clear modes are visible in the data, decreasing in energy with increasing thickness. As the sample thickness tends to zero the modes shift towards the surface plasmon energy (around 2.6eV). Above $\bar{t} = 0.7$ the modes begin to increase in energy and tend towards the values of the Mie scattered solutions. This is not obvious from this image but will be fully justified in the following section. A number of modes are usually present and tend towards different energies as the thickness tends towards $\bar{t} = 1$. From the data it appears that these energies correspond to those of the Mie mode in a spherical void, providing strong evidence for the origins of these features. The modes are not as sharp as the Bragg resonances and appear to vary linearly with sample thickness; these traits are also observed on the well-ordered samples. Figure 6.16 shows the comparison between ordered and disordered 600nm graded samples. On the ordered sample (fig 6.16b) the

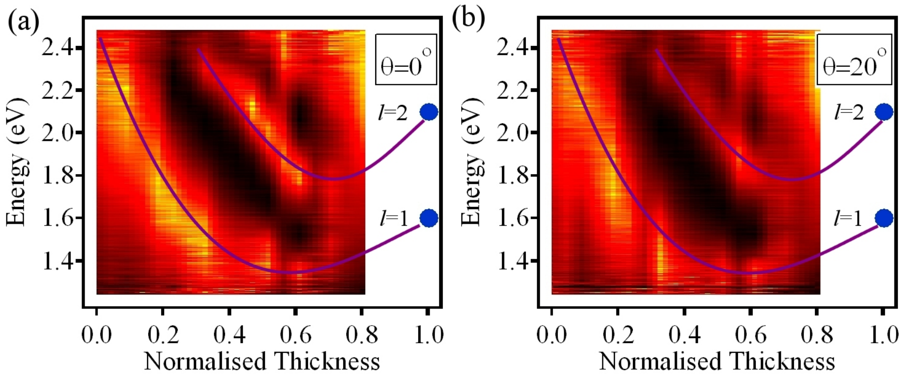

FIGURE 6.15: Position maps of a gold isolated voids with diameters of 600nm. Incident angle as shown. Blue dots show theoretical values of the Mie scattered $l = 1$ and 2 modes, purple line act as a guide to eye.

vertical steaks around $\bar{t} = 0.15$ and 0.35 are due to blemishes on the sample causing extra scattering, and hence reducing the reflectivity, as such these features can be ignored.

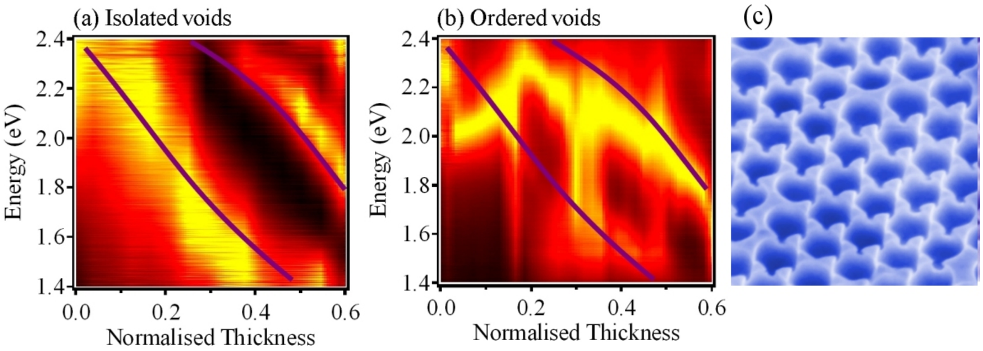

FIGURE 6.16: Position maps for gold samples with void diameters of 600nm, images shown at normal incidence for (a) isolated randomly positioned voids and (b) close packed ordered voids. Purple lines show guide for eye. (c) SEM image of a close packed array of voids at $\bar{t} = 0.6$.

The Bragg mode energy for normal incidence on the ordered sample is around 2.2eV, causing the strong features for thin regions of the sample. This slightly perturbs the upper localised plasmon and all but removes the lower one, although its presence can be seen for $\bar{t} > 0.3$. With this consideration, good agreement between the two sets of data is observed and work on a large number of other samples has shown this to be a general result. This implies that the localised modes act independently of one another and can be considered as isolated. This is a some what surprising result as the voids are seen to be connected with their nearest neighbours and for geometries around and below $\bar{t} = 0.5$ the cavities only offer weak confinement, figure 6.16c. Nonetheless, on all close packed samples for all geometries localised plasmon modes are observed and do not appear to interact with one another.

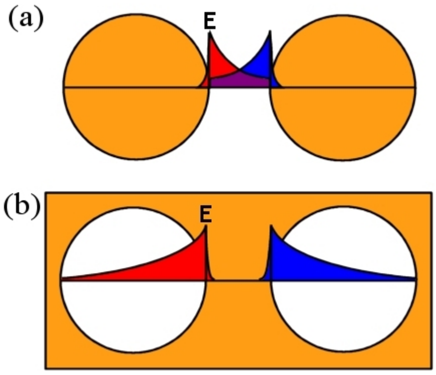

FIGURE 6.17: Schematic of electric fields (a) surrounding metal spheres and (b) inside metallic voids.

The reason for this is due to the strong screening of the metal, and emphasises a big difference between the localised plasmons on spheres and in voids, shown schematically in figure 6.17. For a sphere the electric field decays over a distance of hundreds on nanometres, allowing strong interactions between localised plasmons. Since the metal screens the electric field within 20nm this is not the case for localised void plasmons. The interconnections between the voids are of sub-wavelength dimensions so cannot efficiently couple radiation between cavities. Furthermore, the curvature of the dishes always acts to localise the fields within the individual cavities. This helps stop the electric fields in adjoining cavities from overlapping significantly with one another.

The localised nature of the modes on ordered samples allows for easier experimentation. The very weak absorption profiles of the isolated voids increases to almost total absorption for an array of many cavities. This allows a far greater variety of experiments to be performed, bringing further insight to the energetics of the localised plasmon resonances.

6.3.2 Perfect Matched Plasmon Absorption

The previous section has outlined some of the properties of the observed localised plasmon modes on the nano-structured surfaces. This shows that at $\bar{t} = 1$ the features are at a similar energy to those calculated by Mie plasmon theory. However, since it is possible to calculate exact solutions for this geometries above $\bar{t} = 1$, it is worth studying this thickness region in a little more detail.

Figure 6.18 shows a position map for a gold sample with a void diameter of 500nm. This again shows the drop in localised plasmon energy with increasing thickness, up to $\bar{t} = 1$. However, above this thickness the modes begin to increase in energy, tending toward the calculated Mie plasmon solutions at higher energies.

While the origins of this counterintuitive energy shift are not obvious, their character has been identified by our theoretical collaborators of T. V. Teperik *et al.* In this work they

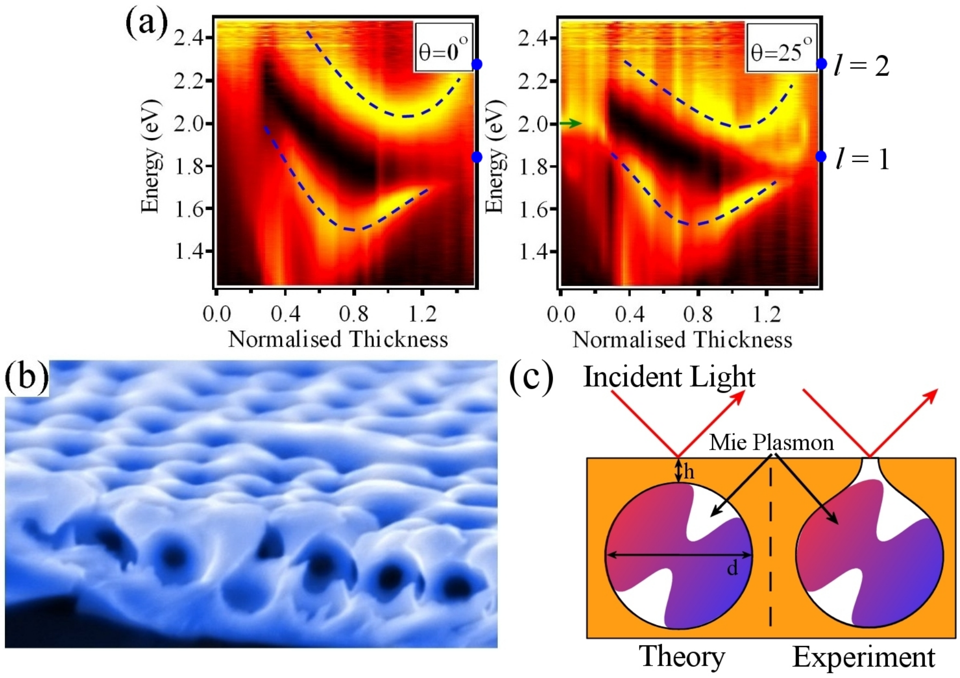

FIGURE 6.18: (a) Position maps for a gold 500nm sample for different incident angles. Green arrows show energies of Bragg plasmon modes, blue dashed lines show Mie plasmon modes. (b) SEM image of a similar sample close to the same thickness (700nm gold sample at $\bar{t} = 1.2$). (c) Schematic of theoretical and experimental sample geometries.

considered the rigorous solutions to the electromagnetic solutions for arrays of spherical cavities embedded within a metallic medium, figure 6.18c (truncated voids are not yet possible to model). This work allows optical coupling into the cavities by making the top layer of metal thinner than the skin depth (which is of order 25nm for gold at visible wavelengths). This allows the accurate calculations of the Mie plasmon modes, whilst also achieving a perturbation of the isolated cavity.

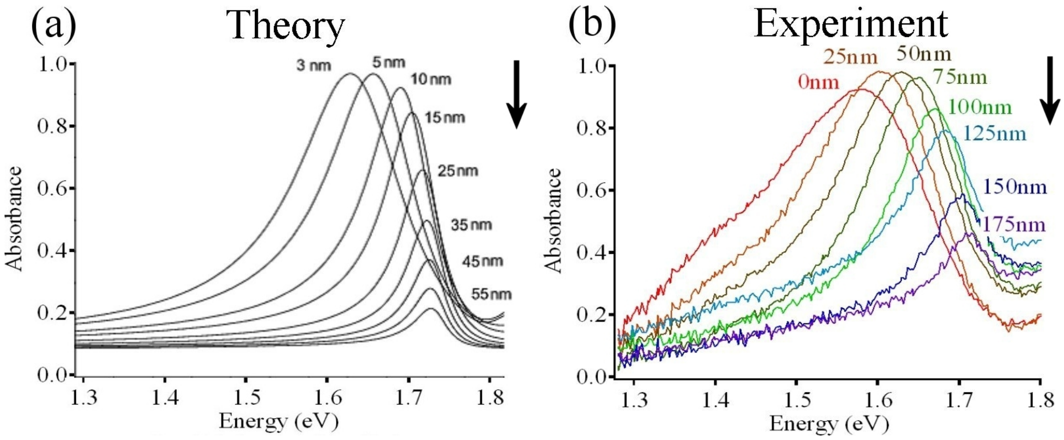

FIGURE 6.19: Comparison between (a) theory and (b) experiment of the highly localised mode above $\bar{t} = 1$. Arrows shown energy of isolated Mie plasmon mode. The difference in thickness between theory and experiment is due to the precise geometries involve.

Figure 6.19a shows a set of extracted absorption spectra taken at different thicknesses through figure 6.18. This is compared to the simulated response of the system, plotted in figure 6.19b. As can be seen, the profile of the mode with increasing thickness is computed to be almost identical to the experimental case. The theoretical model can be understood by considering the direct optical coupling with the Mie mode. When the top layer of metal is very thick, no coupling between the incident optical field and the localised Mie plasmon is possible. This means the Mie plasmon energy will be that calculated for an isolated cavity. The line width of the mode will be set by non-radiative damping as the mode has no optical field to decay into. However, since no coupling to the localised mode is possible, no absorption will be observed in the reflectivity spectra. As the metal top layer is made thinner, evanescent coupling becomes possible between the surface and localised fields. This will have several effects: firstly, since coupling between the fields is now possible, the mode will be observed as a drop in reflectivity. As the coupling increases with reducing thickness, the amount of absorption will also increase, as observed. The increase in coupling allows radiative damping of the localised plasmon, and so with decreasing top layer thickness the width of the resonance also increases. Finally, the increased coupling gives rise to an increased mode volume, and so the energy of the Mie plasmon drops with decreasing top layer thickness.

The only difference between theory and experiment is the thickness of the top layer required to produce the same shift in energy. This can be understood through the difference in the exact geometries. Theoretically, the system is modelled as an enclosed sphere while experimentally the voids maintain a small air channel (fig 6.18b and c). The optimum coupling in the experimental case is at a thickness above $\bar{t} = 1$ of about 30nm, compared to 5nm for the theoretical case. This six-fold increase in distance represents an increased coupling between the cavity and the surface due to the air channel. The comparable peak widths between experiment and theory imply that the coupling is purely evanescent even in the presence of the air channel, which is again expected as the hole is smaller than 100nm in diameter.

This experiment is very similar to those performed on the transmission through sub-wavelength holes[15]. The difference between the experiments is that instead of enhanced transmission, the sample acts as an efficient optical absorber. The experimental data shows at least 99% absorption of incident light over all incident angles. This perfect absorption is a very interesting optical effect under intense current study[11]. In theory these perfect absorbers should also act as perfect emitters of black body radiation[94], paving the way for further interesting experiments.

This experiment has two important conclusions. Firstly, above $\bar{t} = 1$ both theory and experiment show the same behaviour. This provides evidence that the observed plasmon modes can be expressed as Mie scattered fields, and can be understood through the theories presented in chapter 3. The pure Mie plasmon modes observed in the data are continuations of the localised plasmons observed to drop in energy with increasing thickness. Therefore, these plasmons are closely related to pure Mie modes, and will also be termed Mie plasmons. The second observation is that while the initial data showed the Mie plasmons dropping in energy towards the values calculated for an isolated void, this is only fortuitous. This is shown in figure 6.18, where the $l = 2$ Mie mode drops in energy toward the $l = 1$ value at $\bar{t} = 1$. Above this height, however, the Mie plasmon increases in energy back towards the $l = 2$ calculated state. This is an important consideration, especially when considering the modelling of the truncated structures.

6.3.3 Pitch Dependence

With an understanding of the localised plasmons at $\bar{t} = 1$, further experiments are conducted to understand the properties of these modes when the sample thickness is reduced. The first of these is the pitch dependence.

The pitch dependence of the localised plasmons was analysed using samples of pitches, 500nm, 600nm, 700nm and 900nm. Figure 6.20a shows an extracted position map of these samples, the size of the marker corresponds to the depth of the absorption feature. As with the Bragg plasmon data, the y-axis has been scaled with the pitch to allow direct comparisons between samples. This data was taken using an optical microscope at ten times magnification; this corresponds to a numerical aperture of 0.3, which subsequently allows the excitation of plasmons between normalised wavelength values of about 0.8 to 1. These features align with the normalisation of pitch as described in the previous section.

While some correlation between different normalised pitches can be seen, sharp modes are not reconstructed as might be expected. Referring to chapter 3 the dispersion of the Mie modes was shown to depend on the size of the voids as well as the momentum of the resonance. For low angular momenta, as in the experimental case, a linear relationship can be empirically obtained for an extra energy shift dependent on the void size. This shift is calculated by setting the scale factor for the 500nm sample data to zero then apply the equation $E' = E + \frac{23.\Delta D}{100.D}$ where ΔD is the change in pitch relative to the 500nm sample. This has been applied to the data shown in figure 6.20b. With this shift in place a much improved reconstruction of the modes is observed. This provides stronger experimental evidence for the modelled dispersion of the Mie modes as well as showing the total scalability of the system. It should again be noted that while the Mie plasmon modes appear to tend towards the calculated energies (shown as black triangles) this is a coincidence. The samples used to perform these experiments did not have thicknesses above $\bar{t} = 1$, so this thickness region could not be analysed. However, from previous discussion it is known that the Mie plasmon start to increase in energy at $\bar{t} = 1$, and then tend towards the pure Mie mode values.

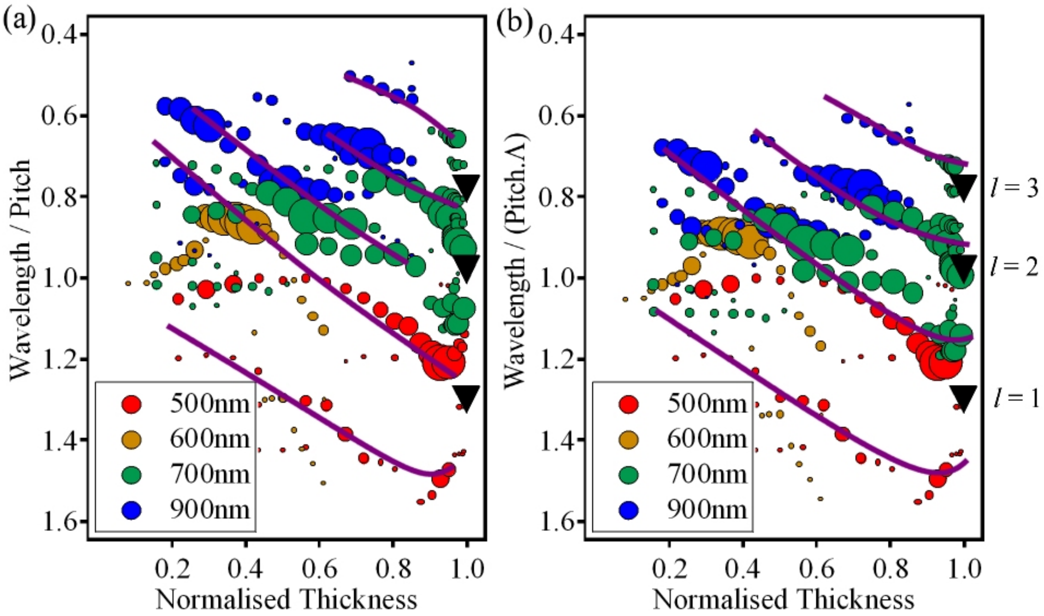

FIGURE 6.20: Position maps showing the extracted absorption features of four different sample pitches, size of marker represents amount of absorption, purple lines show guide to eye. Black triangles represent theoretical energies of calculated Mie resonances. (a) Features have been solely normalised to void diameter, and (b) Dispersion of localised plasmon is also taken into account

The observed trend of the Mie modes passes through the point where the dimensions of the system are equal to the wavelength of light. This can be viewed as a boundary between two different optical regimes. When a structure is much bigger than the wavelength of light, the interactions can be modelled in terms of rays; this greatly simplifies the solutions of the observed behaviour by ignoring the wave nature of the light. For structures smaller than the wavelength of light, the ray model breaks down, instead requiring a more thorough, currently intractable, model to be produced based on wave-physics. Experimentally, cavities between 350nm and 5μm have been analysed, always using visible and infrared light. In all cases similar Mie modes are observed, following the universal trends shown in figure 6.20b. Since the experiments move from the regimes of ray-optics to wave-equations some discrepancies should be expected at different size scales. Since no clear evidence for this behaviour has been found, it might be concluded that the solutions to the ray-optics model are still valid even in the sub-wavelength regime. This allows the constructions of a much simpler, more intuitive, model, as will be described later in this chapter.

6.3.4 Polarisation Dependence

It has been shown that the localised plasmons observed in truncated spherical voids are closely related to those of pure Mie resonances. Mie plasmons contain no polarisation information due to the spherical symmetry within the void; therefore, it would be expected that all possible polarisation configurations should show similar features. These polarisation configurations are shown in figure 6.21 for the 600nm sample at a thickness of $\bar{t} = 0.7$.

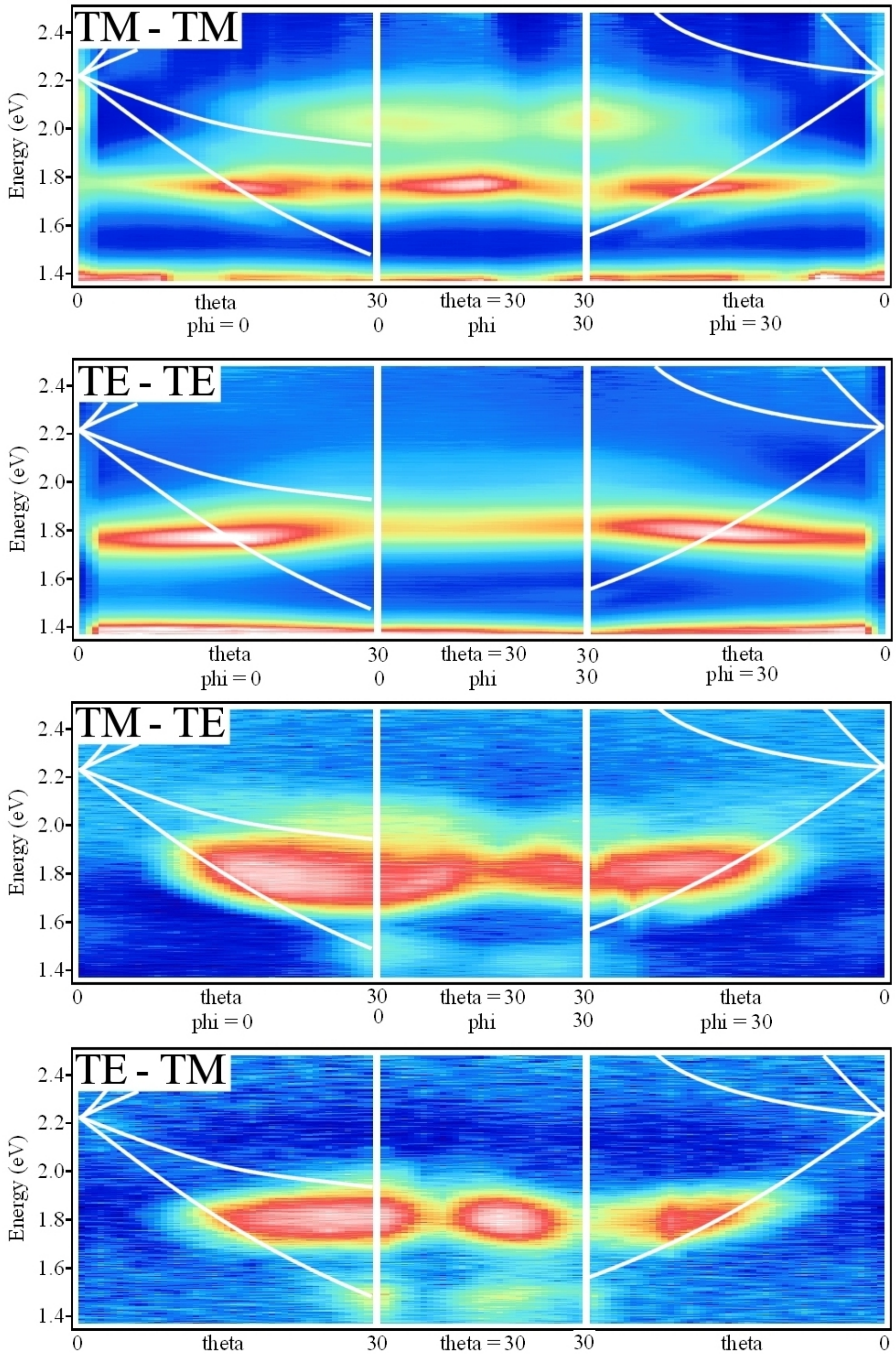

FIGURE 6.21: Dispersion maps for different laser and analyser polarisation configurations. Data taken from a gold sample, void diameter = 600nm, $\bar{t} = 0.7$. White lines show calculated diffraction energies. Cross polarised data has a reversed colour scale since it is showing the amount of polarisation rotation, not absorption.

Two strongly localised modes are clear in both sets of co-polarised data, one around

1.8eV the other at 1.4eV. A third weak mode is also present in the TM-TM data, and its intensity appears to be linked with the intensity of the 1.8eV Mie plasmon. Since TM-polarised light can strongly excite SPP's this is attributed to a weakly mixed Bragg mode persisting at these thicknesses - this will be justified in the following chapter. In the TE-TE data only the two pure Mie modes are visible. Therefore, the co-polarised data shows that both input polarisations can couple equally to the Mie plasmon modes, as would be expected.

The cross-polarised data also shows the expected Mie modes. The data now shows the intensity of polarisation rotated light, which is 100 times weaker than that of the incident light (colour scales have been reversed for easier comparison). The clear difference between the co- and cross- polarised data is that for near-normal incidence the polarisation-rotated modes appear to have zero intensity. This observation can be extended to say that the intensity of the polarisation rotated Mie modes only exists when diffraction is allowed - only possible when ω(k) is at higher energy than the lowest theory lines shown in figure 6.21. Before trying to understand this result it is useful to digress from the polarisation experiments and reconsider the first experiment outlined in this chapter.

6.3.4.1 Mie Plasmon Enhanced Diffraction

At the start of this chapter the diffractive properties of a sample were studied. This used a sample with a thickness of near $\bar{t} = 1$ and showed that light of different wavelengths was diffracted at different angles, exactly as expected from diffraction theory. There was, however, a complexity in the data associated with the intensity of the diffracted light. This was shown to vary in a systematic manner by about a factor of five between different wavelengths, repeated in figure 6.22a.

To understand this observation a further experiment has been performed. In this experiment the intensity of the first order diffracted beam was measured for all incident pump angles. In figure 6.22a, a single pump angle was used (45^o in this case) and all outgoing angle were detected. This leads to a curved line through energy and angle. As the incident angle (θ_i) is decreased, this curve shifts to higher energies and detected angles (θ_d) following the diffraction equation:

$$\theta_d = sin^{-1}\left(\frac{n\lambda}{\Gamma} + sin(\theta_i)\right) \tag{6.4}$$

in figure 6.22c the intensity along this curved diffraction line is extracted and plotted as a vertical line at the incident angle of the pump light. For a shallow diffraction grating, where surface structure can be completely ignored, this image would be a single intensity to the right of the theory line and no intensity to the left - where no diffraction

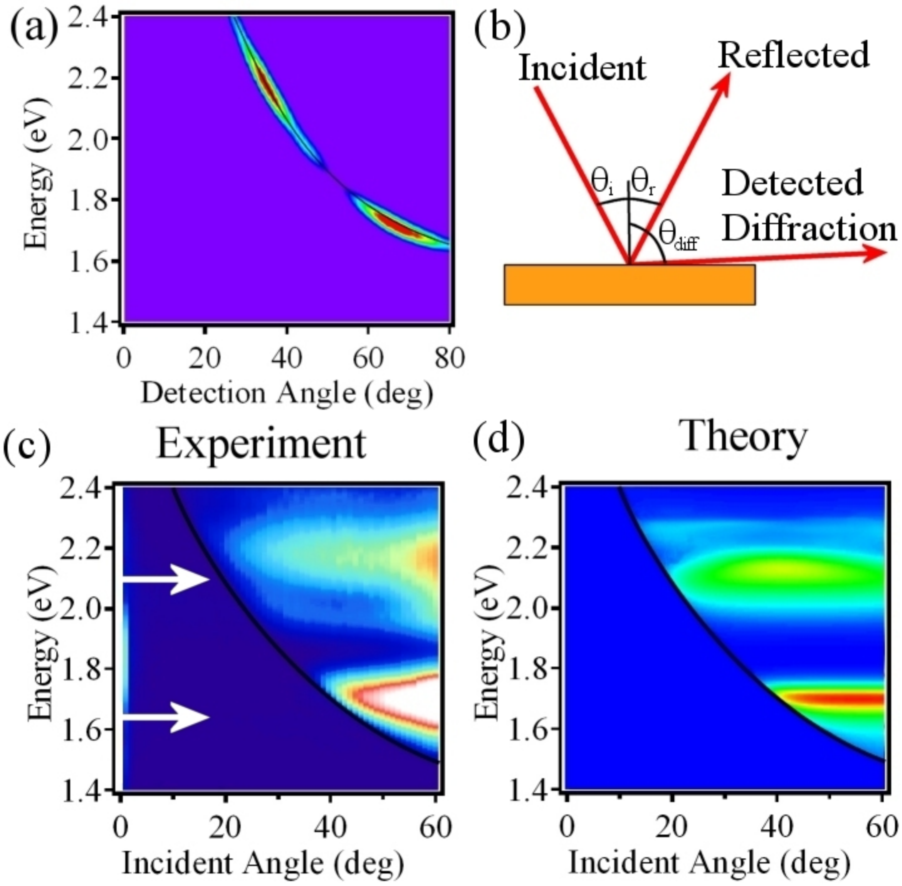

FIGURE 6.22: (a) Detector scan performed on a gold 500nm void diameter sample at $\bar{t} = 1$, $\theta_i = 45^o$ to observed diffracted light. (b) Schematic of incident, reflected and diffracted beams. (c) Intensity of first order diffracted beam as a function of incident angle. (d) Theoretical calculation of (c).

is allowed. In figure 6.22c there is no diffracted intensity to the left of the diffraction line, as expected. However, the intensity variation seen in the diffracted beam resolves clearly into two bands on the right hand side the diffraction line. The arrows in the figure correspond to the energies of the Mie plasmon modes at this thickness. A clear correlation between the Mie plasmon energies and the enhancement in the diffracted signal can be observed.

Again, since the experiment is performed near $\bar{t} = 1$, the same theoretical frame work used to calculate the perfectly matched absorption can be utilised by the collaborative theory group. The simulation of this problem is shown in figure 6.22d. As can be seen, there is close correlation between theory and experiment. This Mie plasmon enhanced diffraction is due an increased coupling into the diffracted beam. Similarly, it can be seen that the Mie plasmons couple better to the optical field through the diffracted orders, by the same argument.

It is now possible to return to the polarisation experiment shown in figure 6.21. A very similar behaviour is observed in the cross polarised data to that shown for the Mie enhanced diffraction. The difference is that the polarisation experiment is performed in the reflection direction - or zeroth order diffraction, not the first order.

The data shows that Mie plasmons are only observed when scattering of the incident light into the first order diffracted mode is allowed. This implies a second order scattering process is responsible. Here, re-radiated light from the Mie plasmon modes is scattered into the first order diffracted mode, and then back to the zeroth order where it is emitted. While this process will occur for both polarisations, due to the small signal the effect will only be observed in the cross-polarisation configuration.

6.3.5 Modelling of Mie Plasmons

Whist it is possible to precisely calculate the energies of Mie plasmon modes for encapsulated voids, currently it is not possible to do the same for truncated spherical structures. The reason for this is symmetry. An encapsulated sphere is symmetric in all directions so the Maxwell's wave equations simplify to a set of exact solutions. When the symmetry is broken these spherically symmetric solutions can no longer be used and it is not possible to simplify the equations to find resonant modes. For this reason, this section presents two models to account for the energy of the Mie plasmons in truncated spherical voids. These are briefly shown in figure 6.23.

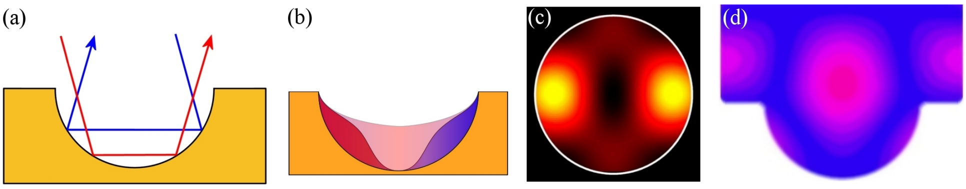

FIGURE 6.23: Different Models of Mie plasmons. (a) Ray path analysis of the structure to find destructive interference. (b) Plasmon standing wave in two-dimensions (c) Electric field distribution calculated through Mie scattering in a perfect void (d) Finite difference time domain modelling of the structure.

The first approach (fig 6.22a) is based on ray optics and assumes the Mie plasmon is a pure optical mode within a cavity. Here, the phases of all possible ray paths through the cavity are summed together. After the phase change upon reflection is also taken into account the destructive interference modes of the system are calculated and compared with the experimental data. The second approach (fig 6.22b) is to model the Mie plasmon as a pure SPP pinned to the metal's surface. This plasmon is assumed to be a standing wave trapped within the dish and pinned at the void rims. Using this model, plasmon modes can be found and compared to the experimental data. Both modelling techniques are intuitive and less mathematically rigorous than a full electromagnetic solution (fig 6.22c), but are shown to produce results somewhat matching the experimental data. The following section will compare the results from these models with calculations done using a finite difference time domain computer simulations (fig 6.22d).

6.3.5.1 Ray-Optics Model

The first method of modelling the optical properties of the truncated voids starts from work performed by the previous post-graduate student working on this project[95]. Figure 6.24a shows images from polarisation experiments performed on 20μm diameter voids. It was quickly found that the co- and cross-polarised reflected distributions came from light 'bouncing' off the wall of the cavity and acquiring a polarisation rotation.

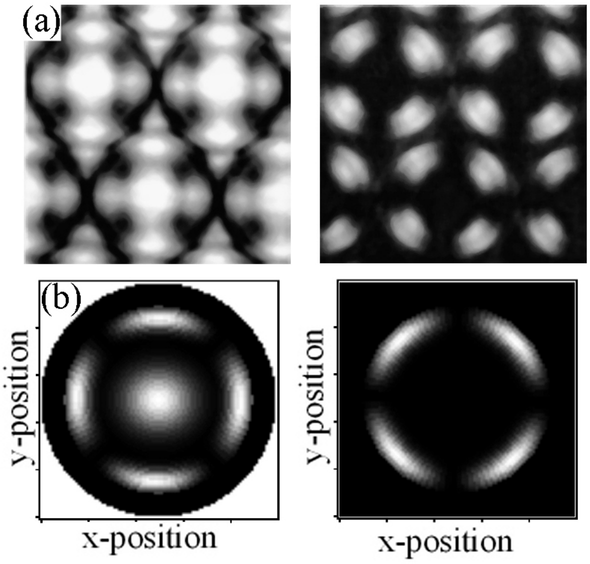

FIGURE 6.24: (a) Images of co- and cross-polarised reflections from 20μm voids. (b) Theoretically expected output from the same cavity. From [12]

Sets of reflectivity minima were also observed for these larger structures, and the energy of these minima were found to vary with thickness[12]. This provided the starting point for a model based on rays traversing the cavity to be formulated. This model is shown schematically in figure 6.25a.

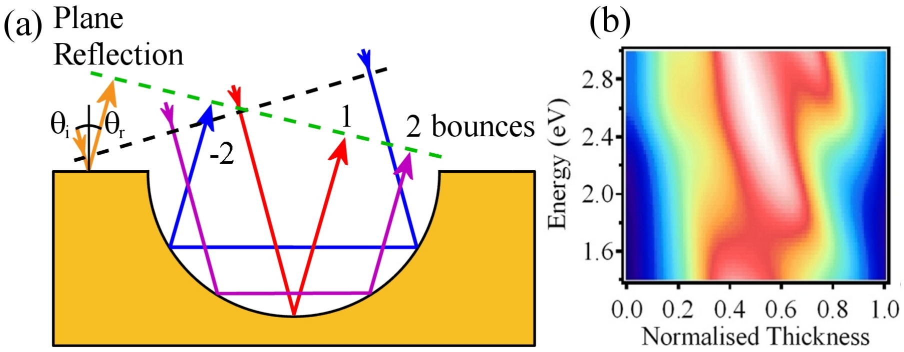

FIGURE 6.25: (a) Schematic of a plane reflection off the flat metals surface along with 1, 2 and -2 bounces within the cavity. Dashed lines show points from where ray path distances are calculated (b) Theoretical position map using a three-dimensional ray path interference model for a 600nm cavity

For this two-dimensional case a set of rays is brought onto the surface at an angle θ_i. All possible reflections are then considered and a set of ray paths is produced. Only rays leaving the surface in the reflected direction, θ_r (within a range of angle $\Delta\theta$ set by the experimental configuration) , will influence the observed reflectivity, so all other ray paths can be discounted from the model. This leaves contributions from rays of integer numbers of bounces through the cavity. Figure 6.25 shows one, two and minus two bounces along with the reflection off the top surface. For each ray path the total distance between the phase front incident on the surface (black dotted line) and the front leaving the surface (green dotted line) is computed. If light of a specific wavelength illuminates the cavity it will travel the different ray paths, and acquire a different phase depending on the distance it has travelled. The interference between these different phases leads to a modulation in the total observed intensity. If the calculation is performed in three dimensions and the solid angles of each bounce are properly accounted for, a theoretical position map can be produced. One such calculation is shown in figure 6.25b for a 600nm diameter cavity at $\bar{t} = 0.5$. This calculation shows a set of reflectivity minima, dropping in energy as the thickness of the sample increases, an identical trend to that found experimentally. As has been previously noted, the ray approximation should break down when the structures become smaller than the wavelength of light. No obvious change in the experimental optical response is observed as the as the structures pass through this size scale so it is argued that the ray-approximation is still valid.

There are, however, a number of free parameters used in this model, which make quantitative prediction difficult. The first parameter to be considered is the number of bounces the light makes while travelling around the void. Studies have shown that in the two-bounce configuration the curvature of the dish efficiently re-collimates the reflected light[12], while other numbers of bounces lead to more diffuse light, although for one bounce the large cross-section should still provide a noticeable effect. From this, it can be assumed that at least one and two bounces must be considered. Figure 6.26a shows the dependence on the energy of the interference minima for numbers of bounces from 1 to 1001. In this figure the phase change on reflection from each surface has been considered to be zero (if included, when considering large numbers of bounces the phase change on reflection becomes the dominant term, making results hard to interpret).

This shows that there is a large difference between one and two bounces. However, above this the modes tend quickly to a universal dependence, equal to that of light propagating along the surface of the metal (fig 6.26b). This is similar in many ways to a surface plasmon mode, although no coupling to the surface is included in the model. To incorporate some essence of the plasmon, the phase shift on reflection from the metal can be applied for each bounce. However, before any further analysis is presented, a look at the other free parameter should be considered: the Gouy shift.

The Gouy phase shift arises when a beam of light passes through a focal point[96, 97]. Around the focal point the beam is laterally confined and this, through the uncertainty

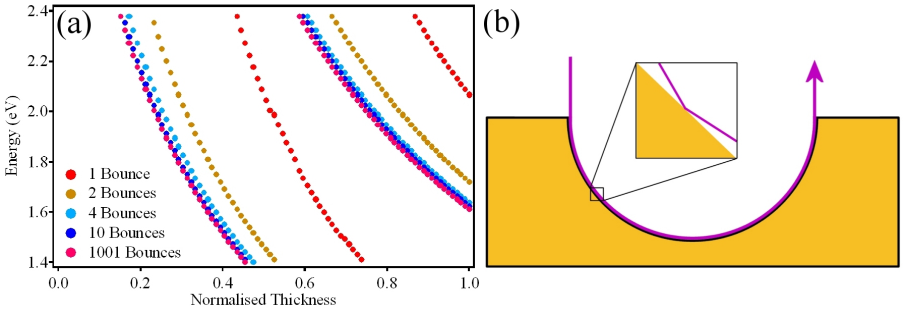

FIGURE 6.26: (a) Graph showing expected energies of absorption features at different normalised thicknesses. Cavities have a diameter of 600nm, numbers of bounces as shown. (b) Schematic of large number of bounces effectively appearing as a ray travelling along the metals surface

principle, leads to an increase in lateral beam momentum. Due to momentum conservation, this subsequently leads to a decrease in momentum in the propagation direction, which manifests itself as a change in phase. When the total phase change through the focus is summed from $-\infty$ to $+\infty$ it exactly equals π. For a Gaussian beam profile, this phase change occurs mainly within a distance equal to the beam waist. The ray-optics model presented so far depends critically on the final phase of the outgoing light to calculate the interference, and since focussing effect are present within the cavity, the Gouy shift cannot be discounted. However, due to the sub-wavelength character of the dish, the distances the light can travel are less then that of the beam waist and so a full shift would not be expected.

To match the ray optics model with the data it is assumed that the field produced by the rays should match the angular momentum of the Mie modes. This is shown schematically in figure 6.27, and shows that one bounce should be the matched with l = 1 and two bounces should be matched with l = 2. Figure 6.28 shows the ray-optics theory with the experimental data from the isolated void sample.

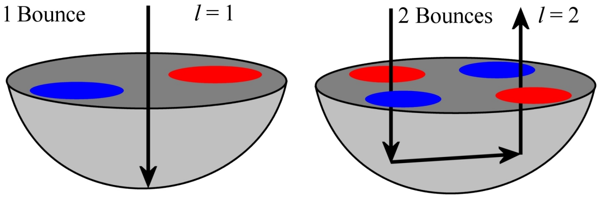

FIGURE 6.27: Schematic showing link between number of bounces and Mie plasmon angular momentum.

Here, the exact phase shift upon reflection is taken into account and the destructive interference for normal incident light of one and two bounces is calculated. It is found that by varying the Gouy shift of one and two bounces independently it is possible to fit the energy of the ray-optics modes at $\bar{t}$ = 1 to those calculated through the isolated void calculation. Due to the presence of multiple interference minima, these values of Gouy shift also turn out to be best for fitting to the experimental data (as shown). This

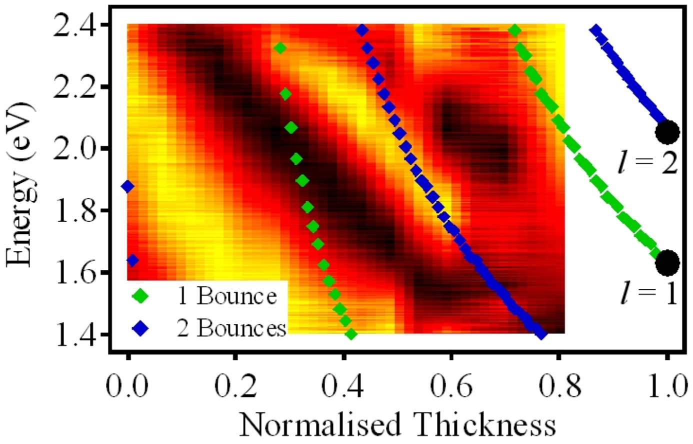

FIGURE 6.28: Graph showing interference modes for 1 and 2 bounces, compared to data from 600nm isolated voids and the energies of the $l = 1$ and 2 Mie modes.

fitting required a Gouy shift of zero for one bounce and a shift of 0.4π for two bounces. This might be expected since a ray path undergoing one-bounce is only weakly focused and a 40% shift is consistent with the amount of the beam waist a two-bounce ray would pass through.

Whilst these values of Gouy shift have optimised the fitting, there are a number of problems. Firstly, the presence of multiple interference minima means the modes that have been fitted to the experimental data are different to those that have been fitted to the energies at $\bar{t} = 1$. This means that that the predicted modes drop to much lower energies at $\bar{t} = 1$ than is observed experimentally. Linked to this problem, the gradient, $E(\bar{t})$, of the modes is also greater than that of the experimental data. The reason for these differences is, at least in part, due to the plasmon dispersion being different to that of light. The experimental modes always tend towards the two-dimensional plasmon energy of 2.5eV at $\bar{t} = 0$. However, the phase change of reflection varies little around this energy, and hence fails to add a plasmonic effect to the ray picture. Secondly, it has been shown that due to the increased confinement the plasmon modes increase in energy around $\bar{t} = 1$. This is also not included in the ray optics approach and why theory and experiment differ at $\bar{t} = 1$.

Whilst the energies of the Mie plasmons are not fully reconstructed using this model, the trend of decreasing mode energy with increasing film thickness is clear. When the rays are reflected from the surface a screening charge must be set up within the metal. This screening is a surface charge oscillation and since this will match the fields shown in figure 6.27, the different ray paths will set up charge oscillations. Since the cavities are on the wavelength of light these surface charge oscillations will interact with one another, and form a standing wave surface plasmon oscillation, the topic of the second model to be outlined in the following section.

A further problem with the ray-optics model is the interference minima vary in energy with incident angle, unlike the experimental data. This links with a further prediction of a ray-optics approach - that of forbidden ray paths.

6.3.5.2 Clipping

One aspect of the ray model not yet discussed is that for certain thicknesses and incident angles ray paths will be forbidden; as outlined in figure 6.29.

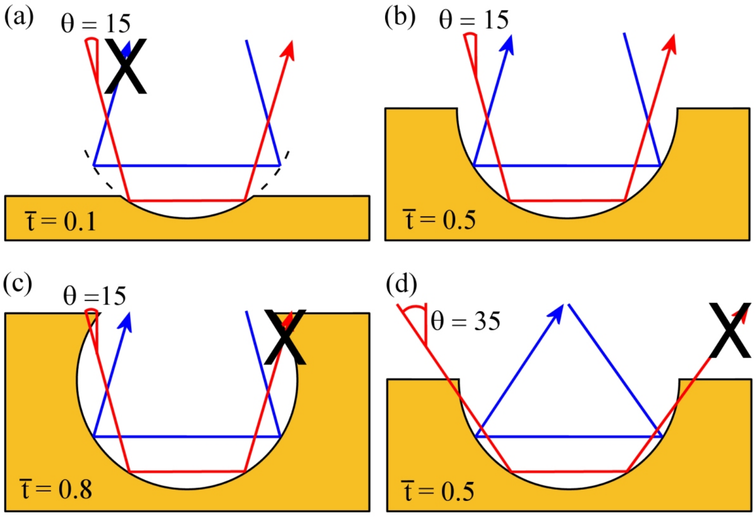

FIGURE 6.29: Schematic representations of 2 and -2 bounce ray paths with a cavity of (a) $\bar{t} = 0.1$, $\theta = 15^o$, (b) $\bar{t} = 0.5$ $\theta = 15^o$, (c) $\bar{t} = 0.8$ $\theta = 15^o$, (d) $\bar{t} = 0.5$ $\theta = 35^o$.

In this figure only the forward and backward propagating two-bounce rays are considered, however, clearly these results extend to all other possible paths. This shows that for dishes at $\bar{t} = 0.1$ the two-bounce ray can only exist above $\theta = 15^o$ (all negative values of θ are impossible). As the thickness increases, for the same incident angle, both ray paths become possible (fig 6.29b) and then only the reverse bounce (fig 6.29c). Figure 6.29d also outlines the clipping of rays through the changing of the incident angle at one thickness. Geometrically, it is possible to calculate for different thicknesses and incident angles which configurations of bounces are permitted, this is shown in figure 6.30 for one, two and minus two bounces.

Figure 6.30b shows two sets of experimental data from close packed 700nm and 900nm void arrays. This data has been averaged over all observed energies to remove Bragg modes and strengthen localised states, although similar features can be observed for single energies.

The most prominent feature in both sets of data is the bright band starting near $\bar{t} = 0.2$ at normal incidence and increasing to $\bar{t} = 0.5$ by $\theta = 80^o$. This can be compared with the predicted band in the theory, leading to the possible conclusion that only when both ± 2 bounces are allowed is there a significant coupling - the brown and yellow

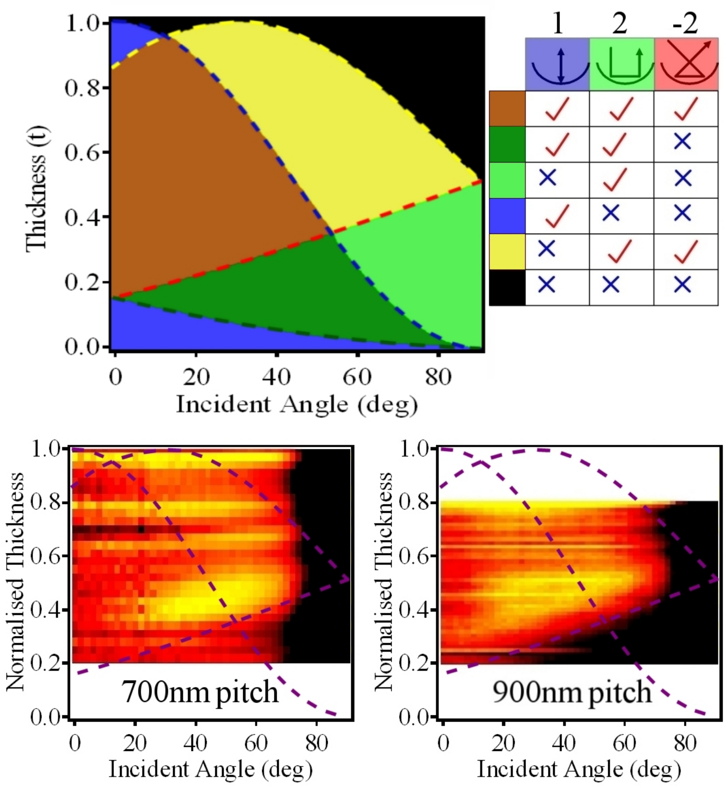

	1	2	-2
🟫	✓	✓	✓
🟩	✓	✓	✗
🟩	✗	✓	✗
🟦	✓	✗	✗
🟨	✗	✓	✓
⬛	✗	✗	✗

FIGURE 6.30: (a) Theoretical model for the clipping of 1, 2 and -2 bounces. (b) Experimental reconstructions of total absorption for normalised thickness vs. incident angle, data is averaged over all energies.

regions. Unfortunately the lack of data below $\bar{t} = 0.2$ makes these claims hard to fully justify and the fact that SPP effects are strongest in this region adds complexity to the results. Whilst there is some correlation between theory and experiment, no clear forbidden regions are visible in the data. This observation is also true for all other samples analysed to date, meaning that ray clipping does not have a strong influence on the observed modes. This can be understood through the highly plasmonic nature of the modes, allowing coupling to those which are forbidden in the ray picture. This increased mode coupling would arise if the electric field distribution were not purely located within the void, but also existed above the cavity. This symmetry of the true field distribution also accounts for why the energies of the Mie modes are independent of incident angle, unlike that predicted by the ray-optics model. This, it will be shown in a later section, is indeed predicted through finite difference modelling.

It must therefore be concluded that while the ray-optics approach is of interest, it will require further modification to fully account for the plasmonic nature of the modes.

6.3.5.3 Standing Plasmon Wave Model

An alternative approach to the modelling the plasmon modes of a truncated void is to assume the existence of a one-dimensional standing wave within the dish. This wave can consist of an arbitrary number of nodes and is pinned at the void rims, shown schematically in figure 6.31.

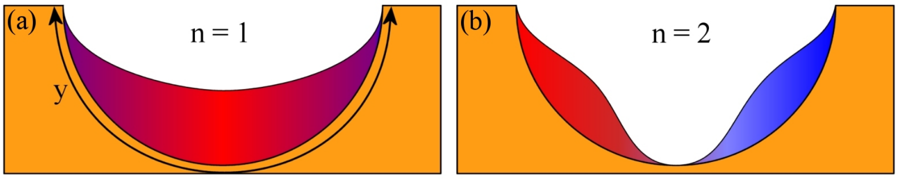

FIGURE 6.31: Pictorial representation of plasmon standing wave model showing (a) 1 mode, and (b) 2 modes.

This model calculates the wavelength of the standing wave localised plasmon using the equation:

$$\lambda_{LP} = \frac{2y}{n} = 2\left[\frac{2.r.cos^{-1}\left(\frac{r-t}{r}\right)}{n}\right] \tag{6.5}$$

where n is an integer and corresponds to the number of half wavelengths that will fit into the curved rim-rim distance, y. Subsequent use of the surface plasmon dispersion relation leads to the equation:

$$E = \frac{2\pi\hbar c}{e\lambda_{LP}}\sqrt{\frac{\hat{\epsilon}_M + \epsilon_d}{\hat{\epsilon}_M \epsilon_d}} \tag{6.6}$$

where, again, $\hat{\epsilon}_M$ and ϵ_d are the dielectric functions of the metal and dielectric respectively. These equations, therefore, provide a set of energies for the localised plasmons purely in terms of the cavity radius and sample thickness.

This simple model automatically ensures that the calculated modes are plasmonic and depend on the sample thickness. At $\bar{t} = 1$ this model produces a standing wave solution the same as that used in the Mie scattering theory, although only in one symmetry direction. Figure 6.32a shows the solutions to the standing wave equations for a 600nm cavity, plotted as energy vs. normalised thickness and overlying the experimental data from the sample of isolated voids.

Figure 6.32a shows a strong correlation between the standing wave plasmon model and the data. The angular momentum of the calculated modes matches those seen experimentally, although it should also be emphasised that the model does not tend to the correct energy at $\bar{t} = 1$. This is because the plasmon standing wave model has no means to incorporate the increase in energy above $\bar{t} = 1$.

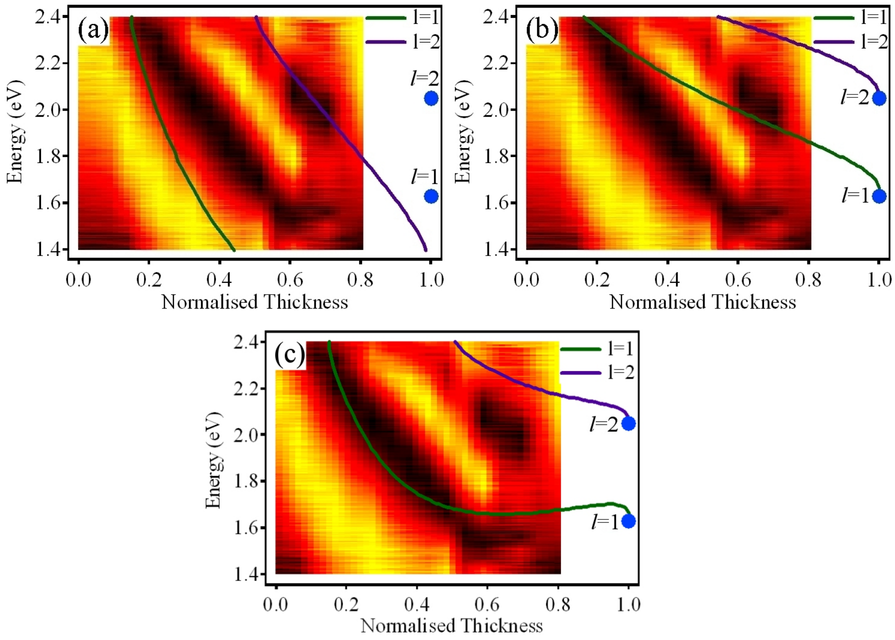

FIGURE 6.32: Position map of isolated 600nm gold voids. Blue circles show theoretical position of Mie resonances. (a) Overlaid theory for simple SPP standing wave. (b) Overlaid theory for SPP standing wave using dispersions of encapsulated void. (c) Overlaid theory combining previous two methods.

For a consistent argument to be constructed the number of electric field maxima in the standing wave model should coincide with those of the Mie scattered solutions at $\bar{t} = 1$. The standing wave model, therefore, requires a shift to higher energies as the sample becomes thicker. Chapter 3 outlined the dispersion relations for Mie modes for spheres and in voids. This showed that the energy of different modes was, for voids, indeed shifted up in energy relative to that of a flat surface. This is shown in figure 6.33, where the SPP dispersions on smooth gold and in encapsulated 600nm diameter void are compared.

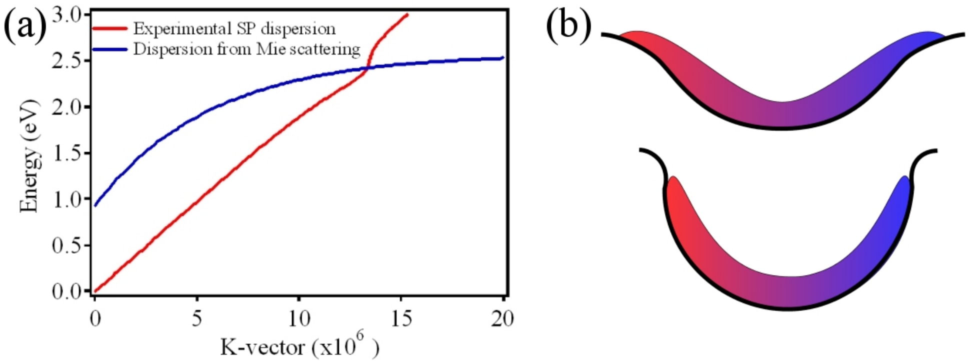

FIGURE 6.33: Dispersions of a SPP on a smooth gold surface and in an encapsulated gold void of diameter 600nm.

This figure again shows that the plasmon dispersion of an encapsulated void is at a higher energy than that of a smooth surface. This modified dispersion also tends to the two-dimensional surface plasmon energy as k increases, as is seen experimentally. The universality of this scaling relationship provides the possibility of correcting the standing wave plasmon solutions. If the dispersion relation for an encapsulated void is now used to relate the k-vector of the standing wave to the energy of the mode, a new theoretical mode is produced, shown in figure 6.32b again compared to the experimental data. This alteration to account for the three-dimensional curvature fixes the energies of the standing wave plasmons to be equal to those of the Mie scattered solutions at $\bar{t} = 1$. The solutions also tend to the surface plasmon energy as the sample thickness tends to zero, as seen experimentally. While this modified model has enforced accurate energies at both $\bar{t} = 0$ and 1, the fitting in-between these values is inconsistent with the data. It can be concluded that the model using the dispersion calculated from the Mie scattering solutions is accurate when the voids are completely encapsulated. When the surfaces are thinner than $\bar{t} = 0.5$ then the dispersion of a flat surface is correct. Between these values a combination of the models is required. As a first attempt to model this figure 6.32c used the equation

$$E = \frac{\hbar c}{e}[(1-\bar{t})k_{flat} + \bar{t}.k_{void}] \tag{6.7}$$

to combine the two dispersion relations. This shows the shape of the experimental Mie plasmon modes but does not reproduce accurate energies. The theory also still tends to the energy of the encapsulated Mie plasmon from higher energies, not lower as seen experimentally. However, it can be seen that by applying a different weighting to the different dispersion components a better fit can be found. This could be performed but with no physical reasoning behind this scaling it is perhaps better to conclude by analysing the implications of the model. The modelling of the Mie plasmons as a standing waves with a dispersion equal to that of a smooth gold surface appears accurate below $\bar{t} = 0.5$. At $\bar{t} = 1$ the mode energy must be calculated through a rigorous solution to Maxwell's equations, as the simple model does not take into account the extra energy associated with the confinement of the field. Between $0.5 < \bar{t} < 1$ there is some, but not complete, mode confinement. This leads to a dispersion relation for the Mie mode somewhere between a smooth and an encapsulated surface. Up to $\bar{t} = 0.5$ there is little confinement within the cavity, with a smooth rim leading onto the surface. However, above $\bar{t} = 0.5$ the surface becomes more confining, as depicted in figure 6.33b. This analysis leads to an idea about the electric field distribution of the Mie plasmon, and is discussed in the following section.

6.3.6 Visualisation

Two methods for understanding the optical properties of truncated, sub-wavelength metallic spherical voids have been proposed, both of which seem to converge to similar answers as do the results from Mie scattering theory and experimental data. It is thus useful to now take stock of the models and try to understand the electric field distributions in these systems. Comparisons can also be made with finite difference simulations performed using the commercially available software package (Maxwell by Ansoft). Figure 6.34 sketches the rough intensity distributions from each of the models. While the distributions look somewhat different, some similarities can be drawn. Figure 6.34a depicts what the ray-optics model would look like, showing the different bounces and the approximate intensities that should be formed. This is quite crude, although it shows three intensity maxima around the dish, reminiscent of the standing wave model. Figure 6.34b shows three standing wave SPP modes within a void. This model has been shown to have similarities with both the Mie plasmon calculations and the excitation of surface charges from the ray optics model. Figure 6.34c shows the exact Mie calculations for the magnitude of the electric field. The two modes look somewhat similar to the 1 and 2 bounce predicted distributions as well as those of the standing waves. Any model should converge onto these distributions as the void tends to full ball height. The truncation of the spherical geometry is likely to mix together higher order Mie modes with those present at $\bar{t} = 1$. This would increase the mode energies, as observed, and produce a non-spherically symmetric field distribution. Further work on this model is currently underway as a precise method to model the distributions. Figure 6.34d shows a 'best guess' of what the real intensity distributions might look like based on the previous three models. Here the field forms several maxima on the voids surface, as would be predicted through the standing wave model, as well as taking an intensity distribution within the cavity similar to that of the two-bounce ray path. It has also been estimated from previous analysis that the electric field will not be strictly pinned within the void but extend above and to the sides of the cavity as well. To model such a mode profile the best method will be to add together a number of Mie plasmons, calculated in the spherical void geometry. If performed correctly, this will enhance the mode intensity within the truncated void, while weakening it above. This would lead to the increasing energy with decreasing thickness, tending to the two-dimensional plasmon energy as seen experimentally. Currently such a model has not yet been successfully created so instead the use of finite difference modelling has been employed.

In this technique, a spherical gold void is defined within the electromagnetic simulation program. The void is placed in a vacuum and a plane wave is introduced into the system. The boundary conditions are set up so that the outer edges of the defined region produce no back reflections. Finally, a fine mesh is defined throughout the structure. Since the program is solving a three-dimensional system, a limiting factor in these experiments is computer memory. For calculations of the field within a truncated void, wavelengths down to the diameter of the cavity could be performed with reasonable confidence. This allowed a mesh size of around 20 finite regions per wavelength, and provided sufficient resolution for the problem to be solved without producing anomalies in the intensity distributions (formed when the mesh size is bigger than the smallest part of the mode

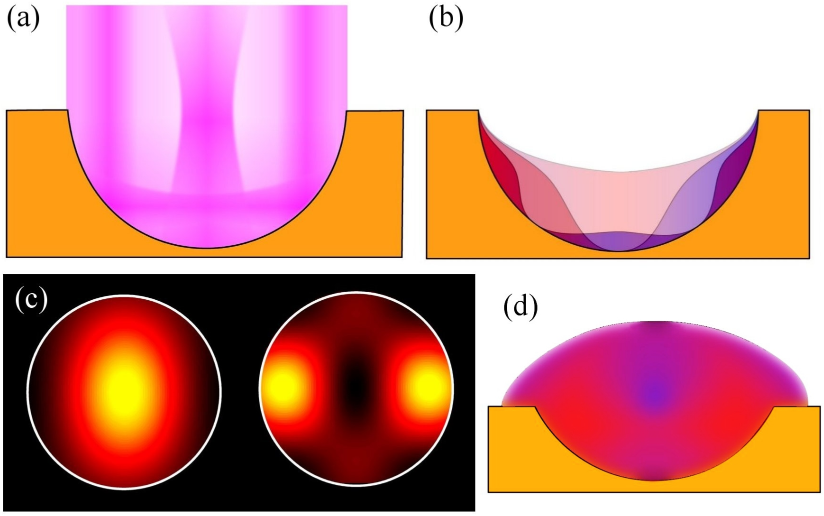

Figure 6.34: (a) Cartoon of possible intensity distribution according to a ray-optics approach. (b) Possible electric field profile proposed by the pure standing SPP wave model.(c) Exact solutions to the field distributions of the Mie scattering equations. (d) Authors best guess of field distribution of a truncated sphere based on the previous models.

profile). The program solves Maxwell's equations for each block, taking into account the surrounding regions; this is performed iteratively until a single solution is obtained. The construction of other geometries presented with published field distributions provide a stringent test for the reliability of the results[98, 61]. Subsequently the modelling of a range of truncated void geometries illuminated at different angles and wavelengths was performed. A selection of these results is shown in figure 6.35. In each case images are presented showing the magnitude of the electric field polarised in the same direction as the slice taken through the three dimensional cavity; the different images in each set represent the evolution of the electric field through one optical cycle. Parts a-c show a 700nm cavity illuminated with 980nm light for three geometries of thicknesses $\bar{t} = 0.25$, 0.5 and 0.75 respectively. Part d shows a 900nm cavity at $\bar{t} = 0.5$ illuminated with 500nm light.

In all cases, although often subtle, there is an electric field pinned to the dish, looking very similar to those predicted earlier. There is also a strong focussing of the light similar to that seen in the ray-optics approach. It is also observed that the electric field distribution does indeed exist above the confines of the cavity. This distribution is close to symmetric above and below the void rim, although, the mode intensity is greater when inside the cavity due to the stronger confinement, also as predicted. For both the thicknesses of $\bar{t} = 0.25$ and 0.75 the field regains an almost plane-wave nature as it leaves the simulated region. This is not the case for the $\bar{t} = 0.5$ case where the light has been strongly diffracted and leaves at various angles. The electric field is also found to be strongly concentrated at the focal point of the cavity. This is also true for the $\bar{t} = 0.75$ case, however, now the field seems to have become almost completely localised within

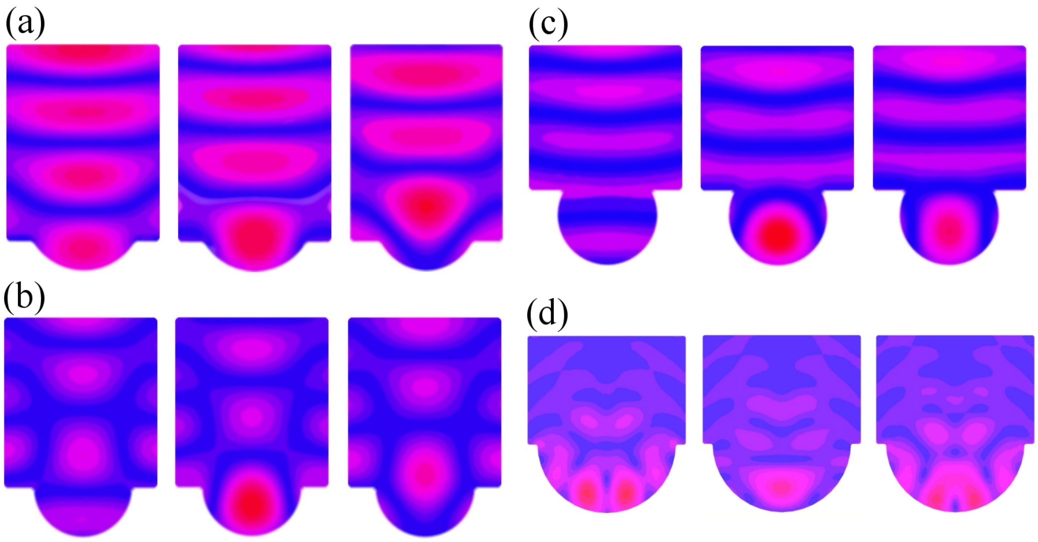

FIGURE 6.35: Finite difference time domain modelling of the absolute electric field within a three-dimensional truncated void. (a) $\bar{t} = 0.25$, (b) $\bar{t} = 0.5$ and (c) $\bar{t} = 0.75$, for a cavity of diameter 700nm, illuminated at normal incidence with 980nm light. (d) Cavity of diameter 900nm illuminated with light of wavelength 500nm, $\bar{t} = 0.5$. Colour scale runs from blue (minimum field) to red (maximum field).

the void. As the cavity is made bigger and the frequency is increased two things are observed. Firstly the excitation of a quadrupole mode within the cavity, and secondly a strong coupling with the surface as the light becomes closer to the plasmon resonance.

These findings add weight to previous postulations and do not show any serious differences over the expected profiles. The simulation package can also produce maps for the poynting vector in a time-average system, this is plotted in figure 6.36 using the same conditions as the previous simulation.

This clearly shows two energy maxima on the surface of the dish as well as a large field enhancement at the focal point of the void, and a clear collimation of the output energy. The inset shows a simple ray trace of the system for comparison - the basic shapes of the two images are similar, continuing the understanding that even in sub-wavelength cavities a ray approach is to some degree valid.

While finite difference modelling can produce some interesting results, the current limitations of computer resources do not allow the full experimental problem to be addressed. This is particularly true when considering possible interactions between cavities, or the interactions between surface and localised plasmons. There is also an issue with computer simulations that it is hard to know if the answer produced is representative of the solution to the real problem. Slight changes in boundary conditions and mesh construction can lead to different results. It is felt that the simulations shown in this thesis are accurate in terms of electric field distributions, however, as yet no quantitative values for field strength or absorption can be extracted.

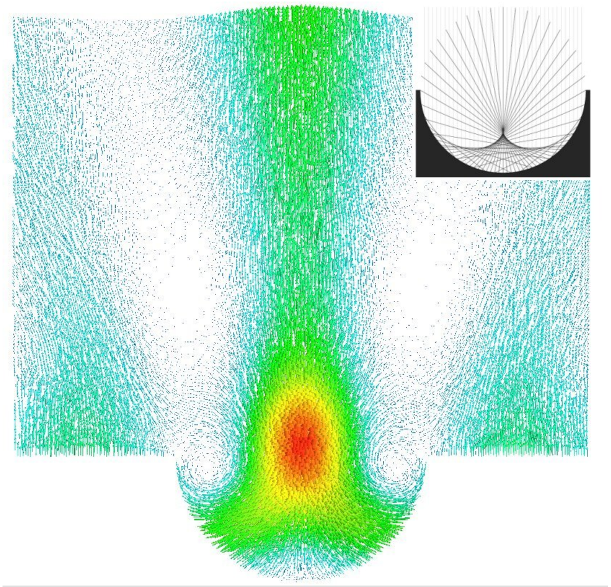

Figure 6.36: Finite difference time domain modelling of the Poynting vector within a three-dimensional truncated void, diameter = 700nm, wavelength = 980nm and $\bar{t} = 0.5$. Colour scale runs from white (minimum) to red (maximum). Inset shows ray model for the structure for comparison.

Whilst experimental verification of the true electric field is difficult, the optical trapping of small fluorescent particles can be used to find intensity maxima. Figure 6.37a shows the principle of optical trapping. Here, a dielectric sphere, of diameter greater than the wavelength of light, is placed off axis in a weakly focused Gaussian beam. This system can be modelled using ray optics, and two rays symmetric about the spheres centre are shown, ‘a’ and ‘b’. These rays will refract through the sphere and give rise to forces F_a and F_b in the direction of the momentum change. This force arises from radiation pressure, which is ordinarily small. However, if a laser is used the flux density can be high enough to make these forces significant[99]. Because the intensity of ray ‘a’ is greater than that of ‘b’ the force exerted will also be greater. If the net force striking the particle is calculated it can be resolved into two components. The scattering force, F_{scat}, which acts to push the particle in the direction of the laser, and the gradient force, F_{grad}, which acts to push the particle to the point of greatest intensity perpendicular to the laser propagation direction. It can now been seen that if the focus is sufficiently strong, the gradient force will be greater than the scattering force and the particle will become trapped at the point of greatest intensity - the focal point. These results can also be extended to systems where the particle size is less than that of the wavelength of light.

Experimentally a low concentration of 900nm fluorescent spheres is placed in solution above an array of 2μm dishes, $\bar{t} = 0.3$. A pulsed 1048nm laser was used to trap the spheres, while doubling of the same source provided the energy to make the particles fluoresce. Figure 6.37 shows an image of the observed fluorescence after the trapping beam had been on for several seconds, allowing time for some spheres to become trapped.

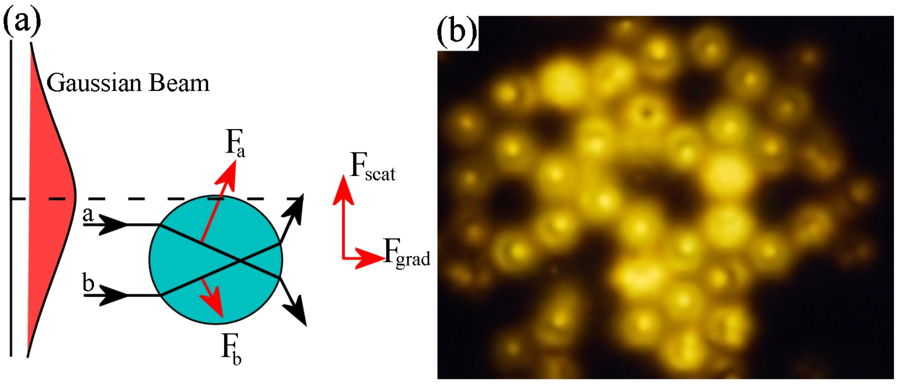

FIGURE 6.37: (a) Schematic of optical trapping principle. (b) Image of 900nm fluorescent dye spheres optically trapped above an array of 2μm dishes, $\bar{t} = 0.3$.

Initially the particles move randomly through the solution according to Brownian motion, however, as soon as the IR laser is activated the particles quickly become trapped above the dishes. Now, the fluorescence intensity increases dramatically as the cavities act to collimate and channel much more of the light to the camera. This behaviour conclusively shows that the spheres become trapped in the regions of greatest field strength. The observations of continued particle jitter during trapping and the re-dispersion when the trapping laser is cut off, also show that the spheres do not become stuck to the surface. Analysis of figure 6.37 shows that some spheres are not trapped above the centre of the dishes but to one side. A ring of light can also be observed arising from the effective re-collimation of the emitted light through the two-bounce path, while mirror images of the particles can also often be observed. This experiment shows that the field above the dish is firstly greatly enhanced and secondly is of at least dipole nature. This finding is in good agreement with the models presented in this chapter.

6.4 Conclusions

This chapter has shown that the nano-structured surfaces studied in this thesis support two very different types of plasmons, a delocalised Bragg plasmon and a localised Mie plasmon.

Found primarily at the thin end of the samples, Bragg plasmons can be modelled using a weak-scattering approximation, meaning that the structure of the sample has little influence on the dispersion of the plasmon. This assumption becomes less valid when the surfaces become thicker, and the effect of the voids perturbs the Bragg plasmon dispersion. It has been shown that, as a first approximation, an increased propagation distance can be added to the dispersion relation to fit the data. It has also been found that the Bragg plasmons universally scale with pitch, as expected.

In stark comparison, Mie plasmons appear to be purely localised plasmonic states residing within every metallic dish. These states resemble Mie scattered electric field distributions and are completely independent, even though the cavities connect with their nearest neighbours. Precise models for these states are possible when the cavities form encapsulated voids, and the correlation between theory and experiment is very good. For truncated cavities, it has been shown that these modes can be modelled intuitively as standing waves, both tied to the metals surface and in the free-space within the voids. Again, it has been shown that Mie plasmons also scale universally with void size, however, this requires the use of a modified dispersion relation to take into account the increased field confinement and the three-dimensional curvature of the metal surface. The coupling to the Mie plasmons to the optical field has also been shown to enhance the amount of diffracted and polarisation rotated light leaving the samples and leads to the interesting phenomena of perfect optical absorption at the Mie plasmon energy.

Interestingly, both plasmon types exist for most sample thicknesses, and hence geometries. The existence of both Bragg and Mie plasmons at similar energies leads to an observed alteration in the dispersions of the different plasmon modes. This observation calls for closer inspection, and is one of the main topics of the following chapter.

Chapter 7

Plasmon Interactions and Control

With a greater knowledge into the properties and energetics of the Bragg and Mie plasmons, further studies can be conducted. This chapter shows how the different plasmons interact with one another on different regions of the samples. Both mode mixing and anticrossing is observed between the localised and delocalised states depending of sample orientation and thickness. Experiments are then performed to understand how the observed Bragg and Mie plasmon dispersions are altered when excited on different metal substrates. Finally, experiments are conducted to understand the variations in plasmon energy when the refractive index of the top dielectric layer is changed. By understanding how plasmons interact in such systems, key insights can be gained to guide the design of integrated optical-plasmon circuits, as well as gaining further insights into the complex world of nano-optics.

7.1 Plasmon Coupling and Interactions

It has been noted many times in the previous chapter that the different plasmon states are shifted from their expected energies due to their interaction with neighbouring modes. This section explores these interactions in more detail.

It has been shown that the energy of Bragg modes can be tuned by varying the angle of incidence at a certain point on the sample; it has also been shown that the Mie plasmon energies can be controlled by varying the surface geometry. This provides ample control to bring the two types of plasmon into resonance with one another, and then observe how they interact[44]. Figure 7.1 shows data from a 500nm sample, at thicknesses from $\bar{t} = 0.9$ to 1.3.

At $\bar{t} = 0.9$, two Mie plasmons are present, corresponding to the $l = 1$ and 2 states. These states are strongly localised by the almost encapsulated geometry, fig 7.1a. At a thickness of $\bar{t} = 1.3$ the voids become completely encapsulated, stopping optical coupling

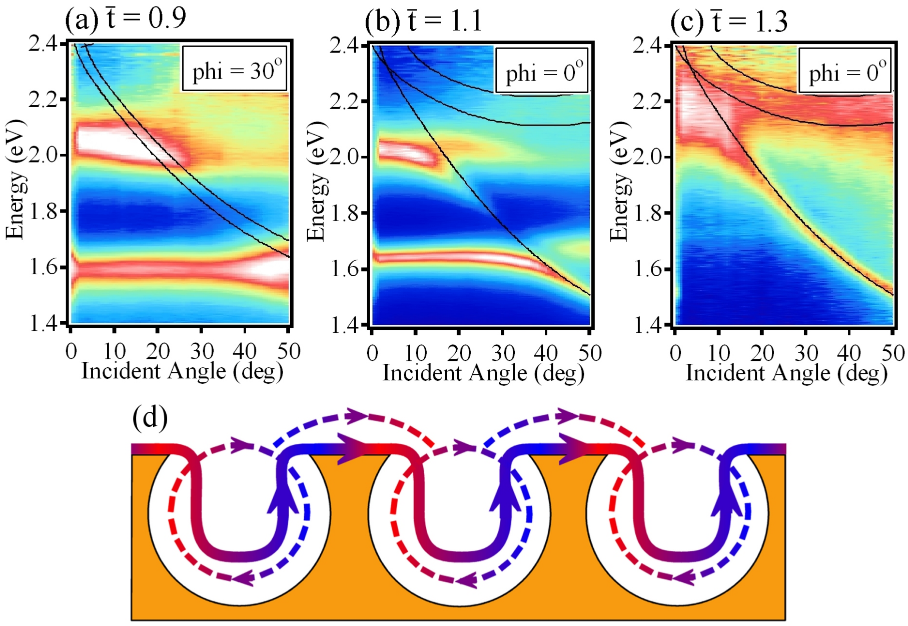

Figure 7.1: Dispersion maps of a 500nm gold sample at, (a) $\bar{t} = 0.9$, (b) $\bar{t} = 1.1$ and (c) $\bar{t} = 1.3$. (d) Schematic of two mixed modes, solid line represents Bragg plasmon dropping into voids, dashed line represents Mie modes hopping between cavities.

to the Mie modes. Now, however, the surface is not flat but possesses a close packed array of islands arising from the faster growth between the voids (as shown in figure 4.14). This geometry excites Bragg modes strongly (fig 7.1c). It can be seen that by selecting appropriate value for the sample thickness the Bragg mode will cross both Mie plasmon modes. This is shown in fig 7.1b, for a normalised thickness $\bar{t} = 1.1$. Here the surfaces form funnels leading into the voids. The Mie plasmons are now tightly confined, but still optically active and are clearly observed. Bragg modes are also strong and, away from positions where the modes cross, the two types of plasmon follow their normal dispersions. Near resonance, however, the dispersion is altered dramatically with the two modes showing strong anticrossing behaviour. This is observed most clearly when the Bragg crosses the lower, $l = 1$, mode but is also present for the upper mode. The localised modes are more strongly coupled to the incident light than the Bragg modes and so are clearer[68, 69]. This provides a means to infer that the lower energy mixed states, at resonance, are more localised in nature than the higher energy state. These modes correspond to Mie plasmons hopping between dishes via Bragg modes which drop into and out of the voids, shown schematically in figure 7.1d.

A more complex behaviour is shown in figure 7.2. This data is taken from a 600nm sample between thicknesses of $\bar{t} = 0.1$ and 0.65. For a thickness of $\bar{t} = 0.1$ only Bragg modes exist, and follow the expected dispersion. When the thickness is increased to $\bar{t} = 0.2$ a Mie mode corresponding to $l = 1$ appears at 2.4eV. This has little influence on the Bragg modes below 1.9eV, however, it has a pronounced effect on the modes above this energy. Here, the localised state can be observed, but the Bragg modes appear to no longer persist. Figure 7.3 shows angle maps at the energies corresponding to the dashed

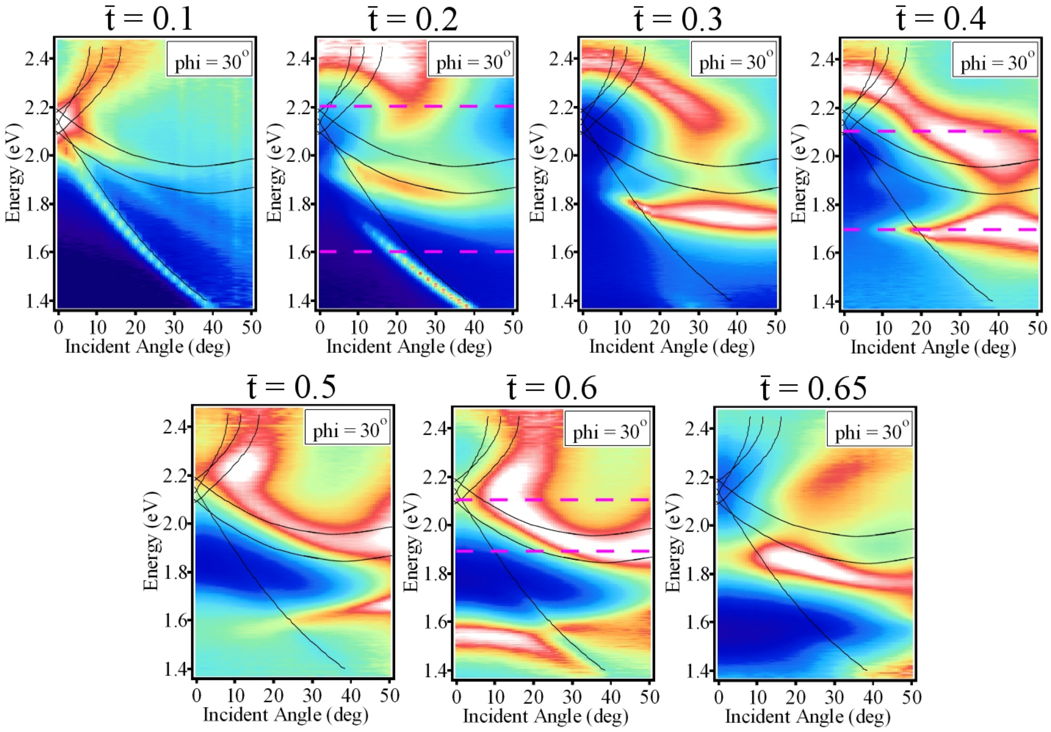

FIGURE 7.2: Film strip of dispersion maps on a 600nm gold sample for positions between $\bar{t} = 0.1$ and $\bar{t} = 0.65$. Purple lines indicate cuts shown in figure 7.3 [hotlink to video by clicking on image in electronic version]

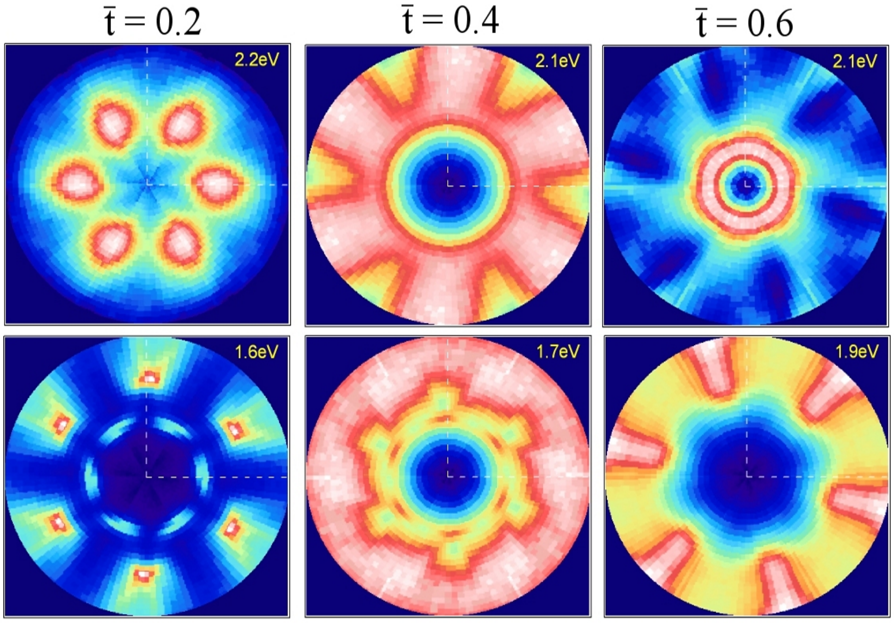

FIGURE 7.3: Angle maps through related to figure 7.2. (a) $\bar{t} = 0.2$. (b) $\bar{t} = 0.4$. (c) $\bar{t} = 0.6$. [hotlink to video by clicking on text in electronic version]

purple lines in figure 7.2. For this thickness at 1.6eV the mode is clearly delocalised, possessing a six-fold symmetry, however, the cut at 2.2eV also shows strong orientation dependence, providing evidence that the Bragg modes still exist. On closer inspection of the dispersion map, it appears that the Bragg mode has been shifted to lower energies by 0.1eV and no longer exists at normal incidence. As the thickness is increased further the Bragg modes completely lose their normal dispersion and become strongly mixed with the Mie plasmon, this also forces their energies to much lower values. At $\bar{t} = 0.4$ the flat dispersions of the bands indicate purely localised modes. If compared to the data from the isolated voids it would be expected that the $l = 1$ mode should have dropped down to an energy of 1.4eV with the $l = 2$ mode appearing near 2.2eV. The data in figure 7.2 shows only a small shift in the mixed modes energies. By analysing the angle dependence at $\bar{t} = 0.4$ it can be seen that the mixed state around 2.1eV smoothly converts from a Mie-like mode to a Bragg-like one with increasing incident angle. The lower mixed mode at 1.7eV can be seen to possess the opposite behaviour, converting from Bragg-like to Mie-like. This could well be related to positions of the un-perturbed Bragg modes (solid lines), although the mixing is so thorough at this thickness that this is uncertain. If the thickness is increased further to $\bar{t} = 0.6$, Mie modes are expected at 1.3eV and 2eV. The lower of these Mie modes has regained a pure localised nature, although interactions with the Bragg plasmons cause an increase in mode energy to 1.65eV (0.35eV higher in energy than expected). Anticrossing behaviour with a, now almost pure, Bragg mode is also clearly observed. The higher energy mixed mode also appears to be mainly Bragg-like in character, with little evidence of the $l = 2$ Mie mode. Again, the mode ceases to exist at normal incidence. An angle map of this mode shows the dispersion to be delocalised in nature except near 2.1eV where the mode appears to localise. This type of behaviour has been observed for a number of samples and it is proposed to arise from an antisymmetric combination of two dipolar Bragg and Mie modes. This resultant quadrupole plasmonic state can no longer interact with the incident optical field and hence no longer appears in the data. At the thickest part of the sample, $\bar{t} = 0.65$, the interaction of the $l = 2$ mode and the Bragg modes now becomes the dominant mixed state and shares many similarities with the mixed states described above.

From this data a number of conclusions can be drawn. Firstly, the interaction between the Mie and Bragg plasmons is extremely strong, with both types of plasmon often perturbed in energy by up to 0.5eV. This makes the task of understanding the properties of the separate states a more complicated task, and why, in the previous section, all small shifts in energy from expected values were ignored. When a single Bragg mode interacts with a Mie mode a simple anticrossing can often be expected, however, when several Bragg modes are of a similar energy the mode distributions change dramatically. These interactions cannot be fully modelled at present, although progress is underway. The second conclusion that can be drawn from the data is that the mode mixing allows the Bragg modes to propagate on a surface so highly structured it would seem unlikely a delocalised mode could exist. The converse could also be true with the Bragg modes aiding the existence of a localised mode when the geometry is close to that of a smooth surface, although Mie modes on near smooth surfaces are observed on the sample of isolated voids.

Since it has been postulated that the coupling between Bragg and Mie modes depends on their in-plane momentum, this can be tested by observing the mode characteristics at different incident angles and sample orientations. Figure 7.4 shows position maps of the sample at normal incidence and then at $\theta = 30^o$ with orientations of $\phi = 0^o$ and 30^o.

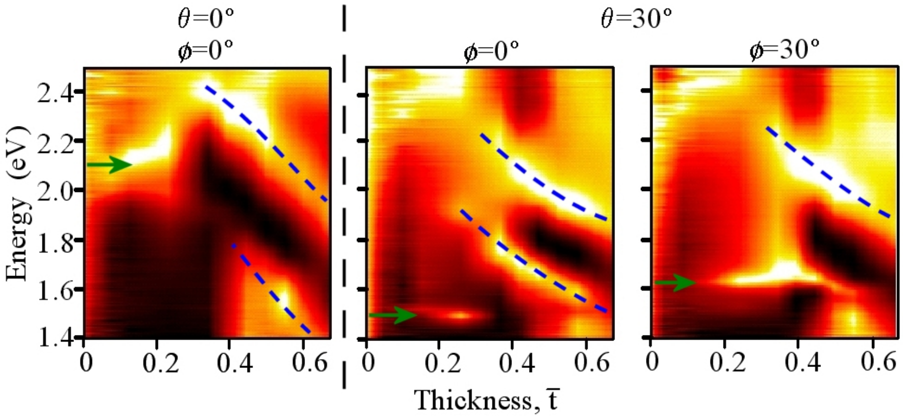

FIGURE 7.4: Position maps for a gold 600nm sample for different incident angles and sample orientations, as shown. Green arrows show energies of Bragg plasmon modes, blue dashed lines show Mie plasmon modes.

For the thinnest region of the sample ($\bar{t} < 0.3$) only pure Bragg modes exist (indicated with green arrows). At normal incidence this is a state at 2.1eV. At $\theta = 30^o$ the modes are split and only one of the six Bragg modes is clearly observable for each of the orientation (1.5eV at $\phi = 0^o$ and 1.6eV at $\phi = 30^o$). The normal incidence data has been presented previously where it was noted that the lower Mie mode can only be observed for $\bar{t} > 0.4$, with the upper mode also being shown to be slightly perturbed from the expected position. These alterations in the Mie mode energy and strength can now be pinned to mixing with the Bragg modes. For an incident angle of 30^o the upper Mie modes are no longer near any Bragg resonances and regain their expected profile. The lower mode has now been brought into resonance with the Bragg mode and shows markedly different properties depending on the sample orientation.

This data allows an understanding of the mixing process to be built up. When considering the $\theta = 30^o$ data, there are two clear types of plasmon interaction depending on the sample orientation. This can be understood through the simplified model for the plasmons under these conditions, depicted in figure 7.5

In the data the Mie plasmon corresponds to the $l = 1$ dipole state. For this model it will be assumed that the Mie plasmons oscillate purely in the plane of the surface, as depicted in figure 7.5. Experimentally, with the exception of normal incidence, the resolved field of the Mie plasmons across the cavity will not be symmetric; however, the same conclusions can be drawn. The Bragg plasmons will be excited in the direction of

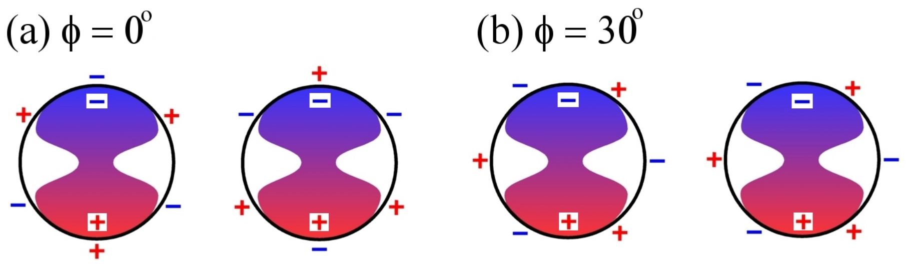

FIGURE 7.5: Schematic of the field distributions of the Mie and Bragg plasmons as seen from above a void of (a) $\phi = 0^o$ and (b) $\phi = 30^o$. Mie plasmon field represented by colour, Bragg plasmon field by markers.

the grating and, for this model, will be assumed to be dipolar in nature, a reasonable assumption for the structures studied. For the lower plasmon branch, shown in the data, the Bragg plasmon modes are primarily located on the metals surface, not over the voids.

Under all sample orientations six Bragg plasmons will be excited, corresponding to three sets of dipoles equally spaced around the cavity. Concentrating on a line in the plane of the Mie plasmon dipole (up the page for figure 7.5) at $\phi = 0^o$ the electric fields of both the Bragg and the Mie plasmons oscillate along the same plane. Under these conditions and at one point in time there are two possible distributions of the Bragg dipole moments, as shown. Each distribution will have a different energy corresponding to the different sum of the dipoles, and so there will be a splitting into two energy states. For $\phi = 30^o$, there is only one possible field distribution, and so no such splitting will be observed. These conclusions are exactly those observed in the data.

If the upper Bragg plasmon branch is considered then delocalised plasmon modes will be concentrated within the voids. This will lead to a stronger mixing between Bragg and Mie modes due to the greater field overlap. This is often observed in the data, although due to the correlation between Mie mode and Bragg energies only the interaction between the upper Bragg branch and the $l = 2$ Mie mode can be observed, which does not lead to the same mixing with sample orientation.

7.1.1 More Plasmons Interactions

This thesis has introduced the presence of both Bragg and Mie plasmons as well as mixed modes on the nano-structures surfaces. Whilst a full theory accounting for all the observed modes cannot be expressed, all of the data can be understood through a number of simple models. However, when the observed energy range is increased to include the infra red and larger incident angles are also recorded, some further phenomena appear. Figure 7.6 shows the position maps of a gold sample with a void diameter of 600nm for a range of incident angles. This is one of the samples already studied in this thesis, and shows the expected Bragg and Mie modes.

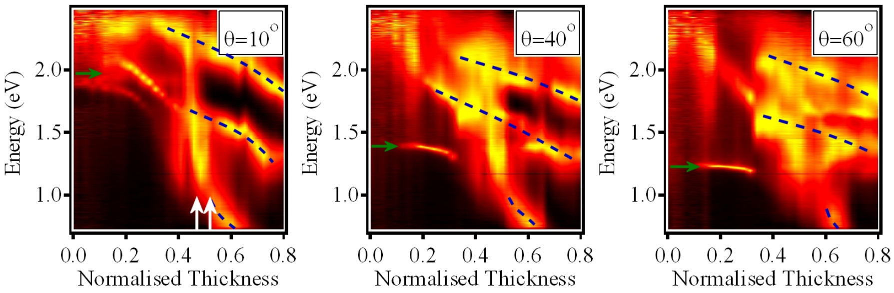

FIGURE 7.6: Position maps of a gold sample, diameter = 600nm. Green arrows show energies of Bragg plasmon modes, blue dashed lines show Mie plasmon modes. White arrows show thicknesses used in the dispersion maps in figure 7.7. [hotlink to video by clicking on image in electronic version]

It is interesting to now look at $\bar{t} = 0.5$, and see that between the energies of 1eV and 1.5eV there appears to be a broad region of absorption. This feature appears to couple to the Mie plasmons and is disrupted by the presence of Bragg plasmons as well. The presence of this mode cannot be understood through any of the models so far considered, and appears on all sample studied to date. To gain further insight into these plasmon modes figure 7.7 plots the dispersion at $\bar{t} = 0.5$ and 0.55.

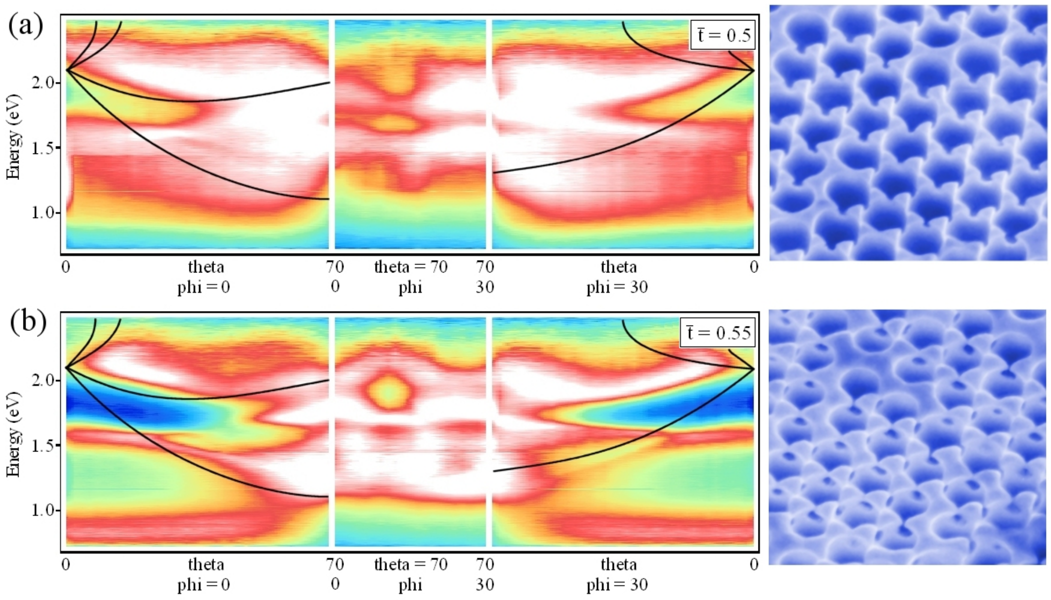

FIGURE 7.7: Dispersion maps taken from the thicknesses shown in figure 7.6. SEM images of the surface at each thickness also shown. [hotlink to video by clicking on image in electronic version]

At $\bar{t} = 0.5$ the broad absorption occurring between 1eV and 1.5eV can be seen. As the incident angle increases above $\theta = 50^o$ this feature links with the Mie mode at 2.3eV to form a mode which absorbs light across the visible spectrum. These modes are found to be completely localised over the whole energy range and absorb more than 90% of the incident light. When the thickness is increased to $\bar{t} = 0.55$ the three pure Mie modes are recovered ($l = 0$, 1 and 2). However, above $\theta = 60^o$ strong absorption across the whole energy range is again observed. These modes are localised, although at 1.5eV some mixing with a Bragg plasmon is observed.

This data is now becoming increasingly complicated and hard to interpret; however, some speculations on the origins of these features can be made. Figure 7.7 also shows SEM images of the surface. These images again show the true complexity of the surface. At $\bar{t}$ = 0.5 there are triangular islands in-between the voids that have tip sharper than 50nm. At the thickness is increased, these connect to form bowtie shapes. These shapes have been shown to support localised plasmons and at the point where the tips of the triangle touch the electric field can be enhanced by more that 10^3[100]. At these thicknesses there is also the formation of the windows between the voids. These structures might also be expected to support localised plasmon modes. It is also of note that the lowest observed Mie mode is the $l = 0$ state. This state has no equivalent mode on a spherical particle but mathematically can exist for a void. The electric field profile is a single, spherically symmetric, intensity maximum. This mode, may therefore not be sustainable below $\bar{t} = 0.5$, and there is current uncertainty about its true energetics.

There are, therefore, quite a number of possible sources to account for the absorption features observed. Each represents a real challenge to model thoroughly, and interactions between all the different plasmons will make the situation even more complicated. Progress is being made on full solutions to these geometries, although a complete understanding it still a way off. Therefore, attention will now be tuned to looking at how the different plasmon are effected by the used of substrates made from different metals.

7.2 Response to Different Metals

Throughout this thesis, all samples considered have been made from gold. This is because gold electro-deposits well and is very stable, allowing measurements to be performed over several years (and beyond). However, the electro-deposition technique is extremely versatile and the chemists working on this collaborative project have also deposited materials such as silver, platinum and nickel, which will be discussed in this section, as well as palladium and copper, of which the results are too preliminary to be included in this thesis.

7.2.1 Silver

Whilst the general appearance of the silver samples is similar to those made of gold, there are some important differences. Firstly, silver can be considered to be a perfect metal in the visible spectral region, making the plasmon modes on silver surfaces stronger due to the reduced absorption. Secondly the deposition technique, as shown previously, does not yet work above $\bar{t} = 0.5$, and below this thickness the samples also have a higher intrinsic roughness.

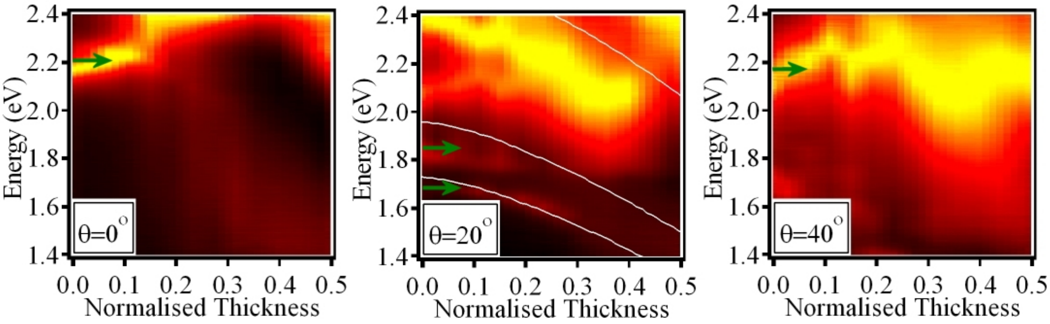

FIGURE 7.8: Position maps for a 600nm silver sample, $\phi = 0^o$, incident angle as shown. Expected Bragg plasmon behaviour plotted on middle image (white). Green arrows show energies of Bragg plasmon modes. [hotlink to video by clicking on image in electronic version]

Figure 7.8 shows three position maps for a silver sample with a void diameter of 600nm at several incident angles. Bragg plasmon modes are clearly evident and fit well with theoretical calculations (see chapter 6), plotted for $\theta = 20^o$. Weak Mie modes are also visible, especially at normal incidence, which also fit well with those expected from the insight gained from gold samples. While the Bragg and Mie plasmon modes appear similar for both gold and silver the interactions between them are somewhat different. An example of this is shown in figures 7.9 and 7.10.

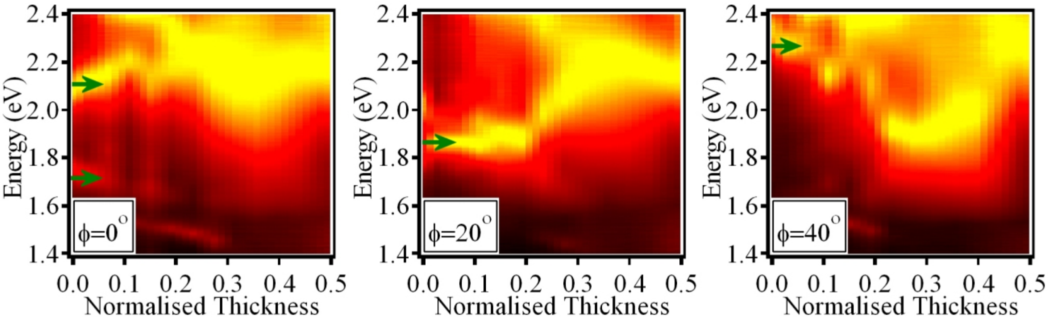

FIGURE 7.9: Position maps for a 600nm silver sample at an incident angle of 30^o, sample orientations as shown. Green arrows show energies of Bragg plasmon modes. [hotlink to video by clicking on image in electronic version]

Figure 7.9 shows a film strip of position maps for an incident angle of 30^o whilst varying the sample orientation. This image can be compared to figure 7.4 for a 600nm gold sample. The striking difference with the silver sample is how dependent on orientation the features are. There also appears to be a lack of clearly observable Mie modes in the data. Under closer inspection, it is found that only the modes at the far left of the images are pure Bragg plasmons, for all other thicknesses there is a mixing with Mie modes leading to a broadening of the resonance and a more complex dispersion. Whilst mixing occurs, the Bragg plasmons seem always dominant, and show little localisation,

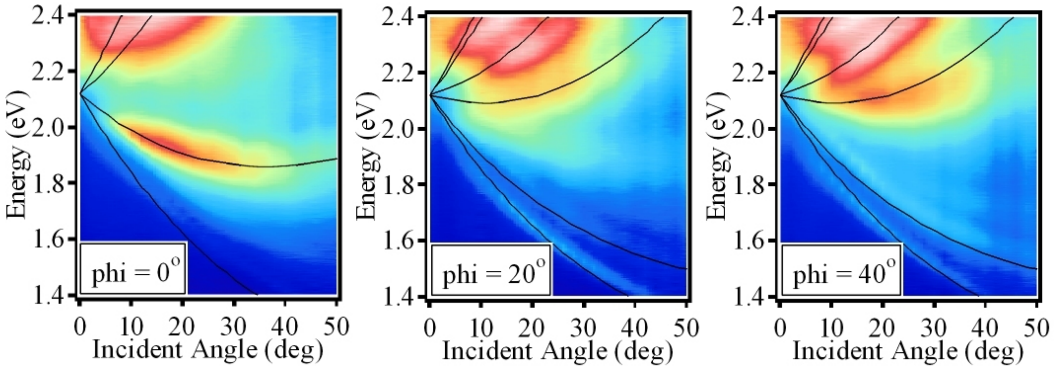

FIGURE 7.10: Dispersion plot of a 600nm silver sample at $\bar{t} = 0.2$ for different sample orientations, as shown. [hotlink to video by clicking on image in electronic version]

this is illustrated in figure 7.10. The dispersion plots show the Bragg plasmon modes are far more absorbing at these energies, but also drag these mixed states with them as they shift in energy. As with the gold samples, there is little absorption at normal incidence indicating the formation of an optically inactive quadrupole mode. When no Bragg plasmons are near the Mie plasmon energies the absorption is weak (this effect is clearest in the linked video). These effects can be understood if the Bragg plasmons interact more strongly with the incident light than the Mie plasmons. Indeed, over all silver samples analysed the Bragg plasmon modes appear sharp and highly absorptive, while Mie modes often seem weak or absent. Unfortunately the plasmon dynamics above half height, while showing some interesting features, cannot be used in analysis due to the random and erratic growth - this is an issue of current concern and is being addressed. One possible reason for the weakness of the Mie plasmons is the increased roughness of the silver samples over ones made from gold. This roughness will cause hot-spots of electric field and could be sufficient to disrupt the Mie field distributions, causing a loss to the strength of the mode. Bragg plasmons are delocalised, and so may only interact weakly with these hot-spots, and hence not be perturbed in the same way.

By measuring the normal incident energy of the Bragg plasmons for silver samples of different void sizes the effective dispersion with respect to sample pitch can be calculated, shown in figure 7.11. This can be compared to figure 6.7 for gold in the pervious chapter.

The properties of silver, in the visible spectrum, can be seen to fit well with the Drude oscillator model, as predicted. The effective experimental plasmon dispersion with sample pitch also fits very well with these curves. This is different to the gold samples, where the energy was measured to be consistently lower than would be expected theoretically (see figure 6.7). The reason for this discrepancy was accounted for by an increase in effective pitch due to imperfections in the template formation. The 600nm diameter silver sample used in the experiment shown in figure 7.11 was of exceptional quality. This could account for lack of increase in the effective pitch. Unfortunately, the sample is not available to test this, and so further experimental verification is required.

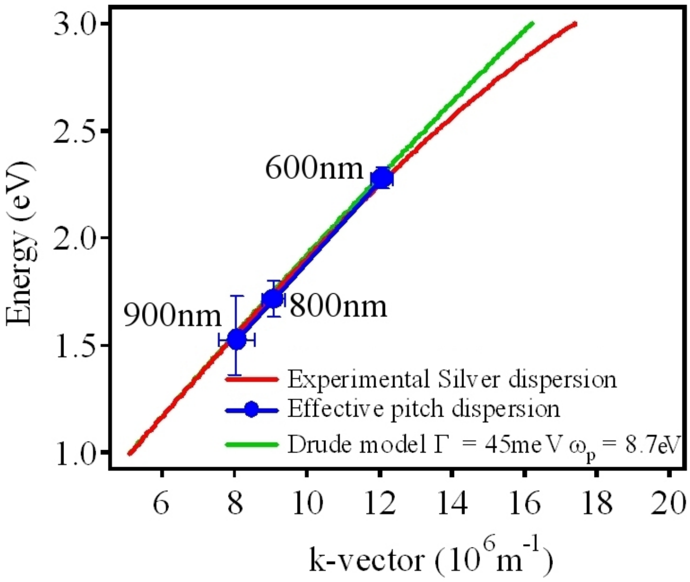

FIGURE 7.11: Extracted energy of normal incidence SPP modes on silver as a function k-vector calculated using sample pitches of 900nm, 800nm and 600nm.

7.2.2 Platinum

So far only one platinum sample has been closely studied. This sample has a void diameter of 700nm and is well ordered, smooth, and suffers from none of the problems associated with the growth of silver. This allows thicknesses up to $\bar{t} = 1$ to be grown and studied. Platinum can support weak surface plasmons that have a dispersion very similar to that of light. Figures 7.12 shows a set of dispersion plots at a thickness of $\bar{t}$ = 0.1.

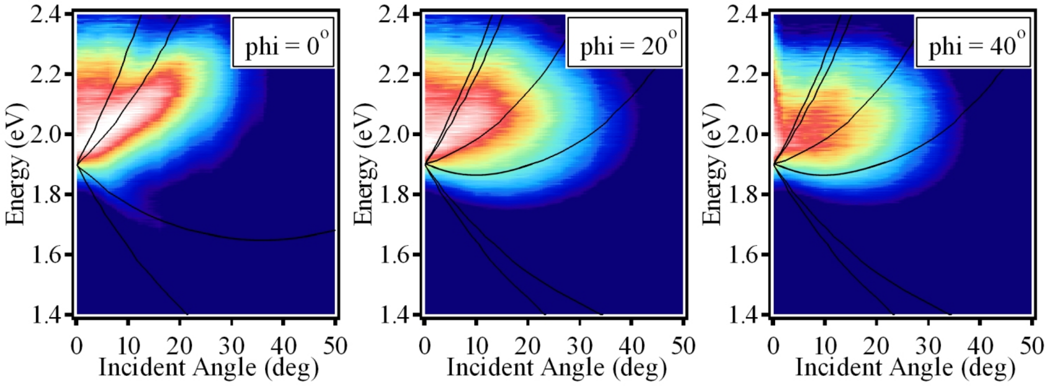

FIGURE 7.12: Dispersion maps for a platinum sample at $\bar{t}$ = 0.1, void diameter = 700nm. [hotlink to video by clicking on image in electronic version]

The dispersion for the platinum appears somewhat different to those of silver and gold. Whilst there appears to be some delocalised features, they are hard to resolve and the mode profile appears more Mie-like than Bragg-like; it is only when the angle plots are viewed that clear delocalised behaviour is seen, figure 7.13.

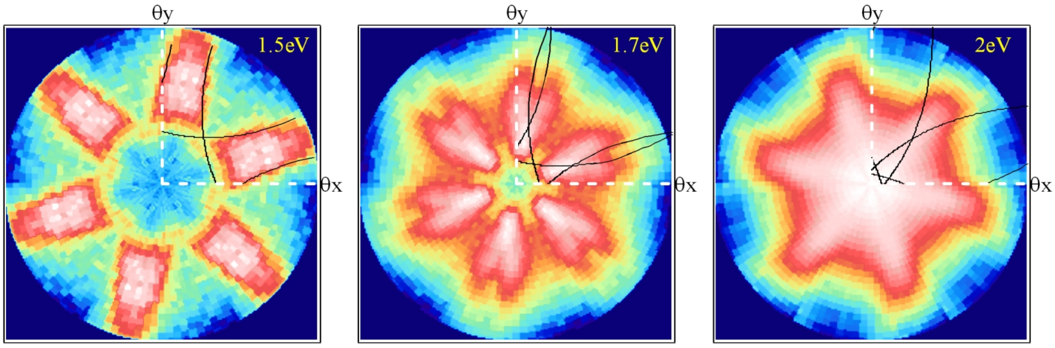

Figure 7.13: Angle map taking cuts through figure 7.12, as shown. [hotlink to video by clicking on image in electronic version]

These features could be diffractive or plasmonic; however, the amount of absorption along with the observed interactions with Mie plasmons leads to the conclusion that the modes are surface plasmonic in nature. The plasmon mixing appears strong, with the Mie plasmons dominating much of the plasmon dispersion. This mixing is probably responsible for the weakness of the Bragg modes away from Mie mode at around 2eV. The Mie mode behaviour is also quite complex on this sample as shown in figure 7.14.

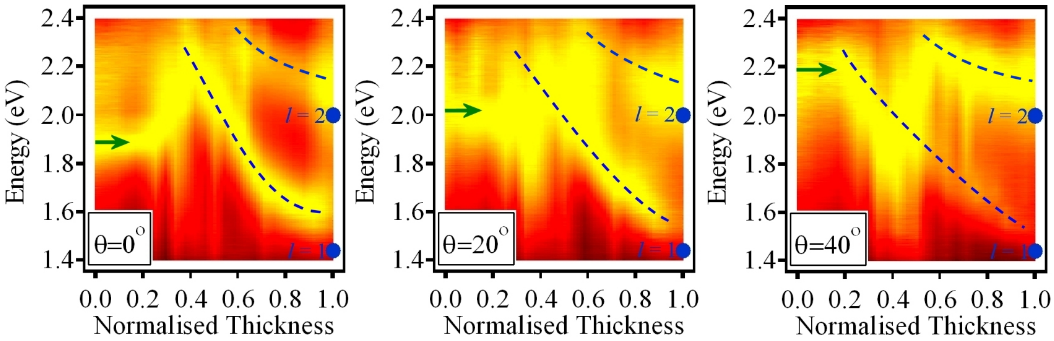

Figure 7.14: Position map of the platinum sample, void diameter = 700nm, $\phi = 0^o$ Calculated Mie modes also shown. Green arrows show energies of Bragg plasmon modes, blue dashed lines show Mie plasmon modes. [hotlink to video by clicking on image in electronic version]

Strong Mie modes are clearly observed in the data, and at low incident angles their energies tend to those predicted by theory. However, above $\theta = 25^o$ the lower Mie mode starts to strongly interact with the one at higher energy. By $\theta = 50^o$ the lower Mie mode has all but disappeared. Analysis shows that the interaction between the modes is dependent on orientation, indicating the process is mediated by Bragg plasmons. SEM studies of the surface have found that the platinum is very smooth and that the domain ordering is of exceptional quality. These two factors will lead to a strengthening of the Bragg modes and subsequently strong mixing. The voids also appear to encapsulate more easily than those made from gold. This is why the Mie modes tend directly to the calculated energies. Why, however, the interactions are so different from anything seen before is still of great interest and requires further studies.

7.2.3 Nickel

The final single metal samples to be analysed are those of nickel. Nickel has only a very weak plasmon mode, due to strong interband absorption, so should not strongly exhibit Bragg or Mie plasmons. The nickel samples have been found to plate well and are smooth. Two position maps for a 600nm void size sample are shown in figure 7.15.

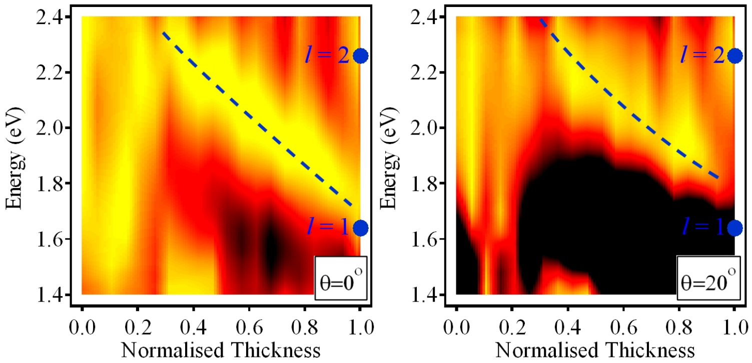

FIGURE 7.15: Position map of a nickel sample, void diameter = 600nm, ϕ = 0^o. Calculated Mie modes also shown. Blue dashed lines show Mie plasmon modes. [hotlink to video by clicking on image in electronic version]

At no point on the sample were any delocalised modes observed and the data is less well resolved due to a higher overall absorption from the nickel. Mie modes are again clearly visible and do not appear to shift significantly with changing incident angle. As with the other metals the Mie modes appear to tend to the exact spherical void solutions at $\bar{t} = 1$. In this case, the Mie modes must be almost purely optical and only weakly couple to the electrons inside the metal. Some links can again be made the ray-clipping prediction, in particular the reduced intensity below 1.8eV at $\theta = 20^o$, however, the presence of only one strong Mie mode makes this hard to verify.

7.2.4 Multilayer Metal Structures

Several combined multilayer metal samples have so far been produced. Whilst the proof of production has been shown the sample quality is, in some cases, not as good as the single metal samples.

Figure 7.16 shows a position map of 600nm void diameter sample produced using the double deposition technique outlined in chapter 4. This produces a graded thickness gold sample with the final 100nm made from nickel.

Strong Mie and Bragg modes are both observed for this sample. A strong Mie mode is expected, however, appears not to tend to the expected Mie solution at $\bar{t} = 1$. This can be understood if the mode is limited to the gold part of the sample. This means at a sample thickness of $\bar{t} = 1$, the plasmon only observes a thickness of $\bar{t} = 0.8$. This is

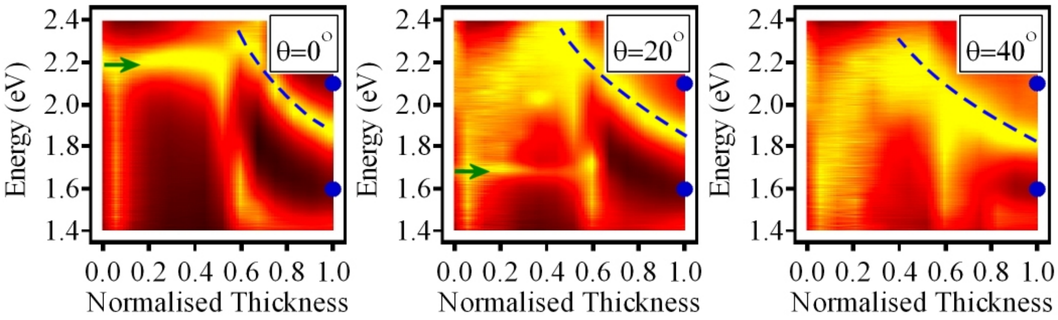

FIGURE 7.16: Position maps of a 600nm void diameter double deposited sample made from graded gold topped with nickel. $\phi = 0^o$ in all cases, incident angle as shown. Green arrows show energies of Bragg plasmon modes, blue dashed lines show Mie plasmon modes.

consistent with the Mie scattered solutions. Interestingly, the data shows a strong Bragg plasmon, not expected for this sample. This plasmon could arise for a number of reasons. Firstly, whilst the surface is covered in nickel, the voids are made from gold. This means a Bragg plasmon with an electric field primarily concentrated within the dishes might be uninfluenced by the nickel. Secondly, the nickel surface appears quite rough, and so it is possible that some gold may still be present on the surface. There is also the possibility that the nickel could be thin enough to 'borrow' the plasmon activity from the gold, a process sometimes observed in SERS experiments[101]. However, neither of these possibilities seem to correlate with the Mie plasmon data, which appears to find the nickel layer completely plasmon inactive.

The second double deposited sample is the inverse of the first, a graded 600nm void diameter nickel sample with the top 100nm made from gold. A set of positions maps for this sample are shown in figure 7.17.

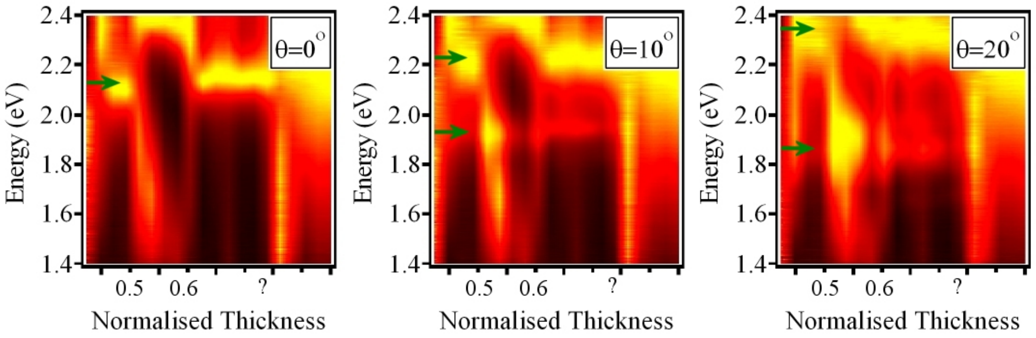

FIGURE 7.17: Position maps of a 600nm void diameter double deposited sample made from graded nickel topped with gold. $\phi = 0^o$ in all cases, incident angle as shown. Green arrows show energies of Bragg plasmon modes.

SEM analysis of this sample has shown that the deposition procedure has not worked as well as for the first sample. This is because the nickel oxidises quickly, preventing the smooth deposition of the top gold layer. However, some information can be gained from this sample. Whilst the surface geometry is hard to define, it still possesses an ordered domain of features, and these can excite Bragg modes on the surface. This is to be expected as the top surface is gold. Mie modes would only be expected to be weak. However, due to the poor surface structuring, it is hard to conclude on their presence.

Whilst preliminary, the results from the two multilayer samples show some interesting results. It is hoped that by improving the plating technique, and producing a number of samples of varying void size, the properties of these systems will be much better understood. Also of interest is the production of samples made from three metal layers. This could make a nickel sample with a thin gold ring at half height, and allow greater control over the positioning of plasmons within the three-dimensional geometry. This work is to be continued after the completion of this thesis.

7.3 Tuning Plasmons with Refractive Index

Active alteration of the plasmon energies on these nano-structured surfaces would allow a fantastic level of control for possible future applications. In this section the response of the plasmon is studied as the refractive index of the dielectric top layer is varied. It has been shown that Bragg modes are highly sensitive to slight variations in refractive index, and this effect has been used to form molecular sensors[73]. In the work in this thesis, the emphasis still lies on understanding the properties of the plasmons in the nano-structures, although interesting information can be found about the wetting of the surfaces.

Two techniques have been employed to study the effect of changing the refractive index of the dielectric material. One uses a polarised microscope to study the plasmon modes near normal incidence, when different refractive index fluids are placed on the surface. The other uses the automatic goniometer to study the full angle dependence of the plasmon modes in the presence of both air and water. In both cases a small fluid cell is created by using a glass cover slip, raised by around 200μm from the gold surface and fixed in place with double sided sticky tape.

Figure 7.18 shows dispersion plots for a 600nm sample at $\bar{t} = 0.1$ in air and water. In both sets of data the glass cover slip is present to allow direct comparisons between the data. The theoretical dispersions are also marked on the images and can be seen to fit very well with the data. To incorporate the layer of water into the model a value of $\epsilon_d = 1.77$ (n = 1.33) is used in the effective dielectric constant formula, restated in equation 7.1. This dielectric constant is suitable over the range of energies considered[102].

$$\hat{k} = \frac{\omega}{c}\sqrt{\frac{\hat{\epsilon}_m \epsilon_d}{\hat{\epsilon}_m + \epsilon_d}} \tag{7.1}$$

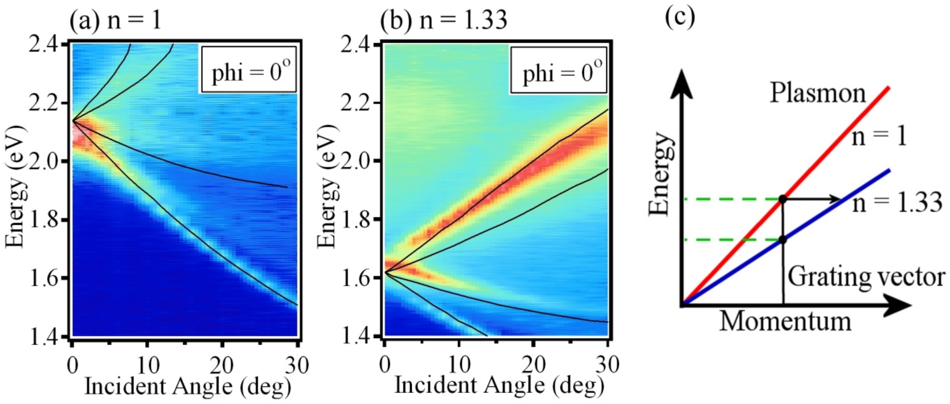

FIGURE 7.18: Dispersion maps for a 600nm gold sample in (a) air and (b) water. (c) Schematic showing change in dispersion relation with increasing refractive index of dielectric layer.

The change in plasmon energy for different refractive indices can be understood by considering the momentum conservation of the optical field. If light starts in free-space then passes into the fluid cell the in-plane component of its momentum will increase, as shown in figure 7.18c. The crossing point between the grating vector and the plasmon dispersion provides the solution to the observed mode. Since the periodicity of the structure remains constant, the solution for light in water will be of a lower frequency than in air. For diffractive effects a shift exactly equal to the refractive index is expected. For surface plasmons the shift will be slightly smaller due to the effective dielectric constant dependence on the refractive indices of both media (equation 7.1). The data fits well with that of a shifted Bragg plasmon mode, as would be expected. To further test the wetting of the surface, potassium chloride was added to the water. Potassium chloride molecules have a smaller attractive force between then than water molecules. This means that a solution of pure potassium chloride has a lower contact angle than water. Adding potassium chloride to the water creates a mixture and so an average contact angle. This reduced contact angle ensures the dishes fully wet. No variation in the dispersion was observed, indicating that the thin samples wet completely. This is in agreement with the experiments studying the contact angle of liquid on the surface.

Further investigations were conducted using a polarised microscope and index matching fluids of refractive indices of n = 1.3 and 1.5. There is some degree of uncertainty in the wettability of the surface, and for this reason the refractive index fluids were heated to 60^{o}C within the cell for twenty minutes while mild pressure was applied, this ensures that the voids would be filled with the fluid for all the sample geometries. Reflection spectra were obtained at 10 times magnification for a similar sample to the one used in the previous experiments (void diameter = 600nm), this data is shown in figure 7.19.

Here the y-axis shows energy multiplied by the effective refractive index. This is used to normalise out the effect of the different index fluids. The size of the marker at each point corresponds to the amount of absorption, while the colours show the data from the

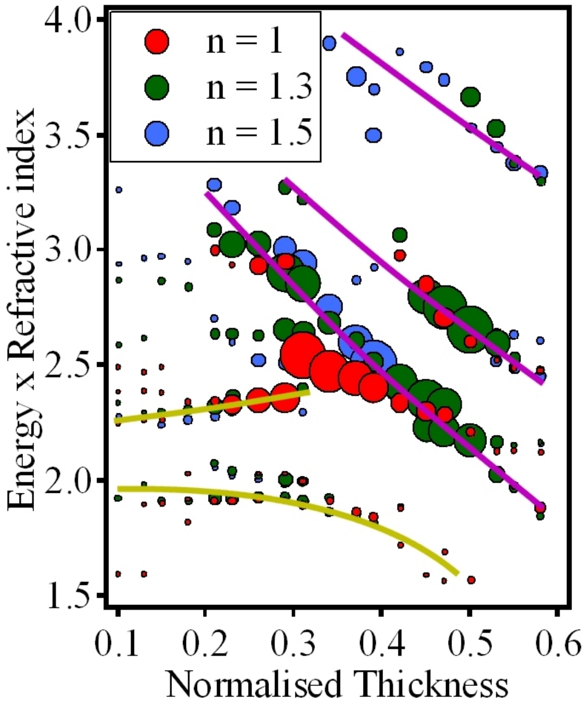

FIGURE 7.19: Position map of extracted absorption features from a 600nm sample. Energy is normalised to effective Bragg plasmon refractive index for accurate reconstruction of original mode profile. Gold and purple lines show guide to eye for Bragg and Mie modes respectively.

different fluids. Since the liquids have been heated and pressurised, wetting is expected over the whole sample. For shallow regions of the sample two clear modes are observed, indicated with the gold lines. These correspond to Bragg modes with the splitting caused by the numerical aperture of the objective providing a maximum illumination angle of 8^o. Again, when the data is scaled by the effective refractive index the initial energies are recovered with a high degree of correlation. Also clear in figure 7.19 is that the Mie plasmon modes also scale well with refractive index (the guide to eye shown in purple). This can be understood by considering the increase in wavelength with refractive index. If, for simplicity, the plasmon standing-wave model is considered, then this increased wavelength will lead to interference occurring at longer wavelengths. Again, a pure optical mode will scale with exactly the value of the refractive index, while a plasmon mode will scale with the effective refractive index. The best fitting for the data is when the effective refractive index is used (as shown in figure 7.19), providing further evidence that the observed modes are plasmonic in nature. Using the refractive index fluid it is also possible to reach higher energy modes which are both ordinarily out of the range of the spectrometer and deep within the surface plasmon absorption band. The top Mie mode in figure 7.19 corresponds to the $l = 3$ state and its extrapolated value at full ball height corresponds well to the theoretical value of 3.1eV.

Further analysis has been conducted by performing full angle and position scans for the sample in air and water. Figure 7.18 shows the combinations of normal incident position scans performed in both media.

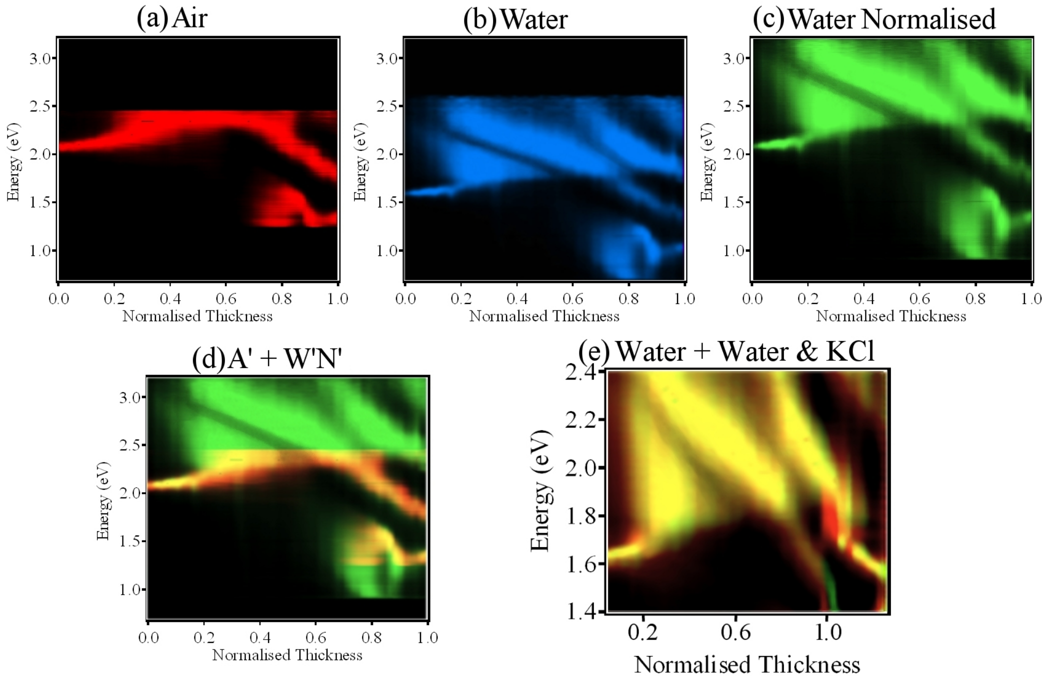

Figure 7.20: Position maps for a 600nm gold sample in (a) air, (b) water and (c) water with the energy normalised by the refractive index. (d) Data from (a) and (c) overlaid. (e) Position map showing overlaid data from the cell filled with water (red) and water with added potassium chloride (green). Maximum colour intensity shows maximum absorption.

Red data represents experiments performed in air with the cover slip in place, blue data the addition of water to the cell and green data shows the water data normalised to compensate for the refractive index (a, b and c respectively in figure 7.20). Figure 7.20d show the combination of the data taken in a air and normalised water. A good agreement between the energies of the SPP mode is shown (2eV for $\bar{t} < 0.2$), in agreement with previous experiments. It should be noted that the separation of the two Mie modes is very close to a factor of 1.3, making analysis of this data all the more tricky. However, the important change between the air and water data is the new Mie mode observed at 2.5eV for $\bar{t} = 0.1$ and dropping to 2.0eV for $\bar{t} = 0.6$. Good correlations between air and the normalised water data can be observed for this mode, implying that the cavities have filled with fluid. This is not a certainty considering the work on contact angle performed in chapter 4. Here, it was found that the contact angle rose to a maximum of 140^o around half height, making the surface strongly hydrophobic. To try to resolve this issue potassium chloride was added to a water solution to reduce the contact angle and promote wetting. No change was observed in the position map, figure 7.20e, so it must be concluded that the dishes were already filled.

This filling may arise for a number of reasons. The fluid cell is filled from one end and, while the contact angle of the sample may be large, the smooth gold surrounding it allows wetting. This must lead to a sharp change in contact angle as the water reaches the sample, and potentially the surrounding gold forces a wetting of the voids. The water is also tightly confined within the cell, this will add pressure to the liquid, perhaps sufficient to force wetting. While this provides a consistent argument, further complexities are found for $\bar{t} > 1$. Shown in figure 7.20e, a clear step in the Mie mode energy is observed, along with a sharpening of the resonance, around $\bar{t} = 1$.

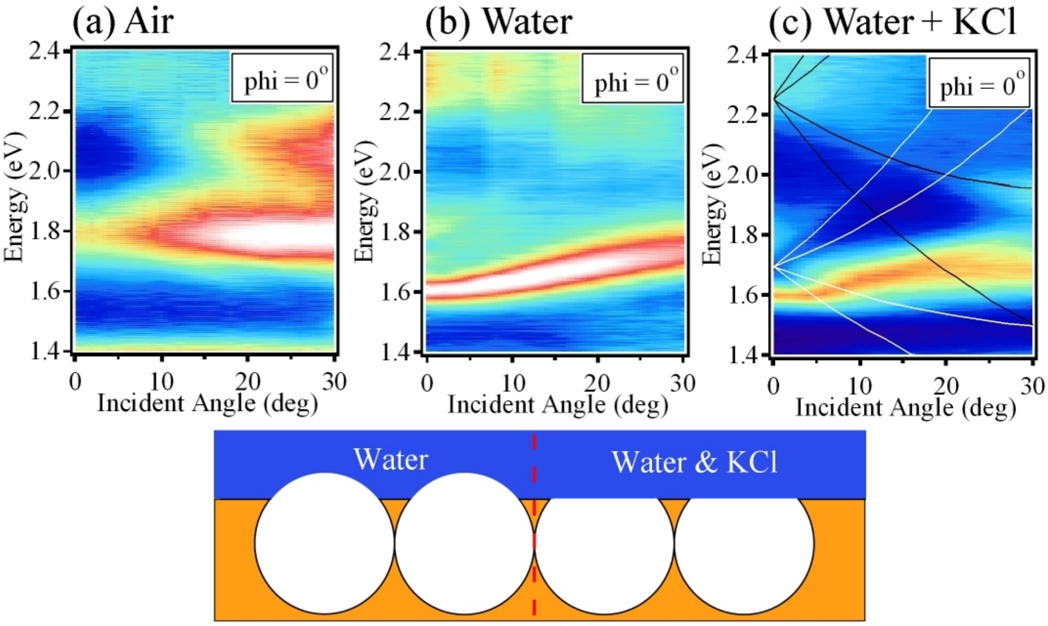

FIGURE 7.21: Dispersion plots at $\bar{t} = 0.75$ in (a) air, (b) water and (c) water with potassium chloride, white and black line corresponds to Bragg plasmon dispersions in water and air respectively . Below shows a sketch of possible surface wetting.

To study these features further figure 7.21 shows the mode dispersion. For this geometry it is believed that wetting does not occur (for water or water with KCl), due to the narrow pore mouth. When pure water is used, the contact angle forms a bubble above the cavity, in effect forming a spherical air cavity. This has the effect of reducing the energy of the Mie plasmon resonance because the better cavity definition reduces the mixing of higher order modes. The line width of the modes is also reduced as coupling to the plasmon mode can now occur evanescently from the water. This also explains why the mode is now optically active at normal incidence. With the addition of KCl the contact angle is reduced but no wetting of the cavity occurs. This has little effect on the geometry but slightly breaks the symmetry of the cavity, broadening the plasmon mode.

A strange feature of the dispersion plots in figure 7.21b and c is the broad delocalised modes above the Mie plasmon. Both features can be fitted to the Bragg plasmon theory, shown in black and white. One mode (drawn in white) requires the use of the dielectric constant of water, as expected. The higher energy mode (drawn in black), however, requires the use of the dielectric constant of air to fit the data. The feature is more like diffraction than a Bragg plasmon, appearing as steps rather than sharp dips. However, the energies of the features cannot be fitted to diffraction theory and the absorption is too strong, indicating a plasmonic mode. This feature, therefore, appears to be a Bragg plasmon that is concentrated in the air pockets above the cavities. This is an interesting possibility, although the modes are stronger in the water with KCl which cannot so far be explained. Work is continuing to understand these features.

7.4 Conclusions

This chapter has outlined the experiments performed to study the more advanced energetics of the plasmon modes observed on the nano-structured substrates. The observation of interactions between Bragg and Mie plasmons has provided a rich source of interesting plasmonic features. It has been shown that anticrossing is observed between the two types of plasmons, leading to mixed plasmon states. These states have very different dispersions to those of the original plasmons and depend on the sample orientation as well as the precise surface geometry.

The use of different metals has also been shown to alter the plasmonic behaviour in quite pronounced ways. These changes are due to the different plasmonic properties of the metals, and show there is still much work to be done before a full understanding of SPP is achieved. The use of multilayer metal structures could also provide the ground for some very interesting experiments by strictly controlling the plasmon active regions of different sample geometries.

The effect of the refractive index of the dielectric top layer has also been shown to strongly alter the plasmon dispersion. It has been shown that both Bragg and Mie plasmons behave in a predictable manner with changing refractive index, and the results obtained lead to some interesting conclusions about the wetting of the surfaces.

Chapter 8

Surface Enhanced Raman Scattering

Many applications require the detection of small numbers of molecules in varying environments. The difference in energy between an incident and a scattered photon corresponds to a vibrational mode of a molecule. This provides a ‘fingerprint’ of the illuminated material[103, 104, 22], and is known as Raman spectroscopy. Unlike infrared absorption or fluorescence spectroscopy, Raman can simultaneously identify many different chemicals, requires no sample preparation and can be performed in almost any environment. Unfortunately, Raman scattering has a very small cross-section, some 12-14 orders of magnitude below that of fluorescence. For this reason, Raman spectroscopy has only found limited use outside the laboratory[105]. In 1974, all this was set to change when M. Fleischman published a paper providing a method to enhance the Raman scattered light from molecules by bringing them into contact with a roughened metallic substrate[106]. Over the years this technique has become known as Surface Enhanced Raman Scattering (SERS), and enhancement factors up to 10^{14} have been reported[19]. However, until recently[107] SERS signals have been plagued by irreproducibility and not achieved the potential initially hoped for. A further frustration has been the lack of a full understanding of the processes responsible for the reported enhancement factors, again arising from the lack of reproducible data. This (we hope) will soon be very different.

8.1 The Raman Effect

The Raman effect, named after its discoverer Sir C. V. Raman is, in essence, the inelastic scattering of light off illuminated molecules. Figure 8.1 shows a schematic representation of the associated energy levels involved in this scattering process.

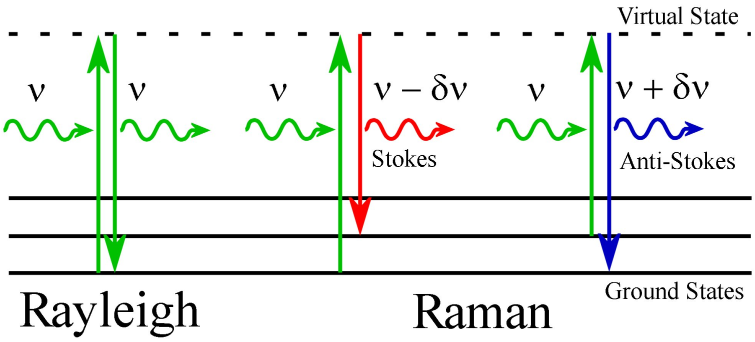

FIGURE 8.1: Energy levels involved in Rayleigh, Stokes and Anti-Stokes scattering. All transitions pass through the virtual state.

The majority of light incident on a molecule will undergo Rayleigh scattering; this is an elastic scattering mechanism where the outgoing light leaves with the same energy as the incident, but in a random direction. In Raman scattering, however, the scattered light can lose or gain energy to the molecule's internal vibrational levels, known as Stokes and Anti-Stokes transitions respectively. For all three scattering mechanisms the upper state is said to be virtual. Intuitively, Raman scattering via this virtual state can be considered as the polarisation of the molecules electron cloud, shown schematically in figure 8.2.

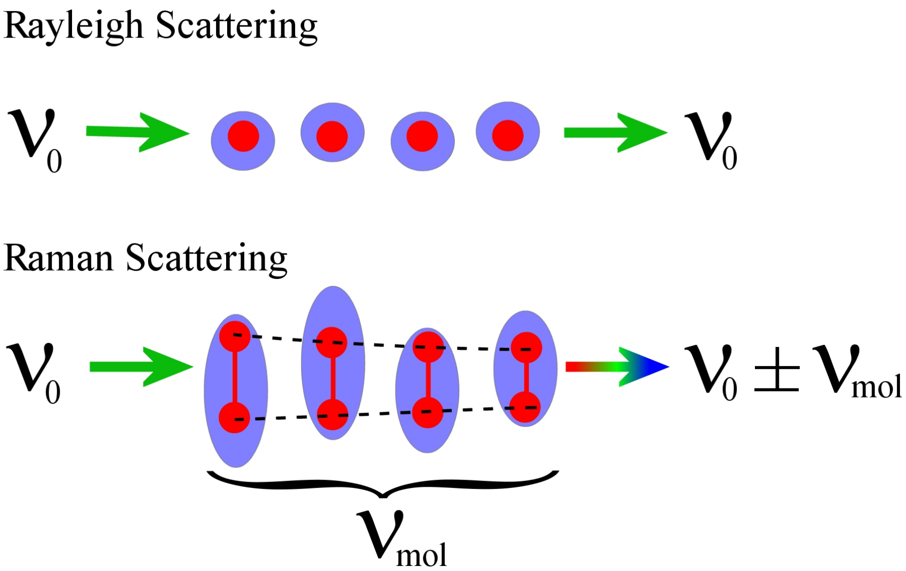

FIGURE 8.2: Polarisation models for Rayleigh and Raman scattering, showing the origins of the different scattered energies.

Upon illumination, the electric field of the incident light will force the electron cloud surrounding the molecule to oscillate. The oscillating electrons will then re-radiate an optical field that is identical to that of the incident one. In the case of figure 8.2a the electron cloud is symmetric situated around a single atom and thus the re-radiated light is equally probable in any in-plane direction and will always bee of the same frequency as the incident light, this is Rayleigh scattering.

Figure 8.2b shows the case of a simple molecule consisting of two atoms. It can be assumed that at a finite temperature the atoms will oscillate with some frequency, ν_{mol} which is small compared with the optical field. The electron cloud surrounding the molecule will oscillate at the frequency of the incident light, but the absolute shape of the cloud will vary at the frequency of the molecular vibrations (exaggerated in the figure). This oscillation in the shape of the electron cloud will subsequently alter the optical field generated. A Fourier analysis of the scattered light will now contain frequency components equal to the initial light as well as frequencies both higher and lower than the initial light. These frequencies are the Raman scattered fields. Furthermore, if the molecule is not vibrating, at any given moment in time the electron cloud will form a dipole moment across the atoms. Different atoms will feel a different field and so a different force will be applied to each atom. This is sufficient to induce a vibrational mode within the molecule and so induce Raman scattering. Clearly the probability of inducing the transition is small as the molecular field is oscillation quickly compared to the atomic motion, and so will effectively average to zero. This give some intuition into my why Raman scattering is weak.

From this relatively simple model, we can see that if the intensity of the incident field is increased, the molecule will be forced to oscillate with a larger amplitude, and hence increase the likelihood of a molecular transition.

While this intuitive model provides an explanation of the Raman effect, a full quantum mechanical treatment is required to gain quantitative answers. While this is beyond the scope of this thesis, it is worth explaining the principles behind such an understanding[108]. The treatment calculates an induced transition moment by considering the perturbation of the wavefunctions of the scattering molecule by the electric field of the incident light. This is written:

$$P_{nm} = \int \psi_m^* P \psi_n d\tau \tag{8.1}$$

where P_{nm} is the induced dipole moment, ψ_m and ψ_n are time independent wavefunctions of the states m and n. This leads to the result:

$$P_{nm} = \frac{1}{h} \sum_r \left(\frac{M_{nr} M_{rm}}{\nu_{rn} - \nu_0} + \frac{M_{nr} M_{rm}}{\nu_{rm} + \nu_0} \right) E \tag{8.2}$$

where h is Planck's constant, r corresponds to any level of the unperturbed molecule, ν_{rn} and ν_{rm} are the frequencies of the transitions given by the subscripts, M_{nr}, M_{rm} denote the transition moments and finally E is the electric field vector of the incident light. The intensity of light scattered by a given state can be written as:

$$I_{nm} \propto N_n \left(\nu_0 + \nu_{nm}\right)^4 P_{nm}^2 \tag{8.3}$$

where N_n is the number of molecules in the initial state. This equation shows the power dependence of the Raman scattering will be linearly proportional to that of the incident light and increases with the fourth power to the frequency. The term P_{nm} involves the summation of transition moments from the initial state to all other unperturbed molecular states multiplied by the sum of transition moments from all states to the final state. This sum of all possible transitions between the initial and final state can be linked to polarisation of the entire electron cloud and is the definition of the virtual state shown in figure 8.1. Practically, it is rare that all energy levels and their associated transition moments within a molecule are known, however, this approach does lead to a better understanding of Raman scattering from a fundamental viewpoint. In particular the theory helps to explain the resonant Raman effect, where Raman scattering is greatly enhanced when the frequency of the incident light is similar to that of an electronic transition within the molecule[109].

8.2 Surface Enhanced Raman Scattering

In his initial publication, M. Fleischman attributed the increase in Raman signal to the increased area of a roughened silver electrode adsorbing a larger number of molecules than expected. Although published as a curiosity, other groups quickly realised that the intensity was far too large to fit this hypothesis, and started their own research[110, 111]. Interest has continued to flourish over the past 30 years with many papers being published on both experimental and theoretical aspects of this effect.

SERS intensities are strongest from metal surfaces exhibiting some form of roughness and experiments to date have used a number of techniques to achieve this roughness. The initial experiments were performed on electrochemically roughened surfaces formed by cycling the deposition potential to continually deposit and then strip metal from a surface. After several cycles, samples become covered in sharp random features with sizes up to around 20nm. A similar approach is to evaporate or vapour deposit metal 'badly' onto a surface to form a similar rough texture. A different approach is to use a colloidal solution or deposit colloids onto a surface. This gives greater control of the particle sizes and separations, and has been favoured in much of the recent work[20, 19]. A final approach has been to employ lithographic techniques to precisely define a structure, and then deposit a smooth metal film over the top. Of all the techniques this is the only one with a high level of control, however, it has received minimal interest, mainly because it is believed SERS comes from nanometre structures, not the micron scale ones from the lithographic route. This technique is most similar to the approach being adopted for the work in this thesis, and it will be shown that large enhancements are indeed possible from such structures.

Current theories suggest SERS arises from two effects, an electromagnetic contribution and a chemical contribution. The two effects are often intimately linked and there is still a degree of uncertainty to the level of enhancement from each[112, 113]. Common belief is that the electromagnetic enhancement is by far the greater of the two; however, this uncertainty comes from a difficulty at the very heart of the SERS experiments. Because samples are random in nature it is hard to quantify where the SERS signal has come from. What is more, returning to the same point at a later stage may give a different result! With this uncertainty in results, it is hard to prove any one theory is correct, so both will be discussed separately.

8.2.1 Electromagnetic Enhancement

Arising from the increased surface electric field generated by surface plasmons, the electromagnetic enhancement mechanism is believed to be understood and fits with much of the experimental data[105, 114, 115].

As a simple approach, equation 8.3 can be rewritten in terms of the incident intensity, I, number of molecules, N and a term corresponding to the Raman cross-section, σ. To estimate the SERS to Stokes frequencies two new terms are added, expressing the enhancement factors of the electric field the laser and Raman scattered energies, $A\left(\nu_L\right)$ and $A\left(\nu_S\right)$ respectively.

$$P^{SERS}\left(\nu_s\right) = N\sigma\left|A\left(\nu_L\right)\right|^2\left|A\left(\nu_S\right)\right|^2 I\left(\nu_L\right) \tag{8.4}$$

By considering a molecule close to a metal sphere embedded within a dielectric, and using the equations from chapter 3, the enhancement can be written as the ratio of the field at the position of the molecule and the incident field.

$$A\left(\nu\right) = \frac{E_M\left(\nu\right)}{E_0\left(\nu\right)}\,\frac{\epsilon-\epsilon_0}{\epsilon+2\epsilon_0}\left(\frac{r}{r+d}\right)^3 \tag{8.5}$$

This term is maximised when $\epsilon = -2\epsilon_0$, and the imaginary part of the dielectric constant is small, corresponding to a surface plasmon resonance, as seen for colloidal particles[66, 105]. This equation can be repeated for the enhancement of the Stokes field, giving rise to an expression for the full enhancement of the system.

$$G_{em}\left(\nu_S\right) = \left|A\left(\nu_L\right)\right|^2\left|A\left(\nu_S\right)\right|^2 \approx \left|\frac{\epsilon\left(\nu_L\right)-\epsilon_0}{\epsilon\left(\nu_L\right)+2\epsilon_0}\right|^2\left|\frac{\epsilon\left(\nu_S\right)-\epsilon_0}{\epsilon\left(\nu_S\right)+2\epsilon_0}\right|^2\left(\frac{r}{r+d}\right)^{12} \tag{8.6}$$

Whilst this is a somewhat simplistic approach it provides similar results to other methods[116, 18]. The equations state that the level of enhancement should drop off quickly with distance from the surface, and should scale linearly with the incident power, both of which have been verified experimentally[112]. It can also be seen that the SERS is strongest when both excitation and scattered fields are in resonance with a surface plasmon, making it possible to understand the SERS as a five step process, as shown in figure 8.3.

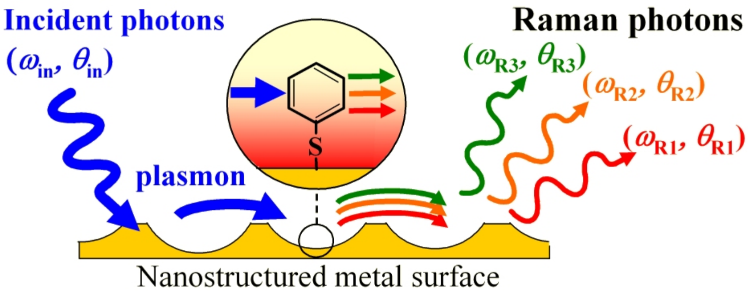

FIGURE 8.3: Schematic of the SERS process: 1. Optical field excites surface plasmon mode, 2. Surface plasmon polarises molecules on the metals surface. 3. Polarised molecules scatter surface plasmon to Stokes and Anti Stokes frequencies. 4. Surface plasmon scatters back into optical field.

Light is incident on a surface at a certain angle, θ_i, and can excite a surface plasmon. The large electric field of the plasmon will polarise molecules bound to the surface, creating large effective dipole moments within them. If a molecule now changes vibrational state then the molecular polarisation will be altered. This change in polarisation subsequently affects the emitted plasmon, leading to a new plasmon surface field. Finally the surface plasmon can couple into an outgoing Raman scattered photon. It has been shown in previous chapters that the energy of SPP modes is highly dependent on angle and so it can be postulated that different Raman scattered photons should leave the surface at different angles if enhanced via a SPP mode. This can be tested experimentally, as will be shown in the following chapter.

8.2.2 Chemical Enhancement

The electromagnetic enhancement model can be constructed to fit much of the current experimental data; however, there are a number of cases where this model simply does not work and a different approach is required. It has been observed that the molecules methane and ethane produce SERS spectra one-hundred times less intense than those of benzene, even though the ordinary Raman spectra are of equivalent intensity. It is in light of this, and a number of other experiments[113, 117], that chemical enhancement methods have been proposed. Often referred to as a first-layer effect, since it requires direct contact between molecule and the metal substrate, the chemical enhancement factor is often considered to be around one or two orders of magnitude. This enhancement factor combines with the electromagnetic enhancement by a multiplication, so while much smaller would potentially be observable experimentally. A number of sources have been postulated to be responsible for the chemical enhancement, however, experimental proof is hard to come by[118, 105].

The first, and perhaps most compelling, argument is that the chemisorption of molecules to a metal surface broadens their electronic states as well as forming a new electronic state, allowing a resonant Raman process to occur, this is schematically shown in figure 8.4.

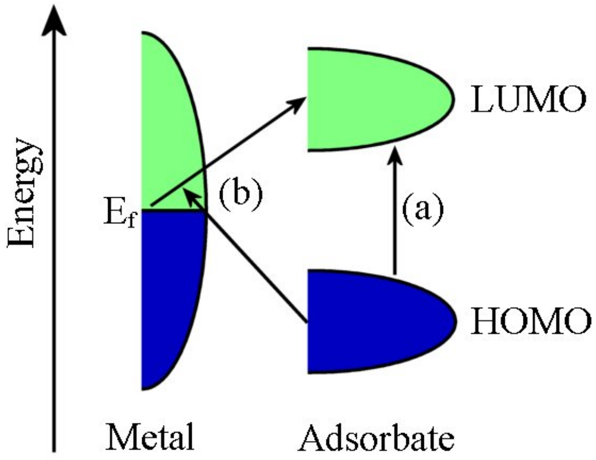

FIGURE 8.4: Charge transfer model for chemical SERS enhancement.

The Fermi level of the metal is assumed to be midway between the highest occupied molecular orbital (HOMO) and the lowest unoccupied molecular orbital (LUMO); this is a reasonable assumption for most molecules[105]. Resonance Raman, indicated by (a), requires photon energies in the ultraviolet, however, the charge transfer through the intermediate metallic site, (b), brings this energy into the visible, and allow possible Raman transitions to occur. This system also gives rise to the possibility of what is known as dynamical charge transfer. In this effect, a photon excites an electron into a high energy state. This electron then transfers to the LUMO state and excites a molecular vibration before returning to the metal and thermalising. It is also possible that a broadening of the electronic transitions increases the excitation cross section of the electromagnetic SERS effect. An interesting extension to this model is that surface roughness helps increase electron-hole production in the metal, as well as coupling the excited electrons to the vibrational modes of a molecule. This produces a broadband Raman spectrum often referred to as the luminescence background, which is always present in laser excitation SERS experiments[113].

8.3 Conclusions

This chapter has introduced the effect of surface enhanced Raman scattering. While many experiments have been performed to prove the existence of SERS, the origins of the effect are still poorly understood. SERS it only observed from metals that exhibit surface plasmons, implying that the electromagnetic contribution is by far the most important effect. Other chemical processes, it is therefore reasonable to surmise, performing only a minor role, although the multiplicity of the contributions to the final scattering intensity means this process should be possible to observe. To gain a full understanding of physics behind these effects it is clear that more experiments are needed with a greater emphasis on the fundamentals. One such experiment is the study into the angle dependence of the SERS process, and the verification of the five step process postulated in figure 8.3. A greater understanding into the SERS process would allow the optimisation of the enhancement factors from different surfaces, and would be useful in the creation of Raman molecular detection systems.

Chapter 9

Experimental SERS

9.1 Introduction

The previous chapter has outlined the processes believed to be responsible for the observed Raman enhancements found in molecule-metal systems. While an exact theory has not yet been found, it is clear that plasmon active surfaces are crucial, and the electromagnetic mechanism probably produces much of the observed enhancement. With samples that possess easily tuneable localised and delocalised plasmons, as well as a setup capable of observing highly resolved angular and spectral information, the way is paved for many interesting experiments. This chapter will first outline some of the preliminary experiments performed by members of the Southampton chemistry department as well as the author. These show excellent enhancements in the observed Raman spectra, high stability, and close to perfect reproducibility, along with other expected features. A section will then be presented on the strong correlation between both localised and delocalised plasmons with the observed Raman signal, and show conclusive proofs of both in- and out-going resonances. This is followed by a brief look at the potential application and challenges facing this work.

9.2 SERS Characterisation and Understanding

This section outlines the research undertaken to understand some of the fundamental properties of the SERS process on the nano-structured samples. The molecule of choice for these studies is benzene thiol, a benzene ring with a sulphur atom attached to one of the carbon bonds (fig 9.1 inset). A typical Raman spectrum is shown in figure 9.1 with the nature of the different observed transitions shown. It is customary for Raman spectra to be plotted in terms of the Raman shift:

$$Raman\ Shift(cm^{-1}) = \frac{(E_{laser} - E_{Raman\,peak})}{100hc} \tag{9.1}$$

where E_{laser} and $E_{Raman\,peak}$ are the energies of the excitation laser and the observed energy of the spectra respectively. For this thesis, the spectra will also be plotted against energy in most cases.

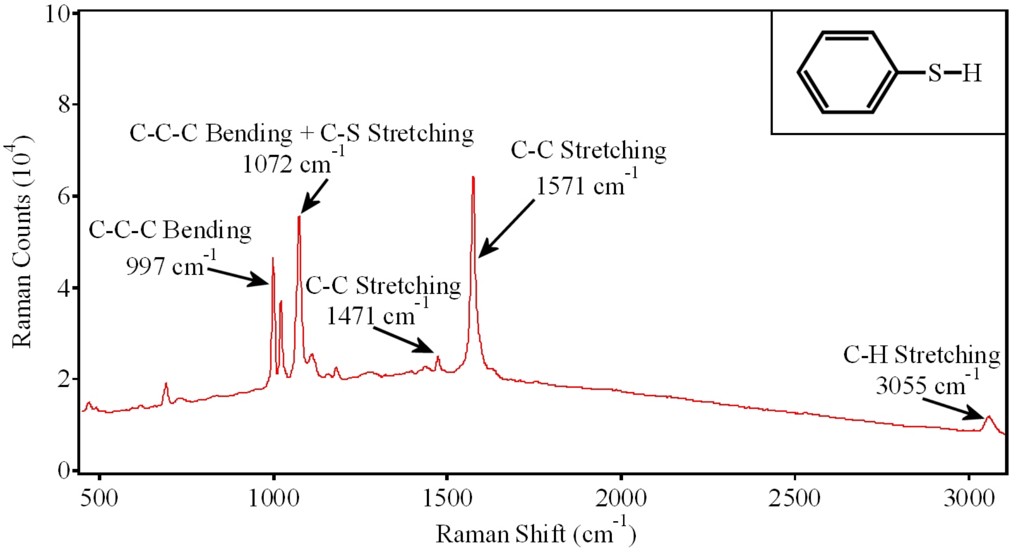

FIGURE 9.1: Image showing a typical SERS spectra for benzene thiol (shown in the inset), the different peaks correspond to different molecular modes, as shown.

A sample is cleaned by placing it in a stirred bath of tetrahydraflouran for two hours. Subsequent emersion in a 1mmol solution of benzene thiol in ethanol allows a monolayer of molecules to attach to the metals surface. In this process the sulphur atom chemisorbs onto the surface, and the hydrogen is released. This process is given two hours; however, much of the attachment occurs within the first few minutes. The metal-sulphur bond is strong but also allows the benzene ring freedom of in-plane motion. After some time molecules will pack onto the surface in a self assembled monolayer, but will maintain a large enough spacing for each molecule to be considered independent. A final wash in ethanol removes all molecules not attached to the surface, which can be verified through the absence of the S-H bond in the Raman spectra[119, 120].

9.2.1 Enhancement and Reproducibility

The enhancement factor, G, of a surface is calculated using the method described by Z-Q. Tian *et al.*[121], using the equation:

$$G = \frac{c_{\infty} N_A \sigma h I_{surf}}{R I_{bulk}} \tag{9.2}$$

where I_{surf} is the intensity of the Raman peak detected on the SERS surface, I_{bulk} is the Raman intensity of a solution with concentration c_{∞}. N_A is Avagadro's number, h is the confocal volume of the spectrometer and σ is the surface area occupied by the adsorbate. Finally, R is the roughness factor of the surfaces. This is found by measuring the charge associated with the removal of oxide from the metals surface[122]. For gold the oxide forms a monolayer and so the current produced when stripping this layer provides a measure of the total surface area. Any extra surface area over that expected from a perfectly smooth metal film is therefore due to increased roughness. Using this technique it has been found that the surface of the gold nano-structures have a very low roughness. However, for the case of equation 9.2 the increase in surface area, due to the pattering, leads to the use of a roughness factor of 1.6 over that expected for a perfectly smooth surface. The enhancement of the surfaces is found to be $3 \text{x} 10^6$[123], which is similar to the reported values for other SERS active systems[124], and a good two orders of magnitude better than the enhancement found on a roughened electrode. While this level of enhancement cannot be fully understood, it is in agreement with some perditions made from the electromagnetic model of SERS[114, 125].

By taking 100 Raman spectra at random positions over a 0.5cm^2 region of an un-graded sample the variation in peak intensity was found to be less than 10%. This should be compared to the variation in intensity from a roughened surface of over 1000%! Clearly a big improvement; a comparison with other presented material is not truly possible as the reproducibility factors are not published.

9.2.2 Wavelength, Power and Polarisation Dependence

With knowledge that the recorded Raman spectra are consistent and reproducible, it is possible to measure different aspects of the SERS process.

Initial attempts to record angle dependent SERS used a diode-pumped, frequency-doubled Nd:YVO$_4$ laser operating at 532nm. This provided no Raman signal but successfully burned holes on the surfaces. When the switch to using a near infrared laser was made Raman experiments became possible. A more stringent test of excitation wavelength has been performed using a Renishaw Raman 2000 system. This has shown that for silver, gold and platinum the enhancement increases as the pump frequency shifts from green to infrared. For gold the increased enhancement between pumping at 633nm and 758nm is found to be of order 3 times, while a laser wavelength of 514nm is found to give a 13 times enhancement over 758nm. For silver and platinum the increase in Raman signal between pumping at 514nm and 758nm pump sources is found to be 150 times. This difference in enhancement factor comes from the plasmonic properties of the different metals, along with the SPP resonances of the individual samples[113, 125].

The power dependence of the SERS process for a 600nm silver sample has also been measured using the Renishaw microscope system pumped at 633nm. In this experiment the power dependence of both the Stokes and Anti-Stokes peaks at ±1072cm^{-1} was recorded; the laser power was 3mW and was focused to a spot size of 5μm^2, this data is plotted in figure 9.2.

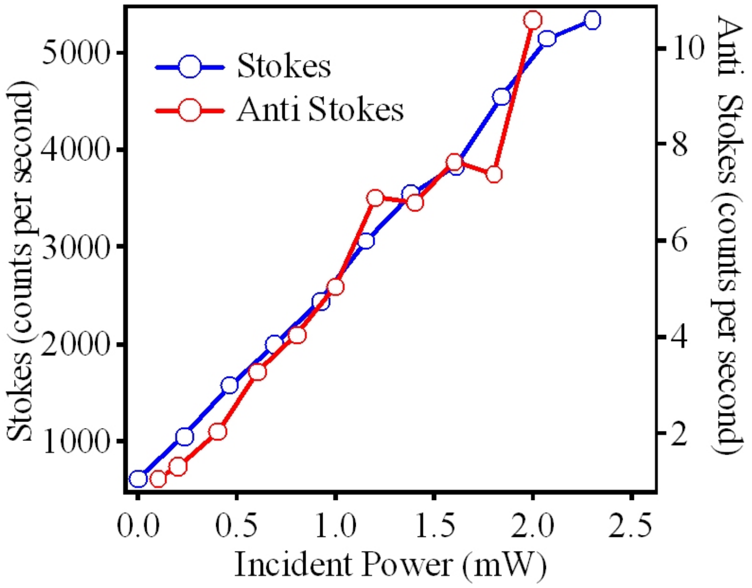

FIGURE 9.2: Graph showing power dependence of both Stokes and anti-Stokes transitions. Performed on a silver sample, void size = 600nm, $\bar{t}$ = 0.2

As the SERS process on the Stokes side is sensitive to the square of the incident electric field, it follows it should have a linear dependence with pump intensity. The data, which has been averaged over a number of repeats, shows the enhancement to be linear with pump power over the range of powers accessible to the pump laser, as expected. This result has also been confirmed for gold samples, both on and off plasmon resonances and is consistent with the literature[126]. The intensity of the anti-Stokes Raman signal is 500 times weaker than that of the Stokes because the process requires a molecule to be in an excited state, and then scatter back to one of lower energy. This process is random and depends on the temperature of the molecules surroundings. There is much interest in analysing the ratio between the Stokes and anti-Stokes signals to provide information on the effective temperature of the molecules involved in the SERS process, and hence give some information on the true enhancement factors. At the range of powers used for our experiments the anti-Stokes signal varies linearly with power. This implies that there is no pumping of the molecule to a higher vibrational state, which would lead to a relative increase in the anti-Stokes signal over the Stokes. This is again to be expected, as an enhancement sufficient for vibrational pumping requires a local field intensity close to that capable of annihilating the molecule under study. The benzene thiol molecules still produce Raman spectra after days of constant illumination so it is reasonable to assume the experiments are performed far from these field strengths - this is also consistent with the measured enhancement factors in the pervious section. It is also interesting to look at the Stokes and anti-Stokes spectra, shown in figure 9.3.

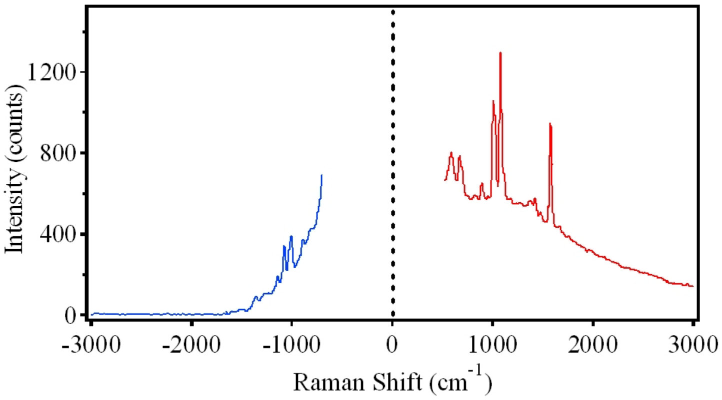

Figure 9.3: Graph showing both Stokes and anti-Stokes Raman signals. Performed on a silver sample, void size = 600nm, $\bar{t}$ = 0.2

Whilst the ratio between peaks of the same wave-number is constant for various powers, this figure clearly shows that intensity distributions of the two spectra are quite different. Anti-Stokes intensity drop much more quickly with wave number than the Stokes intensities. This rapid decrease can again be attributed to the decrease in probability of molecules existing in high vibrational states at room temperature. Interestingly, the background signal also drops in intensity in the same manner as the Raman peaks, providing evidence that this signal is closely linked to the SERS process. The background is always observed and its shape seems to be dependent on the type of molecules and metal involved as well as pump and detection wavelengths. Currently there is much debate over the origin of this background, although plasmon enhanced fluorescence is a strong contender.

Finally, the polarisation dependence of the SERS signal is tested. Whilst the Raman process scatters randomly, plasmons are polarisation dependent, and so should affect the scattered light. Experimentally, some variations in intensity have been observed with changing polarisation, but no clear correlation between polarisation and Raman intensity can be found. There are a number of reasons for this: firstly the intensity of the Raman spectra is greatly reduced after passing through the polariser, making detection more difficult. Secondly, it is not clear exactly what polarisation dependence would be expected, since both TE and TM plasmons have been shown to exist on the substrates. To fully understand any relationship a full study for all sample orientations and output polarisations should (and hopefully will) be conducted. However, it is suffice to say that the dependence is small and therefore need not be worried about in the following sections where all polarisations are detected.

9.3 The Plasmonic Connection

It has long been known that plasmons are an essential part of the SERS process. What is less well understood is the precise origins of this massive enhancement. To try and begin to answer this question the plasmon active surfaces discussed throughout this thesis are put through exhaustive sets of experiments using the set up described in chapter 5. It has already been found that the surfaces have excellent enhancement factors and near perfect reproducibility of SERS signals. This allows a single point to be illuminated for 12 hours while the computer controlled goniometer records the intensity of Raman scattered light at different pump and detection angles as well as sample orientations. The plasmon dispersion plots, discussed in chapter 6, are used to find plasmon resonances, then the excitation laser wavelength can be tuned accordingly. If a single pump angle is used and the detector is scanned through all output angles a detector scan is built up. Detector scans map the output resonances in the SERS process, and can be compared to the plasmon resonances to find correlations. A similar technique can be used to map the input resonances by maintaining a constant detection angle and scanning the pump light. These two techniques are known as pump- and detector- scans and have been discussed in chapter 5. Besides this, the surfaces exhibit surface and localised plasmon modes, which can be tested to observe their SERS coupling efficiencies.

9.3.1 Localised Plasmon SERS

The overwhelming majority of SERS experiments published use localised plasmons, excited on either rough surfaces or colloidal particles. In these experiments, the particle sizes are on the nanometre scale and the largest SERS signals appear when two particles are close enough for their electric fields to be enhanced in the tiny gap separating them. The definition of a localised plasmon in this thesis is the Mie scattered electric field in a sub-micron cup. It has been found that the walls of the cavity are smooth and from the optical dispersion it is known that there is limited interaction between adjacent cavities. This would not at first sight appear to be the best structures for observing SERS; however, as the previous section has already outlined, enhancement values of a similar order to those reported in the literature are observed. To start to understand the connection between the two seemingly different sample types, a deeper analysis of the SERS from the localised plasmon is required. Due to the high angular resolution of the goniometer setup, the pump laser is only weakly focused onto the sample using a 30cm focal length lens. The fibre detector is also 26cm from the sample and for this reason, together with the fact that the Raman enhancement of gold is significantly smaller that that of silver, a three minute integration time is required using a cooled CCD camera. A pump intensity of 100mW is also required to obtain a reasonable signal from a system with an effective numerical aperture 10 times smaller that that of a standard Raman microscope system (leading to a 100 times reduction in signal strength). In fact, it is only because the enhancement factors of the surfaces are so high that any Raman signal can be observed.

Figure 9.4 shows a reflection spectra and a Raman detector scan for a 900nm void size gold sample, position at $\bar{t} = 0.8$ to exhibit a strong localised plasmon. The reflectance varies slightly with incident angle, however, there is strong absorption across the whole range of angles and other experiments have shown this to be an almost purely localised mode with some weak mixing. The excitation laser is tuned to 1.63eV and brought in at 15^o to the sample normal, designated by the (X) in plots a and b.

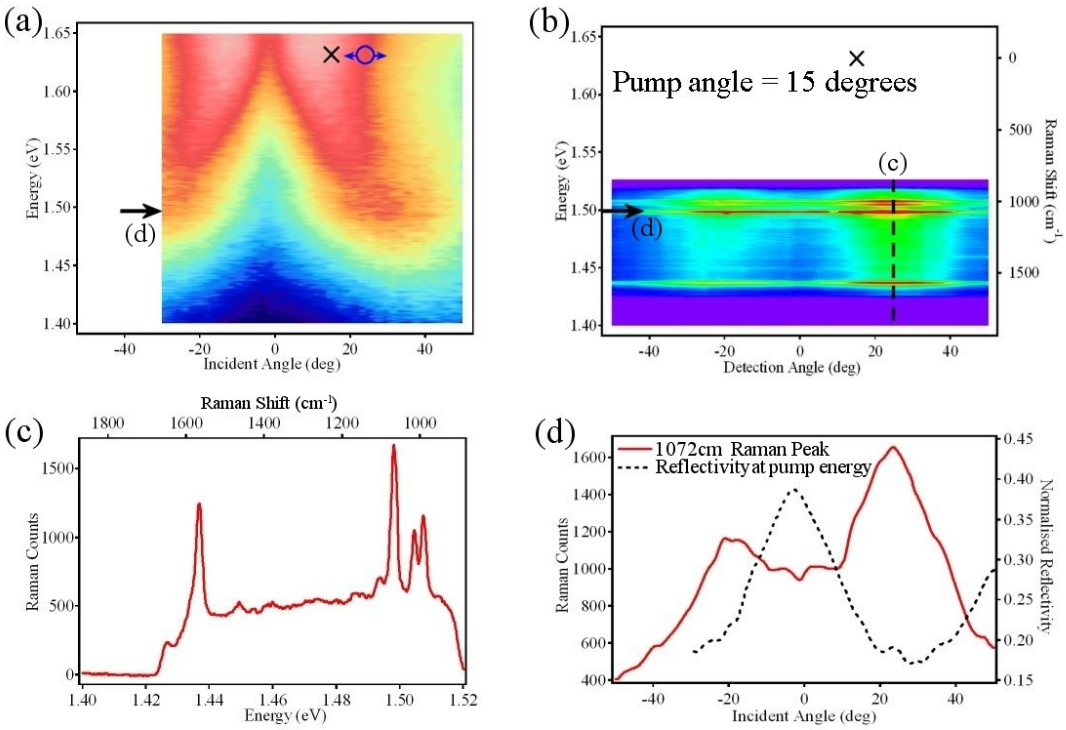

FIGURE 9.4: (a) Reflectivity scan of a Mie plasmon, the cross shows angle and energy of pump laser in detector scan, the circle shows detection angle for pump scan. (b) Detector scan as defined in (a). Cuts through this image show are shown in: (c) Raman spectra and (d) angular dependence, reflectivity shown for comparison.

The detector arm is then scanned 50^o either side of normal, collecting the SERS spectra as it goes. As shown in 9.4b there is a clear enhancement in the observed SERS signal in the presence of the plasmon mode, the lack of data in the top half of the image is a constraint of the filters used to cut light near the excitation frequency. Figure 9.4c shows a spectral cut through the image presented in b, showing the expected Raman peaks of benzene thiol. The broadening of the peaks relative to those shown previously is due to the lower resolution of the spectrometer. Figure 9.4d shows the more interesting angular cut through the data, showing the SERS signal and the reflection spectrum for one energy and different incident angles. Here, a clear correlation between increased absorption and enhanced SERS is evident. This shows the direct link between plasmons and enhanced Raman scattering.

At the same sample position a pump scan can now be performed with a detection angle of 23^o, indicated by the circle ($\circ$) in the reflectance plot (fig 9.4a, and fig 9.5a). The pump scan provides information about ingoing resonances and since the pump laser is only a single frequency the information in figure 9.4a can be depicted on a single graph, as shown in figure 9.4b.

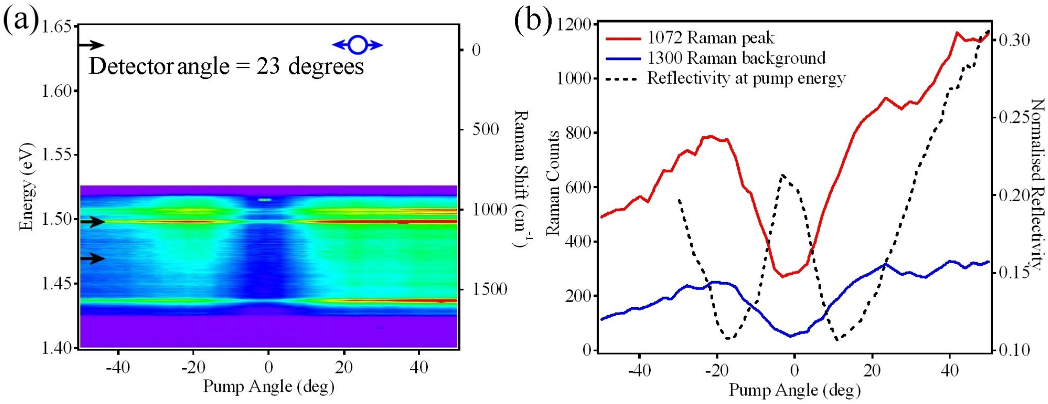

FIGURE 9.5: (a) Pump scan as defined in figure 9.4, (b) Cuts through (a) showing correlation with reflectivity.

Both the angle dependence of the 1072cm^{-1} peak and the background at 1300cm^{-1} are shown, along with the reflection spectra at the pump angle. Again, good agreement between peak absorption and maximum SERS signal is observed, although the enhancement persists and indeed increases at larger scan angles - the reason for this is uncertain but possibly indicates the presence of a plasmon mode component not detected in the reflection spectra. Both peak and background again show the same profile, once again indicating the connected relevance of the background in understanding of the SERS process. This proves that the background is linked to the SERS process and acquires an equal enhancement to the Raman peaks.

9.3.2 Bragg Plasmon SERS

Using a 700nm gold sample at $\bar{t} = 0.2$ a strong Bragg plasmon mode can be observed. The reflectivity of this position is shown in figure 9.6a. Using this data an excitation wavelength of 775nm was used at an angle of 7^o to directly pump one of the Bragg modes. The angle dependence of the Raman scattered light was then recorded. This data is shown in figure 9.6b and clearly shows the correlation between the shape of the plasmon dispersion and the angle dependence of the SERS. This quite unambiguously shows the plasmon enhancing the outgoing resonance of the SERS process. The clear implication of this data is that the observed Raman scattered light from the adsorbed molecules is first re-emitted into a plasmon state, and not a photon one. This supports the five step plasmon model of SERS presented in the previous chapter. The enhancement in the background can also be seen to follow the profile of the plasmon absorption.

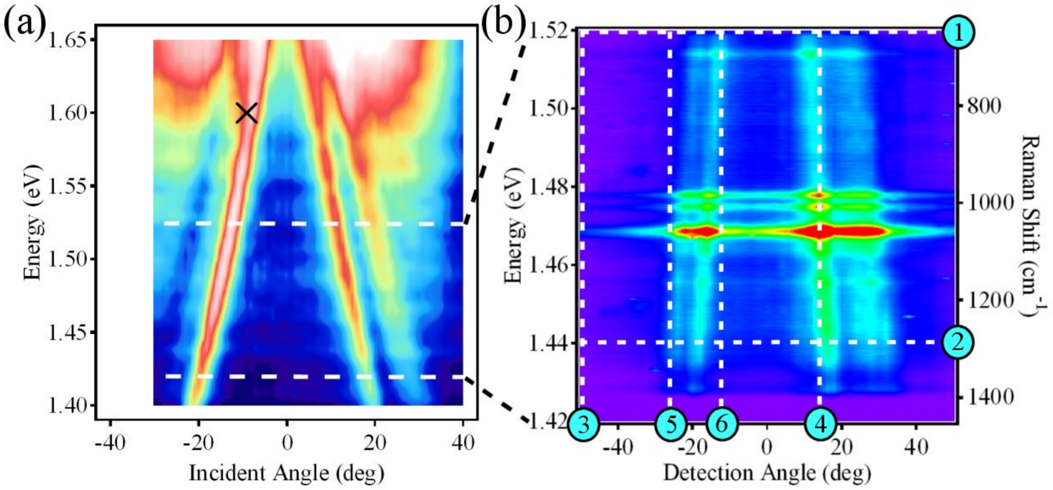

FIGURE 9.6: (a) Reflectivity of a Bragg mode. (b) Detector scan taken from position (a), pump angle indicated by (x).

Figure 9.7 now shows a number of cuts through figure 9.6 to reiterate and enforce the data thus far presented.

In figure 9.7a, the correlation between absorption and Raman signal is explicitly presented. This shows the direct link between the plasmon resonances and the Raman signal. The data shows an increased angular width of the Raman peaks over the detected plasmon resonances. The reflectivity experiments use the super continuum laser that is well collimated and has a spot size of about 2mm on the collimation lens, this allows an angular resolution of 1^o. The Raman scattered light is incoherent and filling the whole of the collection lens, reducing the angular resolution of the experiment to around 4^o and leading to the observed broadening of angle resolved data.

Figure 9.7b shows Raman spectra both on and off the Bragg plasmon resonance. This shows that the plasmon resonance accounts directly for an enhancement factor of ten, a feature that is consistent throughout all the experiments performed to date. This poses some very interesting questions since on a smooth gold surface, in the absence of structuring and where no plasmon modes exist, the Raman intensity is essentially zero. This means the plasmon is required for the full $3x10^6$ enhancement (the total enhancement observed in the experiment), but only directly provides one order of magnitude in the angular resonance. One possible explanation for this is non-resonant SERS emission arising from molecules at sites with additional highly localised plasmons. Although these sites absorb photons very weakly, they can efficiently couple to the larger scale Mie and Bragg plasmons. These sites would also have a broad range of energies and emit in all directions. Due to their small size these highly localised plasmon can more effectively couple to molecules and hence become a major source of Raman scattering. To prove this hypothesis, further work is required from both theoretical and experimental sides of the project.

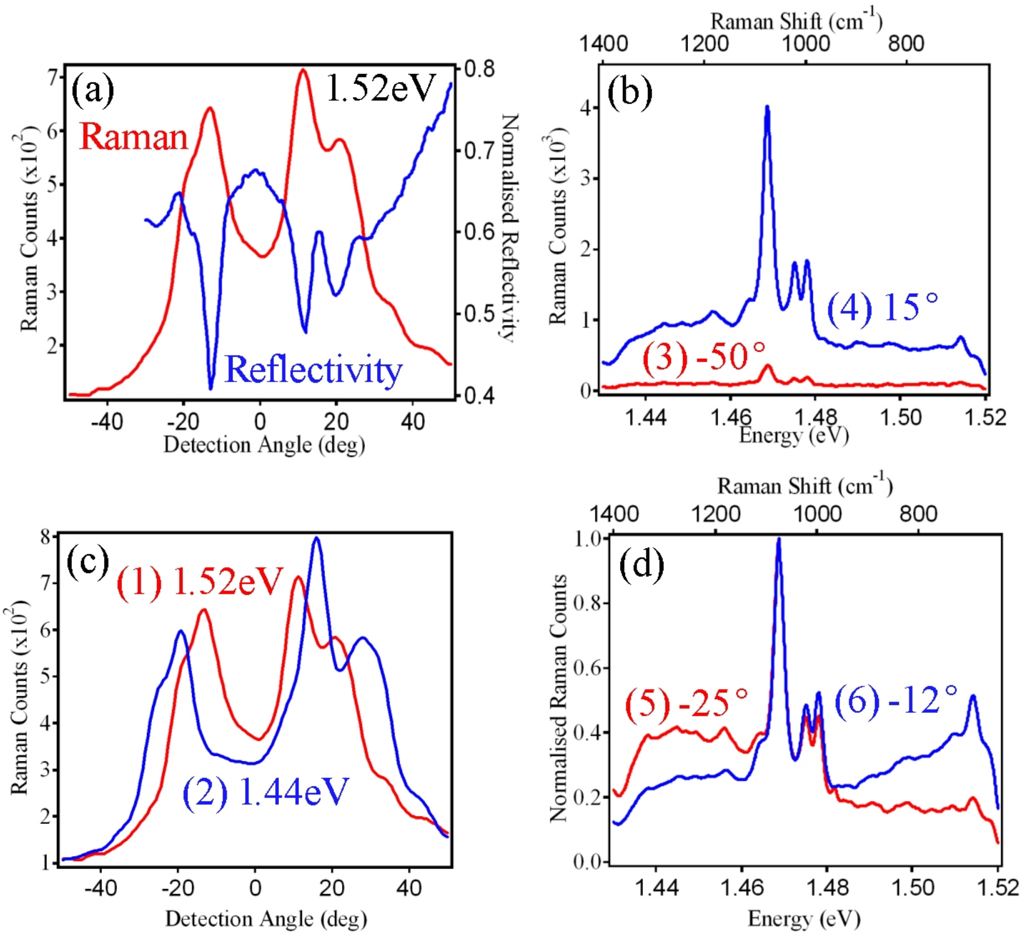

FIGURE 9.7: Analysis of figure 9.6b. (a) Comparison between reflectivity and SERS. (b) SERS spectra on and off resonance. (c) Angular SERS at two energies. (d) Spectra at two angles.

The graphs c and d in figure 9.7 are designed to show one of the important implications of this work - the strong angular dependence of the SERS effect. In figure 9.7c, two angular slices at constant energies are shown. This emphasises the change in observed signal simply from altering the detection angle. In a standard confocal Raman microscope the numerical aperture of the lens defines the range of observed angles. In the presented case, an objective with a viewing angle less than about 20^o would not observe the majority of the enhanced signal, greatly reducing the efficiency of the experiment. This effect could also be used as a powerful tool by enhancing different wavelengths at different angles: the SERS substrate can be designed to both enhance and split the Raman lines directly onto a photo-detector. A further point outlined here is the need for careful design of SERS experiments to understand how the resonances will affect the signal under different conditions. Figure 9.7d shows a 'normal' SERS spectrum for benzene thiol at two different detection angles. Ordinarily the relative intensities of different Raman peaks are used to understand the orientation of bonds within a molecule relative to the surface. However, it can be seen that a plasmon mode can alter the relative strength of these modes, making simple analysis flawed. The data presented here is of course an extreme case of this effect, but nonetheless it is an important consideration when comparing different molecular bonds experimentally examined under different conditions.

Figure 9.8 shows the reflectivity and Raman pump scans from a 900nm sample at $\bar{t} = 0.1$. Again, strong Bragg modes are observed. The laser is tuned to a wavelength of 760nm and the detector is set to 1^o.

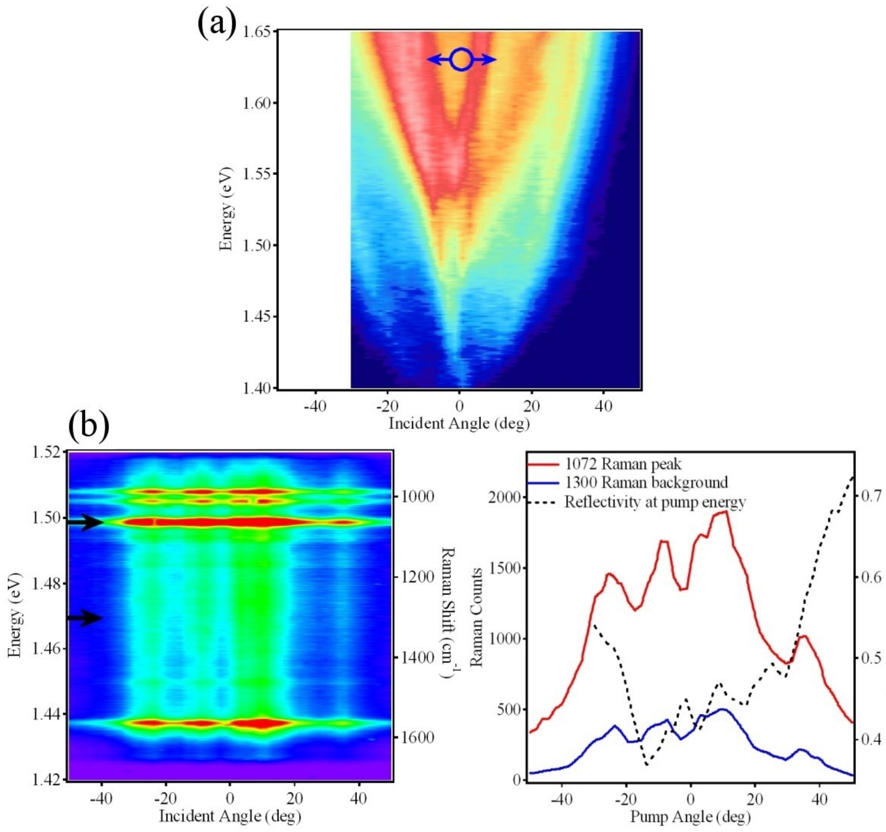

FIGURE 9.8: (a) Reflectivity showing a set of Bragg plasmon modes, the circle show angle of the detector in the pump scan. (b) Pump scan and cross section, also shown is the reflectivity of the pump laser wavelength.

This data clearly resolve the input plasmon resonances of the surface. This is proven because the Raman enhancement matches the absorption profile at only the excitation energy, not the detected energies. The overall level of plasmon enhancement again seems to be independent of energy, with the background following the same intensity distribution as the peaks.

Interestingly, the level of enhancement from Bragg and Mie plasmons is very similar. Experiments have also been performed using mixed plasmon modes, and again the level of enhancement is the same. This similarity implies that the cross-sections, and electric field strengths, for both localised and delocalised plasmons are very similar.

9.4 Different Metals

In the fields of plasmonics and surface enhanced Raman spectroscopy, silver is very often the metal of choice. This is because surface plasmons on silver are less attenuated than on gold. This leads to stronger resonances and allowing experiments to be performed more easily. However, silver quickly oxidises and so samples do not last for prolonged periods, unless protected.

SERS experiments are performed on the same silver samples used to understand to plasmonic properties and, again, benzene thiol is used as a Raman active molecule. To avoid the problem of oxidation experiments were performed within a day of sample production; however, no changes in the spectra were observed after several weeks. This is because the surface layer of benzene thiol slows the oxidation of the silver, although sample degradation is observed over the course of a year. In chapter 7, analysis of the silver samples showed the response to be dominated by mixed modes of primarily Bragg plasmon nature. Again, it should be stated that data is not recorded above $\bar{t} > 0.5$ due to problems with the growth of silver. This means strong Mie plasmon modes could not be studied for these samples. Figure 9.9 summarises the SERS response observed for many different silver samples.

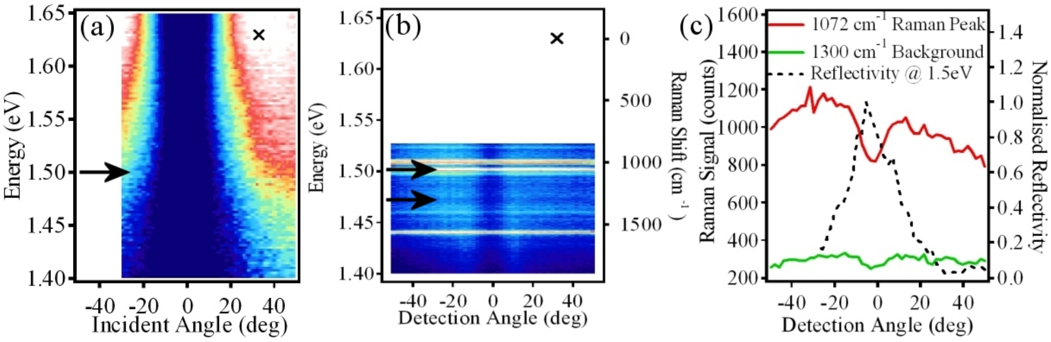

FIGURE 9.9: (a) Reflectivity of a 800nm silver sample at $\bar{t} = 0.3$ (b) Detector scan of Raman emission from same point. (c) Cuts through (a) and (b) as shown.

These measurements only required an integration time of 30s (compared to 3 minutes for the gold samples), consistent with approximately an order of magnitude increase in enhancement between silver and gold[123]. As expected, there is an increase in the Raman signal with angle in the presence of a plasmon mode; however, the increase in counts is small. This small increase is in fact due to only a small decrease in the intensity of the off-resonance SERS signal. This is similar to the observations on gold, only more pronounced, with a 20% variation between on and off resonance. This large off-resonance signal is attributed to the increased roughness of the silver samples over their gold counterparts. This increased roughness has been observed through electrochemical analysis and is expected due to the faster growth rates of silver films. The increased roughness of the silver films could well increase the density of molecular level hot spots, and so increases the SERS signal for all energies and angles, adding support to the previous theory.

The silver samples also have a plasmon enhanced background. It is found that the Raman peak intensities for silver, relative the intensity of the background, are about twice that seen on gold samples. This shows that the increased enhancement factor affects the direct Raman scattering process more strongly than the process responsible for the background. This adds weight to the notion that the background is related to a chemical enhancement mechanism and further work on different metals may be able to shed more light on this idea.

Experiments have also been attempted to observe SERS on the platinum, nickel and mixed gold/nickel, nickel/gold samples. Unfortunately, due to the reduced enhancement factors of these materials, no angle resolved data has yet been obtained. Thorough analysis will soon be carried out using the Renishaw microscope system, where Raman signals can indeed be observed.

9.5 Application and Conclusion

Throughout this thesis there has been continual mention of the capabilities of SERS for real applications. The Raman process is very useful to distinguish the presence of different molecules due to the unique set of vibrational states possessed by each. It has been shown that the substrates used in this thesis are reproducible, and can be used after countless cleaning procedures as well as left in ambient conditions for at least two years (no degradation has been observed over the past few years on any of the gold samples). The robustness of the samples also allows the accurate measurements of process such as electrochemical SERS[107]. In this technique Raman spectra are recorded while the electric potential across the molecules is varied. The electric field controls the bonding of certain molecules to metal surfaces. By observing the change in Raman spectra with potential it is possible to understand the molecule-metal bonding in greater detail. Again, the high reproducibility of the surfaces allows more accurate data to be collected than has previously been possible.

When used in a standard Raman microscope setup with silver nano-structured substrates, a strong signal can be obtained in one second - sufficiently quick for real time detection. It should also be noted that the surfaces could potentially be cheap to produce, requiring only a solution of micro-spheres and a little gold.

There is a choice between the use of Bragg or Mie plasmons to enhance the Raman signal. While the two types of plasmon provide almost equal enhancement factors the Bragg plasmons have several advantages. Firstly, as discussed previously, the dispersion of the delocalised modes lead to efficient beaming of the SERS light. This allows the substrates to be placed at a distance from the collection optics in, for example, hazardous environments. The control over the plasmon dispersion also allows for the design of devices that split the different Raman lines into various spatial locations, as shown in figure 9.10.

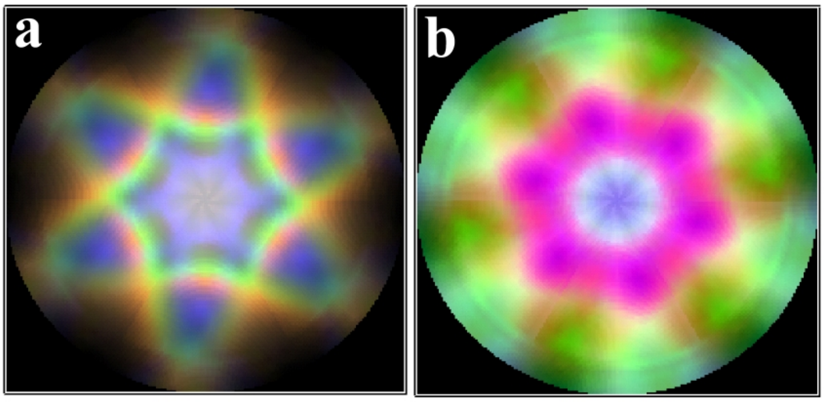

FIGURE 9.10: Angle plots of a 900nm gold sample for (a) a Bragg mode at $\bar{t} = 0.2$ and (b) a Mie mode at $\bar{t} = 0.5$. In each case three energies are shown corresponding to the plasmon dispersions at 998cm^{-1} (red), 1573cm^{-1} (green), and 3055cm^{-1} (blue) if a pump laser of 600nm is used. These images correspond to the expected Raman image collected in the back focal plane of a microscope objective.

This image takes the plasmon dispersions at three Raman peak energies. Since it has been shown that the Raman peaks are enhanced at these plasmon modes, these images simulate the output Raman scattered light from the surface. This indicates how effectively different Raman lines can be sent to different spatial locations for direct detection by a CCD camera. This splitting and beaming of the Raman scattered light combined with the enhancement could greatly simplify device architecture. One of the most important applications of molecular detection is in micro-fluidic systems for rapid detection of different molecular species. It has previously been shown that the wetting of nano-structured surfaces is still something of an uncertainty and, since the most common solvent is water, it makes sense to use thin substrates to allow total wetting and hence maximum contact between the surfaces and the molecules to be detected; this again favours the use of Bragg plasmons.

While the surfaces considered in this thesis are not currently being used beyond the laboratory, similar substrates have recently been commercialised[21, 127]. These are square arrays of holes on the micron scale, produced using a commercial optical lithography system and then coated with a gold top layer. These substrates have attracted much interest and hold the potential for success, with the key physics coming from the experiments performed on the nano-void samples discussed above. This emphasises some of the true potential in fully understanding the properties of surface plasmons.

Chapter 10

Plasmon-Exciton Coupling

10.1 Introduction

The final experiments outlined in this thesis deal with coupling between plasmons and molecular semiconductors. The aggregation of certain types of molecules on a surface allows the formation of delocalised exciton state. These can interact strongly with surface plasmons to form an exciton-plasmon mixed state[128, 129]. It has been found that emission into a surface plasmon mode becomes dominant when a light emitter is brought within 50nm of a metals surface[128]. This has the effect of enhancing the spontaneous emission rate of the light emitter and has been proposed as a system to improve the emission from laser diodes[130]. The observations of the interactions between these organic semiconductors with plasmon active surfaces are therefore useful to improve the understanding into such systems.

10.2 J-Aggregate Preparation

To produce a surface exciton mode the properties of cyanine dyes are used. Figure 10.1 outlines the remarkable properties of these dyes when they are cast onto a smooth surface.

These molecules have an electron donor group at one end and an electron acceptor group at the other[131]. This asymmetry produces a large static dipole moment along the length of the molecule. The cyanine dye of choice for these experiments is known as NK2751, the chemical structure of this molecule is shown in figure 10.1a. In solution, and at room temperature, these molecules act independently and exhibit a broad monomer absorption feature centred at 2.3eV due to the dipole moment. When, however, this solution is cast onto a surface, the dipolar nature of the molecules causes them to align. This acts to form large self-assembled molecular arrays, as shown in figure 10.1c. This

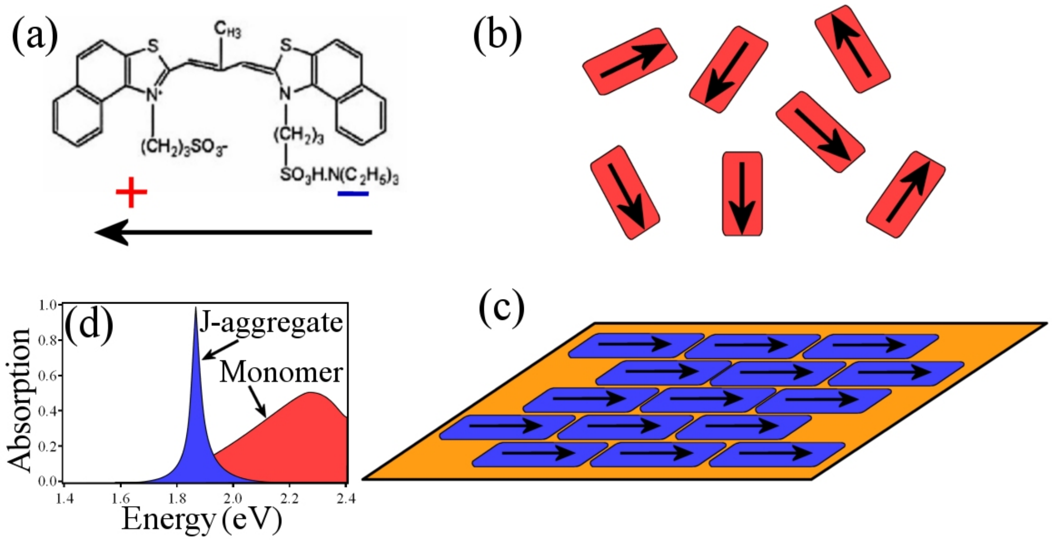

Figure 10.1: (a) Chemical structure of cyanine dye, dipole moment also shown. (b) Pictorial representation of molecules in solution and (c) when aggregated, giving rise to different absorption spectra (d) due to the delocalisation of the exciton state.

aggregation makes the molecular film extremely well ordered and correlates the effect of the individual dipoles, creating a much larger dipole moment.

An alternative model for this system is to view each molecule as a small piece of semiconductor containing one electron-hole pair, or equivalently an exciton. Upon aggregation the molecules are sufficiently closely spaced for the excitons to delocalise through the strongly correlated interactions. This forms an exciton energy band and reduces the energy of the electrical transition, and hence the absorption. The molecular alignment also reducing the line-width of the transition, figure 10.1d.

It has been found that a simple drop casting technique of pure cyanine molecules in methanol can lead to the formation of good J-aggregate films on the nano-structured surfaces. Once aggregated, the molecules appear stable for prolonged time scales (greater than a few weeks), and allow measurements of the absorption spectra as well as fluorescence to be recorded at different angles.

10.3 Optical Measurements

Using the same automated goniometer setup used for the plasmon experiments the angle resolved absorption of the J-aggregated nano-structures surfaces can be recorded. The sample of choice for this experiment is a 600nm gold sample, whose optical properties have been studied in detail. Figure 10.2a shows the dispersion of the pure Bragg plasmon on a nano-structured surface with no J-aggregate at $\bar{t} = 0.2$. This can be compared to figure 10.2b that shows the same sample position, only now covered with a thin J-aggregate film.

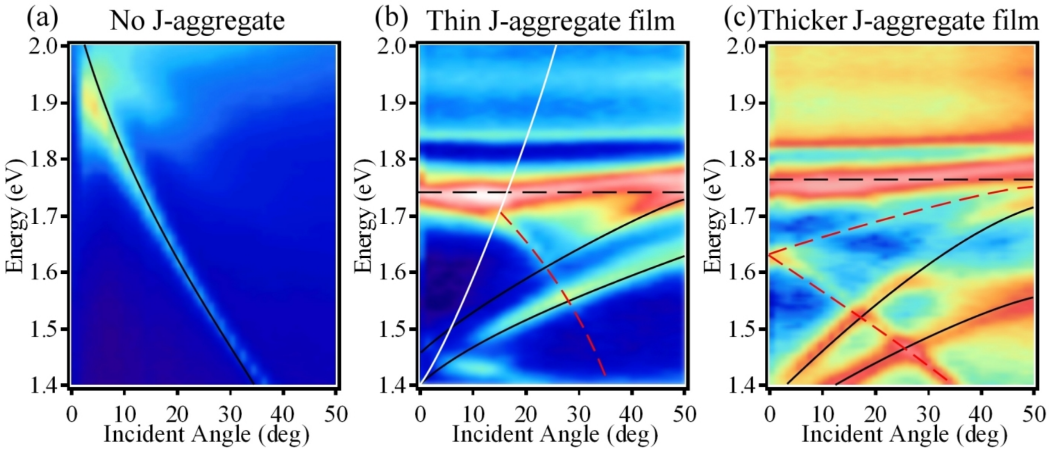

FIGURE 10.2: Dispersion maps of a gold sample, void diameter = 600nm, $\phi = 0^o$ and $\bar{t} = 0.2$. (a) No J-aggregate, (b) a thin J-aggregate layer and (c) a thicker J-aggregate layer. White line shows plasmon dispersion in a dielectric material, n = 1.6. Black solid line shows calculated plasmon dispersion in J-aggregate, dashed line shows exciton absorption band, red dashed line shows calculated SPP wave-guiding mode.

The molecular coverage of the surface has two strong influences on the observed spectra. Firstly, the thin molecular film has a ‘spectrally-resonant’ high refractive index, this was shown in chapter 7 to reduce the Bragg plasmon energy through in-plane momentum conservation. The white line in figure 10.2b shows the expected dispersion if the refractive index of the J-aggregate film was a constant value of 1.6 at all energies. The second effect of the J-aggregate film is the strong localised absorption from the exciton state at 1.75eV. If the plasmon and the exciton were independent their modes would cross around 10^o (white and dashed black lines in figure 10.2b). However, coupling between the SPP and exciton modes occur, and an anticrossing behaviour is observed. This is understood through a mixing between SPP and exciton modes, forming a new set of mixed states. These mixed states correspond to an oscillation between a surface charge fluctuation and an excited exciton state. Using elipsometry the complex refractive index of a thin J-aggregate film on smooth gold can be found[130]. These values can then be used to find the complex dielectric function for J-aggregate/gold structure as a function of energy. The dielectric function of the exciton resonance fits well with that of a simple Lorentz oscillator, shown in figure 10.3a, and for simplicity it is these values that are used to fit the data. This dielectric profile leads to an increase in absorption at the exciton resonance energy as well as a rapid change in the real part of the dielectric constant at the energies around it. Figure 10.3b shows the dispersion relation for both light travelling through the J-aggregate medium and a SPP travelling along the interface between gold and the J-aggregate layer. This model uses the experimental dielectric constants of gold and those shown in figure 10.3a for the J-aggregate.

Using these dispersion relations the theoretical modes of SPPs and light within the J-aggregate layer can be estimated. These are shown in figure 10.2b - solid black lines and red dashed line correspond to dispersions of SPPs and light respectively. A good

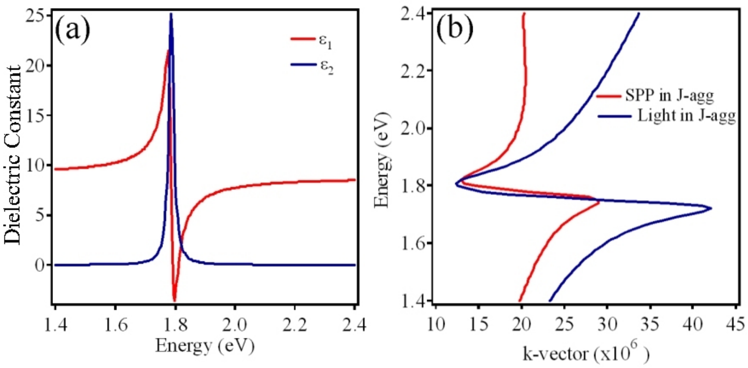

Figure 10.3: (a) Graph showing dielectric constant of a oscillator used to model J-aggregate properties (b) Dispersion of light in a J-aggregated medium and SPPs in a metal/J-aggregate system.

fitting between experiment and theory can be achieved with both dispersion relations indicating the presence of both a SPP mode and a waveguiding mode. A free parameter in this fitting is the absolute film thickness because the physical properties of the cyanine dyes are not easily available. By varying the amount of dye drop cast onto the surface, control over the relative film thickness can be achieved; this is shown in figure 10.2b and c. It is always possible to fit theory lines to both SPP and waveguiding modes. Unfortunately, due uncertainties in the mode confinement within the J-aggregate layer, the fitting parameters cannot currently be converted into an absolute film thickness.

To try to resolve this problem current work is being performed to calculate the electric field profiles of the different observed modes. Figure 10.4 shows the current estimates of the SPP mode and a second order waveguide mode.

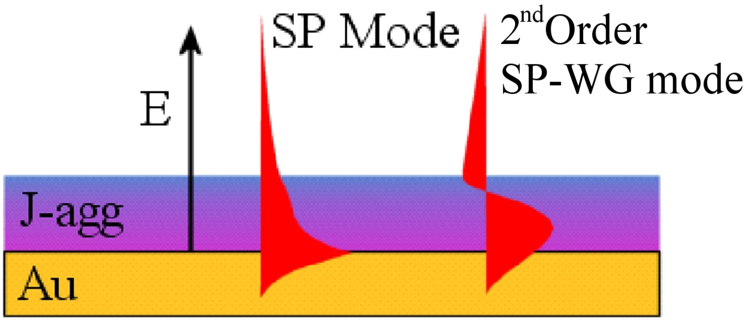

Figure 10.4: Schematic of electric field for both SPP and wave-guiding modes.

These calculated distributions are based on the same parameters used to calculate the dispersion so should relate precisely to the actual surface fields. This figure shows the plasmon mode to have a maximum electric field at the surface, and decay exponentially into the dielectric, as shown previously. The wave-guiding mode has a maximum electric field within the dielectric layer, as would be expected. The second order wave-guiding mode is shown here, corresponding to the mode shown in the data. However, due to the proximity of the surface, this mode also has an electric field component inside the metal. This corresponds to an optical mode coupled to a surface plasmon, which would be expected at these length scales. Work is continuing to fully model the optical properties of J-aggregate films on gold.

10.4 Fluorescence Measurements

The exciton states of the cyanine dyes are highly fluorescent and can be pumped at 2.3eV using a diode-pumped, frequency-doubled Nd:YVO$_4$ laser operating at 532nm. Experimentally, the setup is equivalent to that used for the SERS detection, except for the use of different pump and detection wavelengths. Again, due to the small numerical aperture of the setup, data is acquired using the cooled CCD camera with a spectrometer. A pump power of 100mW is also required, which causes photodecomposition of the molecules when illuminated for more than a few hours. For this reason, so far only detector scans have been performed on the fluorescent signal. Figure 10.5 shows a comparison between the angular fluorescence signals from a smooth gold surface and from the nano-structured surfaces.

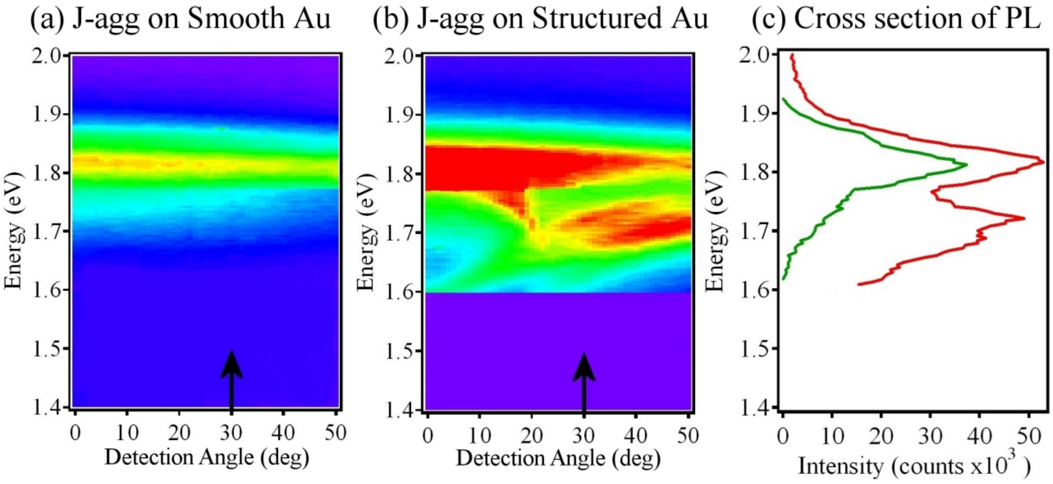

Figure 10.5: Detector scans recording the fluorescence from a J-aggregate film on (a) flat gold and (b) the surface shown in figure 10.2b. (c) Cross-sections of (a) and (b) at 30^o.

On the smooth gold a clear band of fluorescence is observed at 1.8eV. This band corresponds to the decay of exciton states and is close to Gaussian in profile. To lower energies an extended tail in the fluorescence is observed. This relates to intra-band exciton transitions. The data shows a noticeable decrease in intensity with increasing detection angles. This is due to an increased absorption within the film as the in-plane component of the electric field increases.

A clear change in the fluorescence is observed between the smooth and structured surfaces; this is emphasised in the cross section taken at 30^o, shown in figure 10.5c. The presence of the Bragg plasmon has noticeably enhances the fluorescence of the molecules at energies far from the normal fluorescent band. To analyse this further figure 10.6 shows the absorption and fluorescence images, both separately and combined.

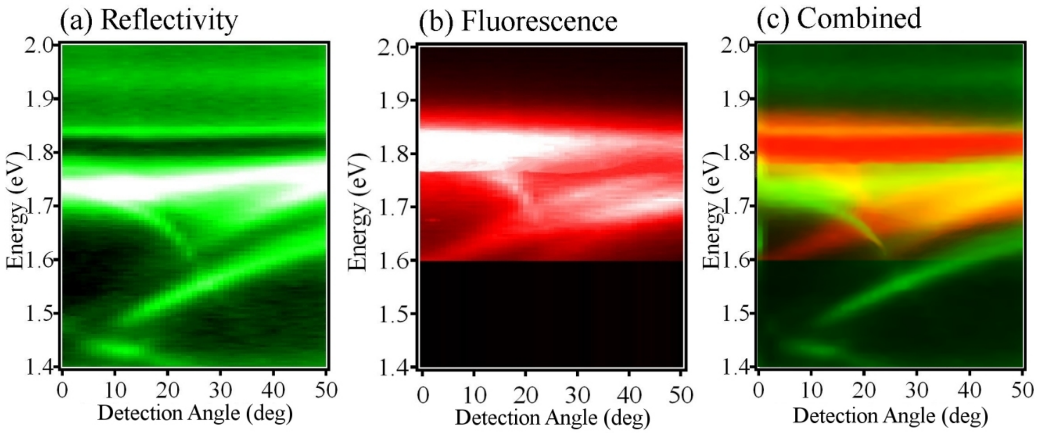

FIGURE 10.6: (a) Reflectivity shown in figure 10.2b, plotted in green colour scale. (b) Fluorescence detector scan shown in figure 10.4b, plotted in red colour scale. (c) Combination of (a) and (b) to show correlation between absorption and fluorescence.

There is a good correlation between the shape of the absorption and fluorescence profiles, indicating a strong relationship. However, on closer inspection the fluorescence appears shifted to higher energies relative to the plasmon modes. This shift is believed to arise from the re-absorption of the emitted light into the plasmon mode. In this model, light incident on the surface excites a surface plasmon. This plasmon mode enhances the density of states an exciton can emit into, creating the new fluorescence profile. At the peak SPP absorption, however, the emitted light can be efficiently re-absorbed. This gives rise to observed photoluminescence at only the SPP absorption edges.

This research is at a very preliminary stage, but is already showing many interesting phenomena. Experiments are currently under way to fully understand the data collected so far, as well as examining other processes such as the interactions between excitons and Mie plasmons. The controllability of the plasmon dispersion allows interesting tests to be performed such as the tuning of the exciton coupling between molecules. This opens the way for a high degree of molecular control as well as having the potential to improve the efficiencies of light emitting devices.

Chapter 11

Conclusions

This thesis has presented a study into the optical properties of nano-structured metallic surfaces under a range of conditions. It has been shown that the technique of template self-assembly and electrochemical deposition can be used to produce well-ordered nano-voids with a range of sizes and from a range of metals. These structures have been thoroughly characterised to understand the physical properties of the sub-micron geometries. Gold structures have been the primary focus of this thesis due to their chemical inactivity and robustness. The surface geometry follows that of the initial template except when the sample thickness becomes close to the diameter of the voids. Here, instead of encapsulating the cavities the structures form funnels leading from the top surface into the spherical cavities.

Both localised and delocalised surface plasmon modes have been found to exist on the samples and these different modes have been analysed in detail using a custom built computer controlled goniometer. Delocalised Bragg modes exist when the samples form arrays of shallow dishes and have been found to fit well with a weak-scattering model. An extension to this model is required as the sample thickness increases to account for the depth of the structures causing a perturbation of the mode energies. Bragg plasmons have been shown to scale linearly with pitch and refractive index as predicted. The polarisation dependence of the Bragg plasmon modes has also been studied. This data has been shown to be understood from a qualitative perspective through scattering and absorption of the plasmon modes.

Localised Mie plasmons have also, for the first time, been comprehensively studied. These modes have been found to be completely localised within the dishes even for weakly confining geometries. Figure 11.1a repeats a representative result from what is now understood about the Mie plasmon modes.

Around $\bar{t} = 1$ it is possible to compare the experimental data with theoretical electromagnetic calculations. Here, for increasing thicknesses the energy of the Mie plasmons

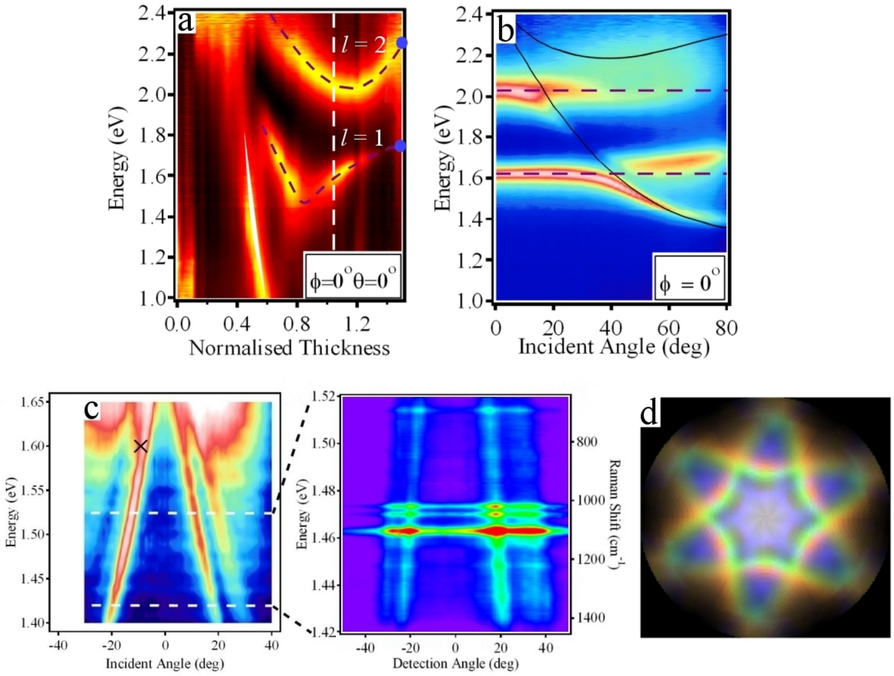

FIGURE 11.1: (a) Position map of gold sample with voids of diameter 500nm. Blue dots show predicted Mie plasmon modes, purple dashed lines act as a guide to eye, white dashed line shows where cut is taken in (b) a dispersion map. This shows two Mie modes - purple lines for guide to eye - and a Bragg mode - black lines show theory using model described previously in this thesis. Note the anti-crossing between the Mie and Bragg modes. (c) Comparison between reflectivity and Raman spectrum on a gold sample with a void diameter of 700nm. This proof of plasmon enhanced SERS leads to (d) the predicted Raman output off this surface if directly images in the back of a microscope objective. Three colours represent the energies of the 998cm^{-1} (red), 1573cm^{-1} (green), and 3055cm^{-1} (blue) Raman transitions.

increase towards that of a totally confined Mie scattered modes trapped within a dielectric bubble in an infinite expanse of metal. The increase in energy is associated with the increase in mode confinement and it has also been found that theoretical and experimental widths of these resonances compare well. Below the encapsulating geometry full analytical solutions to Maxwell's equations are not possible. However, this thesis has shown that the energetics of these modes can be understood through several more intuitive models. The first treats the Mie plasmon as an optical field within the cavity, obeying the principles of ray optics. The destructive interference between different ray paths is analysed and found to have similarities with the experimental data. This result is of interest because the cavities are sometimes smaller than the wavelength of light, where the ray-optics approximation is far from valid. This shows that, at least in this case, a system governed by wave equations can still be modelled in terms of classical rays. Comparisons between the electric field within the cavity predicted through ray-optics and finite different electromagnetic modelling show that many similarities still exist. Unfortunately, the ray-optics model does not take the plasmonic nature of the surfaces into account, and so does not faithfully reproduce the experimental data, although does predict the correct trends. Analysis has shown that this discrepancy indicates something of the true field distributions within the cavities.

The second model considered treats the Mie plasmons as SPP standing wave, pinned at the void rims. This model is only performed in two-dimensions and assumes the void rims are strict field minima. Even with this assumption the theory is quite accurate in its predictions for the energetics of the localised modes. Considering data sets from many samples has allowed the verification that the dispersion of the SPP is modified by the micro-curvature of the surfaces. This, it has been proposed, arises from the concentration of the electric field above the surface. Using the results obtained from analysing encapsulated voids it has been possible to construct a new dispersion for a curved metal surface, and this dispersion not only provides a universal scaling relationship for localised plasmons in dishes of arbitrary radius and thickness, but also provides a close fitting between the data and theory considering the standing wave SPP mode.

These two models have shown that the Mie plasmons observed experimentally can be considered as SPPs pinned on the void surfaces as well as an optical mode localised in free space. This is also backed up through considering the plasmons as mixtures of Mie scattered modes, and conceptually this is consistent with finite difference modelling of individual voids.

Further studies of these localised plasmons have found that the coupling to the optical field leads to interesting effects. Perfect absorption of the incident light has been observed in the highly localised modes near $\bar{t} = 1$, with at least 99% of the incident light coupled into the plasmon resonances. This is one of the first observations of tuneable perfect absorption through metallic structuring and directly leads to two interesting possibilities. The first is the perfect emission of black body radiation, a phenomenon directly relating to perfect absorption. This would allow the construction of perfectly emitting lighting elements as well as the removal of black body radiation in other spectra regions - such as the infra red to further increase device efficiency. The second possibility is that of perfect transmission. If the cavity were produced symmetrically within a thin film, light could be perfectly coupled from both sides, and so allow 100% transmission through the structure. This has been studied theoretically[72], and could be of potential interest for nano-lithographic techniques.

Further work has then been conducted on understanding the interactions between Bragg and Mie plasmons. It has been shown that the energies of Bragg plasmons are highly dependent on the angle of the incident light as well as the sample orientation. It has also been shown that the Mie plasmon energies can be independently controlled by altering the geometry of the structuring through a change of film thickness. This allows Bragg and Mie plasmons to be brought into and out of resonance with one another at will. Figure 11.1b shows data from a gold sample with a void diameter of 500nm at $\bar{t} = 1.1$. At this geometry and Mie plasmons are highly confined - indicated by the sharp resonances. The top surface also forms a good quality grating and so Bragg plasmons are also effectively excited. By altering the sample orientation the energy of the Bragg plasmons can be made to pass through that of the Mie plasmon, as shown. A strong coupling between the two types of plasmon is been observed, forming new mixed plasmon modes. This is the first observation of the interaction between localised and delocalised plasmons[44], and can be understood in terms of Mie plasmons hopping between voids and Bragg plasmons drop into the voids as they pass. A model for this mixing has been shown, considering the effect in terms of the dipolar interaction between surface charges. This model correctly predicts the effect of surface symmetry of the mode interactions. This mixing process is not only interesting from fundamental perspective but could also provide a means to control the flow of plasmons through a device, an essential component if a plasmonic computer is ever to be built.

Samples made from a variety of metals have also been studied. This has shown that the properties of the Bragg and Mie plasmons, as well as the mixing between the different plasmons, are altered depending on the properties of the metal used. This work is continuing into the study of structures made from multiple metal layer, allowing much greater control over the positioning of the plasmon modes on the surfaces. Tuning of the dielectric top layer has also been studied and relates precisely to that expected through theoretical considerations.

From this understanding of the electromagnetic properties of the nano-structured surfaces, other experiments have been undertaken. Interactions between SPP and excitons have been observed, leading to new mixed, strongly coupled, states. This mixing provides interesting possibilities to control and study exciton systems at room temperature. The coupling between excitons and plasmons leads to an enhancement in the observed fluorescence from the molecules, and could help improve the efficiencies of light emitting devices.

Finally, this thesis has explored the effect of surface enhanced Raman spectroscopy. While it has long been known that plasmons are an essential ingredient in producing large SERS signals this work has, for the first time, directly shown plasmons enhancing the observed Raman spectra[45], as repeated in figure 11.1c. Furthermore, it has been found that the nano-structured surfaces produce enhancement factors similar to those in the literature, while producing much better reproducibility. This reproducibility is at every point on the surface (something not possible with the samples made from colloids) but also is stable for time spans of at least years after many cleanings and different chemical treatments; again by comparison most other SERS surfaces can only be used once, may provide enhancements for about a month, and cannot be cleaned or reused.

The angle resolved data shown in this thesis is extremely useful for starting to gain a full understanding into the SERS process. This work has shown that while the plasmon modes are essential to SERS, they only directly contribute one order of magnitude (at both input and output resonances) to the observed signal. This leads to the proposal that the SPP waves themselves couple to highly localised plasmons, probably of the nanometre size scale. These localised states couple very poorly to light and so are inactive on smooth gold but couple well to the molecules on the surface. It is thus necessary to have both large and small scale plasmons to efficiently couple an optical field to a molecule and observe a strong Raman signal.

The ability to tune both the localised and delocalised plasmons directly through sample geometry and angle of incident light makes it possible to optimise the SERS signals from different Raman lines. This can be done by specifying the laser wavelength and molecule to be studied. A plasmon resonance can then be adjusted through, for example, tuning a localised plasmon to the laser wavelength by setting the sample pitch and thickness. The sample orientation can then be set to match the wavelength of the Bragg plasmon with the Raman line of interest. The output resonance can then be observed at the correct output angle - given by the Bragg plasmon dispersion.

A further advancement on this has been proposed and is shown in figure 11.1d. Here, it is shown through simulation of the plasmon dispersions that it is possible to simultaneously optimise the enhancement of three different Raman lines. It is then possible to send the light from each line to different directions to be detected by a single CCD camera. This data multiplexing idea could further speed up molecular detection applications.

The use of more controlled processing techniques, such as photolithography, would improve the quality of ordering; however, such processes are, at least currently, not capable of producing spherical geometries. Of greater importance, the gain in the sharpness of a Bragg plasmon resonance for a precisely defined structure comes at the cost of a much more expensive and time consuming production process. Hence, it is concluded that the surfaces studied in this thesis have great potential for future molecular sensor applications.

This thesis has provided answers to many of the original questions posed on the true energetics of surface plasmon on nano-structured metal surface. There are, of course, many questions still to be answered. Some of these questions have reached a more theoretical region of study, in, for example, the mathematical understanding of the Mie modes or the full understanding of the SERS processes.

Other questions require further experimentation to be performed, as commented throughout this thesis. These experiments are mainly concerned with more complex sample architectures, such as the multilayer metal structures, which have been mentioned but are currently at a preliminary stage of experiments.

Towards further applications, there are a number of possible paths. There is interest in using the structures to produce nano-scale resonators[132], which, if filled with a gain medium, could form ultra-low threshold lasers. There are also other sample architectures that could be of great interest for different applications. A combination of photolithography and template self-assembly could allow the production of plasmon waveguides and integrated circuits. If the coupling between Bragg and Mie plasmons could be controlled many interesting systems can also be envisaged. Further work on the optimisation of SERS substrates could be very useful for future sensor applications and the enhanced emission from catalytic metals such as platinum is also of great practical use.

Appendix A

Derivations

A.1 Finding Electric Charge Density

Using the material equations stated in chapter 2 (equation 2.5), Maxwell's equations take the form:

$$\nabla \cdot \mathbf{H} = 0 \tag{A.1}$$

$$\nabla \cdot \mathbf{E} = \frac{\rho}{\epsilon} \tag{A.2}$$

$$\nabla \times \mathbf{E} + \mu \frac{\delta \mathbf{H}}{\delta t} = 0 \tag{A.3}$$

$$\nabla \times \mathbf{H} - \epsilon \frac{\delta \mathbf{E}}{\delta t} = \sigma \mathbf{E} \tag{A.4}$$

Taking the divergence of equation A.4 leads to:

$$\nabla \cdot (\nabla \times \mathbf{H}) - \epsilon \nabla \cdot \frac{\delta \mathbf{E}}{\delta t} = \sigma \nabla \cdot \mathbf{E} \tag{A.5}$$

Since $\nabla \cdot (\nabla \times \mathbf{H}) = 0$, equation A.5 can be substituted into equation A.2 to give:

$$-\frac{\epsilon}{\sigma} \nabla \cdot \frac{\delta \mathbf{E}}{\delta t} = \frac{\rho}{\epsilon} \tag{A.6}$$

This equation can be compared to the temporal differentiation of equation A.2:

$$\nabla \cdot \frac{\delta \mathbf{E}}{\delta t} = \frac{1}{\epsilon} \frac{\delta \rho}{\delta t} \tag{A.7}$$

Now $\frac{\delta \mathbf{E}}{\delta t}$ can be eliminated between eqautions A.6 and A.7 leading to:

$$-\frac{\sigma \rho}{\epsilon} = \frac{\delta \rho}{\delta t} \tag{A.8}$$

This equation can only be valid if ρ takes the form:

$$\rho = \rho_0 e^{-t/\tau} \quad \text{where} \quad \tau = \frac{\epsilon}{\sigma} \tag{A.9}$$

As quoted in chapter 3.

Bibliography

[1] Barnes, W., Dereux, A. & Ebbesen, T. Surface plasmon subwavelength optics. *Nature* **424**, 824 (2003).

[2] Kitson, S., Barnes, W. & Sambles, J. Full photonic band gap for surface modes in the visible. *Phys. Rev. Lett.* **77**, 2670 (1996).

[3] Weeber, J.-C. *et al.* Near-field observation of surface plasmon polariton progagation on thin metal stripes. *Phys. Rev. B.* **64**, 045411 (2001).

[4] Lezec, H. *et al.* Beaming light from a subwavelength aperture. *Science* **297**, 820 (2002).

[5] Vukusic, P. & Sambles, J. Photonic structures in biology. *Nature* **424**, 852 (2003).

[6] Joannopoulos, J., Meade, R. & Winn, J. *Photonic Crystals, Molding the Flow of Light* (Princeton University Press, 1995).

[7] http://www.buy-gemstones.com.

[8] http://www.webelements.com.

[9] http://www.ece.rice.edu/halas/index.html.

[10] Fukui, M. & Ohtsi, M. *Introduction to Optical Nanotechnology* (Ohmsha, 2003).

[11] Teperik, T., Popov, V. & de Abajo, F. G. Void plasmons and total absorption of light in nanoporous metallic films. *Phys. Rev. B.* **71**, 085408 (2005).

[12] Coyle, S., Prakash, G., Baumberg, J., Abdelsalam, M. & Bartlett, P. Spherical micro-mirrors from templated self-assembly: Geometric reflectivity on the micron scale. *Appl. Phys. Lett.* **83**, 767 (2003).

[13] http://www.zyvex.com/nanotech/feynman.html.

[14] Ritchie, R. Plasma losses by fast electrons in thin films. *Phys. Rev.* **106**, 874 (1957).

[15] Ebbesen, T., Lezec, H., Ghaemi, H., Thio, T. & Wolff, P. Extraordinary optical transmission through sub-wavelength hole arrays. *Nature* **391**, 667 (1998).

[16] Shao, D. & Chen, S. Surface-plasmon-assisted nanoscale photolithograph by polarized light. *Appl. Phys. Lett.* **86**, 253107 (2005).

[17] Westcott, S., Jackson, J., Radloff, C. & Halas, N. Relative contributions to the plasmon line shape of metal nanoshells. *Phys. Rev. B.* **66**, 155431 (2002).

[18] Stockman, M., Faleev, S. & Bergman, D. Localization versus delocalization of surface plasmons in nansystems: Can one state have both characteristics? *Phys. Rev. Lett.* **87**, 167401 (2001).

[19] Nie, S. & Emory, S. Probing single molecules and single nanoparticles by surface-enhanced Raman scattering. *Science* **275**, 1102 (1997).

[20] Kneipp, K., Wang, Y., Kneipp, H., Perelman, L. & Itzkan, I. Single molecule detection using surface-enhanced Raman scattering (SERS). *Phys. Rev. Lett.* **78**, 1667 (1997).

[21] http://www.mesophotonics.com.

[22] Cao, Y., Jin, R. & Mirkin, C. Nanparticles with Raman spectroscopic fingerprints for DNA and RNA detection. *Science.* **297**, 1536 (2002).

[23] Sze, S. *Physics of Semiconductor Devices* (John Wiley and Sons, New York, 1981).

[24] Yablonovitch, E. Inhibited spontaneous emission in solid state physics and electronics. *Phys. Rev. Lett.* **58**, 2059 (1987).

[25] John, S. Strong localization of photons in certian disordered dielectric superlattices. *Phys. Rev. Lett.* **58**, 2486 (1987).

[26] Born, M. & Wolf, E. *Principles of Optic, 7th edition, Electromagnetic Theory of Propagation, Interference and Diffraction of Light* (Cambridge University Press, 1999).

[27] Lin, S.-Y., Chow, E., Hietala, V., Villeneuve, P. & Joannopoulos, J. Experimental demonstration of guiding and bending of electromagnetic waves in a photonic crystal. *Science* **282**, 274 (1998).

[28] Wu, L., Gallet, J.-F. & Krauss, T. Dual lattice photonuc-crystal beam splitter. *Appl. Phys. Lett.* **86**, 211106 (2005).

[29] Liu, C.-Y. & Chen, L.-W. Tunable photonic-crystal waveguide machzehnder interferometer achieved bynematic liquid-crystal phase modulation. *Opt. Express.* **12**, 2616 (2004).

[30] Villa, F., Regalado, L., Ramos-Mendieta, F., Gaspar-Armenta, J. & Lopez-Ríos, T. Photonic crystal sensor based on surface waves for thin-film characterization. *Opt. Lett.* **27**, 646 (2002).

[31] Englund, D. *et al.* Controlling the spontaneous emission rate of single quantum dots in a two-dimensional photonic crystal. *Phys. Rev. Lett.* **95**, 013904 (2005).

[32] Hennessy, K., Badolato, A., Petroff, P. & Hu, E. Positioning photonic crystal cavities to single InAs quantum dots. *Photonic. Nanostruct:- Fund. Appl.* **2**, 65 (2004).

[33] Yamamoto, N., Noda, S. & Sasaki, A. New realization method for three-dimensional photonic crystal in the optical wavelength region: Experimental consideration. *Jpn. J. Appl. Phys.* **36**, 1907 (1997).

[34] Yablonovitch, E., Gmitter, T. & Leung, K. Photonic band structure: The face-centered case employing nonspherical atoms. *Phys. Rev. Lett.* **67**, 2295 (1991).

[35] Johnson, S. & Joannopoulos, J. Three-dimensionally periodic dielectric layered structure with omnidirectional photonic band gap. *Appl. Phys. Lett.* **77**, 3490 (2000).

[36] Toader, O., Berciu, M. & John, S. Photonic band gaps based on tetagonal lattices of slated pores. *Phys. Rev. Lett.* **90**, 233901 (2003).

[37] Velev, O., Tessier, P., Lenhoff, A. & Kaler, E. Materials: A class of porous metallic nanostructures. *Nature.* **389**, 447 (1997).

[38] Busch, K. & John, S. Photonic band gap in certain self-organizing systems. *Phys. Rev. E.* **58**, 3896 (1998).

[39] Norris, D. & Vlasov, Y. Chemical approaches to three-dimensional semiconductor photonic crystals. *Adv. Mater.* **13**, 371 (2001).

[40] Johnson, S., Ollivier, P. & Mallouk, T. Ordered mesoporous polymers of tunable pore size from colloidal silica templates. *Science.* **283**, 963 (1999).

[41] Bartlett, P., Baumberg, J., Birkin, P., Ghanem, M. & Netti, M. Highly ordered macroporous gold and platinum films formed by electrochemical deposition through templates assembled from submicron diameter monodisperse polystyrene spheres. *Chem. Mater.* **14**, 2199 (2002).

[42] John, S. & Busch, K. Photonic bandgap formation and tunability in certain self-organizing systems. *J. Lightwave. Technol.* **17**, 1931 (1999).

[43] Lin, Y., Herman, P. & Darmawikarta, K. Design and holographic fabrication of tetragonal and cubic photonic crystals with phase mask: toward the mass-production of three-dimensional photonic crystals. *Appl. Phys. Lett.* **86**, 071117 (2005).

[44] Kelf, T., Sugawara, Y., Baumberg, J., Abdelsalam, M. & Bartlett, P. Plasmonic bandgaps and trapped plasmons on nanostructured metal surfaces. *Phys. Rev. Lett.* **95**, 116802 (2005).

[45] Baumberg, J. *et al.* Angle-resolved surface-enhanced Raman scattering on metallic nanostructured plasmonic crystals. *Nano. Lett.* **5**, 2262 (2005).

[46] Faraday, M. The bakerian lecture: Experimental relations of gold (and other metals) to light. *Phil. Trans.* **147**, 145 (1835).

[47] Kupratakuln, S. & Fletcher, G. Electron band structure of gold. *J. Phys. C.* **2**, 1886 (1969).

[48] Suffczynski, M. Optical constants of metals. *Phys. Rev.* **117**, 663 (1960).

[49] Lynch, D. & Hunter, W. *Comments on the Optical Constants of Metals and an Introduction to the Data for Several Metals* (Academic Press, Boston, 1985).

[50] Johnson, P. & Christy, R. Optical constants of the nobal metals. *Phys. Rev. B.* **6**, 4370 (1972).

[51] Ordal, M. *et al.* Optical properties of the metals Al, Co, Cu, Au, Fe, Pb, Ni, Pd, Pt, Ag, Ti and W in the infrared and far infrared. *Appl. Optics.* **22**, 1099 (1983).

[52] Sambles, J., Bradbery, G. & Yang, F. Optical excitation of surfrace plasmons: an introduction. *Contemp. Phys.* **32**, 173 (1991).

[53] Barker, A. Optical measurements of surface plasmons in gold. *Phys. Rev. B.* **8**, 5418 (1973).

[54] Raether, H. *Surface Plasmons on Smooth and Rough Surfaces and on Gratings* (Springer-Verlag, 1988).

[55] Nash, D. & Sambles, J. Simultaneous observation of surface plasmons on both sides of thin silver films. *J. Mod. Optic.* **46**, 1793 (1999).

[56] Craig, A., Olson, G. & Sarid, D. Experimental observation of the long-range surface-plasmon polariton. *Opt. Lett.* **8**, 380 (1983).

[57] Hessel, A. & Oliner, A. A new theory of wood's anomalies on optical gratings. *Appl. Optics.* **4**, 1275 (1965).

[58] Barnes, W., Preist, T., Kitson, S. & Sambles, J. Physical origin of photonic energy gaps in the propagation of surface plasmons on gratings. *Phys. Rev. B.* **54**, 6227 (1996).

[59] Hooper, I. & Sambles, J. Surface plasmon polaritons on thin-slab metal gratings. *Phys. Rev. B.* **67**, 235404 (2003).

[60] Christ, A., Zentgraf, T. & Kuhl, J. Optical properties of planar photonic crystal structures: Experiment and theory. *Phys. Rev. B.* **70**, 125113 (2004).

[61] Kreiter, M., Mittler, S., Knoll, W. & Sambles, J. Surface plasmon-related resonances on deep and asymmetric gold gratings. *Phys. Rev. B.* **65**, 125415 (2002).

[62] Hooper, I. & Sambles, J. Dispersion of surface plasmon polaritons on short-pitch metal gratings. *Phys. Rev. B.* **65**, 165432 (2002).

[63] Watts, R., Preist, T. & Sambles, J. Sharp surface-plasmon resonaces on deep diffraction gratings. *Phys. Rev. Lett.* **79**, 3978 (1997).

[64] Perney, N. *et al.* Tuning localized plasmons in nanostructured substractes for surface-enhanced Raman scattering. *Opt. Express.* **14**, 847 (2005).

[65] Teperik, T., Popov, V. & de Abajo, F. G. Radiative decay of plasmons in a metallic nanoshell. *Phys. Rev. B.* **69**, 155402 (2004).

[66] Bohren, C. & Huffman, D. *Absorption and Scattering of Light by Small Particles* (John Wiley and Sons, New York, 1998).

[67] Boardman, A. *Electromagnetic Surface Modes* (John Wiley and Sons, New York, 1982).

[68] Lucas, A. Plasmon cohesive energy of voids and void lattices in irradiated metals. *Phys. Rev. B.* **7**, 3527 (1973).

[69] Coyle, S. *et al.* Confined plasmons in metallic nanocavities. *Phys. Rev. Lett.* **87**, 176801 (2001).

[70] Netti, M. *et al.* Confined surface plasmons in gold photonic nanocavities. *Adv. Mater.* **13**, 1368 (2001).

[71] Teperik, T., Popov, V. & de Abajo, F. G. Giant light absorption by plasmons in a nanoporous metal film. *Phys. Status. Solidi A.* **202**, 362 (2005).

[72] de Abajo, F. G., Gomez-Santos, G., Blanco, L., Borisov, A. & Shabanov, S. Tunneling mechanism of light transmission through metallic films. *Phys. Rev. Lett.* **95**, 067403 (2005).

[73] Homola, J., Yee, S. & Gauglitz, G. Surface plasmon resonace sensors: review. *Sensor. Actuat. B-Chem.* **54**, 3 (1999).

[74] Zayats, A. & Smolyaninov, I. Near-field photonics: surface plasmon polaritons and localized surface plasmons. *J. Opt. A: Pure Appl. Opt.* **5**, 16 (2003).

[75] Lezec, H. & Thio, T. Diffracted evanescent wave model for enhanced and suppressed optical transmission through subwavelength hole arrays. *Opt. Express.* **12**, 3629 (2004).

[76] Cao, Q. & Lalanne, P. Negative role of surface plasmons in the transmission of metallic gratings with very narrow slits. *Phys. Rev. Lett.* **88**, 057403 (2002).

[77] Ditlbacher, H., Kren, J., Schider, G., Leitner, A. & Aussenegg, F. Two-dimensional optics with surface plasmon polaritons. *Appl. Phys. Lett.* **81**, 1762 (2002).

[78] Maier, S. *et al.* Plasmonics - a route to nanoscale optical devices. *Adv. Mater.* **13**, 1501 (2001).

[79] Tanaka, K. & Tanaka, M. Simulations of nanometric optical circuits based on surface plasmon polariton gap waveguides. *Appl. Phys. Lett.* **82**, 1158 (2003).

[80] http://www.nanoplextech.com/index.html.

[81] Okamoto, K. *et al.* Surface-plasmon-enhanced light emitters based on ingan quantum wells. *Nat. Mater.* **3**, 601 (2004).

[82] Gruhlke, R., Holland, W. & Hall, D. Surface-pasmon cross coupling in molecular fluorescence near a corrugated thin metal film. *Phys. Rev. Lett.* **56**, 2838 (1986).

[83] Bartlett, P., Baumberg, J., Coyle, S. & Abdelsalam, M. Optical properties of nanostructured metal films. *Faraday Discuss.* **125** (2003).

[84] Zoorob, M., Charlton, M., Parker, G., Baumberg, J. & Netti, M. Complete photonic bandgaps in 12-fold symmetric quasicrystals. *Nature.* **404**, 740 (2000).

[85] Dimitrov, A., Miwa, T. & Nagayama, K. A comparison between the optical properties of amorphous and crystalline monolayers of silica particles. *Langmuir.* **15**, 5257 (1999).

[86] Liang, Z., Susha, A. & Caruso, F. Metallodielectric opals of layer-by-layer processed coated colloids. *Adv. Mater.* **14**, 1160 (2002).

[87] Abdelsalam, M., Bartlett, P., Kelf, T. & Baumberg, J. Wetting of regularly structureed gold surfaces. *Langmuir* **21**, 1753 (2005).

[88] Wenzel, R. Resistance of solid surfaces to wetting by water. *Ind. Eng. Chem.* **28**, 988 (1936).

[89] Cassie, A. & Baxter, S. Wettability of porous surfaces. *Faraday Discuss.* **40**, 546 (1944).

[90] http://www.blazephotonics.com.

[91] Corporation, N. *Diffraction Grating Handbook* (NewPort, 2005).

[92] Watts, R. & Sambles, J. Polarization conversion from blazed diffraction gratings. *J. Mod. Optic.* **44**, 1231 (1997).

[93] Bryan-Brown, G. & Sambles, J. Polarization conversion through the excitation of surface plasmons on a metallic gratings. *J. Mod. Optic.* **37**, 1227 (1997).

[94] Greffet, J.-J. *et al.* Coherent emission of light by thermal sources. *Nature.* **416**, 61 (2002).

[95] Coyle, S. *Chameleon Metals - Investigating The Response To Light Of Sub-Wavelength Metallic Meshes* (Ph.D Thesis, University of Southampton, UK, 2004).

[96] Ackemann, T., Grosse-Nobis, W. & Lippi, G. The gouy phase shift, the average phase lag of fourier components of hermite-gaussian modes and their application to resonance conditions in optical cavities. *Opt. Commun.* **189**, 5 (2001).

[97] Hariharan, P. & Robinson, P. The gouy phase shift as a geometrical quantum effect. *J. Mod. Optic.* **43**, 219 (1996).

[98] Skigin, D. & Depine, R. Surface shape resonances and surface plasmon polariton excitations in bottle-shaped metallic gratings. *Phys. Rev. E.* **63**, 046608 (2001).

[99] Ashkin, A. Optical trapping and manipulation of neutral particles using lasers. *P. Natl. Acad. Sci. USA.* **94**, 4853 (1997).

[100] Schuck, P., Fromm, D., Sundaramurthy, A., Kino, G. & Moerner, W. Improving the mismatch between light and nanoscale objects with gold bowtie nanoantennas. *Phys. Rev. Lett.* **94**, 017402 (2005).

[101] Tian, Z.-Q. *et al.* Surface-enhanced raman scattering from transition metals with special surface morphology and nanoparticle shape. *Faraday. Discuss.* **132** (2005).

[102] http://www.philiplaven.com/p20.html.

[103] Campion, A. & Kambhampati, P. Surface-enhanced Raman scattering. *Chem. Soc. Rev.* **27**, 241 (1998).

[104] Xu, H., Bjerneld, E., Kall, M. & Borjesson, L. Spectroscopy of single hemoglobin molecules by surface enhanced Raman scattering. *Phys. Rev. Lett.* **83**, 4357 (1999).

[105] Kneipp, K., Kneipp, H., Itzkan, I., Dasari, R. & Feld, M. Surface-enhanced Raman scattering and biophysics. *J. Phys.: Condens. Matter.* **14**, 597 (2002).

[106] Fleischmann, M., Hendra, P. & McQuillan, A. Raman spectra of pyridine adsorbed at a silver electrode. *Chem. Phys. Lett.* **26**, 163 (1974).

[107] Abdelsalam, M. *et al.* Electrochemical SERS at a structured gold surface. *Electrochem. Commun.* **7**, 740 (2005).

[108] Szymanski, H. *Raman Spectroscopy, Theory and Practice* (Plenum Press, 1967).

[109] Li, W.-H., Li, X.-Y. & Yu, N.-T. Surface-enhanced resonance hyper-Raman scattering and surface-enhanced resonance Raman scattering of dyes adsorbed on silver electrode and silver colloid: a comparison study. *Chem. Phys. Lett.* **312**, 28 (1999).

[110] Jeanmaire, D. & Duyne, R. V. Surface Raman spectroelectrochemistry part i. heterocyclic, aromatic, and aliphatic amines adsorbed on the anodized silver electrode. *J. Electroanal. Chem.* **84**, 1 (1977).

[111] Albrecht, M. & Creighton, J. Anomalously intense Raman spectra of pyridine at a silver electrode. *J. Am. Chem. Soc.* **99**, 5215 (1977).

[112] Otto, A. *Surface-Enhanced Raman scattering: 'classical' and 'chemical' origins, Topics of Applied Physics 54, 'Light Scattering in Solids', Vol. IV, M* (Springer, 1984).

[113] Moskovits, M. Surface-enhanced spectroscopy. *Rev. Mod. Phys.* **57**, 783 (1985).

[114] Etchegoin, P. *et al.* Electromagnetic contribution to surface enhanced Raman scattering revisited. *J. Chem. Phys.* **119**, 5281 (2003).

[115] Kurosawa, K., Pierce, R., Ushioda, S. & Hemminger, J. Raman scattering and attenuated-total-reflection studies of surface-plasmon polaritons. *Phys. Rev. B.* **33**, 789 (1986).

[116] García-Vidal, F. & Pendry, J. Collective theory for surface enhanced Raman scattering. *Phys. Rev. Lett.* **77**, 1163 (1996).

[117] Kambhampati, P., Child, C., Foster, M. & Campion, A. On the chemical mechanism of surface enhanced Raman scattreing: Experiment and theory. *J. Chem. Phys.* **108**, 5013 (1998).

[118] Otto, A. Theory of first layer and single molecule surface enhanced Raman scattering (SERS). *Phys. Stat. Sol.* **188**, 1455 (2001).

[119] Szafranski, C., Tanner, W., Laibinis, P. & Garrell, R. Surface-enhanced Raman spectroscopy of aromatic thiols and disulfides on gold electrodes. *Langmuir* **14**, 3570 (1998).

[120] Han, S., Lee, S. & Kim, K. Self-assembled monolayers of aromatic thiol and selenol on silver: Comparative study of adsorptivity and stability. *Langmuir* **17**, 6981 (2001).

[121] Tian, Z.-Q., Ren, A.-B. & Wu, D.-Y. Surface-enhanced Raman scattering: From nobal to transition metals and from rough surfaces to ordered nanstructures. *J. Phys. Chem. B.* **106**, 9463 (2002).

[122] Woods, R. & Bard, A. *Electroanalytical Chemistry: A Series of Advances, vol. 9* (Marcel Dekker, New York, 1980).

[123] Cintra, S. *et al.* Sculpted substrates for SERS. *Faraday. Discuss.* **132** (2005).

[124] Félidj, N. *et al.* Optimised surface-enhanced Raman scattering on gold nanoparticle arrays. *Appl. Phys. Lett.* **82**, 3095 (2003).

[125] Brown, R., Wang, J., Tantra, R., Yardley, R. & Milton, M. Electromagnetic modelling of Raman enhancement from nanoscale substrates: a route to estimation of the magnitude of the chemical enhancement mechanism in SERS. *Faraday. Discuss.* **132**, 17 (2005).

[126] Maher, R. *et al.* Stokes/anti-stokes anomalies under surface enhanced Raman scattreing conditions. *J. Chem. Phys.* **120**, 11746 (2004).

[127] Patent: Metal nano-void substrate for enhanced Raman spectroscopy. university of southampton, p20976gb.

[128] Bellessa, J., Bonnand, C. & Plenet, J. Strong coupling between surface plasmons and excitons in an organic semiconductor. *Phys. Rev. Lett.* **93**, 036404 (2004).

[129] Dintinger, J., Klein, S., Bustos, F., Barnes, W. & Ebbesen, T. Strong coupling between surface plasmon-polaritons and organic molecules in subwavelength hole arrays. *Phys. Rev. B.* **71**, 035424 (2005).

[130] Finlayson, C., Prakash, G. & Baumberg, J. Strong exciton-photon coupling in a length tunable optical microcavity with J-aggregate dye heterostructures. *Appl. Phys. Lett.* **86**, 041110 (2005).

[131] Ikegami, K. Spectroscopic study of J aggregates of amphiphilic merocyanine dyes formed in their Langmuir films. *J. Chem. Phys.* **121**, 2337 (2004).

[132] Prakash, G. *et al.* Tunable resonant optical microcavities by self-assembled templating. *Opt. Lett.* **29**, 1500 (2004).